

An Investigation of Polymer Support Structures in Metal Directed Energy Deposition

by

Rebecca Ann Kurfess

B.S., Massachusetts Institute of Technology (2017)

S.M., Massachusetts Institute of Technology (2019)

Submitted to the Department of Mechanical Engineering
in partial fulfillment of the requirements for the degree of

Doctor of Philosophy

at the

MASSACHUSETTS INSTITUTE OF TECHNOLOGY

June 2023

© Rebecca Kurfess. All rights reserved.

The author hereby grants to MIT a nonexclusive, worldwide, irrevocable, royalty-free license to exercise any and all rights under copyright, including to reproduce, preserve, distribute, and publicly display copies of the thesis, or release the thesis under an open-access license.

Author
Department of Mechanical Engineering
March 24, 2023

Certified by
Anastasios John Hart
Professor of Mechanical Engineering
Thesis Co-Supervisor

Certified by
David Hardt
Professor of Mechanical Engineering
Thesis Co-Supervisor

Accepted by
Nicolas Hadjiconstantinou
Chairman, Department Committee on Graduate Theses

An Investigation of Polymer Support Structures in Metal Directed Energy Deposition
by
Rebecca Kurfess

Submitted to the Department of Mechanical Engineering
on March 24, 2023 in partial fulfillment of the
requirements for the degree of
Doctor of Philosophy

Abstract

Metal directed energy deposition (DED) can create complex components and has a high deposition rate compared to other metal additive manufacturing (AM) processes. As a result, DED is of interest to die and mold, energy, and aerospace industries, among others. However, the design space of DED is limited: overhangs steeper than 20° and freestanding bridge geometries are typically difficult or impossible to manufacture without support structures. The difficulty of support deposition and removal in DED necessitates that DED manufacturing of large components is restricted to geometries that do not require supports. The use of a dissimilar material, such as a polymer, as a support would enable lower cost, easily removable supports. The suitability of polymers as substrates in DED has not been explored due to two key unknowns: (1) the effect of the metal DED process on a polymer substrate and (2) the effect of a polymer substrate on the deposited metal. This research investigates the viability of polymers as supports in laser blown-powder DED, providing guidelines for polymer selection and print strategy to avoid detrimental polymer degradation, unsafe combustion conditions, and negative impacts of using a dissimilar substrate on the deposited metal DED component.

An understanding of combustion in the polymer/DED interaction due to laser interactions with the polymer was developed, and a tradeoff between polymer degradation and metal deposition quality was discovered. For successful DED deposition to occur, the polymer must have a high absorptivity: the polymers that facilitated deposition of 316L stainless steel in this research had absorbances greater than 2 absorbance units. Polymers with high temperature fillers, such as glass fibers or carbon fibers, were shown to be effective in mitigating the extreme thermal conditions experienced by the polymer during deposition. Degradation of polymers was measured in a series of single-bead experiments, and a series of thermal models was developed to show the influence of DED parameters and polymer material properties on the penetration of heat into the polymer substrate. Both the experimental measurements and thermal model predictions indicated degradation on the order of 1mm, an acceptable level of degradation. An understanding of the effect of a polymer substrate (CF ABS) on the hardness, microstructure, and porosity of a deposited metal (316L stainless steel) was established. Porosity of the metal was observed due the entrapment of gas from polymer degradation in the molten deposited metal. Carbon from the polymer migrated into the molten metal, causing carbide formation and increasing the hardness of the deposited metal by approximately 70% compared to the expected value. To mitigate these effects, specimens were fabricated with an interlayer cooling time,

lowering the overall temperature of the deposited component and decreasing the time spent by the component at higher temperatures. The mitigation strategy was proven to reduce hardness to the expected level for 316L stainless steel manufactured with DED. Additionally, the introduction of an interlayer cooling time prevented much of the gas due to polymer degradation from infiltrating the metal component, reducing porosity from gas entrapment and cutting overall porosity from 8% to 4%.

The above findings were integrated to produce a bridge component using a polymer support structure. Overall, this research provided a methodology for selecting polymer materials, print parameters, and print strategies to enable the deposition of 316L stainless steel on CF ABS, laying the foundation for polymer support structures in metal DED.

Thesis Supervisors: Anastasios John Hart and David Hardt
Title: Professors of Mechanical Engineering

Acknowledgements

I could not have completed this research without the help and support of so many people. Dad, thank you for inspiring me to pursue engineering and pushing me to get this work done. Mom, thank you for reminding me that it's okay to relax. Alex and Greg, thanks for being pretty cool brothers. Thank you to all of my extended family, including all the in-laws: you've all been an incredible support network.

All my appreciation to my friends and colleagues who encouraged me, brainstormed with me, and on more than one occasion, provided incredibly valuable engineering expertise. At the MDF, Celeste, Aimee, Kristin, Josh, Sara, Rangasayee, Ryan, Dennis, Tom, Matt, Meghan, and so many more. At MIT, Bethany, Lucy, Fiona, Ashley, Kaitlyn, Hannah, Judith, Lee, John, Leo, and again, so many more. Thank you to Kyle for his aggressive assistance and to Regan – enjoy Atlanta!

Thank you to the Mechanosynthesis Group and to my committee: John, Dave, Lonnie, and Ase. The effort that each of you put into my research made it the work it is today.

Finally, all my thanks and love to Austin. You and the pups kept me sane throughout this process, and your love and support has made all the difference in my life.

TABLE OF CONTENTS

Chapter 1. Introduction	21
1.1 Overview of directed energy deposition (DED)	21
1.2 DED design limitations	21
1.3 Research aims and objectives	22
1.4 Thesis organization	23
Chapter 2. Polymer interactions with directed energy deposition	25
2.1 Introduction.....	25
2.2 Background	25
2.2.1 Directed energy deposition and hybrid manufacturing.....	25
2.2.2 Lasers	37
2.3 Laser-polymer characterization	44
2.3.1 Laser spectroscopy.....	45
2.3.2 Haas/HMT hybrid system.....	45
2.3.3 Setup and procedure.....	48
2.4 Results and discussion	50
2.4.1 Polymer absorptivity	50
2.4.2 Polymer combustion	52
2.4.3 Post-printing observations	59
2.5 Conclusions.....	68
Chapter 3. Measurement and modeling of polymer degradation during DED metal deposition.....	71
3.1 Introduction.....	71
3.2 Background.....	71
3.2.1 Polymer combustion	71
3.2.2 Semi-infinite modeling and Rosenthal moving heat source	72

3.3 Methodology	74
3.3.1 Design of experiments	74
3.3.2 Setup and procedure.....	76
3.4 Polymer degradation results.....	77
3.5 Model development and discussion	83
3.5.1 Semi-infinite implementation	83
3.5.2 Rosenthal moving heat source implementation	93
3.5.3 Discussion	98
3.6 Conclusions.....	106
Chapter 4. Effect of polymer substrate on printed metal	107
4.1 Introduction.....	107
4.2 Background.....	107
4.2.1 316L stainless steel	107
4.2.2 Carbide formation	114
4.2.3 Porosity in DED.....	115
4.3 Experiments	117
4.4 Results and discussion	119
4.4.1 Porosity	119
4.4.2 Hardness effects.....	124
4.5 Conclusions.....	125
Chapter 5. Mitigation of polymer effects on deposited metal by interlayer cooling time	127
5.1 Introduction.....	127
5.2 Background.....	127
5.3 Methodology	129

5.4 Results and discussion	130
5.5 Conclusions.....	138
Chapter 6. Polymer support demonstration	139
6.1 Introduction.....	139
6.2 Methodology	139
6.3 Results and discussion	140
6.4 Conclusions.....	143
Chapter 7. Conclusions	145
Chapter 8. Future work	147
Appendix A. Failed PEEK substrate.....	149
Appendix B. G-code	151
B.1 Single-layer experiments.....	151
B.1.1 400mm/min trials	151
B.1.2 800mm/min trials	152
B.2 Metal characterization experiments	153
B.2.1 No interlayer cooling time.....	153
B.2.2 10 second interlayer cooling time	157
B.2.3 30 second interlayer cooling time	161
Appendix C. Single bead test images	167
Appendix D. Thermal circuit modeling.....	185
D.1 Background	185
D.2 Thermal circuit implementation.....	186
D.2.1 Single layer metal deposition model.....	186
D.2.2 Multi-layer metal deposition model.....	198
Appendix E. Thermal model results	211

List of Figures

Figure 1: The (a) powder bed fusion, (b) binder jetting, (c) blown-powder directed energy deposition, and (d) wire-fed directed energy deposition metal additive manufacturing processes. 26

Figure 2: The resolution versus part size for the four metal AM processes [2, 9]. Increasing part size generally results in decreased resolution. 26

Figure 3: DED systems can be classified by both the type of feedstock material and the energy source used [14]. 27

Figure 4: Examples of a (a) blown powder DED system and (b) wire-fed DED system. 28

Figure 5: The effect of varying linear energy of deposition in single-bead, single-layer wire-fed DED experiments [19]. 29

Figure 6: DED is generally limited to (a) overhang angles of 20° or less, and (b) bridged structures and (c) steep overhangs are impossible without supports. 30

Figure 7: Toolpaths generated by the decomposition-based curved slicing method, which reduces the need for support structures in DED but requires a 5-axis system [24]. 31

Figure 8: 3D scans of actual DED print (green) overlaid onto CAD model (red), with excess end segments trimmed off, for a component made (a) without adaptive process control and (b) with adaptive process control, demonstrating the success of this method in increasing possible overhang angle [26]. 32

Figure 9: Digital images of the sample taken before, during, and after etching. (a) Before etching, the red square roughly outlines where the carbon steel support layer was printed. (b) After 10 hours of etching, 1.4mm of carbon steel was removed from each side. (c) After etching showing that the carbon steel was completely etched from the sample. (d) Images of sidewall and bottom with lines etched into a chromium-depleted layer of the component and stainless steel baseplate, where the carbon steel leached the chromium during printing [31]. 33

Figure 10: Two commercially available hybrid systems are (a) Mazak’s wire-arc DED and machining system and (b) Okuma’s blown-powder and machining system. It is also possible to retrofit machine tools with additive capabilities, as (c) HMT did with a Haas machine tool..... 34

Figure 11: A hybrid-manufactured component that has been partially machined. DED was used for the initial shape, and machining was used to obtain a precision surface after printing..... 35

Figure 12: A mold manufactured with conformal cooling channels on a hybrid system by (a) machining the lower half of the channels, (b) using DED to cover the channels, (c) using DED to print the rest of the mold, and (d) machining the mold to a surface finish acceptable for molding (image courtesy of ORNL). 37

Figure 13: Basic construction of a laser [50, 53]. 38

Figure 14: The stimulated emission process. 39

Figure 15: Transmissivity of 0.5mm-thick polycarbonate, indicating that the transmissivity is higher at lower wavelengths [63]. 41

Figure 16: Laser welding of an optically transparent polymer to an optically absorptive polymer. 41

Figure 17: Influence of oxidation (top) and wavelength (bottom) on several copper alloys [75]. 43

Figure 18: Measured temperature dependence of absorptivity A at Nd:YAG- (squares), CO- (triangles) and CO₂-wavelength (circles) of polished iron (I, V) and polished steel 35NCD16 (II, III, IV) [74]. 44

Figure 19: The Haas VF-5/40XT modified by Hybrid Manufacturing Technologies with blown-powder DED and polymer extrusion AM capabilities. 46

Figure 20: The HMT blown powder process (courtesy of Hybrid Manufacturing Technologies)..... 47

Figure 21: The high-speed imaging setup for capturing laser-polymer interactions during the first pass of a DED deposition. 49

Figure 22: Transmittance and absorbance results for PLA. The PLA is more transmissive and less absorptive than the other polymers, and CF ABS is the most absorptive and least transmissive material. 51

Figure 23: Stills from high-speed videos on CF ABS, GF Nylon, GF ABS, PLA, and WF PLA. Circles indicate flaring, and arrows indicate smoke and residue. 53

Figure 24: Diagram of the blown-powder DED process, including the laser focal point, the carrier gas, the nozzle gas, and the shield gas. The combination of these gases results in an inert area around the laser. (Image courtesy of HMT)..... 54

Figure 25: Flaring occurs above the surface during deposition on a CF ABS substrate (top). The location of this flaring coincides with the location of the interaction between the carrier gas and the gaseous combustion byproducts (bottom). 56

Figure 26: Cross sections of single bead tests on GF ABS and PLA. Evidence of transmission can be seen in PLA (boxed in red) but not GF ABS. 57

Figure 27: Increasing power tends to increase in-process flaring, shown here with two CF ABS trials (SB01 at 100 W and SB03 at 300 W) and two PLA trials (SB13 at 100 W and SB15 at 300 W). Images from all trials can be found in Appendix B. 58

Figure 28: Increasing scan speed tends to decrease in-process flaring, shown here with two CF ABS trials (SB01 at 400mm/s and SB02 at 800mm/s) and two PLA trials (SB13 at 400mm/s and SB14 at 800mm/s). Images from all trials can be found in Appendix B. .. 59

Figure 29: The effect of increasing power, shown here with two CF ABS trials (SB01 at 100 W and SB03 at 300 W) and two PLA trials (SB13 at 100 W and SB15 at 300 W). Images from all trials can be found in Appendix B..... 60

Figure 30: The effect of increasing scan speed, shown here with two CF ABS trials (SB01 at 400mm/s and SB02 at 800mm/s) and two PLA trials (SB13 at 400mm/s and SB14 at 800mm/s). Images from all trials can be found in Appendix B..... 61

Figure 31: The effect of increasing power, shown here with two GF ABS trials (SB05 at 100 W and SB07 at 300 W) and two PLA trials (SB13 at 100 W and SB15 at 300 W).. 62

Figure 32: The effect of increasing scan speed, shown here with two GF ABS trials (SB05 at 100 W and SB07 at 300 W) and two PLA trials (SB13 at 100 W and SB15 at 300 W). 63

Figure 33: Evidence of exposed fibers in 100 W, 400mm/min trials on CF ABS (SB01) and GF ABS (SB05). 64

Figure 34: The (a) schematic of and (b) pictures of the ablative reaction of a fiber filled polymer to an extreme thermal environment. 65

Figure 35: Rough surface finish of deposited metal in multiple trials due to adhered unmelted feedstock powder (indicated with arrows). 66

Figure 36: Evidence of porosity due to polymer degradation..... 67

Figure 37: Feedstock powder became embedded in the polymer around the edges of the pass, indicated with arrows. The reflective surfaces circled in PLA trial SB13 indicate melting and re-solidification of the polymer around the embedded feedstock powder.... 68

Figure 38: The ablation process..... 72

Figure 39: Sample preparation for degradation depth measurement. 77

Figure 40: Example of a degradation depth measurement on a GF ABS substrate..... 77

Figure 41: Measured degradation depths for all CF ABS experiments, with measurement error shown in the error bars. 78

Figure 42: Measured degradation depths for all GF ABS experiments..... 79

Figure 43: Measured degradation depths for all GF nylon experiments. 80

Figure 44: Measured degradation depths for all PLA experiments. 81

Figure 45: Measured degradation depths for all WF PLA experiments. 82

Figure 46: Measured degradation depths versus heat per unit length for all polymers. ... 83

Figure 47: Assumptions used for the surface-temperature-based semi-infinite thermal model, where the surface of the polymer is held at a constant temperature beginning at $t=0$ 84

Figure 48: Predicting degradation depth using the semi-infinite thermal model with constant surface temperature as a boundary condition and a scan speed of (a) 400mm/min and (b) 800mm/min..... 86

Figure 49: Assumptions used for the heat-flux-based semi-infinite thermal model, where a constant heat flux is applied to the surface beginning at $t=0$ 87

Figure 50: Predicting degradation depth using the semi-infinite thermal model with constant surface temperature as a boundary condition and print parameters of (a) 100W laser power and 400mm/min scan speed, and (b) 100W laser power and 800mm/min scan speed, (c), 300W laser power and 400mm/min scan speed, and (d) 300W laser power and 800mm/min scan speed..... 89

Figure 51: The effect of increasing density on the predicted temperature at a depth of 1mm, a laser power of 100W, and a scan speed of 400mm/min using the semi-infinite model assuming a constant heat flux at the surface. 90

Figure 52: The effect of increasing thermal capacitance on the predicted temperature at a depth of 1mm, a laser power of 100W, and a scan speed of 400mm/min using the semi-infinite model assuming a constant heat flux at the surface. 91

Figure 53: The effect of increasing thermal conductivity on the predicted temperature at a depth of 1mm, a laser power of 100W, and a scan speed of 400mm/min using the semi-infinite model assuming a constant heat flux at the surface. 92

Figure 54: Assumptions used for the Rosenthal model, where a heat source of power Q moves across a material in the x-direction. 93

Figure 55: Predicting degradation depth at the origin for a single bead, 12.7mm print using the Rosenthal moving heat source model with print parameters of (a) 100W laser power and 400mm/min scan speed, and (b) 100W laser power and 800mm/min scan speed, (c), 300W laser power and 400mm/min scan speed, and (d) 300W laser power and 800mm/min scan speed. 95

Figure 56: The effect of increasing density on the predicted temperature at a depth of 2mm, a laser power of 100W, and a scan speed of 400mm/min using the Rosenthal model. 96

Figure 57: The effect of increasing thermal capacitance on the predicted temperature at a depth of 2mm, a laser power of 100W, and a scan speed of 400mm/min using the Rosenthal model. 97

Figure 58: The effect of increasing thermal conductivity on the predicted temperature at a depth of 2mm, a laser power of 100W, and a scan speed of 400mm/min using the Rosenthal model. 98

Figure 59: Measured degradation depths of CF ABS compared to the three developed thermal models. 100

Figure 60: Measured degradation depths of GF ABS compared to the three developed thermal models. 101

Figure 61: Measured degradation depths of GF nylon compared to the three developed thermal models. 103

Figure 62: Measured degradation depths of PLA compared to the three developed thermal models.	104
Figure 63: Measured degradation depths of WF PLA compared to the three developed thermal models.	105
Figure 64: General structure of a metallic bond, in which valence electrons are shared by all the metal atoms.	108
Figure 65: Generic lattice structure and unit cell, with edge lengths and interaxial angles defined.	108
Figure 66: The 14 lattice structures [96].	110
Figure 67: The (a) body-centered cubic (BCC), (b) face-centered cubic (FCC), and (c) body-centered (BCT) tetragonal structures. Corner atoms are shown in blue, face-centered atoms are shown in green, and atoms in the center of the structure are shown in orange.	111
Figure 68: Location of iron atoms in face-centered cubic austenite, with the small circles indicating the centers of holes between iron atoms, where carbon atoms can be located [104].	112
Figure 69: Solubility of carbon with respect to $M_{23}C_6$ carbides in an 18% Cr-8% Ni stainless steel [120].	114
Figure 70: An example of porosity due to lack of fusion (top) and gas entrapment (bottom) [125, 126].	116
Figure 71: The effect of increasing porosity on the elastic modulus of cast steel [128].	117
Figure 72: Geometry of 316L stainless steel components printed on CF ABS substrates.	119
Figure 73: Top-down view (top) and cross-sectioned image (bottom) of a box comprised of five layers of five 12.7mm-long adjacent passes, deposited on CF ABS with no interlayer cooling time, with arrows to indicate porosity due to gas entrapment.	120
Figure 74: CT scan results showing porosity of 316L stainless steel on CF ABS, with arrows indicating porosity due to gas entrapment.	121
Figure 75: EBSD image showing the microstructure of 316L stainless steel deposited on CF ABS, with larger grains circled.	122

Figure 76: Phase distributions of 316L stainless steel deposited on CF ABS adjacent to the polymer (top) and at the top of the print (bottom). Note that the material adjacent to the polymer has a higher content of chromium carbides and BCC structure. 123

Figure 77: Measured hardness values of 316L stainless steel deposited on CF ABS compared to expected hardness values [133]..... 125

Figure 78: Projection of the calculated FCC surfaces. The lines represent three-phase reactions. The tic marks indicate each hundred degrees starting from 1000 K [136]. ... 128

Figure 79: TTP diagram in a temperature range of 823 K to 1023 K (550°C to 750°C) [137]..... 129

Figure 80: Component printed with no interlayer cooling time (top) and a 30 second interlayer cooling time (bottom). Note the oxidation (dark gray) on the top component compared to the rainbow coloration on the bottom component. 131

Figure 81: CT scans and microscopic cross-sectional images of 316L stainless steel components printed on CF ABS with no interlayer cooling time (top), with solid arrows indicating porosity due to gas entrapment, and 30 seconds of interlayer cooling time (bottom), with dashed arrows indicating porosity due to lack of fusion. 133

Figure 82: Hardness values for component with no interlayer cooling time (light green circles) and 30 seconds of interlayer cooling time (dark green triangles) compared to the expected hardness value from [133]. 135

Figure 83: EBSD image showing grain sized for a component printed with (a) no interlayer cooling time and (b) 30 seconds of interlayer cooling time. Note that the grain sizes in the component with an interlayer cooling time are smaller..... 136

Figure 84: Carbides are present near the substrate in (a) the component with no interlayer cooling time, but not in (b) the component with 30 seconds of interlayer cooling time. Note the reduction of chromium carbides in the component with an interlayer cooling time. 137

Figure 85: Process for the polymer support structure demonstration. 140

Figure 86: A 316L stainless steel cantilever structure printed on top of a CF ABS support. The cantilever is shown with the support (top) and with the support removed (bottom). 141

Figure 87: A failed 316L stainless steel bridge structure printed on top of a CF ABS support that was incorrectly press fit into the metal. 142

Figure 88: A 316L stainless steel bridge structure printed on top of a CF ABS support.	143
Figure 80: 316L stainless steel deposition attempt on PEEK, which resulted in expansion of the polymer and an unsuccessful build.	149
Figure 89: In-process stills for CF ABS single-bead experiments.	167
Figure 90: In-process stills for GF ABS single-bead experiments.	168
Figure 91: In-process stills for GF nylon single-bead experiments.	169
Figure 92: In-process stills for PLA single-bead experiments.	170
Figure 93: In-process stills for WF PLA single-bead experiments.	171
Figure 94: Post-print substrates for CF ABS single-bead experiments.	172
Figure 95: Post-print substrates for GF ABS single-bead experiments.	172
Figure 96: Post-print substrates for GF nylon single-bead experiments.	173
Figure 97: Post-print substrates for PLA single-bead experiments.	173
Figure 98: Post-print substrates for WF PLA single-bead experiments.	174
Figure 99: Top-down microscopic images for CF ABS single-bead experiments.	174
Figure 100: Top-down microscopic images for GF ABS single-bead experiments.	175
Figure 101: Top-down microscopic images for GF nylon single-bead experiments.	176
Figure 102: Top-down microscopic images for PLA single-bead experiments.	177
Figure 103: Top-down microscopic images for PLA single-bead experiments.	178
Figure 104: Cross-sectional microscopic images for CF ABS single-bead experiments.	179
Figure 105: Cross-sectional microscopic images for GF ABS single-bead experiments.	180
Figure 106: Cross-sectional microscopic images for GF nylon single-bead experiments.	181
Figure 107: Cross-sectional microscopic images for PLA single-bead experiments.	182
Figure 108: Cross-sectional microscopic images for WF PLA single-bead experiments.	183
Figure 109: Geometry assumptions used to predict metal temperature T_m and polymer temperature T_p in response to deposition of metal on a polymer substrate.	186

Figure 110: Thermal circuit diagram for a single bead of metal deposited on a polymer substrate.	187
Figure 111: Simplified thermal circuit diagram for a single bead of metal deposited on a polymer substrate.	189
Figure 112: The predicted temperatures of a single metal deposition (top) and the polymer substrate (bottom) over time in response to initial temperature conditions.	193
Figure 113: A metal bead on a polymer substrate exposed to energy from the laser.	193
Figure 114: Thermal circuit of a metal bead on a polymer substrate exposed to energy from a laser.	194
Figure 115: Simplified thermal circuit of a metal bead on a polymer substrate exposed to energy from a laser.	195
Figure 116: The predicted temperatures of a single metal deposition (top) and the polymer substrate (bottom) over time in response to a power impulse input.	198
Figure 117: Geometry assumptions used to predict metal temperature T_m and polymer temperature T_p in response to deposition of a second metal bead on a polymer substrate.	199
Figure 118: Thermal circuit diagram for two beads of metal deposited on a polymer substrate.	200
Figure 119: Simplified thermal circuit diagram for two beads of metal deposited on a polymer substrate.	201
Figure 120: The predicted temperatures of a second deposited metal bead (top), the first deposited bead (middle), and the polymer substrate (bottom) over time in response to initial temperature conditions.	204
Figure 121: A second metal bead on a polymer substrate exposed to energy from the laser.	204
Figure 122: Thermal circuit of a second metal bead on a polymer substrate exposed to energy from a laser.	205
Figure 123: Simplified thermal circuit of a second metal bead on a polymer substrate exposed to energy from a laser.	206

Figure 124: The predicted temperatures of a second deposited metal bead (top), the first deposited bead (middle), and the polymer substrate (bottom) over time in response to an impulse.....	209
Figure 125: An example of a thermal circuit in which a heat source Q is applied to a material with thermal capacitance C and thermal resistance R	210
Figure 126: Semi-infinite temperature model results for varying laser speed on CF ABS.	211
Figure 127: Semi-infinite flux model results for varying laser speed and power on CF ABS.	212
Figure 128: Rosenthal model results for varying laser speed and power on CF ABS....	213
Figure 129: Semi-infinite temperature model results for varying laser speed on PLA. .	214
Figure 130: Semi-infinite flux model results for varying laser speed and power on PLA.	215
Figure 131: Rosenthal model results for varying laser speed and power on PLA.....	216
Figure 132: Semi-infinite temperature model results for varying laser speed on WF PLA.	217
Figure 133: Semi-infinite flux model results for varying laser speed and power on WF PLA.....	218
Figure 134: Rosenthal model results for varying laser speed and power on WF PLA...	219
Figure 135: Semi-infinite temperature model results for varying laser speed on GF ABS.	220
Figure 136: Semi-infinite flux model results for varying laser speed and power on GF ABS.	221
Figure 137: Rosenthal model results for varying laser speed and power on GF ABS. ..	222
Figure 138: Semi-infinite temperature model results for varying laser speed on GF nylon.	223
Figure 139: Semi-infinite flux model results for varying laser speed and power on GF nylon.	224
Figure 140: Rosenthal model results for varying laser speed and power on GF nylon. .	225

List of Tables

Table 1. Common laser mediums and wavelengths [55].	39
Table 2. Polymer transmittance and absorbance at 1,080 nm.	52
Table 3. Design of experiments to derive a linear model of laser power and scan speed.	75
Table 4. Predicted and measured degradation depths for all CF ABS experiments.	99
Table 5. Predicted and measured degradation depths for all GF ABS experiments.	101
Table 6. Predicted and measured degradation depths for all GF nylon experiments.	102
Table 7. Predicted and measured degradation depths for all PLA experiments.	104
Table 8. Predicted and measured degradation depths for all WF PLA experiments.	105
Table 9. Crystal system definitions.	109
Table 10. Thermal circuit components [141, 142].	185
Table 11. Properties and parameters used to define thermal resistivity and capacitance.	187
Table 12. Variable values used for temperature prediction.	191

CHAPTER 1. INTRODUCTION

1.1 Overview of directed energy deposition (DED)

In recent decades, additive manufacturing (AM) use cases have included functional, complex, and customized end-use metal components. A variety of metals, including steel, titanium, and aluminum, can be manufactured using AM processes such as powder bed fusion, binder jetting, and both powder- and wire-based directed energy deposition (DED) [1]. Each of these processes is capable of printing parts ranging from $\sim 10\ \mu\text{m}$ to $\sim 1\text{mm}$ in resolution and from $<1\ \text{cm}$ to $>1\ \text{m}$ in size, with increased part size requiring a sacrifice in resolution [2]. Binder jetting and powder bed fusion are generally used to print smaller parts at higher resolutions, while DED is used for larger parts at lower resolutions. Metal directed energy deposition (DED) is of interest to several industries, including aerospace and mold-making, because of its capacity for manufacturing end-use metal components at larger scales and at higher rates compared to other metal AM processes [2-4]. Metal DED components are large and functional while still taking advantage of the flexibility of AM. DED systems can be categorized by both the type of feedstock utilized during the process and the method used to melt the feedstock prior to deposition.

1.2 DED design limitations

DED systems provide the flexibility of AM with the structural integrity of metals at larger scales than other metal AM processes, but there are still component design limitations. Because AM involves selective deposition of material, steep overhangs and bridges are impossible to manufacture [5]. The generally accepted overhang constraint for AM processes is 45° [6]. However, because the bead produced in the DED process are on the order of 1mm wide, compared to the $100\ \mu\text{m}$ beads in selective laser melting (SLM), overhangs in DED components are more constrained. At its limits, the technology can achieve overhangs at an angle of up to 30° from the vertical, but it is generally understood that overhangs greater than 20° from the vertical will fail [7, 8]. In AM processes like fused filament fabrication (FFF), stereolithography (SLA), and selective laser melting (SLM), support structures are often used to enable overhangs and bridges that would otherwise be impossible to manufacture. These support structures are then removed after the component is completed. Most commonly, the supports in SLA and FFF are thin enough to be

mechanically removed from the main component after the print is completed. In dual-nozzle FFF systems, it is possible to print support structures out of a polymer that can later be dissolved without harming the component. Removal of SLM supports can require machining for removal, but hand tools are also an option for SLM. Support structures in DED, however, are generally not utilized. The higher-volume bead produced by DED is more difficult to support than the lighter, smaller beads in other AM processes, and the larger beads are also more difficult to remove.

1.3 Research aims and objectives

The objective of this research was to explore the suitability of polymers as support structures in the DED process via two key aspects affecting support material success: (1) the effect of metal DED on a polymer, and (2) the effect of a polymer substrate on the deposited DED component. Because both aspects involve the interaction between the support structure material and either the DED process or the deposited metal, much of this research used polymer substrates as a substitute for polymer support structures.

For a polymer to succeed as a support structure, the geometric integrity of the polymer must not be significantly affected during the polymer's response to the DED process. Additionally, combustion of the polymer should remain under control during deposition to avoid safety concerns. The interaction between polymer substrates and the laser used in the DED process was explored first to determine which polymer characteristics affect laser energy absorption. A recommendation for polymer characteristics was then made based on the relationship between laser absorption and successful feedstock deposition. The potential for polymer combustion was investigated, and predictions about the level of combustion based on polymer absorptivity and molecular structure were validated with high-speed imaging. Degradation of the polymer exposed to the DED process through single-bead experiments was measured, and the degradation results were discussed through the lens of several thermal models, as well as an understanding of ablative processes and laser transmissivity.

If the geometric integrity of the polymer is maintained well enough to support a full build, the composition and properties of the deposited metal must also not be significantly altered

by the support structure. To explore the interaction between the deposited metal and a polymer substrate was the porosity, hardness, and microstructure of 316L stainless steel deposited on carbon-fiber-reinforced ABS was characterized. Metallurgical explanations of these characterization results were developed, and these explanations were used to develop a mitigation strategy to prevent significant changes to the metal composition during deposition on a polymer substrate. The mitigation strategy was validated with further characterization. Finally, the use of a polymer support structure was demonstrated via manufacturing of a bridge geometry.

By overcoming the challenges of polymer degradation due to DED exposure and metal composition alterations due to polymer exposure, the polymer support structure approach for DED components was validated. This validation resulted in a successful demonstration of a polymer support structure for a DED bridge component.

1.4 Thesis organization

This thesis is organized into eight chapters. After this introduction, the effect of the DED process on polymers is explored in Chapters 2 and 3. Chapter 2 examines the interactions between lasers and polymers, as the DED system in this research uses a laser as its energy source. Chapter 3 then experimentally determines the degradation of polymers exposed to the DED process. The effect of polymer substrates on the deposited metal component is explored in Chapters 4 and 5. Chapter 4 describes the metal characterization process, and Chapter 5 presents the mitigation strategy used to prevent metal composition changes due to polymer substrate use. Chapter 6 demonstrates the successful use of a polymer as a support structure for a bridge geometry. Chapter 7 presents the final conclusions of this body of research, and Chapter 8 recommends future work to build on the research described in this thesis.

CHAPTER 2. POLYMER INTERACTIONS WITH DIRECTED ENERGY DEPOSITION

2.1 Introduction

Understanding polymer interactions with lasers is key in understanding and predicting the initial response of the polymer to the directed energy deposition (DED) process. The DED system used in this research is laser-based, and the polymer will interact directly with the laser until metal has been deposited. This chapter presents background information on the DED process, polymer combustion, and lasers and their interactions with materials. The methodology for observing the polymer response to the DED process via single-bead experiments is then described, along with the methodology for predicting the degradation byproducts of the polymer. The results of the single-bead experiments are discussed, followed by the conclusions of the chapter.

2.2 Background

Three topics are required to understand the polymer interaction with the DED process: the DED process itself, lasers, and the process of polymer combustion. These three topics will be introduced, and prior work relevant to this research will be discussed.

2.2.1 Directed energy deposition and hybrid manufacturing

The system utilized for all printing experiments in this body of research was a hybrid system, consisting of a machining center retrofitted with polymer extrusion and metal directed energy deposition capabilities. Metal DED was the key process in this research, so an overview of this process is presented, followed by an exploration of the current limitations of DED technology and prior work seeking to overcome these limitations.

2.2.1.1 Metal additive manufacturing

The appeal of functional, complex, and customized end-use parts has resulted in the desire to manufacture metal components with additive manufacturing (AM). A variety of metals, including steel, titanium, and aluminum, can be manufactured using a variety of AM processes, including powder bed fusion, binder jetting, and both powder- and wire-based DED, diagrammed in Figure 1 [1]. Each of these processes can print a range of part sizes at a range of resolutions, as illustrated in Figure 2.

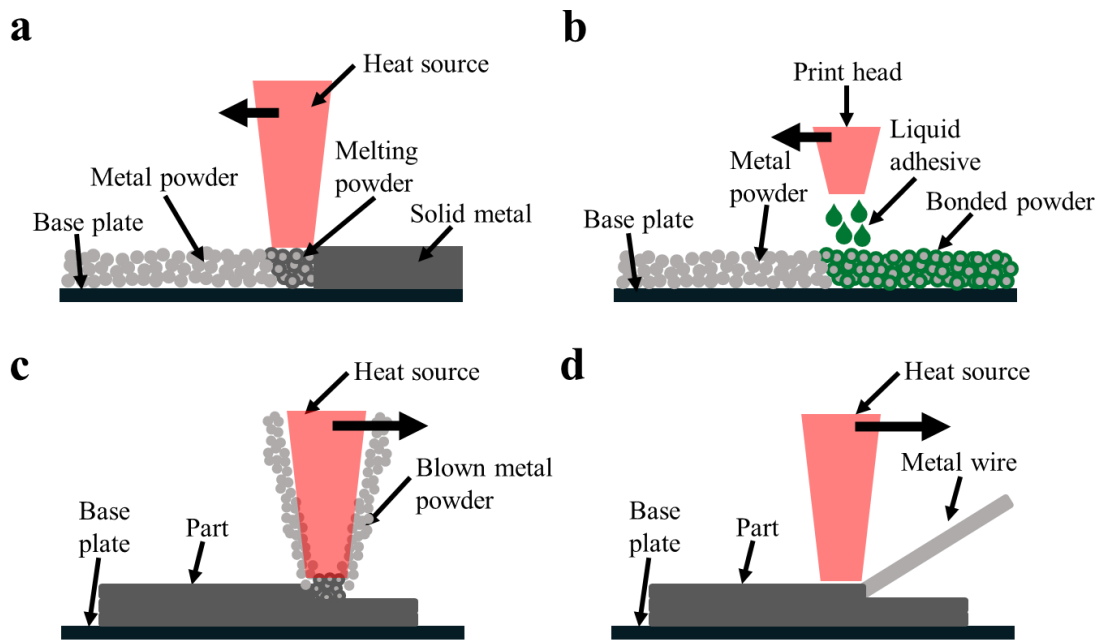


Figure 1: The (a) powder bed fusion, (b) binder jetting, (c) blown-powder directed energy deposition, and (d) wire-fed directed energy deposition metal additive manufacturing processes.

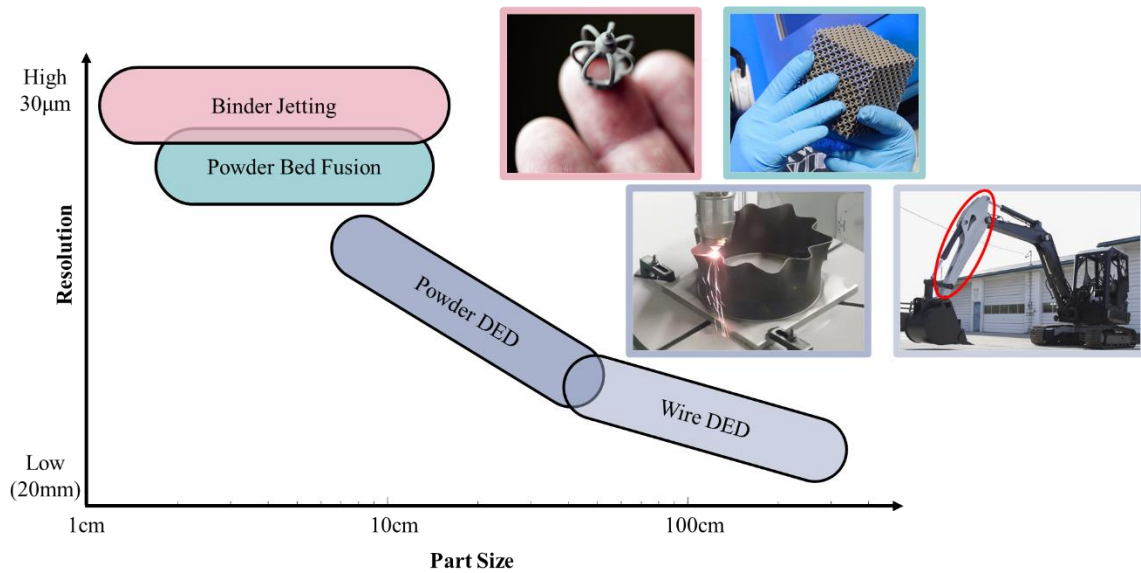


Figure 2: The resolution versus part size for the four metal AM processes [2, 9]. Increasing part size generally results in decreased resolution.

In the powder bed fusion process, a thermal source is used to selectively fuse powder particles together in a bed of feedstock powder [10]. Lasers are the most common thermal

source, but some technologies use electron beams instead, called electron beam melting (EBM) systems [10, 11]. Powder bed fusion components generally have characteristic dimensions less than 10 cm and resolutions of approximately 50 μm [2]. In the binder jetting process, powder particles are selectively glued together by jetting a binder over a bed of feedstock powder [9]. After binder jetting, sintering and several other post-processing steps must be completed to convert a “green” component to an end-use component [9]. Binder jetted components generally have characteristic dimensions on the order of 10 cm and resolutions of approximately 30 μm [2, 9]. In the metal DED process, which is discussed further in 2.2.1.2, components are formed by melting feedstock material as it is being deposited [12]. Overall, metal additive manufacturing enables on-demand production of end-use components, although more process optimization is required to fully exploit the potential of metal AM processes [13].

2.2.1.2 Directed energy deposition process

DED systems can be categorized by both the type of feedstock used in the system and the energy source used to melt the feedstock during deposition, as diagrammed in Figure 3.

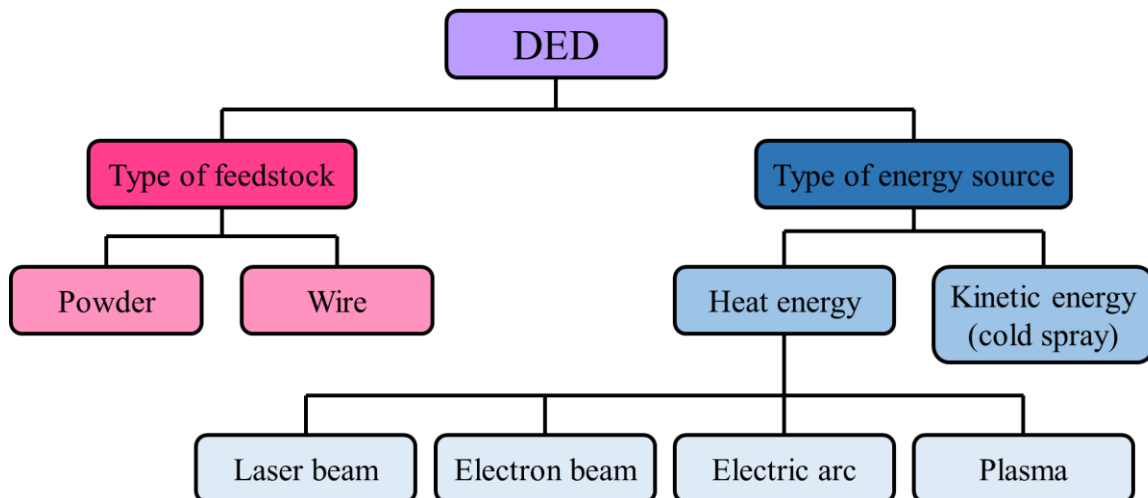


Figure 3: DED systems can be classified by both the type of feedstock material and the energy source used [14].

Blown powder systems, such as the one schematically shown in Figure 4a, utilize metal powder as the feedstock. These systems include laser metal deposition (LMD) and laser engineered net shaping (LENS). Wire-fed systems, or wire-arc additive manufacturing (WAAM), such as the one schematically shown in Figure 4b, utilize metal wire as the

feedstock. Blown powder systems utilize lasers to melt the powder, and wire-fed systems can utilize either lasers, electron beams, or electric arcs to melt the wire. Both blown powder and wire-arc DED systems can deposit metal an order of magnitude faster than powder bed fusion processes, on the order of kilograms per hour [15]. Wire-arc systems generally deposit material at slightly higher rates than blown powder systems, and wire-arc systems result in less material waste, with almost 100% feedstock capture efficiency, compared to less than 80% in blown powder systems [12, 15-17]. DED is a promising technology for several industries, including the mold and die industry, as both a manufacturing method and a repair method [18].

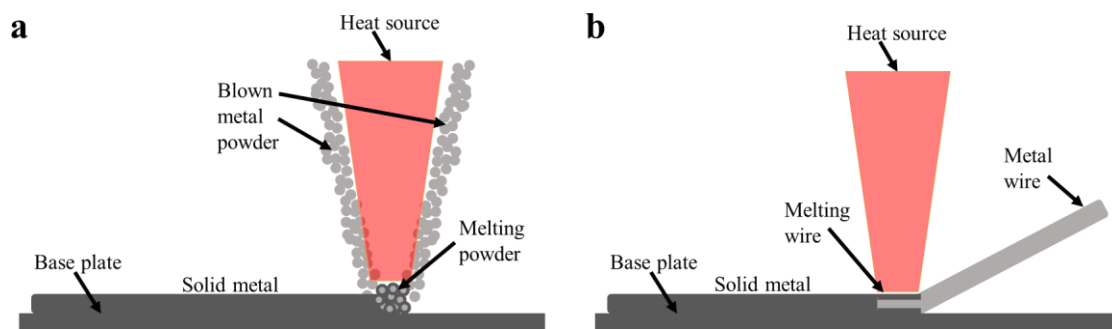
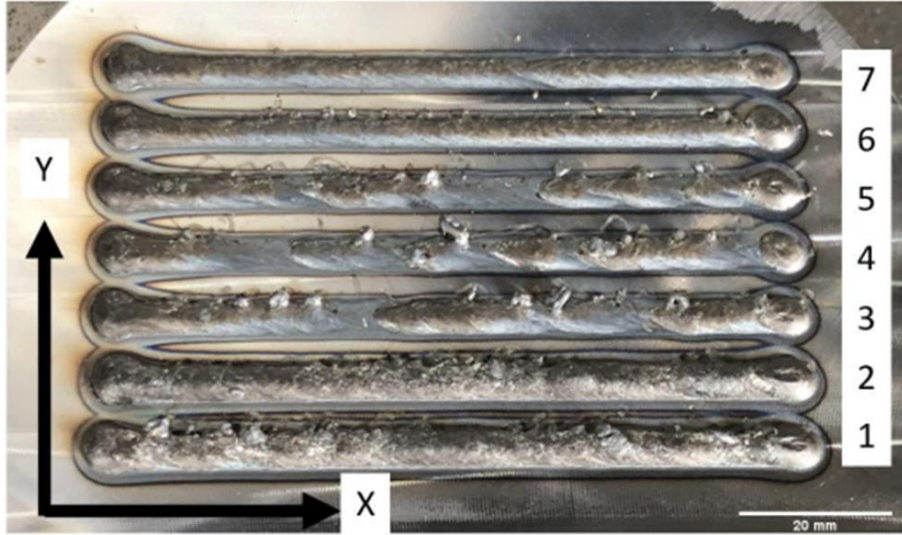


Figure 4: Examples of a (a) blown powder DED system and (b) wire-fed DED system.

DED processes involve multiple variables that must be optimized prior to printing, and significant research has been completed to develop methodologies to perform these optimizations. For example, Feldhausen observed the influence of the linear energy of deposition, determined by wire feed rate, traverse feed rate, hot-wire preheat, and laser power, on bead quality using a Mazak wire-arc system [19]. Figure 5 qualitatively demonstrates the influence these parameters have over bead quality.



	Wire Feed Rate [mm/min]	Traverse Feed Rate [mm/min]	Hot-Wire Preheat [W]	Laser Power [W]	Linear Energy of Deposition [J*s/mm ⁴]
1	5080	762	300	4000	3.90
2	4445	762	300	4000	4.45
3	4445	1500	300	4000	2.26
4	5080	1500	300	4000	1.98
5	5715	1500	300	4000	1.76
6	3810	1500	300	4000	2.64
7	3175	1500	300	4000	3.17

Figure 5: The effect of varying linear energy of deposition in single-bead, single-layer wire-fed DED experiments [19].

Some DED research has also focused on developing a fundamental understanding of the effect of process variables on both the DED process and the final component. For example, Bontha *et al.* applied the 3D Rosenthal solution for a point heat source moving across an infinite substrate to determine a first-order approximation of the thermal conditions in laser-based DED, with the end goal of predicting grain size and morphology in DED components [20]. Beuth and Klingbeil developed a “process map” for laser-powder DED to predict melt pool size, thermal gradients, and maximum residual stress in thin-walled structures [21].

2.2.1.3 DED limitations

Geometries in DED components are more constrained than in other AM processes because the beads produced in the DED process are on the order of 1mm wide, compared to the 100

μm beads in selective laser melting (SLM). As shown in Figure 6, steep overhangs and bridges are impossible to manufacture [5]. These geometries are more limited in DED than in other AM processes due to the large bead size and lack of a powder bed, a feature found in powder bed fusion technologies that provides some support for overhangs. Keicher et al. patented a DED technology with the capacity to print overhangs at or above 60° from the horizontal, while the Stratasys Direct Metal Laser Sintering (DMLS) powder bed fusion process is only capable of manufacturing overhangs at or above 35° from the horizontal [22, 23]. In AM processes like fused filament fabrication (FFF), stereolithography (SLA), and selective laser melting (SLM), support structures are often used to enable overhangs and bridges that would otherwise be impossible to manufacture. These support structures are then removed after the component is completed. Most commonly, the “break-away” supports in SLA and FFF are thin enough to be manually removed from main component, although in dual-nozzle FFF systems, it is possible to print support structures out of a polymer that can later be dissolved without harming the component. SLM supports can require machining for removal, but in some cases can be removed using hand tools. However, support structures in DED are generally not used because the higher volume bead produced by DED is more difficult to support than the lighter, smaller beads in other AM processes. The larger bead size also makes support removal more difficult than in other AM processes.

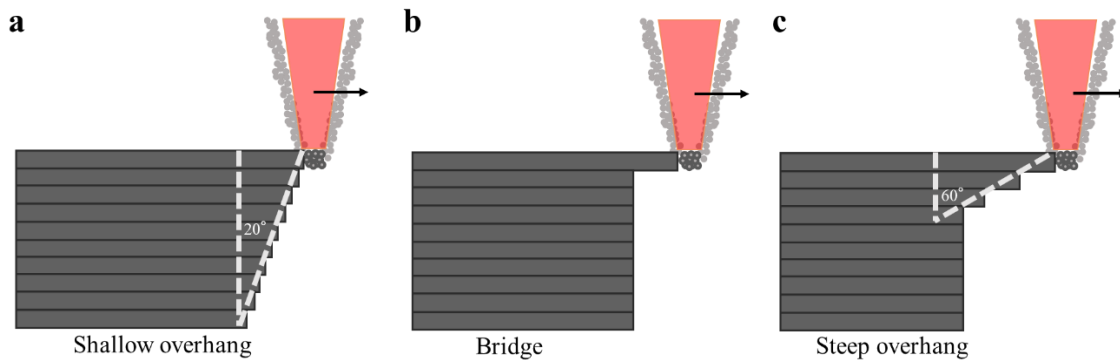


Figure 6: DED is generally limited to (a) overhang angles of 20° or less, and (b) bridged structures and (c) steep overhangs are impossible without supports.

Several strategies for mitigating the support structure issue in DED have been explored, primarily focusing on improving the design, slicing, and printing processes to avoid support requirements. [24]. Five-axis systems, or systems with rotary axes, can be used to

manufacture components with steep overhangs by re-orienting the components during the print, but these systems are costly [25]. Zhao *et al.* presented nonplanar slicing approaches to reduce the need for support structures, shown in Figure 7, but these strategies require five-axis systems to implement.

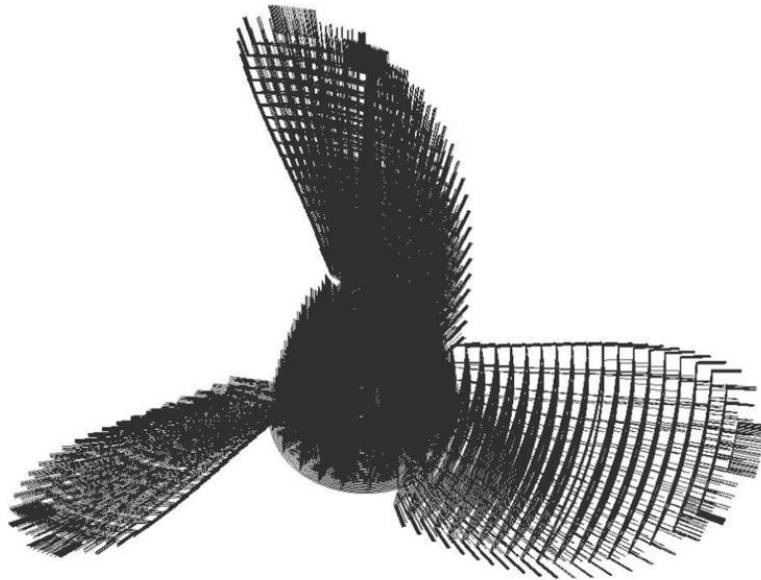


Figure 7: Toolpaths generated by the decomposition-based curved slicing method, which reduces the need for support structures in DED but requires a 5-axis system [24].

Lam *et al.* developed and implemented adaptive process control of a DED process to enable thin-walled components with overhangs up to 37.5° , shown in Figure 8 [26]. Although these overhangs are steeper than those possible without this adaptive process control, the overhang angle is still limited.

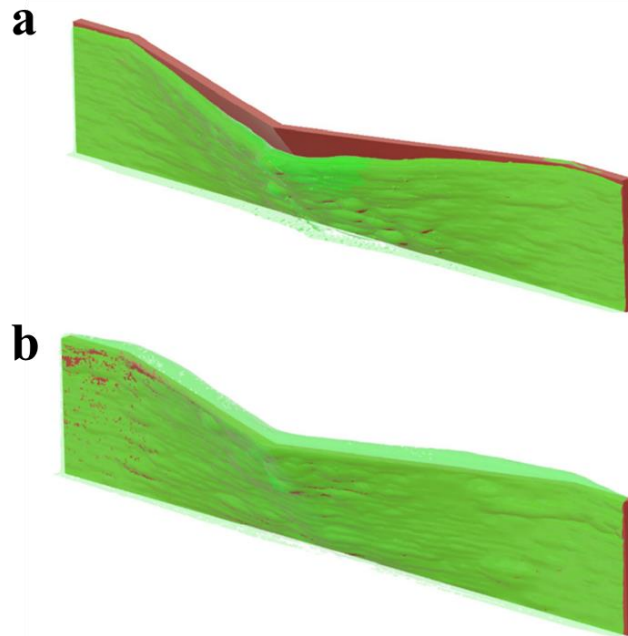


Figure 8: 3D scans of actual DED print (green) overlaid onto CAD model (red), with excess end segments trimmed off, for a component made (a) without adaptive process control and (b) with adaptive process control, demonstrating the success of this method in increasing possible overhang angle [26].

All these strategies expand the design space of DED, but they do not fully eliminate the need for support structures in more complex components. Some research has explored the use of dissolvable metal support structures in both powder bed fusion and DED processes [27-30]. For example, Hildreth *et al.* demonstrated the use of dissolvable metal support structures in DED by fabricating supports for a stainless steel structure out of carbon steel and then dissolving the carbon steel via electrochemical etching, as shown in Figure 9 [31]. This technology is promising, but dissolvable metal support structures add cost and complexity to the build, due to both the feedstock material required and the addition of etching as a post processing step.

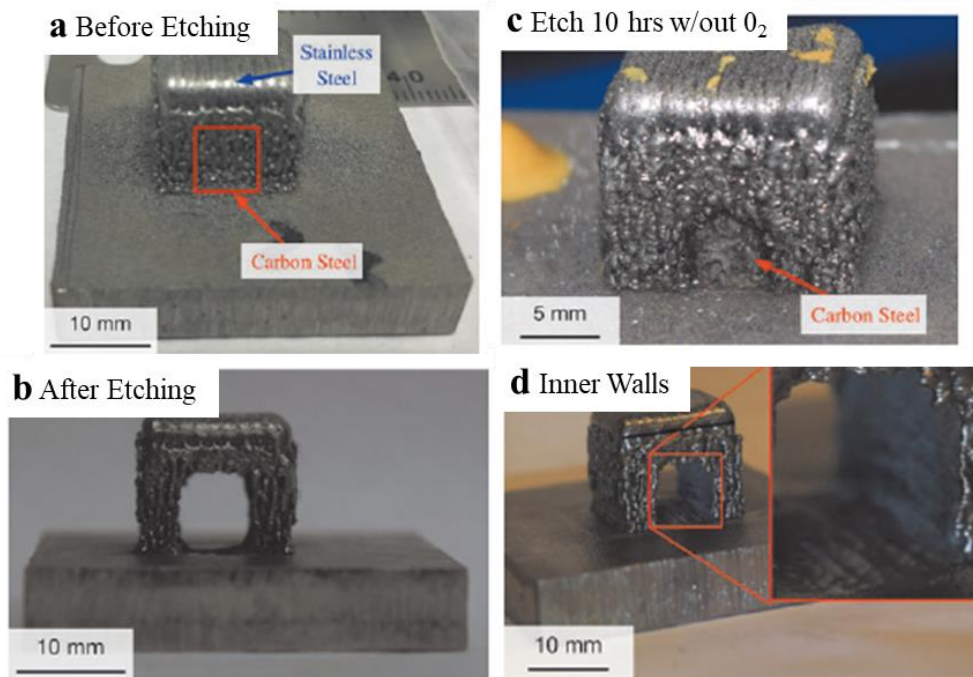


Figure 9: Digital images of the sample taken before, during, and after etching. (a) Before etching, the red square roughly outlines where the carbon steel support layer was printed. (b) After 10 hours of etching, 1.4mm of carbon steel was removed from each side. (c) After etching showing that the carbon steel was completely etched from the sample. (d) Images of sidewall and bottom with lines etched into a chromium-depleted layer of the component and stainless steel baseplate, where the carbon steel leached the chromium during printing [31].

2.2.1.4 Hybrid manufacturing

The term “hybrid manufacturing” can be generally construed as any combination of distinct manufacturing processes in a single machine tool. These combinations can include, for example, mechanical machining and electric discharge machining, laser heat treatment and sheet metal forming, and laser-assisted waterjet cutting [32-35]. However, the term commonly refers to the combination of laser-based AM and computer numerical controlled (CNC) machining [36]. Three examples of these hybrid systems are shown in Figure 10. Figure 10a shows a Mazak system that combines CNC machining with wire-arc DED, Figure 10b shows an Okuma system that combines CNC machining with blown-powder DED, and Figure 10c shows a Haas machine tool retrofitted with blown-powder and polymer extrusion additive capabilities by Hybrid Manufacturing Technologies to create a hybrid system [3, 15, 37].

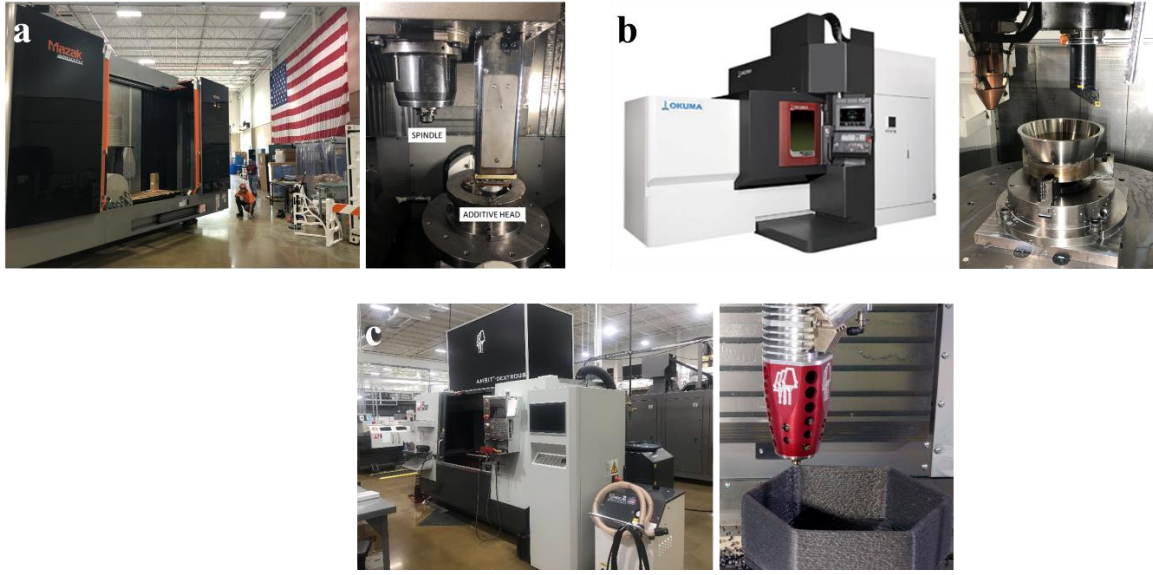


Figure 10: Two commercially available hybrid systems are (a) Mazak’s wire-arc DED and machining system and (b) Okuma’s blown-powder and machining system. It is also possible to retrofit machine tools with additive capabilities, as (c) HMT did with a Haas machine tool.

Hybrid systems combine the benefits of AM, which include geometric flexibility and relatively fast turnaround times, with the benefits of machining, which include high precision and good surface quality. Figure 11 demonstrates the benefits of combining machining and DED: a complex shape was printed, and the rough and imprecise surface of the DED component was then machined away for a smooth and precise final component.

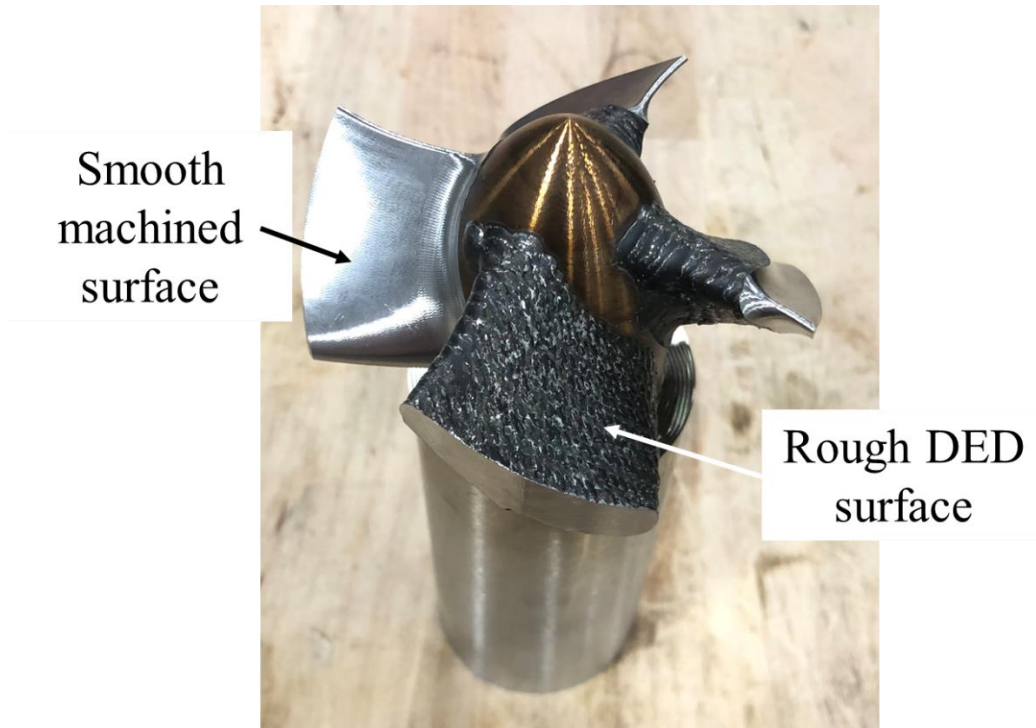


Figure 11: A hybrid-manufactured component that has been partially machined. DED was used for the initial shape, and machining was used to obtain a precision surface after printing.

Current work in hybrid manufacturing ranges from machine design to process modeling and control to part quality control. Kerbrat *et al.* evaluated the manufacturing complexity of components during the design stage, taking into account both machining and layered manufacturing, to provide insight into the manufacturability of various designs [38]. Yang *et al.* characterized the density, microstructure, and mechanical properties of hybrid manufactured components and then determined the effect of heat treatment on these properties [39]. Krimpenis *et al.* developed a robotic arm for hybrid manufacturing to enable retrofitting of machine tools for lower-cost hybrid manufacturing systems [40]. These efforts focus on the hybrid processes themselves, but a significant amount of research has also been completed on the applications of hybrid manufacturing.

Because hybrid manufacturing enables both flexible geometries and precision components, it has proven useful in several fields. In some cases, hybrid manufacturing can be completed at a faster rate than other manufacturing processes. For example, Saleeby *et al.* demonstrated the design and manufacture of a mold for injection molding in under 72

hours, while these molds generally have a lead time on the order of months [4]. Hybrid manufacturing is valuable as a tool for repairing worn or damaged components, as material can simply be deposited over the worn or damaged areas and then machined to the desired geometry [41, 42]. Reddy and Kumar completed a stochastic linear model of hybrid manufacturing to determine situations in which “re-manufacturing,” or the recovery and repair of used products, can be perfectly substituted for regular manufacturing [43]. Not only is hybrid manufacturing useful for the mold and die industry for repair, but also for manufacturing complex mold geometries. As an example, cooling channels are often desirable in heat-based molding processes to reduce cooling times [44]. Hybrid manufacturing enables the inclusion of conformal and complex cooling channels designed to optimize mold cycle times by reducing cooling times [45, 46]. An example of the hybrid manufacturing of conformal cooling channels manufactured at Oak Ridge National Laboratory’s Manufacturing Demonstration Facility is shown in Figure 12.

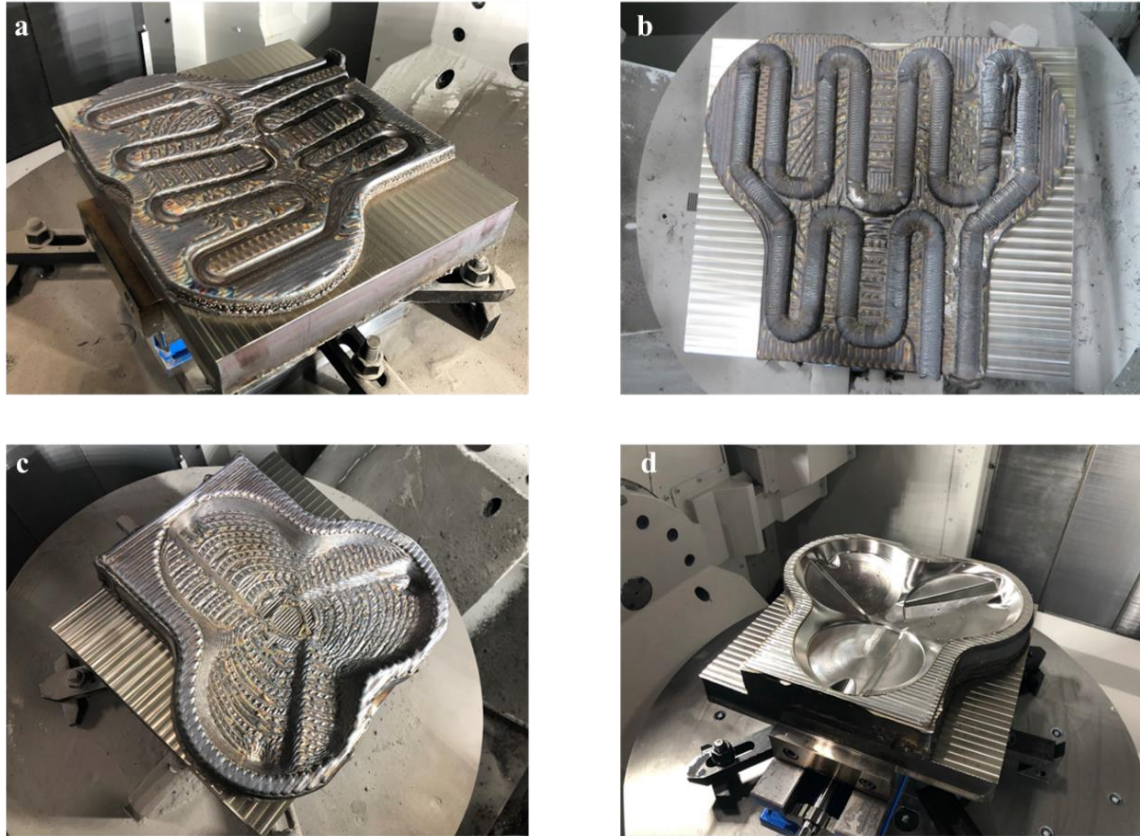


Figure 12: A mold manufactured with conformal cooling channels on a hybrid system by (a) machining the lower half of the channels, (b) using DED to cover the channels, (c) using DED to print the rest of the mold, and (d) machining the mold to a surface finish acceptable for molding (image courtesy of ORNL).

2.2.2 Lasers

In 1959, Gould was the first to describe Light Amplification by the Stimulated Emission of Radiation (laser) [47]. In 1960, Theodore Maiman demonstrated the first functioning laser, which produced red laser light using a ruby crystal, and Schawlow and Townes received the first patent for their Microwave Amplification by Stimulated Emission of Radiation (maser), which later became the laser, in 1960 [48, 49]. Since then, research has produced a wide variety of lasers with a range of amplifying mediums, wavelength outputs, power outputs, and costs.

2.2.2.1 Laser physics

Light Amplification by the Stimulated Emission of Radiation (laser) is the result of light oscillating between two mirrors through an active mechanism capable of amplifying these

oscillations via simulated emission [50]. Einstein mathematically predicted the phenomenon of stimulated emission in 1917, and Ladenburg confirmed Einstein's predictions in 1928 [51, 52]. Stimulated emission results from a photon interacting with an electron in an excited state, causing the electron to drop to a lower energy level and release energy [50].

The basic construction of a laser is shown in Figure 13. The essential elements of a typical laser include a laser medium, which provides atoms, molecules, ions, or a semiconducting crystal, a pumping process to excite the particles in the laser medium, and optical feedback elements to guide the beam of radiation [53]. The pumping process interacts with particles in the laser medium, and the atoms in the medium are excited to some higher quantum energy level. In 1996, Kogelnik and Li wrote one of the fundamental papers on cavity design, geometrically deriving stable mirror curvature ranges that would result in the oscillating beam converging into the cavity, rather than spreading out from the cavity [54].

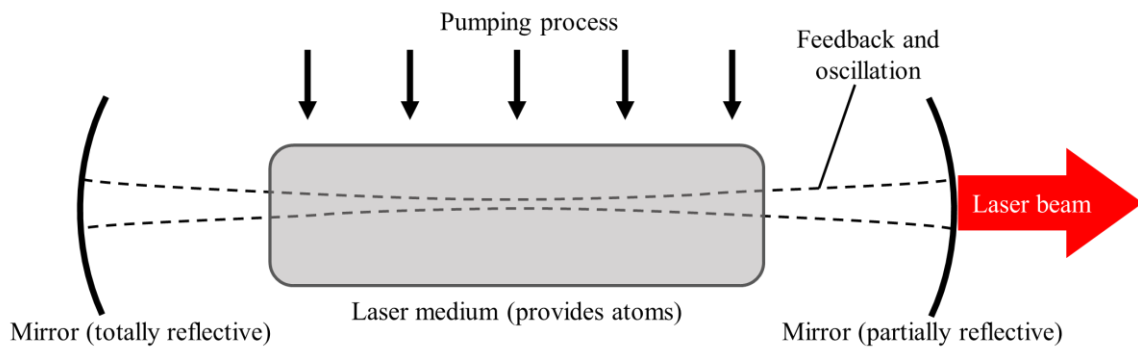


Figure 13: Basic construction of a laser [50, 53].

When enough atoms are excited to a higher energy level, electromagnetic radiation is passed through the excited medium, stimulating the release of photons from the excited atoms, as shown in Figure 14. The released photons then pass through other excited atoms, stimulating the release of more photons to continue the process, resulting in stimulated emission, amplifying the laser [53]. The wavelength of each emitted photon is described by Planck's Law

$$v_{12} = \frac{E_1 - E_2}{h} \tag{2.1}$$

Here, ν is the wavelength, E is the atomic energy level, and h is Planck's constant, equal to 6.626×10^{-34} J·s. In the example in Figure 14, The original photon and the released photon would each have energy

$$E = h\nu_{12} \quad (2.2)$$

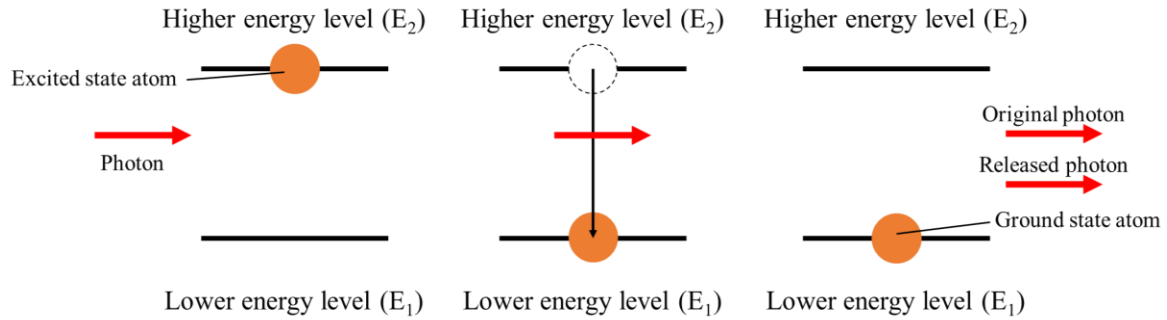


Figure 14: The stimulated emission process.

Because the wavelength of the produced photons is dependent on the energy states of the atoms used to generate the photons, the material used in the laser medium determines the output wavelength of the laser. Therefore, lasers are often classified by their medium, including solid-state lasers, gas lasers, liquid lasers, and semiconductor lasers. A list of commonly used laser mediums and the wavelength produced by those mediums is provided in Table 1.

Table 1. Common laser mediums and wavelengths [55].

Laser gain medium and type	Wavelength(s) (μm)
Carbon dioxide (gas)	10.6
Ruby (solid-state)	0.69
Nd:YAG (neodymium-doped yttrium aluminum garnet) (solid-state)	1.06
Ytterbium-doped fiber laser (solid-state)	1
Rhodamine dye laser (liquid)	0.540-0.680
AlGaInP (aluminum gallium indium phosphide) (semiconductor)	0.63-0.9

2.2.2.2 Laser-polymer interactions

Lasers are used in several polymer-based applications, including polymer welding and laser cutting of polymers. These two processes have different laser requirements. In polymer welding, the polymers being joined must reach a temperature high enough at the joint to promote diffusion of polymer macromolecules across the joint but not exceed the degradation temperature of the polymer [56]. Polymer welding has been studied from a thermal perspective because of its relevance to fused filament fabrication (FFF), in which thermoplastic feedstock is melted and selectively extruded in layers that are joined by polymer welds [57-60]. Laser polymer welding must also consider the optical properties of the polymer being welded. Laser light passing through a material will either be reflected by the material or penetrate through the material [61]. Laser light that penetrates the material will then be either absorbed or transmitted [50]. The reflectivity and absorptivity of a material is dependent on material properties and the wavelength of the laser light [50, 62]. For example, 0.5mm-thick polycarbonate is approximately 90% transmissive at a wavelength of 1000 nm and 1% transmissive at a wavelength of 10000 nm, as shown in Figure 15 [63]. Generally, polymers tend to be more absorptive at lower wavelengths, although the absorptivity of polymers can be tailored by changing the color of the polymers or adding fillers [64]. Chen *et al.* developed a model to describe the effect of carbon black on several polymers and found that increasing carbon black content resulted in increased laser absorption [65].

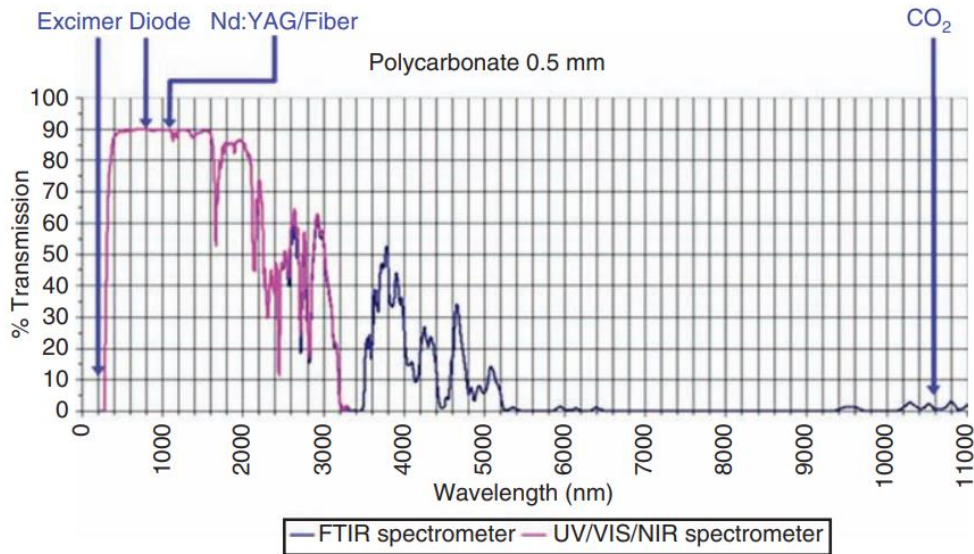


Figure 15: Transmissivity of 0.5mm-thick polycarbonate, indicating that the transmissivity is higher at lower wavelengths [63].

In through-transmission laser welding of polymers, an optically transparent polymer is placed on an absorbing polymer, and the deposition of laser energy occurs at the interface, as shown in Figure 16 [66]. Generally, the power in laser polymer welding is on the order of 5-25 W, with higher powers corresponding to faster scan speeds to keep overall energy density consistent [67]. To avoid absorption of laser energy in the transmitting polymer, diode or fiber lasers are often used, as their lower wavelengths tend to be transmitted through polymers [68, 69].

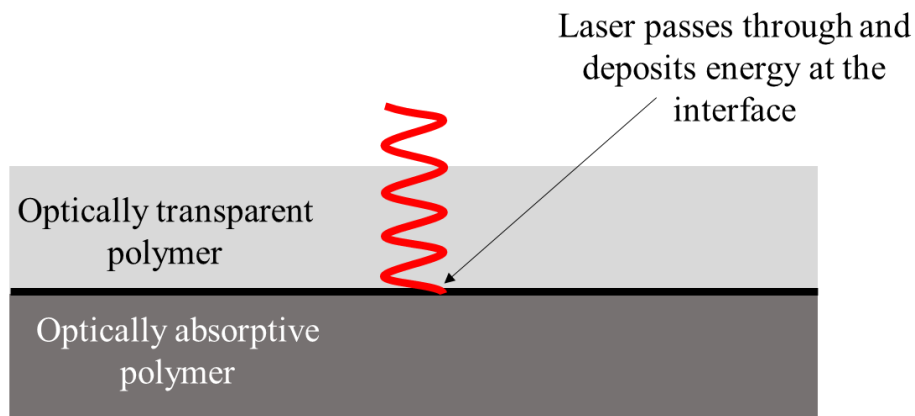


Figure 16: Laser welding of an optically transparent polymer to an optically absorptive polymer.

There are several methods of laser cutting, including vaporization, melt and blow, and thermal stress cracking, and each of these methods has a different temperature requirement [50]. Vaporization, for example, requires that the degradation temperature of the polymer be reached and maintained for long enough to vaporize all the polymer in the region being cut, while minimizing the amount of thermal damage to the region adjacent to the laser path. Laser cutting tends to use lasers at higher wavelengths so that more of the laser energy is absorbed by the polymer. For example, CO₂ lasers, which have a wavelength of 10600 nm, are frequently used in polymer laser cutting [70, 71].

2.2.2.3 Laser-metal interactions

The lasers used in DED tend to be fiber lasers as opposed to CO₂ lasers. Fiber lasers have smaller wavelengths than CO₂ lasers, and these smaller wavelengths are more readily absorbed by the metal feedstock powders used in laser DED processes [72]. The laser used in this research has a wavelength of 1,080±10 nm, while CO₂ lasers have wavelengths around 10,600 nm [15, 73]. DED lasers generally have maximum power outputs on the order of kilowatts: the laser used in this research has a maximum power of 2 kW [15]. As with polymers, the absorptivity of metals is also affected by a variety of factors, including material, wavelength, surface roughness, and temperature [74, 75]. An example of the effects of oxidation and laser wavelength on the absorptivity of several copper alloys is shown in Figure 17. In these elements specifically, oxidation increased the absorptivity, and a decrease in laser wavelength increased the absorptivity.

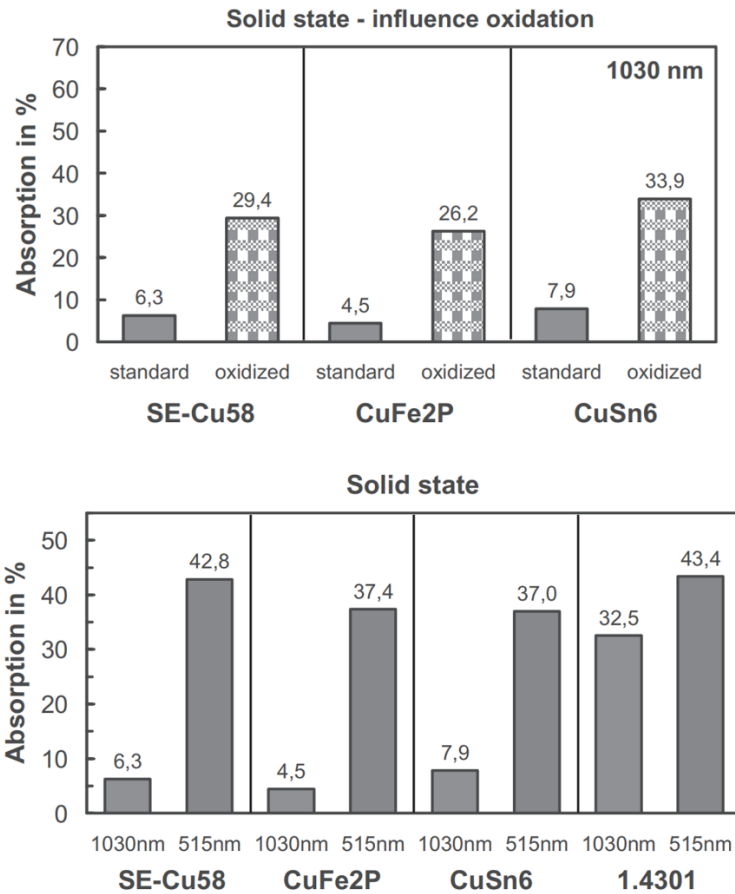


Figure 17: Influence of oxidation (top) and wavelength (bottom) on several copper alloys [75].

The effect of temperature on the absorptivity of iron and steel is shown in Figure 18. In these experiments, increasing temperature resulted in decreasing absorptivity of polished iron and steel under an Nd:YAG laser and increasing absorptivity of polished iron and steel under both CO and CO₂ lasers.

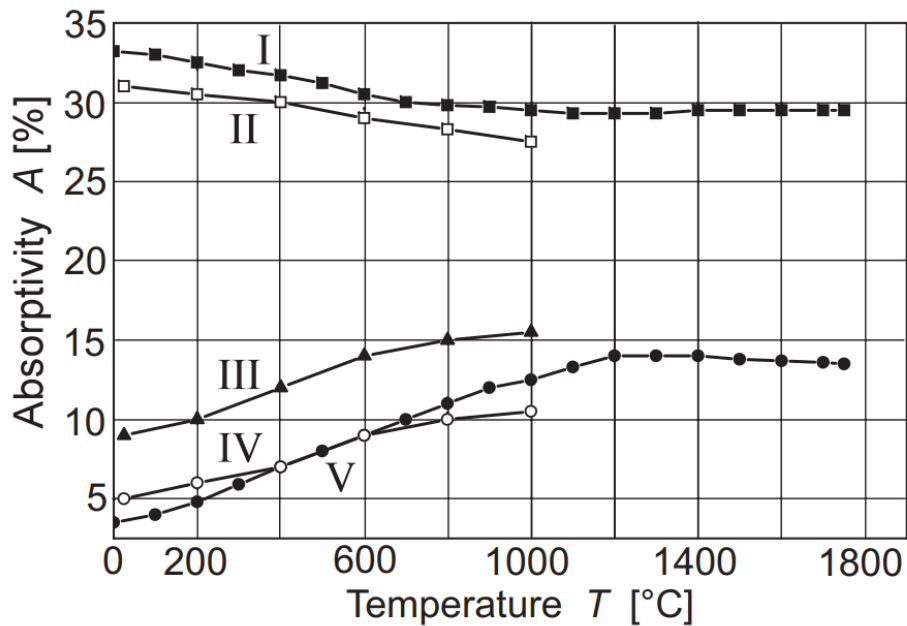


Figure 18: Measured temperature dependence of absorptivity A at Nd:YAG- (squares), CO- (triangles) and CO₂-wavelength (circles) of polished iron (I, V) and polished steel 35NCD16 (II, III, IV) [74].

Laser interactions with the metal in laser DED are different from laser interactions with solid metal because the metal is in a powder form. Prior work has focused on measuring and modeling the interactions of lasers with metal powder, especially for applications in laser powder bed fusion (LPBF) AM. Tran *et al.* performed an analysis of scattering and absorption of a layer of metal powder that included ray tracing simulations and took into account powder packing density [76]. Trapp *et al.* measured the absorptivity of 316L stainless steel, aluminum alloy 1100, and tungsten at 1070 nm during LPBF and found that process parameters such as power and scan speed, along with scattering in the powder layer and melt pool and keyhole formation, can affect absorptivity [77].

2.3 Laser-polymer characterization

To isolate the laser-polymer interaction, laser spectroscopy was performed on the polymers being tested as substrates in this research to determine their absorbances. Then, to observe the interaction between the DED process and the polymer, single deposition passes were completed on a variety of polymer substrates and observed with regular and high-speed cameras. The substrates were cross sectioned after the deposition passes were completed to observe any internal effects of the DED process on the polymer.

2.3.1 Laser spectroscopy

A key aspect of the polymer-DED interaction is the laser-polymer interaction. Polymer absorbance of the laser will affect the success of the polymer support structure in several ways by affecting polymer combustion and degradation, metal powder melting, and metal powder deposition. Accordingly, a series of experiments was performed on candidate polymers to determine their absorbances.

To measure absorptivity, a Perkin Elmer 1050 UVVISNIR spectrophotometer with a three-detector module was used, which measures transmittance using direct transmission mode: the intensity of light of a desired wavelength is measured after passing through the medium being measured and compared to the original intensity of light. The 1050 UVVISNIR spectrophotometer in this setup has a measurement range of 175 nm to 3,300 nm. Specimens of all polymers used in this research were cut into planks of approximately 3mm in thickness using a diamond saw. Each specimen was then sanded to remove significant surface roughness from the cutting process. The wavelength of interest was 1,080 nm, as that is the laser wavelength of the DED system used in this research, so a range of 1,060 nm to 1,100 nm was measured using the spectrophotometer. The absorbance of the polymer was derived from the transmittance measurement using the equation

$$A = \log \frac{1}{T} \quad (2.3)$$

Where A is the absorbance and T is the transmittance.

2.3.2 Haas/HMT hybrid system

The hybrid system used for all deposition experiments in this research was a Haas VF-05/40XT machine tool modified by Hybrid Manufacturing Technologies (HMT) with blown-powder DED and polymer extrusion AM capabilities, shown in Figure 19. The original Haas system, which provides the machining capabilities of the hybrid setup, is a 3-axis CNC machine tool with 1,524mm of travel in the x-direction, 660mm of travel in the y-direction, and 635mm of travel in the z-direction [15]. The maximum spindle speed is 8,100 rpm, the maximum torque is 122 Nm at 2,000 rpm, and the maximum cutting feed rate is 12.7 m/min [15].



Figure 19: The Haas VF-5/40XT modified by Hybrid Manufacturing Technologies with blown-powder DED and polymer extrusion AM capabilities.

The Haas was retrofitted as a hybrid system by HMT via the installation of AMBIT™ metal deposition system. The system consists of the S7-1, a 1mm-spot-size laser cladding head, the S7-2, a 2mm-spot-size laser cladding head, the Core Controller, which provides an nLight continuous wave laser with a maximum laser power of 1,500 W at a wavelength of $1,080 \text{ nm} \pm 10 \text{ nm}$, and the S7-325, a docking mechanism that enables laser, metal powder, and gas supply to the heads. HMT's metal deposition process is shown in Figure 20. Metal feedstock powder is fed through the head and into the path of the laser via a carrier gas. Shield gas flows around the sides of the laser to create an inert environment around the melt pool. Nozzle gas (not shown in Figure 20) flows coaxially with the laser to protect the optics and contribute to the inert environment.

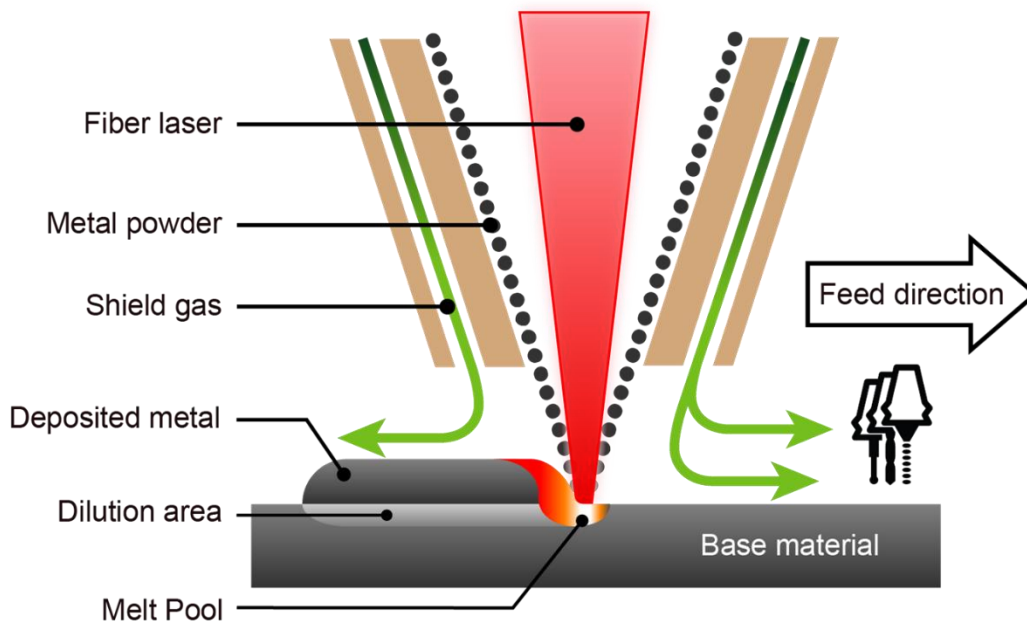


Figure 20: The HMT blown powder process (courtesy of Hybrid Manufacturing Technologies).

The two heads are stored in the Haas tool carousel. Prior to deposition, the hopper storing the metal feedstock powder is heated, generally to 60°C, to eliminate any moisture absorbed by the powder. The head being used is inserted into the tool holder, and the docking mechanism is then attached to the side of the head. The laser on/off status, powder on/off status, and head position and feed rate are all controlled by programming the Haas with G-Code, as is standard for machine tools. The laser power, shield gas flow rate, nozzle gas flow rate, and carrier gas flow rate are controlled through the AMBIT™ controller and must be set prior to beginning a deposition.

HMT also outfitted the Haas with their AMBIT™ PE-1 polymer extrusion system. The system design was based on the design of the Big Area Additive Manufacturing (BAAM) system, which uses a screw extruder to melt and extrude polymer pellet feedstock material [78]. The PE-1 head takes advantage of the spindle in the Haas for the screw extruder and uses an attached vacuum tube to carry feedstock pellets from storage into the head [15]. The PE-1 system is designed to extrude thermoplastic polymers at temperatures up to 300°C out of a 3mm-diameter nozzle [15].

2.3.3 Setup and procedure

Five polymers were selected for testing: carbon-fiber-filled acrylonitrile butadiene styrene (CF ABS), glass-fiber-filled nylon (GF nylon), glass-fiber-filled ABS (GF ABS), neat polylactic acid (PLA), and wood-flour-filled PLA (WF PLA). These polymers were selected because they (1) are easily printable, (2) are readily available, and (3) provide a range of filled and unfilled printable polymers for comparison.

To observe the in-process response of each polymer to the DED process, a Phantom v411 high speed camera was installed off axis to the laser. A 450 nm, 35 nm FWHM (Full-Width at Half Maximum) bandpass filter was used in tandem with a 100 W 450 nm LED to illuminate powder streams and deposition sufficiently for high-speed imaging. The substrates were then mounted in the Haas/HMT system, as shown in Figure 21. A single, 1.27 cm long deposition pass was completed on each substrate using 316 stainless steel powder feedstock. Laser power was set to 100 W, feed rate was set to 600mm/min, shield gas flow was set to 10 L/min, and carrier gas flow rate was set to 4 L/min for all experiments. Feedstock powder mass flow rate was measured to be 9 g/min.

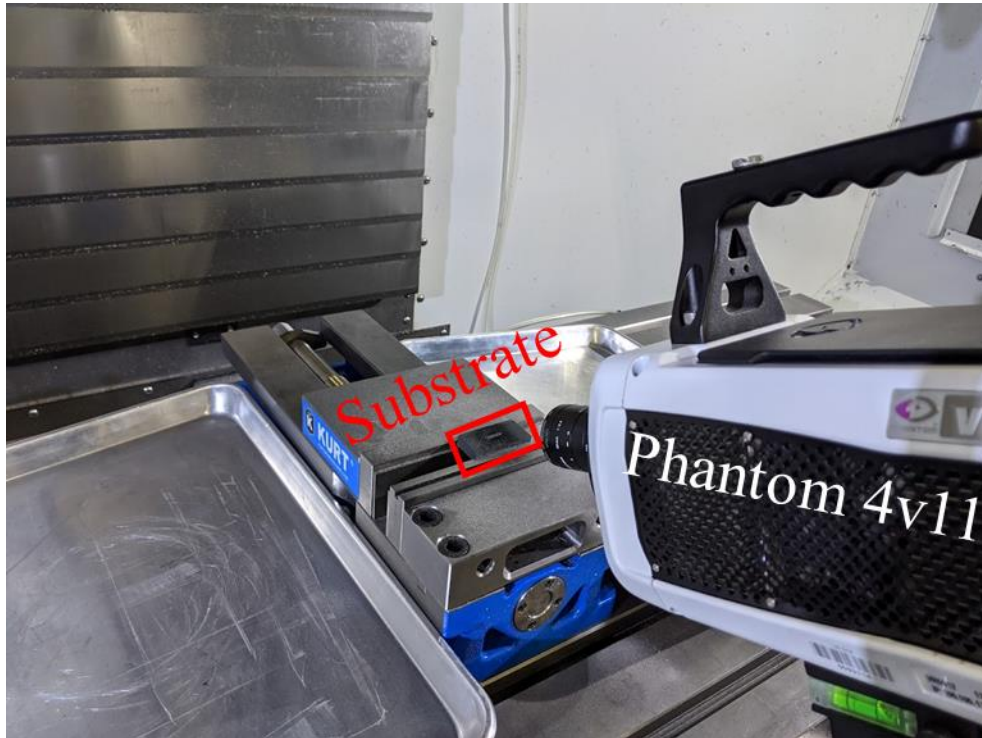


Figure 21: The high-speed imaging setup for capturing laser-polymer interactions during the first pass of a DED deposition.

In the second series of experiments, two key DED parameters were varied in single deposition passes to determine their impact on metal deposition on polymer substrates: laser power and laser scan speed. The design of experiments is discussed more thoroughly in Chapter 3, and the list of experimental parameters is detailed in Table 3. Each of these experiments was recorded using an AXIS fixed dome camera.

Substrates of length 5cm, width 2.5 cm, and height 1.27 cm were manufactured out of each type of polymer for all experiments. A single, 1.27 cm long deposition pass was completed for each experiment using 316 stainless steel powder feedstock on the VF-5/40XT Haas modified by HMT with an AMBIT™ S7-2 High Rate Laser Cladding Head for laser blown-powder DED capabilities. The G-code for all experiments was written by hand and can be found in Appendix A. For all experiments, shield gas flow was set to 10 L/min, and carrier gas flow rate was set to 4 L/min, corresponding to a mass flow rate of 9 g/min. After printing was completed, each of the substrates was visually inspected to determine the

polymer response to the molten metal and laser, including the appearance of any deposited metal, residue that adhered to the polymer surface during deposition, and any loss of geometric integrity of the polymer. The substrates were then microscopically imaged on a Leica S8 APO microscope for further evidence of the polymer response to the molten metal and laser, and the appearance of deposited metal, any exposed fibers, and evidence of polymer melting and degradation.

2.4 Results and discussion

The polymer absorbances were analyzed and compared to one another. Then the high-speed videos were examined for evidence of polymer degradation and combustion, and the variations in combustion across the polymers were analyzed.

2.4.1 Polymer absorptivity

The polymer transmittance and absorbance results for all polymers used in this research are shown in Figure 22. The transmittance and absorbance values for all the polymers are presented in Table 2. The transmittances of all polymers except PLA were under 0.25%, much less than the PLA transmittance of 35.22%. These measurements indicated that all polymers except PLA (CF ABS, GF ABS, GF nylon, WF PLA) will readily absorb the laser energy, while PLA will transmit a significant amount of the laser energy through its depth. As more of the laser energy will be transmitted through a greater depth of the PLA, it was expected that the overall temperature increase of the PLA will be lower compared to the other polymers, hindering successful metal deposition. The absorbance measurements also supported this conclusion, as the CF ABS had the highest absorbance and the absorbances of the other polymers were significantly lower, with PLA having the lowest absorbance.

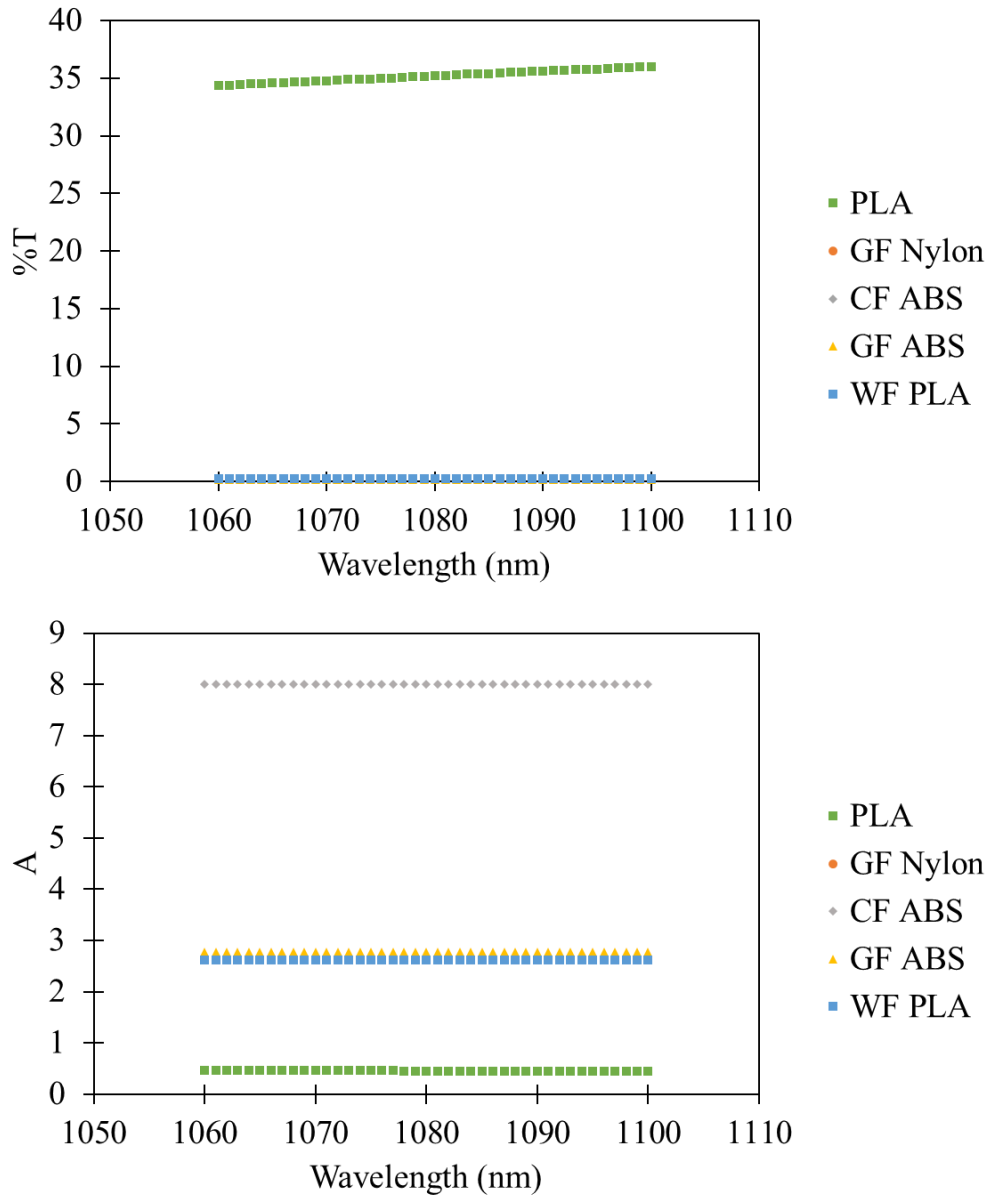


Figure 22: Transmittance and absorbance results for PLA. The PLA is more transmissive and less absorptive than the other polymers, and CF ABS is the most absorptive and least transmissive material.

Table 2. Polymer transmittance and absorbance at 1,080 nm.

Polymer	Transmittance (%)	Absorbance (abs)
CF ABS	0	8
GF ABS	0.1704	2.7686
GF Nylon	0.2254	2.647
PLA	35.22	0.4532
WF PLA	0.2438	2.613

2.4.2 Polymer combustion

In-process still images from the high-speed imaging of the polymer substrates exposed to a single deposition pass are shown in Figure 23. Key differences in combustion and polymer degradation residue were observed between the fiber-filled polymers (CF ABS, GF ABS, and GF nylon) and the non-fiber-filled polymers (PLA and WF PLA). Both PLA materials resulted in less combustion when exposed to the laser, and instead of melting and re-solidifying on the surface of the substrate, the feedstock powder became embedded in the surface of the substrates as the polymers softened during the DED pass and then re-solidified. In contrast to the PLA and WF PLA, the filled polymer substrates resulted in significant combustion when exposed to the laser, circled in red in Figure 23, although the material did not ignite. The images of the filled polymers also show smoke during deposition and sooty residue remaining on the substrates after deposition, indicated with arrows in Figure 23.

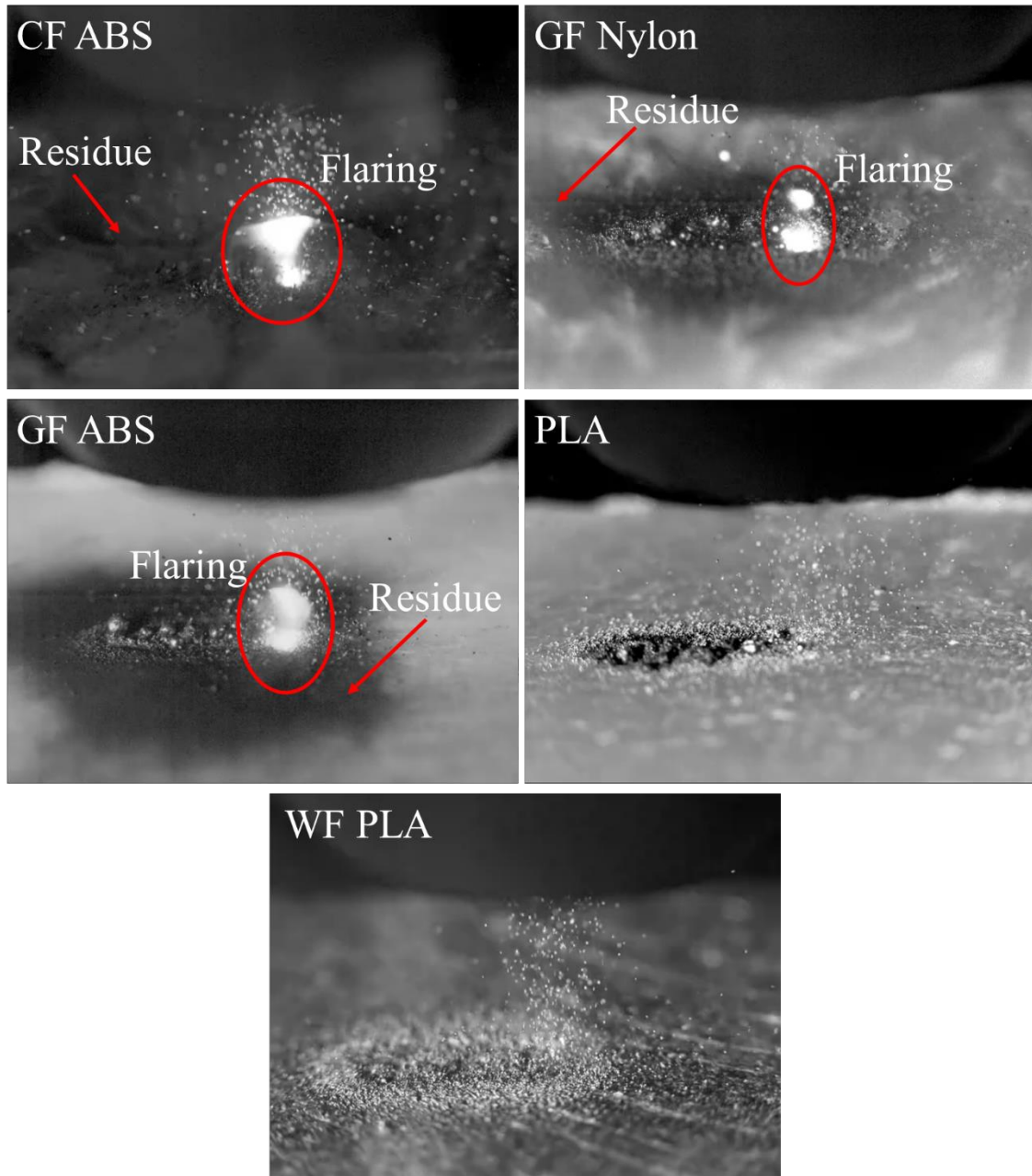


Figure 23: Stills from high-speed videos on CF ABS, GF Nylon, GF ABS, PLA, and WF PLA. Circles indicate flaring, and arrows indicate smoke and residue.

The flaring observed during deposition varied based on the substrate. For flaring to occur at all, three elements must have been present: heat, fuel, and oxygen. When subjecting a carbon-based polymer substrate to the blown-powder DED process, heat is supplied by the laser and fuel is supplied by both the substrate and any flammable degradation byproducts due to polymer combustion. The degradation byproducts are dependent on the degradation

pathways of the polymers, which are complex and difficult to predict under DED conditions. However, Thermo-Calc Software was used to predict the pyrolysis byproducts of each of the polymers at 1400°C to supply a general understanding of potential byproducts. 1 mole of ABS ($C_8H_8 \cdot C_4H_6 \cdot C_3H_3N$)_n was predicted to produce 0.45 moles of carbon char and 0.55 moles of gas, consisting of 92% H₂, 5% N₂, and 3% other gases. 1 mole of Nylon66 ($C_{12}H_{22}N_2O_2$)_n was predicted to produce 0.26 moles of carbon char and 0.74 moles of gas, consisting of 78% H₂, 14% CO, 7% N₂, and 1% other gases. 1 mole of PLA ($C_3H_4O_2$)_n was predicted to produce 0.11 moles of carbon char and 0.89 moles of gas, consisting of 50% CO, 49% H₂, and 1% other gases. Most of the gaseous degradation byproducts are flammable, providing the fuel required for combustion. Oxygen needed to be supplied from the environment. As shown in Figure 24, the HMT system is designed such that the carrier, nozzle, and shield gases create an inert environment around the laser. The presence of flaring in several trials, circled in Figure 23, suggested that oxygen must be infiltrating this inert environment.

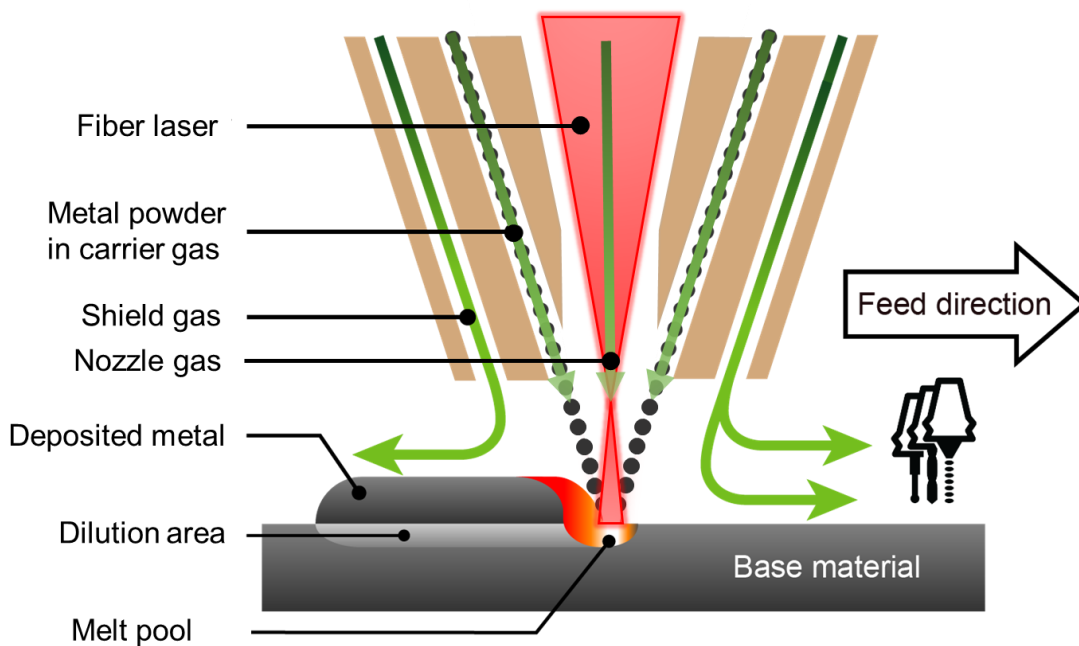


Figure 24: Diagram of the blown-powder DED process, including the laser focal point, the carrier gas, the nozzle gas, and the shield gas. The combination of these gases results in an inert area around the laser. (Image courtesy of HMT)

The flaring observed in these trials also occurred above the surface of the polymer, emphasized for the trial on CF ABS in Figure 25. Figure 25 also shows that the location of this flaring coincided with the location of gaseous byproducts hypothesized to be created during the combustion of the CF ABS. The gaseous byproducts could have provided the fuel for the flaring, and the pressure from the gases likely also created enough turbulence to allow oxygen from the surrounding environment to perturb the inert environment. The byproducts and oxygen, in combination with energy from the laser, were the likely cause of the flaring that occurs above the surface of the polymer.

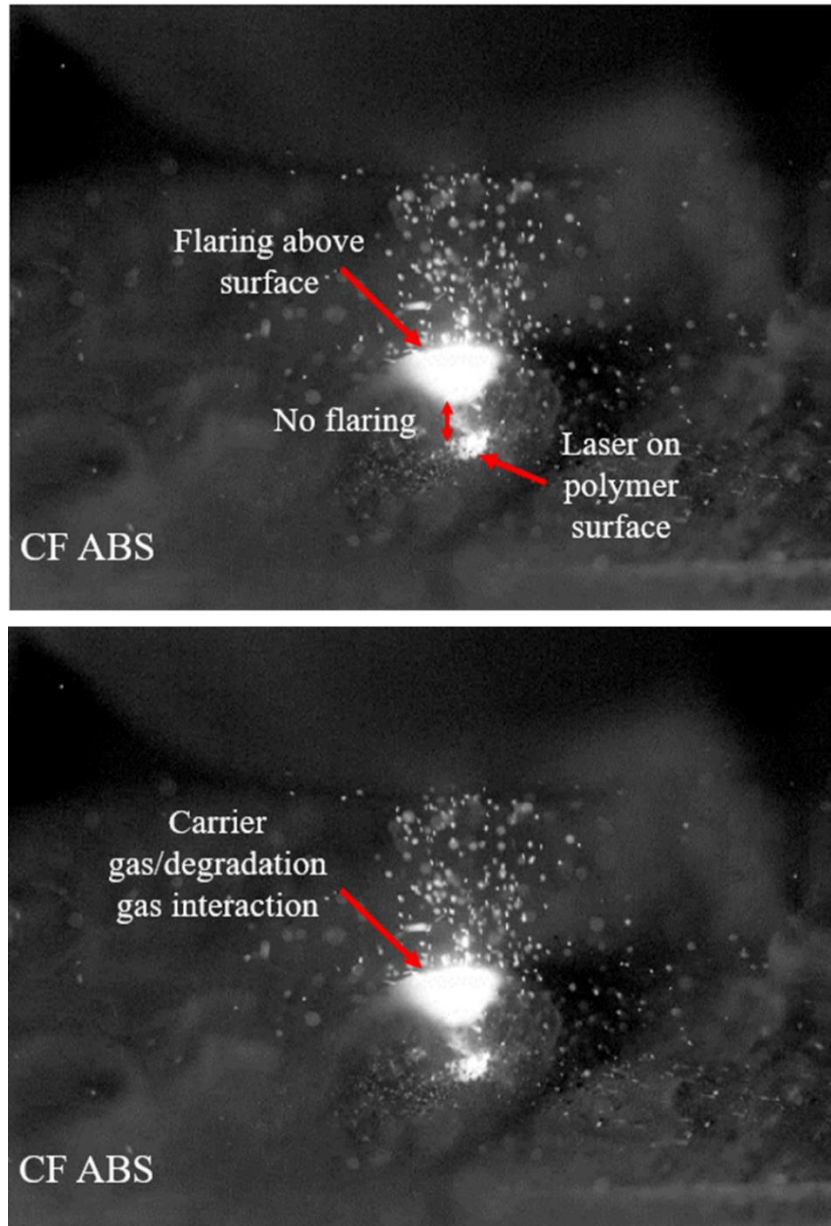


Figure 25: Flaring occurs above the surface during deposition on a CF ABS substrate (top). The location of this flaring coincides with the location of the interaction between the carrier gas and the gaseous combustion byproducts (bottom).

However, flaring did not occur in all specimens. As seen in Figure 23, no flaring was visible from the PLA and WF PLA experiments. The lack of flaring displayed by these polymers was likely the result of their absorptivity. The PLA is less absorptive than the other polymers, so the laser energy required a longer distance to be fully absorbed. In polymers with a higher absorptivity, such as CF ABS, the laser energy was absorbed at a shallow depth, so a small volume of material absorbed the laser energy. Evidence of this can be

seen in Figure 26: in the cross section of PLA (right), swirling from melting and re-solidification of the polymer can be seen at a depth of over 2mm, while no such swirling can be seen in the GF ABS. In this case, a larger volume of material absorbed the laser energy. When the volume of the material absorbing the laser energy was small, the material absorbed enough energy to reach combustion temperatures. When the volume of the material absorbing the laser energy was larger, the material did not absorb enough energy to reach combustion temperatures, and flaring was not observed.

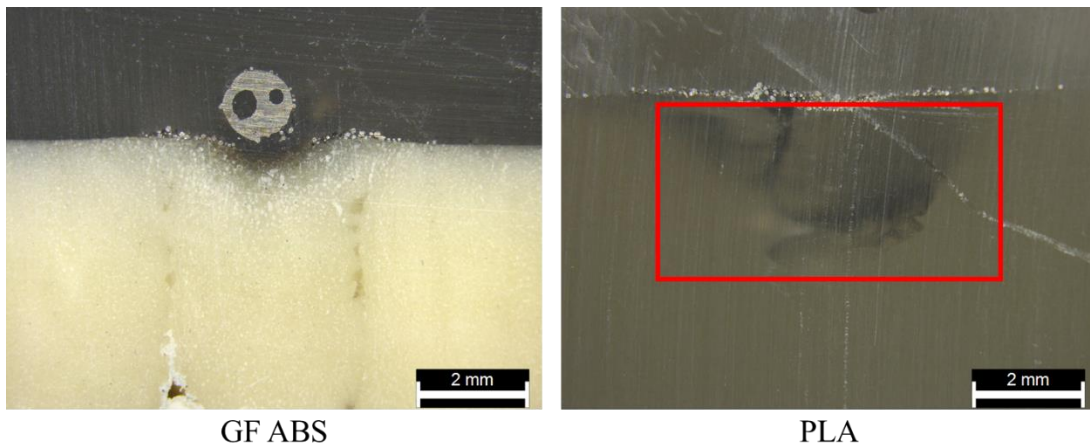


Figure 26: Cross sections of single bead tests on GF ABS and PLA. Evidence of transmission can be seen in PLA (boxed in red) but not GF ABS.

In process videos of each of the experiments in Table 3 were taken, and still images from all videos can be found in Appendix B. Representative stills showing the effect of increasing power on CF ABS and PLA samples are shown in Figure 27. For both substrates, increasing the power while remaining at the same scan speed increased flaring and smoke from polymer degradation during the deposition. The CF ABS samples, as with all the fiber-filled samples, responded to deposition with more flaring and smoke than the PLA samples, indicating that the polymer in these fiber-filled samples experienced more thermal degradation.

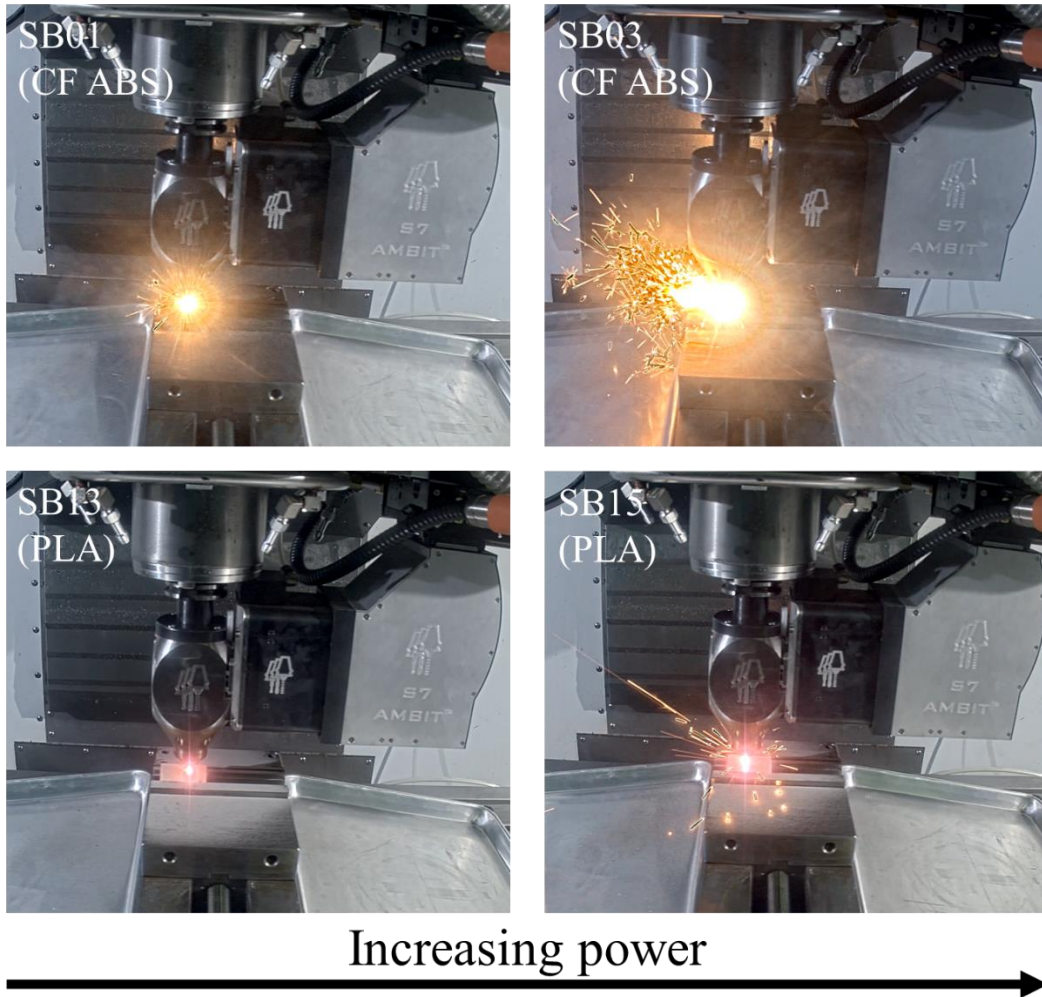


Figure 27: Increasing power tends to increase in-process flaring, shown here with two CF ABS trials (SB01 at 100 W and SB03 at 300 W) and two PLA trials (SB13 at 100 W and SB15 at 300 W). Images from all trials can be found in Appendix B.

Representative stills showing the effect of increasing scan speed on CF ABS and PLA samples are shown in Figure 28. For both substrates, increasing the scan speed while remaining at the same power decreased flaring and smoke from polymer degradation during the deposition. Like the samples in Figure 27, the CF ABS samples, as with all the fiber-filled samples, responded to deposition with more flaring and smoke than the PLA samples, indicating that the polymer in these fiber-filled samples experienced more thermal degradation.

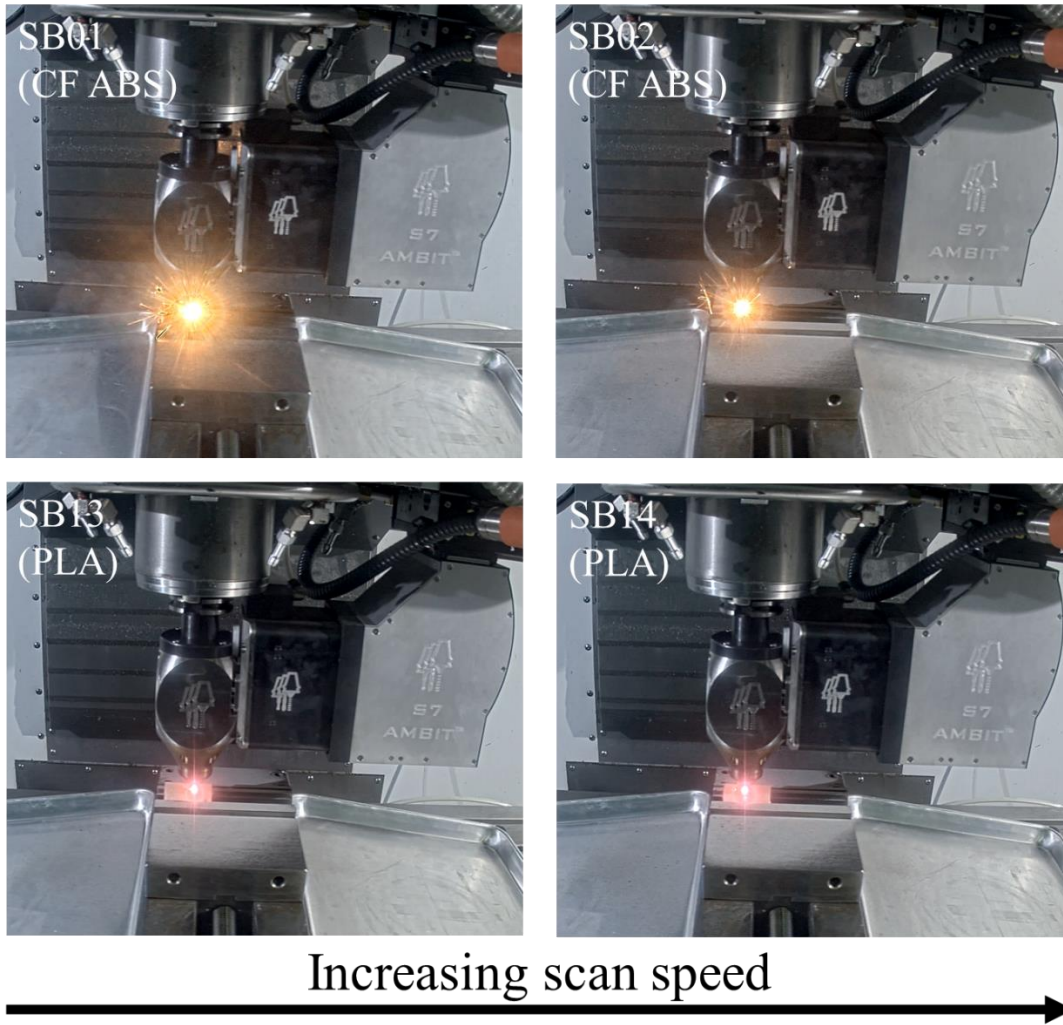


Figure 28: Increasing scan speed tends to decrease in-process flaring, shown here with two CF ABS trials (SB01 at 400mm/s and SB02 at 800mm/s) and two PLA trials (SB13 at 400mm/s and SB14 at 800mm/s). Images from all trials can be found in Appendix B.

2.4.3 Post-printing observations

The substrates for all experiments in Table 3 were visually inspected and imaged after deposition, and the images of all substrates can be found in Appendix B. Representative images showing the effect of increasing power on CF ABS and PLA samples are shown in Figure 29. For both substrates, increasing the power while remaining at the same scan speed increased the amount of charred residue remaining on the substrates after deposition. The CF ABS substrates, as with all the fiber-filled samples, had significantly more residue than the PLA samples, suggesting that the polymer in these fiber-filled samples experienced more thermal degradation. Increasing the power also resulted in more sparking

from the PLA, as evidenced by the presence of melted and re-solidified feedstock material embedded in the PLA outside of the bead.

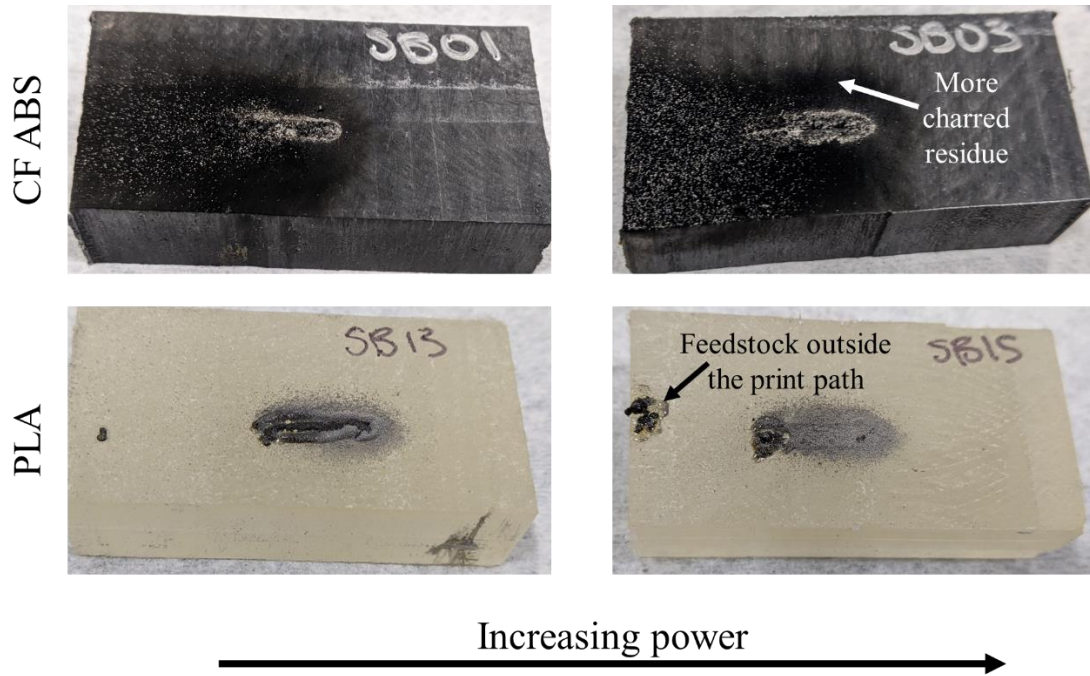


Figure 29: The effect of increasing power, shown here with two CF ABS trials (SB01 at 100 W and SB03 at 300 W) and two PLA trials (SB13 at 100 W and SB15 at 300 W). Images from all trials can be found in Appendix B.

Representative images showing the effect of increasing power on CF ABS and PLA samples are shown in Figure 30. In both trials, increasing the scan speed while remaining at the same power decreased the amount of residue remaining on the substrates after deposition. The CF ABS substrates, as with all the fiber-filled samples, had significantly more residue than the PLA samples, suggesting that the polymer in these fiber-filled samples experienced more thermal degradation.

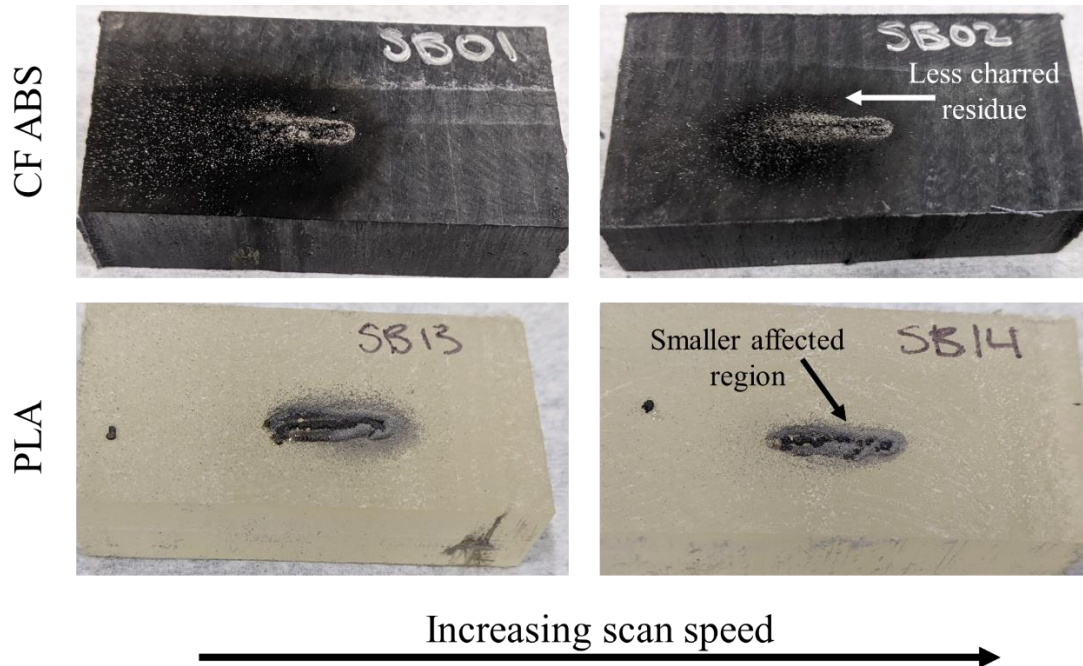


Figure 30: The effect of increasing scan speed, shown here with two CF ABS trials (SB01 at 400mm/s and SB02 at 800mm/s) and two PLA trials (SB13 at 400mm/s and SB14 at 800mm/s). Images from all trials can be found in Appendix B.

The samples were then microscopically imaged, and representative images of the effect of increasing power on GF ABS and PLA samples are shown in Figure 31. Increasing power generally resulted in more feedstock powder being melted and deposited, as more energy was absorbed by the feedstock powder. However, the deposited metal generally decreased in quality with increased power, as evidenced by an increase in visible porosity and in residue on and around the metal after deposition. Both the porosity and the deposited residue is likely due to increased polymer degradation caused by increased laser power. As more of the polymer degraded, more gas was formed as a byproduct, which then infiltrated the polymer and resulted in porosity. Another byproduct of the polymer degradation was the char residue, which coated the deposited metal and the surrounding polymer during deposition.

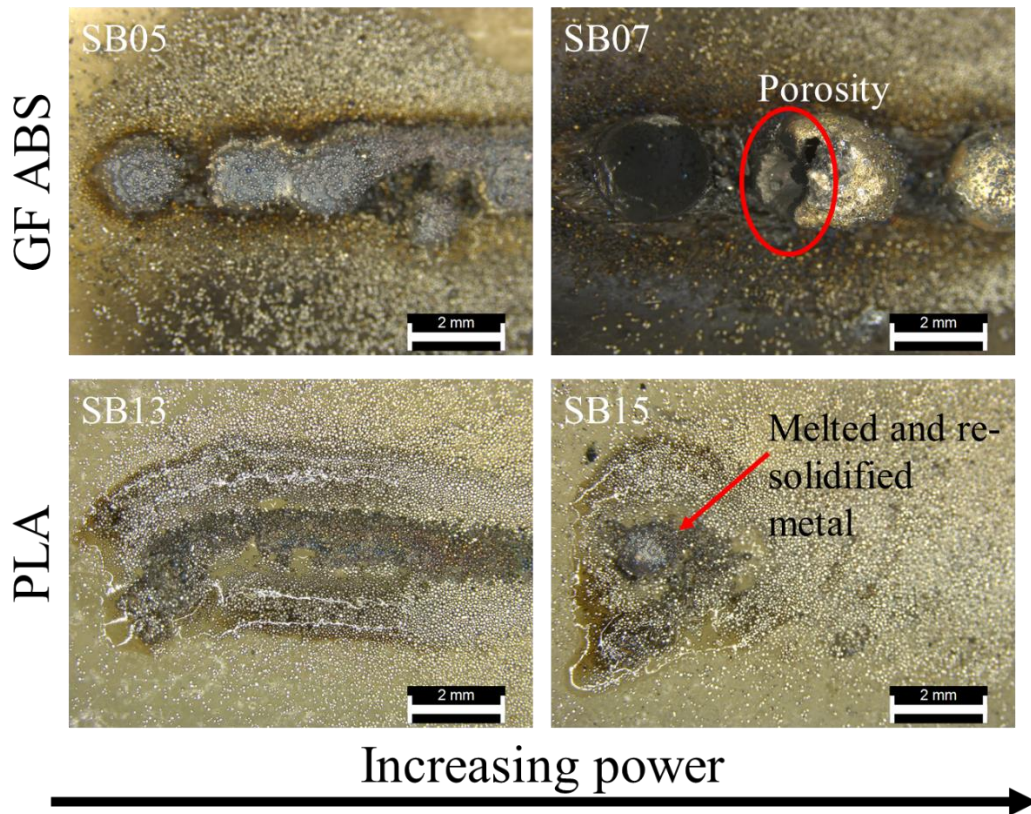


Figure 31: The effect of increasing power, shown here with two GF ABS trials (SB05 at 100 W and SB07 at 300 W) and two PLA trials (SB13 at 100 W and SB15 at 300 W).

Representative images of the effect of increasing scan speed on GF ABS and PLA samples are shown in Figure 32. Increasing scan speed generally resulted in less feedstock powder being melted and deposited, as both the feedstock powder and substrate had less time to absorb the laser power, resulting in less overall energy being absorbed. Increased scan speed also resulted in more residue on the substrate after deposition, although the effect is lesser than the effect of increased power.

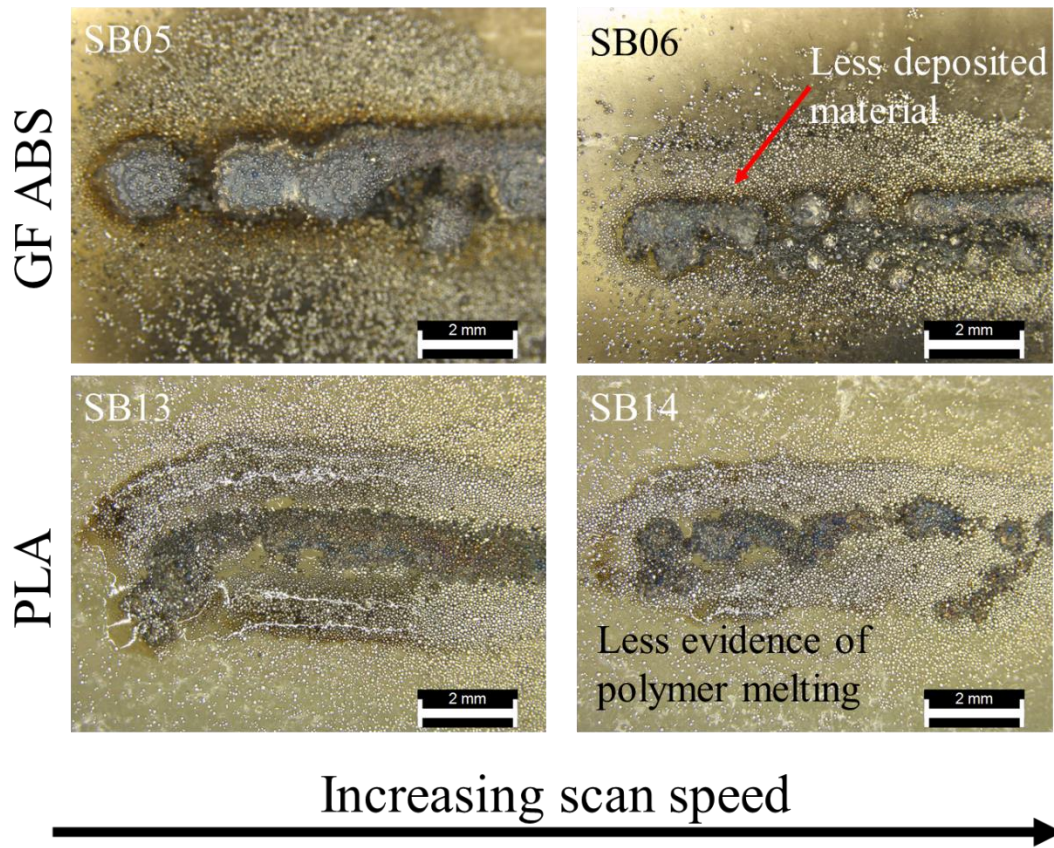


Figure 32: The effect of increasing scan speed, shown here with two GF ABS trials (SB05 at 100 W and SB07 at 300 W) and two PLA trials (SB13 at 100 W and SB15 at 300 W).

Evidence of exposed fibers due to polymer degradation was seen in all fiber-filled samples, a selection of which are shown in Figure 33. These exposed fibers support the hypothesis that upon exposure to the laser, a thin layer of polymer degrades, exposing the fibers embedded within the polymer, as diagrammed in Figure 34. These fibers then serve to protect the rest of the polymer from further thermal degradation, as both glass and carbon fibers can withstand higher temperatures than polymers.

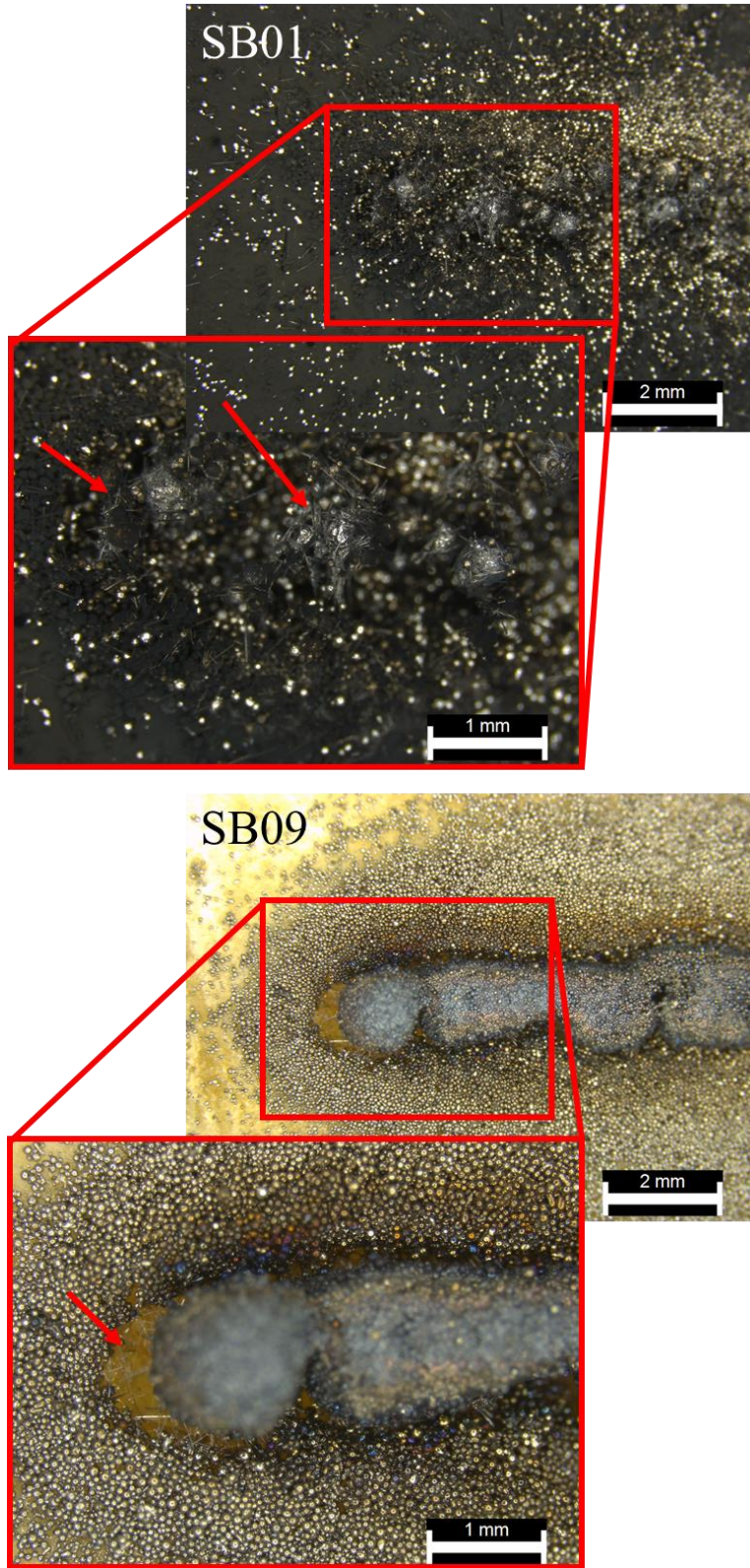


Figure 33: Evidence of exposed fibers in 100 W, 400mm/min trials on CF ABS (SB01) and GF ABS (SB05).

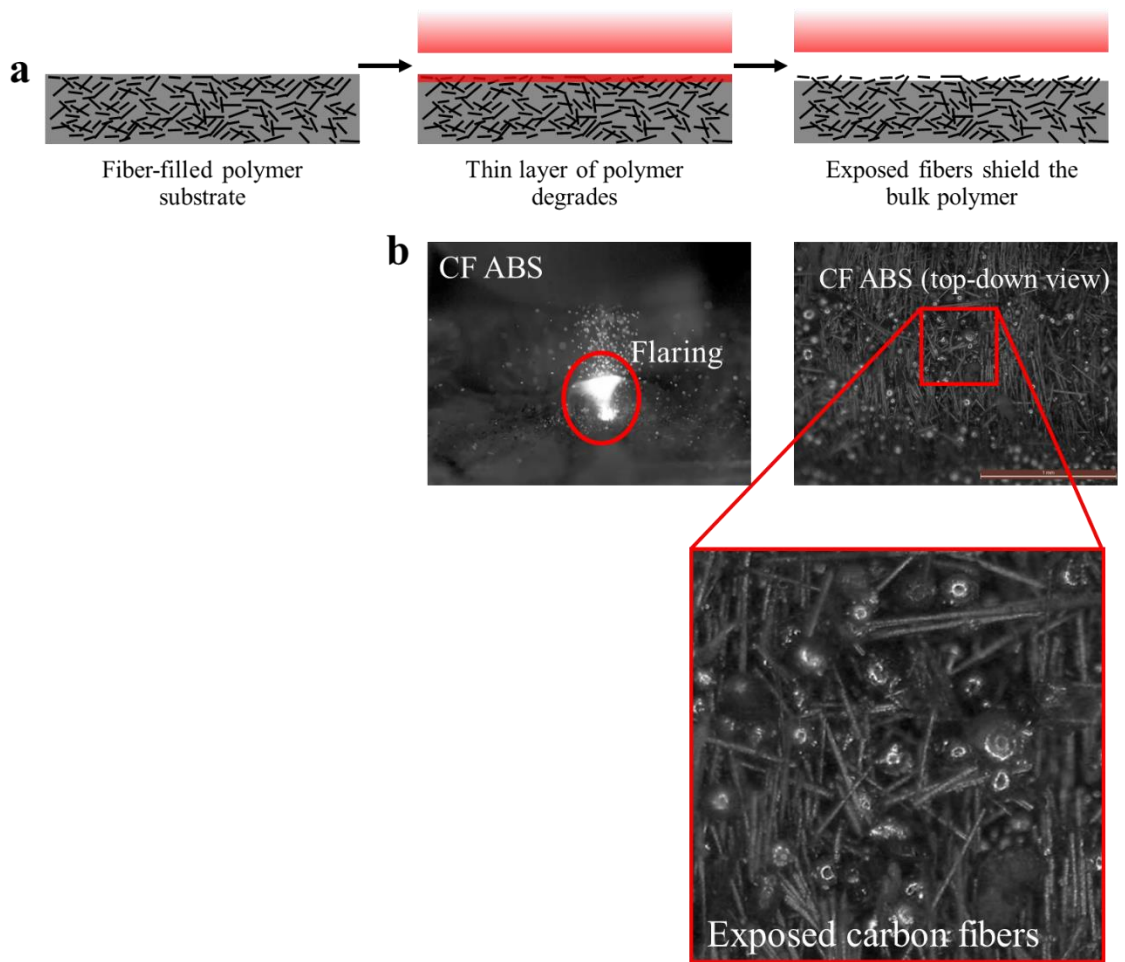


Figure 34: The (a) schematic of and (b) pictures of the ablative reaction of a fiber filled polymer to an extreme thermal environment.

Not all trials resulted in a deposition caused by melting and re-solidification of the feedstock powder, and those depositions that did form had rough surface finishes, as seen in several representative microscopic images in Figure 35. The rough surface finish was caused by feedstock powder adhering to a solidifying deposition that was not at a high enough temperature to melt the powder.

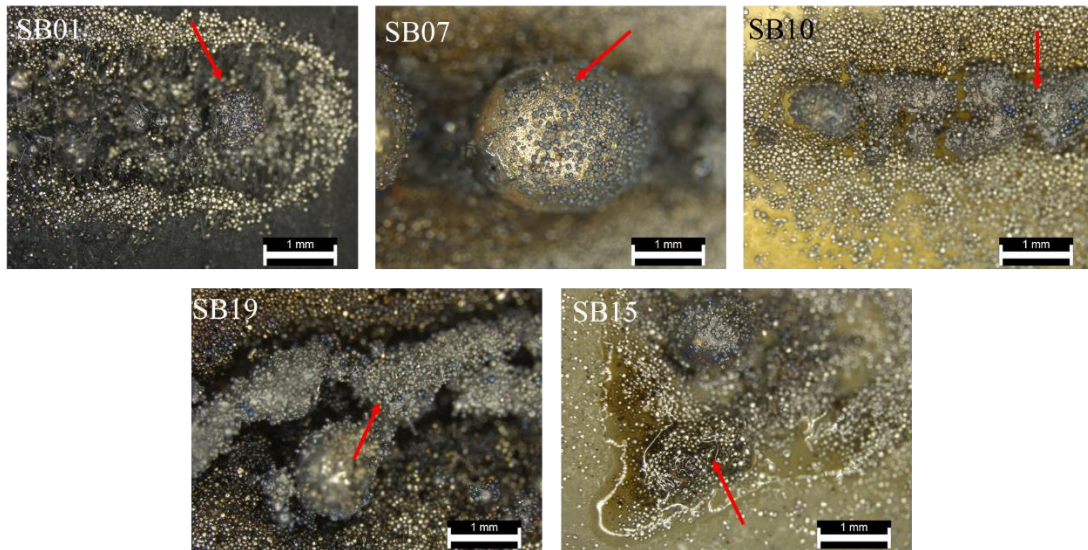


Figure 35: Rough surface finish of deposited metal in multiple trials due to adhered unmelted feedstock powder (indicated with arrows).

The porosity at a higher power shown in Figure 31 was observed in several other trials at higher powers, as shown in Figure 36. This porosity was hypothesized to have been caused by gas produced during polymer infiltrating the molten metal and, in the case of the trials in Figure 36 bursting out of the surface of the deposited metal. This hypothesis is also supported by the results of CT scans completed on larger-scale depositions, which are discussed in Chapters 4 and 5.

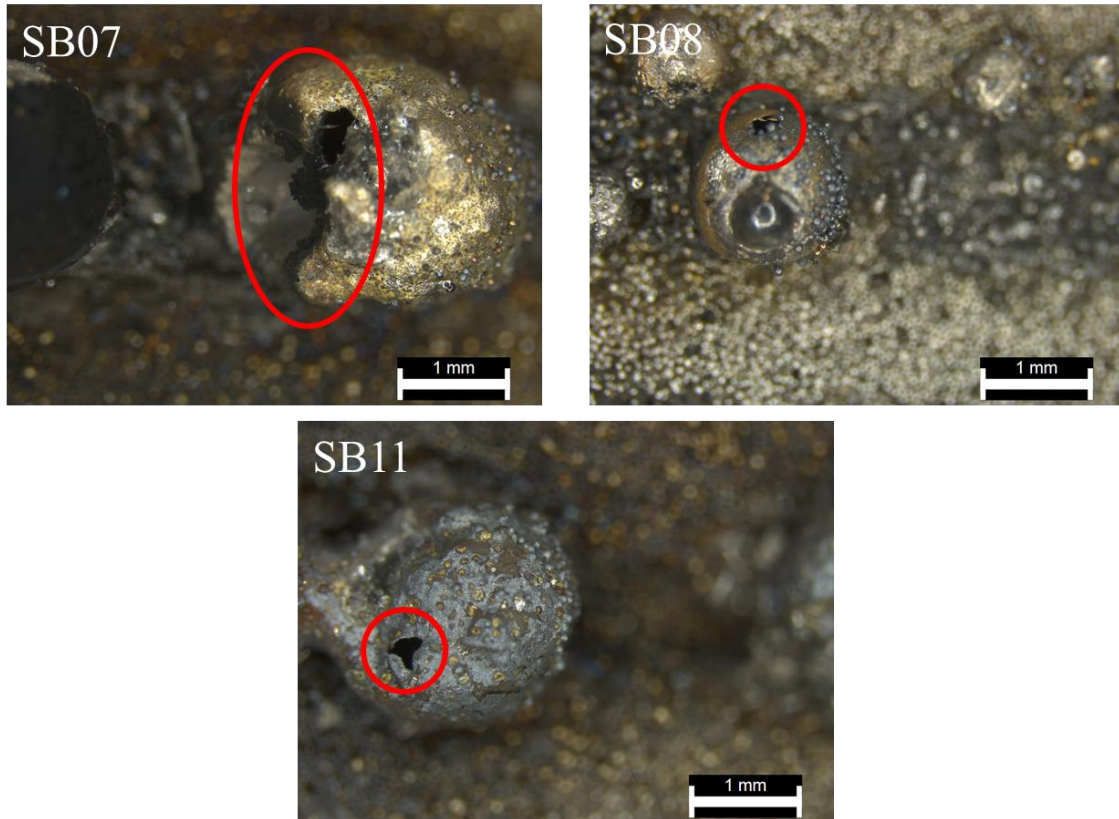


Figure 36: Evidence of porosity due to polymer degradation.

The polymer surrounding the laser track appears to melt and re-solidify during deposition, as evidenced by the embedded powder shown in several representative images in Figure 37. The feedstock powder did not interact with the laser, as it was not in the path of the laser. However, heat transfer within the polymer resulted in some melting of the polymer surrounding the laser track, and the feedstock powder blown onto those melted surfaces was embedded into the polymer.

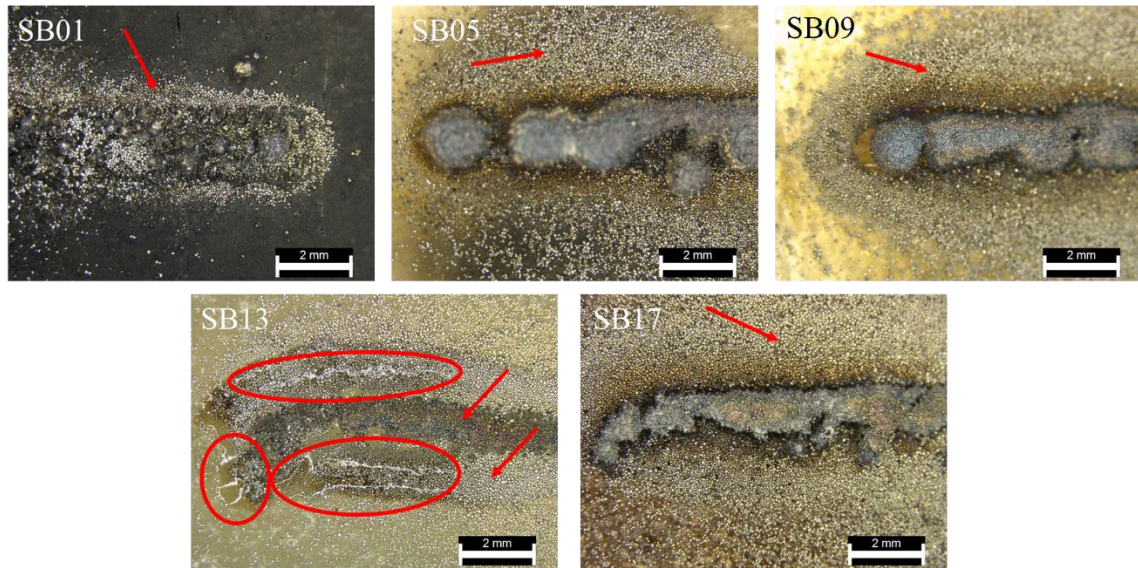


Figure 37: Feedstock powder became embedded in the polymer around the edges of the pass, indicated with arrows. The reflective surfaces circled in PLA trial SB13 indicate melting and re-solidification of the polymer around the embedded feedstock powder.

2.5 Conclusions

For polymer support structures to be considered successful, the polymer-DED interaction must be safe, and metal deposition on a polymer must be possible. In this chapter, the polymer-DED interaction was investigated, focusing specifically on polymer interactions with the laser. Laser spectroscopy was performed to determine the absorbances of the polymers used in this research at 1,080 nm, the wavelength of the laser in the HMT system. Single bead tests were then performed to observe the effect of the DED process on five polymer substrates.

Some combustion was observed during all single bead tests, but significant flaring only occurred during the tests run on CF ABS, GF ABS, and GF nylon. The occurrence of flaring correlates with the absorptivity of the polymer. If the polymer is too transmissive, not enough of the laser energy will be absorbed close to the surface of the polymer for the surface to reach combustion temperatures. The differences in levels of flaring between CF ABS, GF ABS, and GF nylon were attributed to variations in the absorbances of and degradation byproducts produced by the different polymers. The flaring in all three of these

polymers was inconsistent, as the oxygen required to create the flaring was most likely being provided via infiltration of shield gases. These shield gases were disrupted enough by the combustion process to allow some oxygen into the shielded area, enabling flaring. Generally, combustion will occur when enough laser energy is absorbed near the surface of the polymer to reach combustion temperatures and the degradation produces significant flammable byproducts.

Observations of the single-bead experiments during and after the DED process resulted in valuable insights into the printing parameters. There was a tradeoff between polymer degradation and metal deposition: more laser transmission decreased degradation because the laser energy was distributed over a larger volume, but more laser transmission decreased feedstock powder melting by lowering polymer surface temperature. Polymers with fiber fillers are required to facilitate deposition, as the two polymers without fiber fillers had little to no melted and re-solidified metal deposition. Higher laser power and lower scan speed resulted in more flaring, more smokey residue, more metal deposition, and more evidence of porosity. These trends suggest that higher laser power and lower scan speed cause higher temperatures, which will be explored further in Chapter 3.

CHAPTER 3. MEASUREMENT AND MODELING OF POLYMER DEGRADATION DURING DED METAL DEPOSITION

3.1 Introduction

An understanding of the relationships between DED settings, material properties, and predicted polymer degradation is critical in determining the level of degradation expected when exposing a polymer to the DED process. Understanding these relationships enables appropriate deposition parameter selection and ensures that unsuitable polymers are not used as support structures. The methodology for single-bead experiments performed on a variety of polymers using different laser powers and laser scan speeds is presented in this chapter. Polymer degradation results from these experiments are then discussed. This discussion includes the introduction of semi-infinite and Rosenthal thermal models to understand the experimental trends, along with aspects that affect degradation but are not considered in these models, such as polymer transmissivity and ablation.

3.2 Background

Polymer degradation and ablation are key in understanding the degradation experienced by polymer substrates exposed to the DED process. Several semi-infinite thermal models are considered to develop an understanding of the relationships between polymer properties, DED parameters, and polymer degradation. Semi-infinite thermal modeling encompasses all thermal models using the assumption that the heated body has one single-plane surface extending to infinity in all other directions. The semi-infinite models used to support the experimental degradation results include the constant surface temperature model, the constant surface heat flux model, and the Rosenthal moving heat source model.

3.2.1 Polymer combustion

All polymers will eventually degrade, experiencing an irreversible change which eventually leads to failure [79]. This degradation can occur via several mechanisms. Most relevant to this research is degradation by thermal degradation either in the presence of oxygen, known as combustion, or in the absence of oxygen, known as pyrolysis. Pyrolysis occurs in one of three ways: random scission of bonds along the backbone chain, depolymerization, usually initiated at chain ends, and elimination of a low-molecular-weight fragment other than a monomer [79]. In combustion, polymer molecules are

thermally decomposed through oxidation [80]. Although little work has been done specifically in probing the response of polymers to the DED process, much of the work on polymer degradation gives insight into polymers' responses to extreme environments.

The existence of ablative polymers indicates that it is possible for certain polymers to withstand the DED process without significant changes to geometry. Commonly seen in space applications, ablative polymers are designed such that the surface of the material will degrade into a protective char upon exposure to high temperatures, as shown in Figure 38 [81]. For example, carbon-fiber-reinforced phenolic composites were evaluated as a charring ablator for the severe heating environment expected with the Galileo probe [82]. In one study, an R2 carbon phenolic reached surface temperatures of over 1000°C, but the ablation of the material under these conditions protected the bulk polymer, and temperatures at a depth of 0.5 inches did not exceed 115°C [83]. These polymers are good candidates for support structures, as these supports would need to survive contact with the DED energy source and molten metal at least long enough for the metal to solidify sufficiently to support the rest of the metal component.

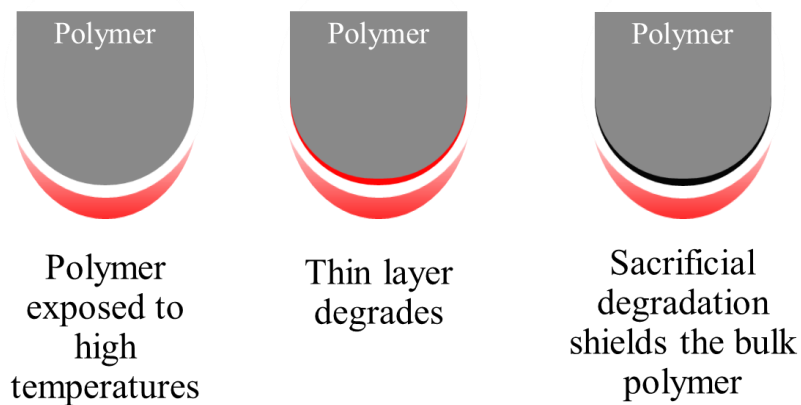


Figure 38: The ablation process.

3.2.2 Semi-infinite modeling and Rosenthal moving heat source

In semi-infinite modeling, the body in question is assumed to be a semi-infinite solid that has a single plane surface extending to infinity in all directions except one. The planar surface has either a temperature or heat flux condition applied to it, and knowledge of the

initial temperature of the solid, the planar surface condition, and the temperature at an infinite depth allows the general heat equation to be solved for the temperature of the solid as a function of depth [84].

Semi-infinite assumptions can also be applied to other, more specific thermal models. For example, Rosenthal used a semi-infinite body assumption in his development of a point moving heat source model to predict heat distribution during welding and cutting [85]. In the Rosenthal model, it is assumed that a quasi-stationary state is reached in the piece: there is no change in the temperature distribution around the heat source as a function of distance. This model predicts the temperature around the point source, which is moving at some velocity, as a function of position and time. This model has its limitations, including predicting that the temperature at the heat source reaches infinity, but the temperature profile approximations have proven useful in multiple research endeavors. For example, Plotkowski *et al.* compared transient results to steady states predictions from the Rosenthal equations to verify and validate a rapid heat transfer calculation methodology for transient melt pool solidification conditions in powder bed metal AM [86]. Promoppatum *et al.* used an FE model and the Rosenthal equation to study thermal and microstructural phenomena in the LPBF of Inconel 718 [87].

Further works expanded and built on the Rosenthal model. For example, in 1942, Jaeger developed a model similar to Rosenthal in that it predicts the temperature of a semi-infinite solid exposed to a moving heat source [88]. However, Jaeger's model does not assume a point source of heat, but rather a heat source of some shape. Additionally, Jaeger's model does not assume the quasi-stationary state assumed in the Rosenthal model. These changes improve the accuracy of the Jaeger model at the cost of increased complexity. Similar to the Rosenthal model, the Jaeger model has been valuable in thermal research since its development. Komanduri and Hou completed thermal analyses on both the arc welding process, developing an analytical solution for the temperature-rise distribution in arc welding of short workpieces and for the laser surface transformation hardening process based on Jaeger's model [89, 90].

3.3 Methodology

3.3.1 Design of experiments

To validate the thermal model prediction of degradation depth, a series of single-pass experiments were performed, and the degradation depth was measured after printing. Two key DED parameters were varied to determine their impact on metal deposition on polymer substrates: laser power and laser scan speed. Five polymers were tested as substrates: carbon-fiber-filled acrylonitrile butadiene styrene (CF ABS), glass-fiber-filled nylon (GF nylon), glass-fiber-filled ABS (GF ABS), neat polylactic acid (PLA), and wood-flour-filled PLA (WF PLA). These polymers were selected because they (1) are easily printable, (2) are readily available, and (3) provide a range of filled and unfilled printable polymers for comparison. For the design of experiments, each polymer was treated as a separate experiment. For each polymer, the linear model was of the form:

$$y = \beta_0 + \beta_1 x_1 + \beta_2 x_2 + \beta_{12} x_{12} \quad 3.1$$

In this model, y represents the output being measured (degradation depth), the β_1 constant indicates the effect of the laser power (x_1) interaction on the output, the β_2 constant indicates the effect of the laser scan speed (x_2) interaction on the output, and the β_{12} constant indicates the effect of the two-way interaction between laser power and scan speed (x_{12}) on the output. To solve the four unknowns in this equation, a minimum of four experiments with varying laser power and scan speed conditions were required. The experiments used to solve this linear model are listed in Table 3. The lower laser power value was based on the minimum reliable power achievable by the experimental system, and the upper laser power value was based on preliminary experiments, which determined that powers above 300 W resulted in significant smoke and polymer residue, causing concerns about damaging the laser optic system. The scan speed parameters were selected to be centered around 600mm/min, the scan speed commonly used for metal-on-metal depositions.

Qualitative observations of the results of these experiments were made and discussed in Chapter 2, and a quantitative relationship between laser power, scan speed, and polymer suitability for each polymer was also desired. To that end, polymer suitability for the single layer tests was determined by the laser degradation depth. This output was measured for

each trial by embedding the sample in resin, cross sectioning the sample, and measuring the maximum degradation depth. These measurements also served as a validation metric for the thermal models presented in Chapter 3.

Table 3. Design of experiments to derive a linear model of laser power and scan speed.

Experiment	Polymer Type	Laser Power (W)	Scan Speed (mm/min)
SB01	CF ABS	100	400
SB02	CF ABS	100	800
SB03	CF ABS	300	400
SB04	CF ABS	300	800
SB05	GF ABS	100	400
SB06	GF ABS	100	800
SB07	GF ABS	300	400
SB08	GF ABS	300	800
SB09	GF Nylon	100	400
SB10	GF Nylon	100	800
SB11	GF Nylon	300	400
SB12	GF Nylon	300	800
SB13	PLA	100	400
SB14	PLA	100	800
SB15	PLA	300	400
SB16	PLA	300	800
SB17	WF PLA	100	400
SB18	WF PLA	100	800
SB19	WF PLA	300	400
SB20	WF PLA	300	800

3.3.2 Setup and procedure

Substrates of length 5cm, width 2.5cm, and height 1.27cm were manufactured out of each type of polymer for all experiments. A single, 1.27cm long deposition pass was completed for each experiment using 316 stainless steel powder feedstock on the VF-5/40XT Haas modified by Hybrid Manufacturing Technologies (HMT) with an AMBIT™ S7-2 High Rate Laser Cladding Head for laser blown-powder DED capabilities. The G-code for all experiments was written by hand and can be found in Appendix A. For all experiments, shield gas flow was set to 10L/min, and carrier gas flow rate was set to 4L/min, corresponding to a mass flow rate of 9g/min. Each of these experiments was recorded using an AXIS fixed dome camera.

After printing is completed, each of the substrates was visually inspected to determine the polymer response to the molten metal and laser, noting the appearance of any deposited metal, residue that adhered to the polymer surface during deposition, and any loss of geometric integrity of the polymer. The substrates were then imaged on a Leica S8 APO microscope for further evidence of the polymer response to the molten metal and laser, and the appearance of deposited metal, any exposed fibers, and evidence of polymer melting and degradation. The samples were then embedded in resin, cross-sectioned at the center of the print as shown in Figure 39 using a diamond saw, and ground first with 500 grit paper and then with 1000 grit paper to remove damage from the cross-sectioning process. The cross sectioned components were then imaged on the same Leica S8 APO microscope to measure the laser degradation depth for each sample. The degradation depth measurement was defined as the depth of polymer degraded by the laser during the DED process, as shown in Figure 39. The measurement was performed five times per cross section to obtain measurement error.

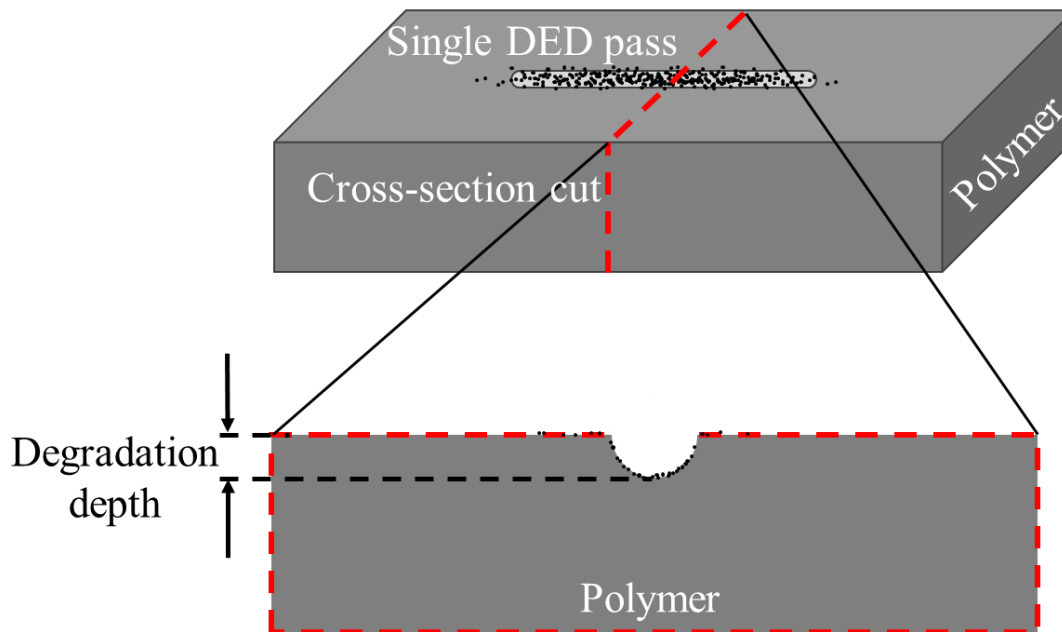


Figure 39: Sample preparation for degradation depth measurement.

3.4 Polymer degradation results

A sample cross-section and degradation measurement on a GF ABS substrate is shown in Figure 40. All cross-sectional images from the single bead experiments are shown in Appendix B.

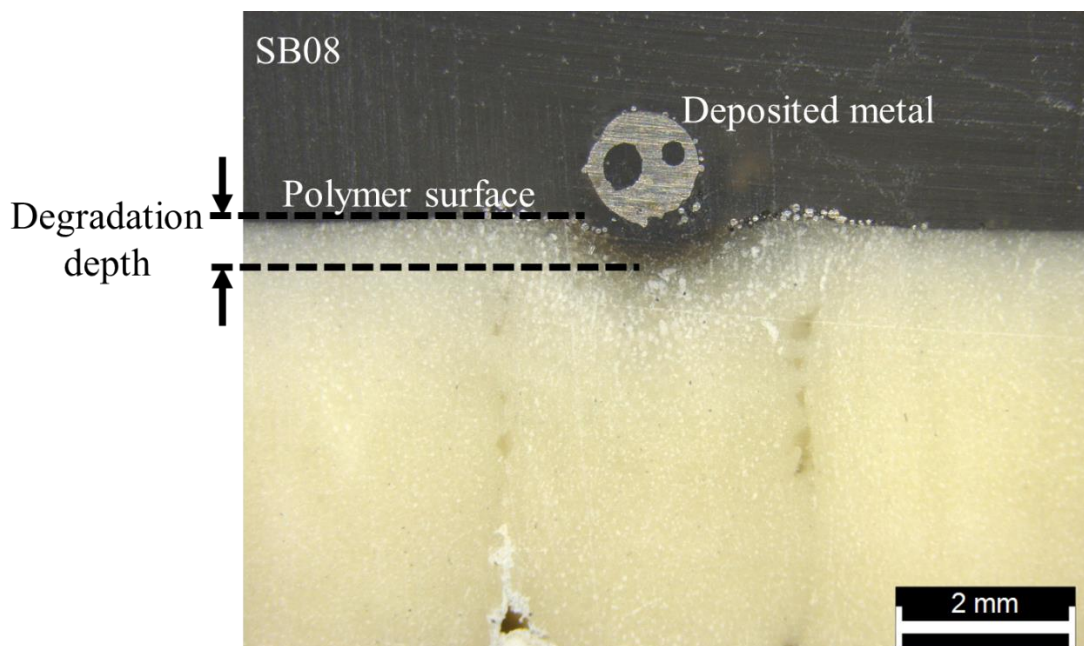


Figure 40: Example of a degradation depth measurement on a GF ABS substrate.

Figure 41 shows the measured degradation depths for all CF ABS trials, with error bars indicating the standard deviation of the error measurements. The degradation depths indicate that an increase in power and a decrease in scan speed tended to increase degradation. The increase in degradation from increasing power was due to increased energy absorbed by the polymer, and the increase in degradation from decreasing scan speed was due to an increase in exposure time of the polymer to the laser power. In these trials, doubling the laser power had a less significant effect on the degradation than halving the scan speed. The differences in effect were likely due to the ablation experienced by the polymer during the DED process.

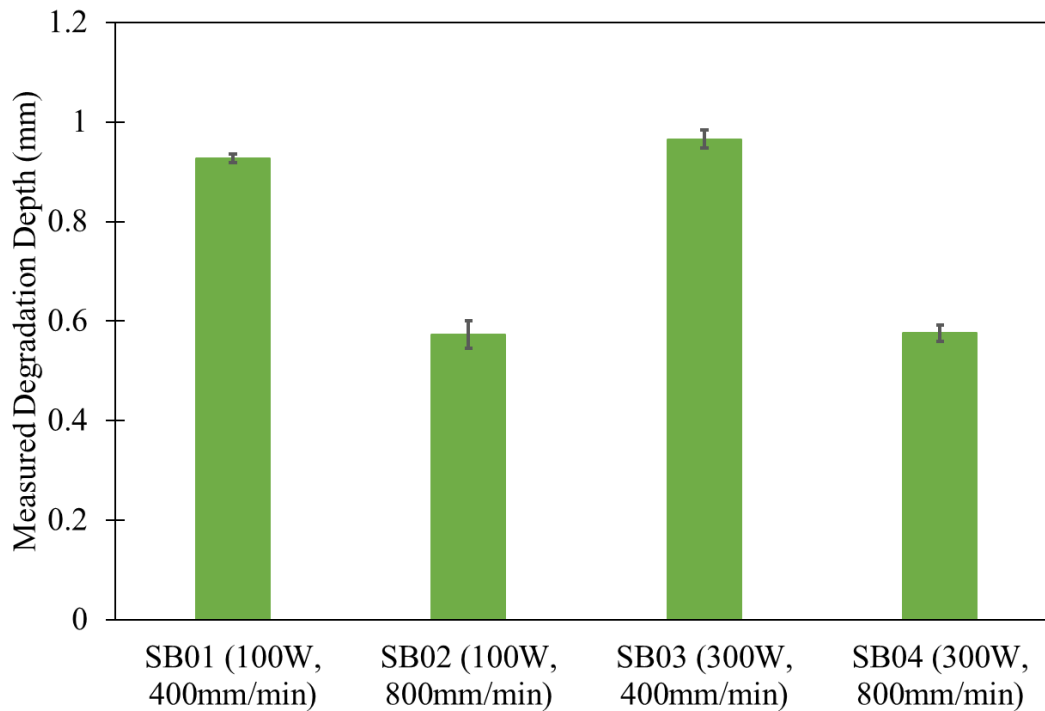


Figure 41: Measured degradation depths for all CF ABS experiments, with measurement error shown in the error bars.

As the polymer was degraded, char formed and the carbon fibers embedded within the material were exposed, protecting the bulk of the polymer from further degradation. Because increasing laser power increased the energy absorbed by the polymer by increasing power levels over the same period of time, a very thin layer at the surface of the polymer was quickly degraded, resulting in char and exposed fibers and protecting the bulk of the polymer. Decreasing scan speed increased the energy absorbed by the polymer by

increasing the amount of time the polymer is exposed laser energy, which did not result in an increase in degradation rate.

Figure 42 shows the measured degradation depths for all GF ABS trials. Like CF ABS, the degradation depths indicate that an increase in power and a decrease in scan speed tended to increase degradation. The increase in degradation from increasing power was due to increased energy absorbed by the polymer, and the increase in degradation from decreasing scan speed was due to an increase in exposure time of the polymer to the laser power.

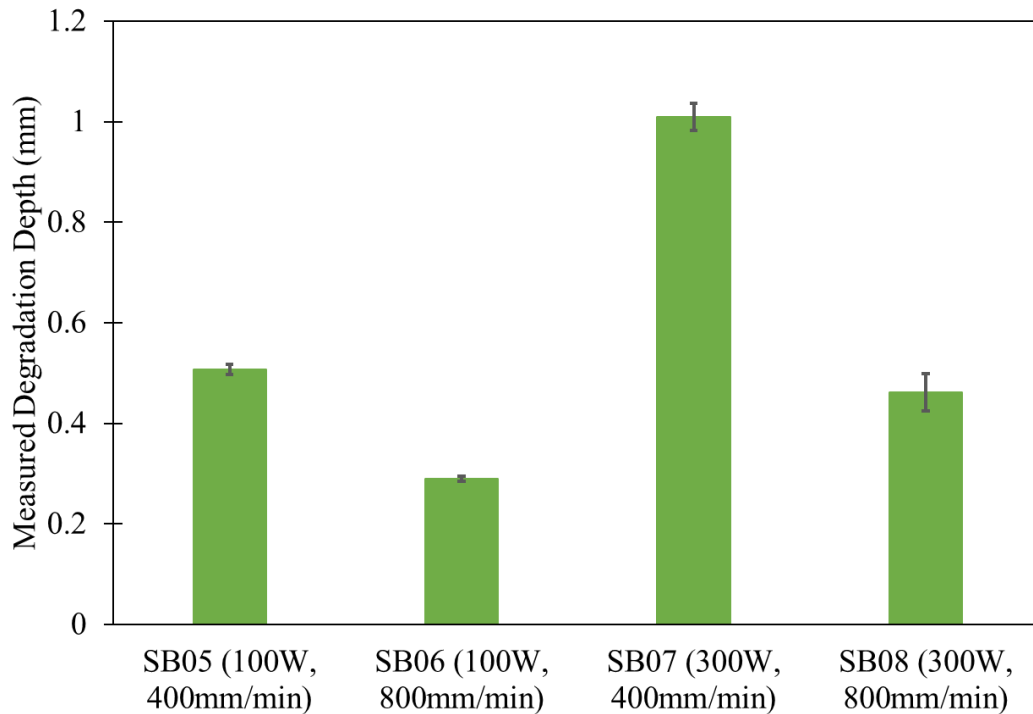


Figure 42: Measured degradation depths for all GF ABS experiments.

In these trials, increasing laser power had a more significant effect on the degradation depth than with CF ABS. The difference in effect between the two polymers was likely due to several reasons: polymer transmissivity differences, material property differences, and metal deposition characteristics. The GF ABS is slightly more transmissive than the CF ABS, so more of the laser energy was absorbed to a greater depth, increasing degradation at higher powers. All the material properties are different, which is likely to affect degradation. One key difference was thermal conductivity: carbon fibers are more conductive than glass fibers, so CF ABS has a higher thermal conductivity than GF ABS.

Finally, the metal deposited on CF ABS during the single-bead experiments was observed to be a spray of small metal beads, while the depositions on GF ABS were observed to be a few larger metal balls. The larger metal balls cooled more slowly than the spray of small metal beads, leading to a difference in polymer degradation, not accounted for in the thermal models developed later in this chapter.

Figure 43 shows the measured degradation depths for all GF nylon trials. Like CF ABS and GF ABS, the degradation depths indicate that an increase in power and a decrease in scan speed tended to increase degradation. The increase in degradation from increasing power was due to increased energy absorbed by the polymer, and the increase in degradation from decreasing scan speed was due to an increase in exposure time of the polymer to the laser power.

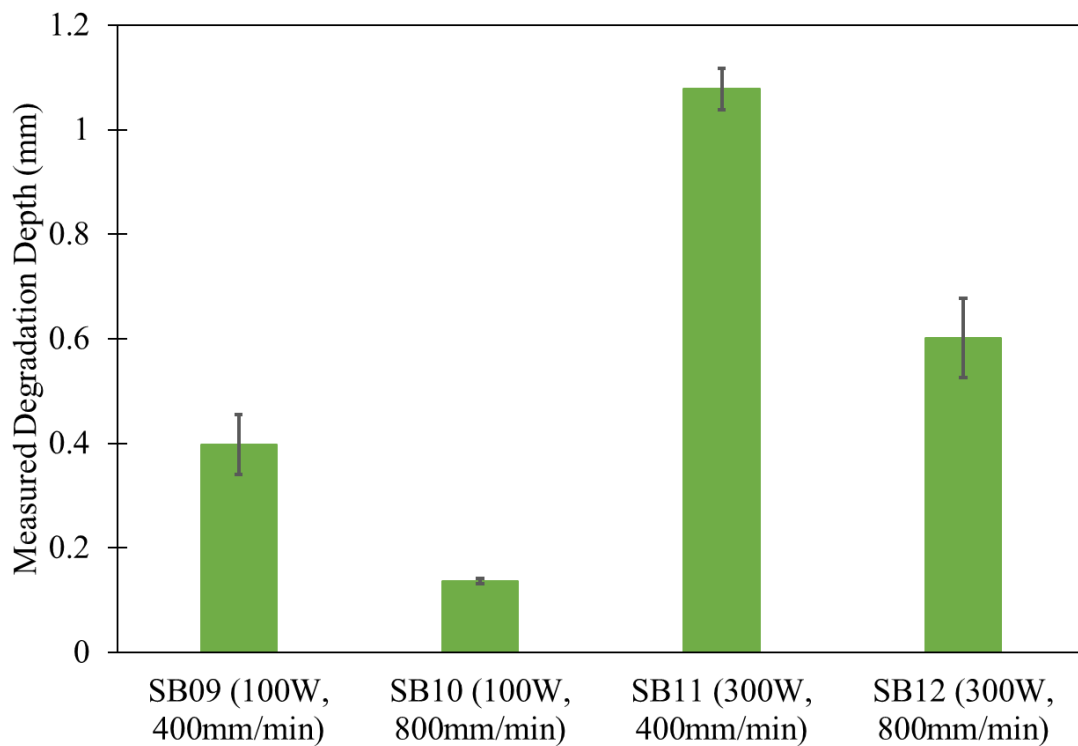


Figure 43: Measured degradation depths for all GF nylon experiments.

Figure 44 shows the measured degradation depths for all PLA trials. As with the previously discussed polymers, the degradation depths indicate that an increase in power and a

decrease in scan speed tended to increase degradation. The increase in degradation from increasing power was due to increased energy absorbed by the polymer, and the increase in degradation from decreasing scan speed was due to an increase in exposure time of the polymer to the laser power.

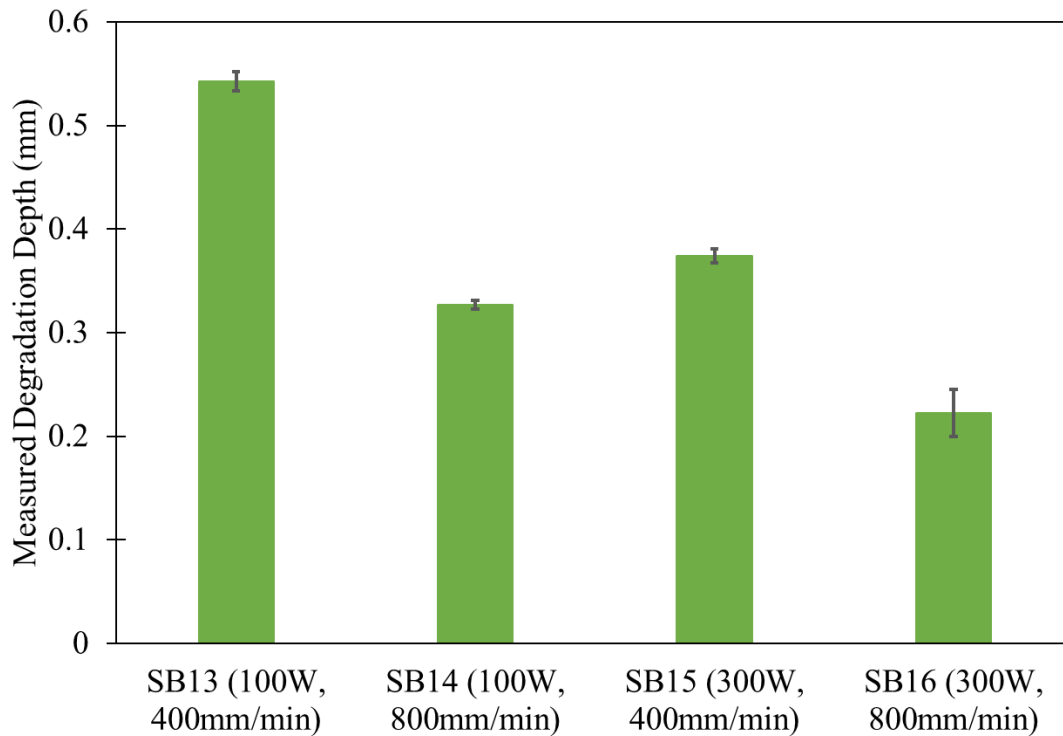


Figure 44: Measured degradation depths for all PLA experiments.

Figure 45 shows the measured degradation depths for all WF PLA trials. As with the other polymers, the degradation depths indicate that an increase in power and a decrease in scan speed tended to increase degradation. The increase in degradation from increasing power was due to increased energy absorbed by the polymer, and the increase in degradation from decreasing scan speed was due to an increase in exposure time of the polymer to the laser power.

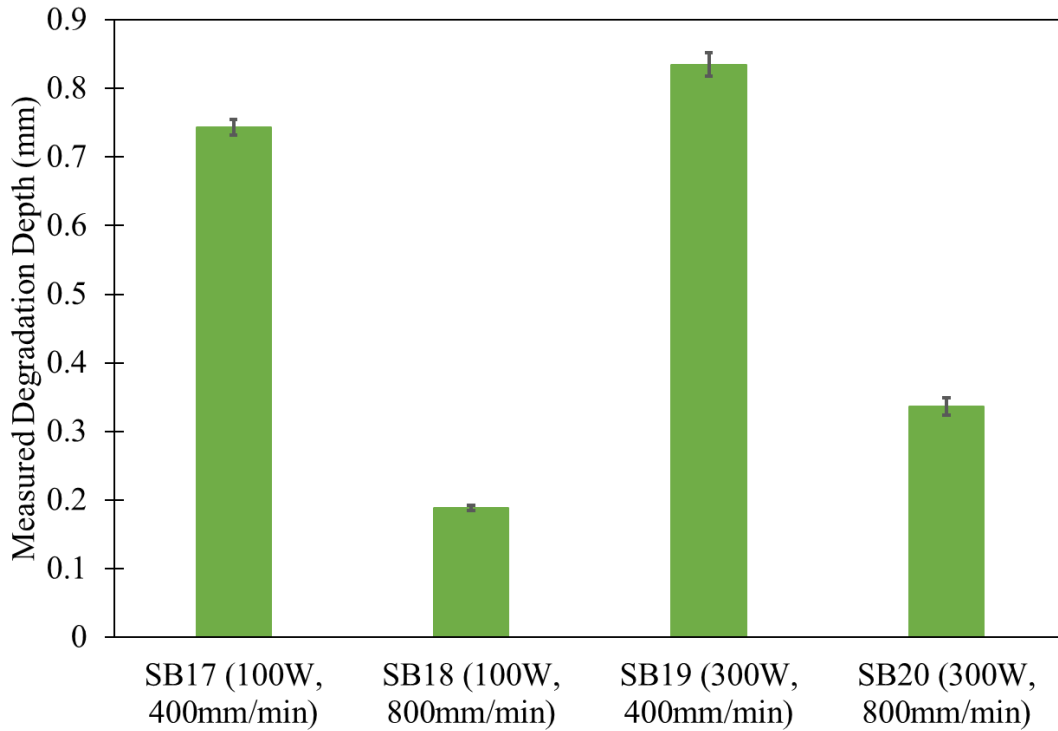


Figure 45: Measured degradation depths for all WF PLA experiments.

To understand the relationship between polymer degradation and both laser power and scan speed, polymer degradation as a function of heat per unit length is plotted in Figure 46. Heat per unit length is a commonly used parameter in welding research that indicates the amount of thermal energy absorbed per unit length of the weld [91-94]. In this case, the heat per unit length was defined as the quotient of the laser power and the scan speed. This representation of the data indicates that the relationship between degradation and both laser power and scan speed was not monotonic. Additionally, the GF nylon trend did not match the trend of the other polymers.

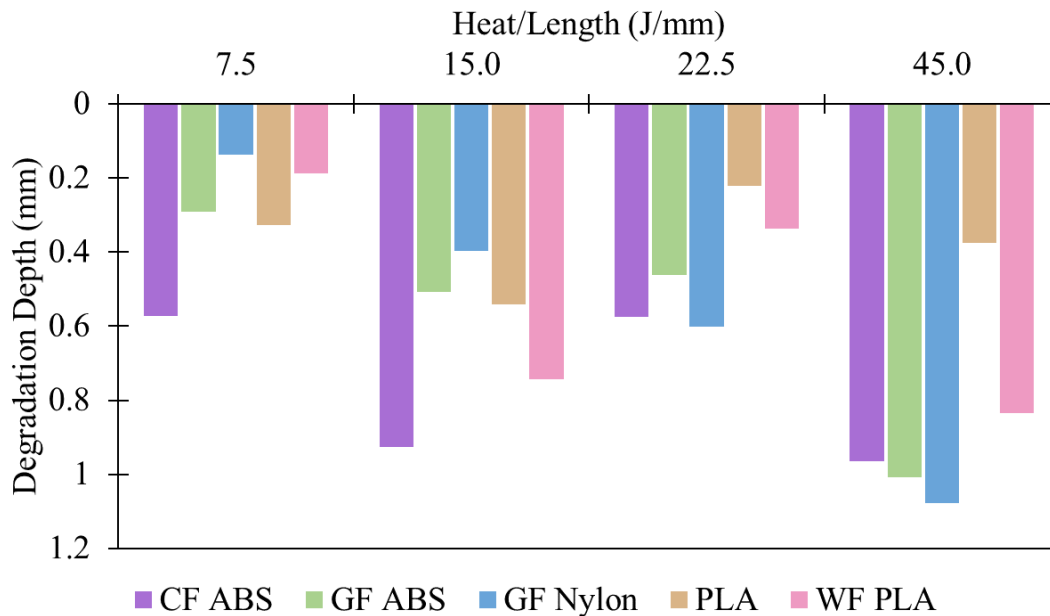


Figure 46: Measured degradation depths versus heat per unit length for all polymers.

3.5 Model development and discussion

To quantify and further understand the relationships between the polymer, the DED process, and the deposited metal, two thermal modeling approaches were used. Semi-infinite modeling provided a first approximation of the polymer temperatures when exposed to the laser, and the Rosenthal moving heat source model afforded a polymer temperature model with a more accurate set of assumptions. A third approach, thermal circuit modeling, was developed to model the polymer-metal system in state-space form. These results are presented in Appendix D.

3.5.1 Semi-infinite implementation

The semi-infinite thermal modeling approach was used to predict temperature of the polymer in response to the DED process as a function of both time and depth.

3.5.1.1 Temperature input approach

To predict the maximum depth of polymer that will reach the degradation temperature of the polymer, the surface of a semi-infinite block of polymer was assumed to be set to the melting temperature of the metal being deposited, as shown in Figure 47. In reality, the metal begins to cool immediately, but setting the temperature to be constant at the melting temperature of the feedstock metal provided a worst-case scenario.

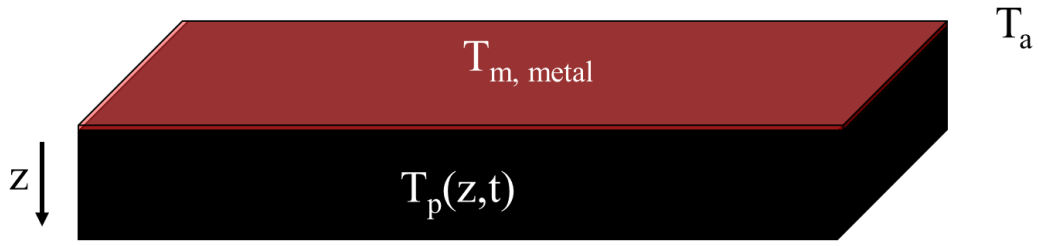


Figure 47: Assumptions used for the surface-temperature-based semi-infinite thermal model, where the surface of the polymer is held at a constant temperature beginning at $t=0$.

The solution to the semi-infinite thermal model with a surface temperature boundary condition is derived in [84]. The general heat equation has the following form

$$\frac{\delta^2 T}{\delta z^2} = \frac{1}{\alpha} \frac{\delta T}{\delta t} \quad (3.2)$$

T is the temperature of the solid, z is the direction of heat transfer, t is time, and α is the thermal diffusivity of the solid, where

$$\alpha = \frac{k}{\rho c_p} \quad (3.3)$$

and k is the thermal conductivity, ρ is the density, and c_p is the thermal capacitance. An initial condition and two boundary conditions were required to solve (3.2). The initial condition was provided by the initial temperature of solid prior to heating, which was assumed to be ambient temperature.

$$T(z, 0) = T_{amb} \quad (3.4)$$

As the solid was assumed to be semi-infinite, one boundary condition was

$$T(z \rightarrow \infty, t) = T_{amb} \quad (3.5)$$

The other boundary condition was provided by the assumption that the surface of the solid was held at the melting temperature of the metal as soon as the print begins

$$T(0, t) = T_{m, metal} \quad (3.6)$$

The solution for the dimensionless temperature is then

$$\frac{T(z, t) - T_{amb}}{T_{amb} - T_{m, metal}} = \operatorname{erf}\left(\frac{z}{\sqrt{4\alpha t}}\right) \quad (3.7)$$

where the function $\operatorname{erf}(\eta)$ is the Gaussian Error Function, defined as

$$\operatorname{erf}(\eta) = \frac{2}{\sqrt{\pi}} \int_0^\eta e^{-u^2} du \quad (3.8)$$

The temperature of the polymer as a function of time and depth into the polymer can then be defined as

$$T(z, t) = (T_{amb} - T_{m,metal})\text{erf}\left(\frac{z}{\sqrt{4\alpha t}}\right) + T_{amb} \quad (3.9)$$

The time of exposure was determined by the time a given point on the polymer surface was exposed to the laser, which depends on both the laser spot diameter (d_{laser}) and the laser scan speed (s_{laser})

$$t_{exposure} = \frac{d_{laser}}{s_{laser}} \quad (3.10)$$

The model was implemented in MATLAB, using the material properties of CF ABS as the substrate properties and the melting temperature of 316L stainless steel as the surface temperature. The models for the other four polymers used in this research are shown in Appendix C. The laser spot size was set to 2mm, and the laser scan speed was set to 400mm/min. The resulting temperature predictions for depths ranging from 0.28mm to 0.33mm are shown in Figure 48a. The polymer was predicted to reach degradation temperatures up to a depth of 0.31mm, and it was therefore predicted that 0.31mm of polymer degrade during the process. Figure 48b shows the temperature predictions for the same scenario but with a scan speed of 800mm/min rather than 400mm/min. In this case, the degradation depth was predicted to be 0.22mm, indicating that an increase in scan speed results in a decrease in degradation depth. This decrease in degradation is due to the decreased exposure of a given volume of polymer to the laser: as the laser scans over the surface faster, each point on the surface spends less time under the laser.

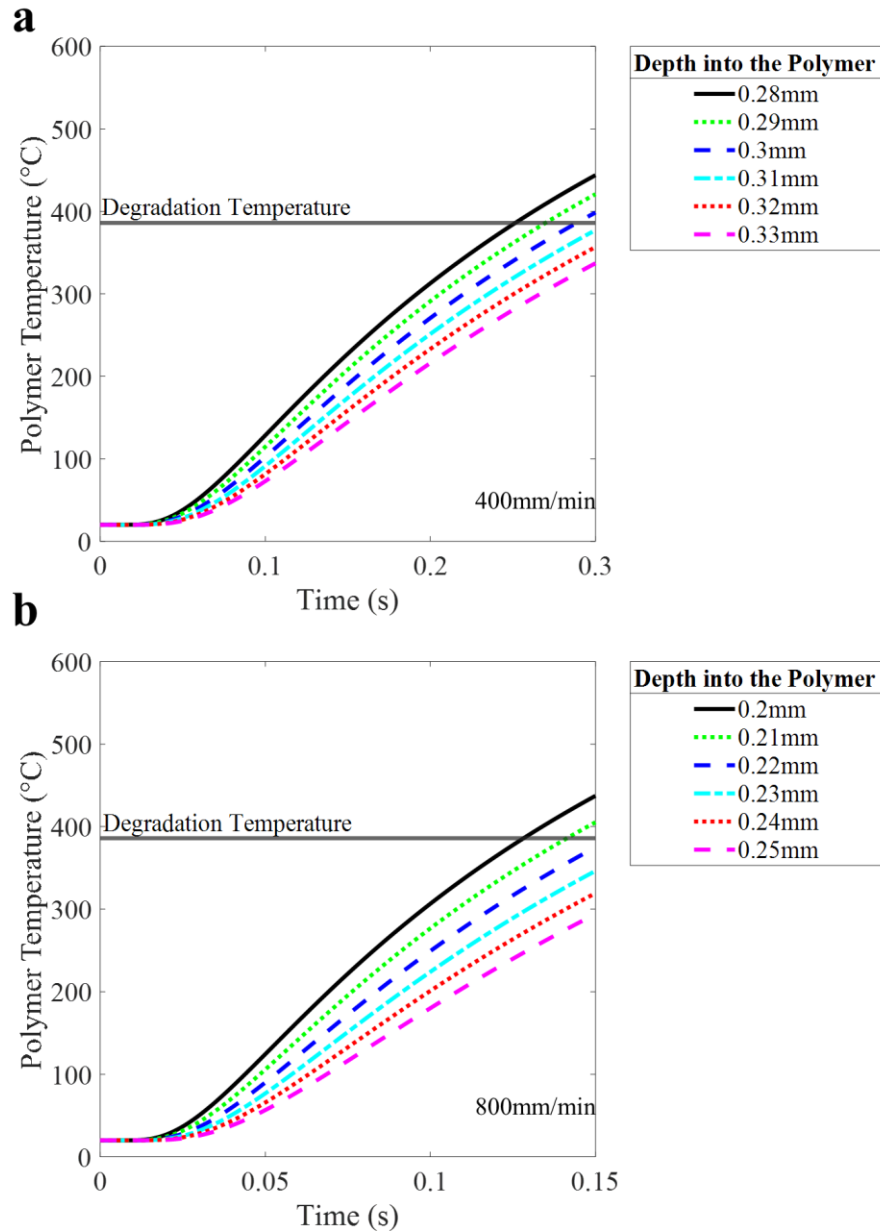


Figure 48: Predicting degradation depth using the semi-infinite thermal model with constant surface temperature as a boundary condition and a scan speed of (a) 400mm/min and (b) 800mm/min.

The surface-temperature-based model is limited in that the surface temperature of the polymer is not constant during the printing process. This model assumed that the surface temperature reaches the melting temperature of the metal being deposited, but the surface temperature is a dependent variable in the printing process and cannot be assumed to be

constant throughout the printing process. For greater model accuracy, one of the boundary conditions must be based on a set and known parameter.

3.5.1.2 Heat flux approach

The laser power is a known constant throughout the printing process, and a model that assumes a constant heat flux from the laser at the surface provides a more accurate prediction of polymer temperatures. The semi-infinite approach can also be used to predict the temperature of the polymer by modeling a constant heat flux at the surface of the polymer, as shown in Figure 49.

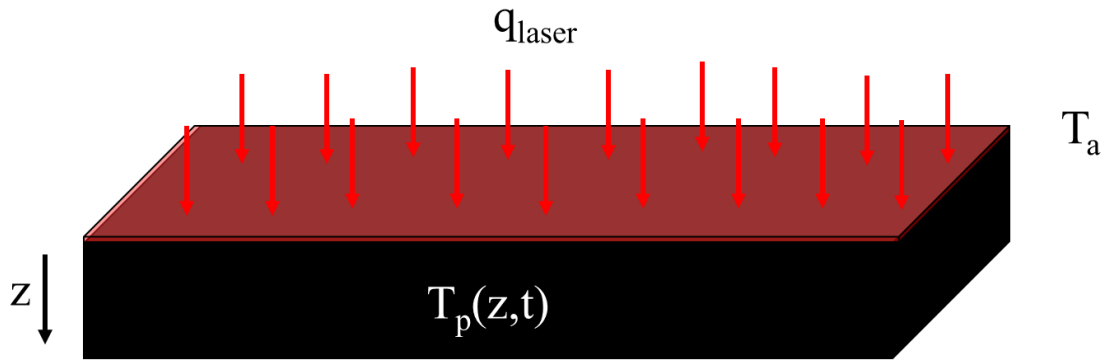


Figure 49: Assumptions used for the heat-flux-based semi-infinite thermal model, where a constant heat flux is applied to the surface beginning at $t=0$.

The solution to the semi-infinite thermal model with a surface heat flux boundary condition was derived in [84]. The general heat equation in (3.76) was once again implemented with the initial condition in (3.78) and the boundary condition in (3.79). The second boundary condition in the case of a constant heat flux at the surface of the polymer is

$$q_{surface} = q_{laser} \quad (3.11)$$

The solution for temperature is then

$$T(z, t) = \frac{2q_{laser}\left(\frac{\alpha t}{\pi}\right)^{\frac{1}{2}}}{k} \exp\left(\frac{-z^2}{4\alpha t}\right) - \frac{q_{laser}z}{k} \operatorname{erfc}\left(\frac{z}{\sqrt{4\alpha z}}\right) + T_{amb} \quad (3.12)$$

The time of exposure was determined by the time a given point on the polymer surface was exposed to the laser, which depends on both the laser spot diameter, d_{laser} , and the laser scan speed, s_{laser} , as shown in equation (3.84).

The model was implemented in MATLAB, using the material properties of CF ABS as the substrate properties and the melting temperature of 316L stainless steel as the surface temperature. The models for the other four polymers used in this research are shown in Appendix C. The laser spot size was set to 2mm, the laser scan speed was set to 400mm/min, and the laser power was set to 100W. The resulting temperature predictions for depths ranging from 0.85mm to 0.9mm are shown in Figure 50a. The polymer was predicted to reach degradation temperatures up to a depth of 0.86mm, and it was therefore predicted that 0.86mm of polymer degrade during the process.

The semi-infinite model with the constant surface heat flux condition can be applied to various scan speed and laser power scenarios, as illustrated in Figure 50. Figure 50b shows the effect of increasing the laser power from 100W to 300W: the predicted degradation depth increased from 0.86mm to 0.91mm, a 5.8% increase. An increase in power resulted in more degradation because there is more energy produced by the laser for the same volume of polymer to absorb. Figure 50c shows the effect of increasing the scan speed from 400mm/min to 800mm/min: the predicted degradation depth decreased from 0.86mm to 0.55mm, a 36% decrease. An increase in scan speed resulted in less degradation because the laser moves across the polymer faster and the polymer therefore has less time to absorb the laser energy. These results indicate that lower power and higher scan speed are ideal for reducing polymer degradation. However, lower power and higher scan speed also reduce the energy available for absorption by the metal feedstock powder. If this energy density becomes too low, the metal will not melt, and the print will not be successful. Therefore, the minimization of polymer degradation is bounded by the parameters necessary for successful metal deposition.

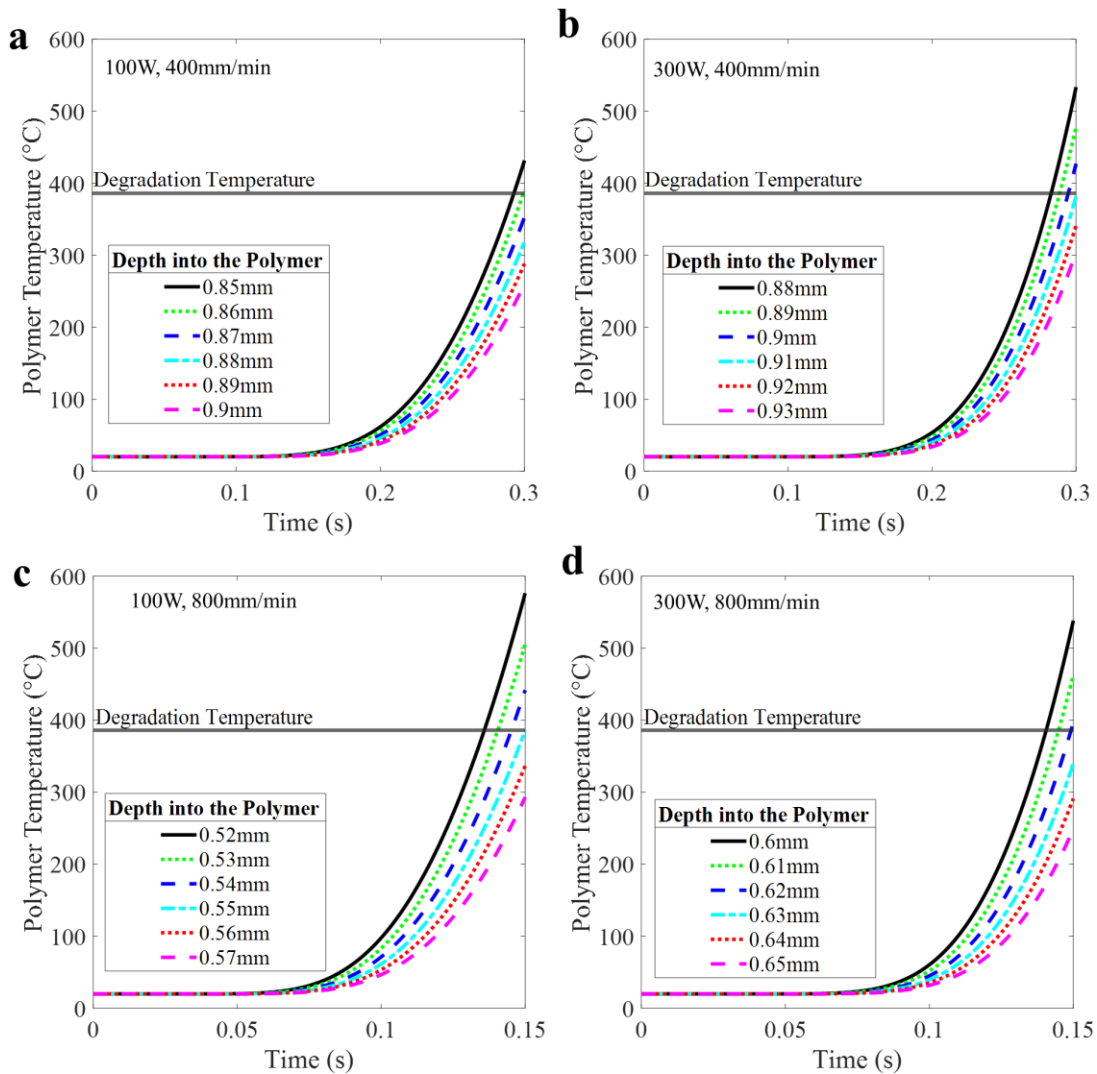


Figure 50: Predicting degradation depth using the semi-infinite thermal model with constant surface temperature as a boundary condition and print parameters of (a) 100W laser power and 400mm/min scan speed, and (b) 100W laser power and 800mm/min scan speed, (c), 300W laser power and 400mm/min scan speed, and (d) 300W laser power and 800mm/min scan speed.

The semi-infinite model with a constant heat flux boundary condition can also be used to determine the effect of polymer material properties on the predicted temperature of the polymer and therefore the polymer degradation depth. Figure 51 shows the effect of varying the polymer density on the predicted temperature of a polymer using the same semi-infinite, constant surface heat flux model. The temperature was calculated at a depth of 1mm, and a laser power of 100W and a scan speed of 400mm/min were used for all

calculations. Increasing density resulted in a decrease in predicted polymer temperature, indicating that polymer degradation decreases in polymers with higher densities. Higher density polymers require more energy to degrade because there is more mass per unit volume, which requires more energy from the laser to heat for a given volume of polymer. This trend suggests that higher density polymers will be more successful in resisting degradation when exposed to the DED process.

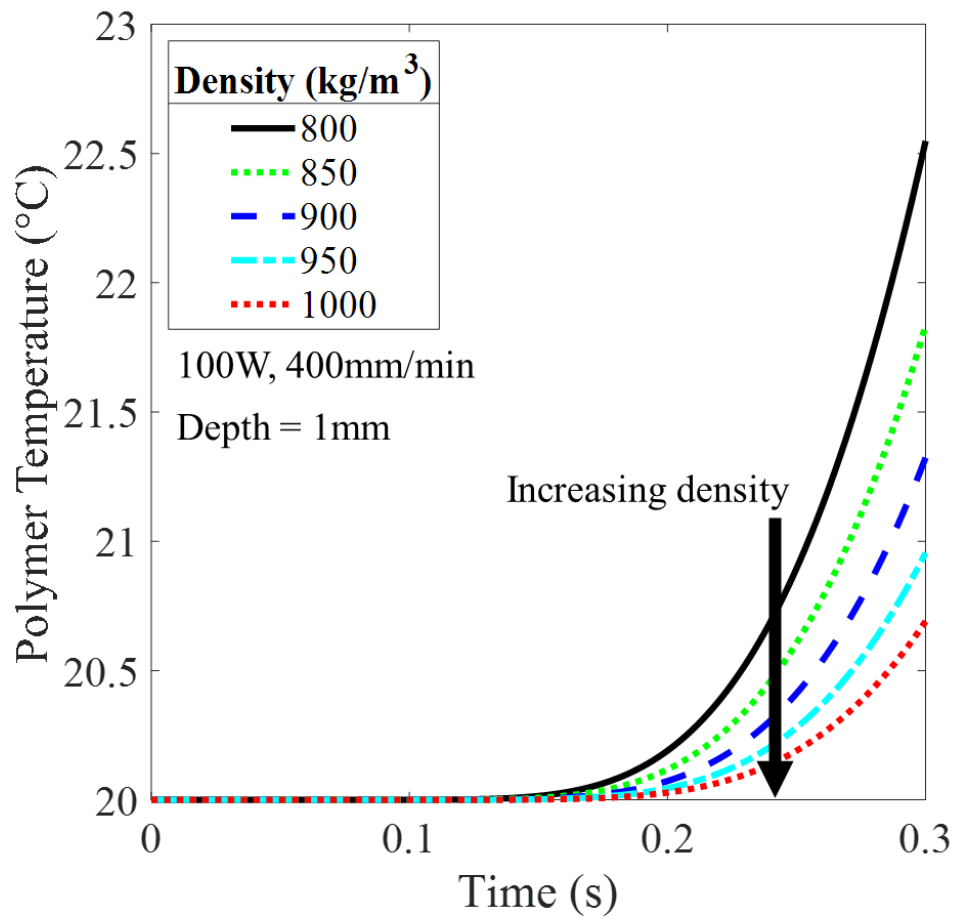


Figure 51: The effect of increasing density on the predicted temperature at a depth of 1mm, a laser power of 100W, and a scan speed of 400mm/min using the semi-infinite model assuming a constant heat flux at the surface.

Figure 52 shows the effect of varying the polymer thermal capacitance on the predicted temperature of a polymer using the same semi-infinite, constant surface heat flux model. The temperature was calculated at a depth of 1mm, and a laser power of 100W and a scan speed of 400mm/min were used for all calculations. Increasing thermal capacitance

resulted in a decrease in predicted polymer temperature, indicating that polymer degradation decreases in polymers with higher thermal capacitance. Thermal capacitance is the amount of heat required to heat a given volume of a material by a unit temperature, so a higher thermal capacitance means that more energy is required to heat the material. Therefore, polymers with a higher thermal capacitance require more energy to achieve the same change in temperature as polymers with a lower thermal capacitance and will therefore degrade less readily. This trend suggests that polymers with a higher thermal capacitance will be more successful in resisting degradation when exposed to the DED process.

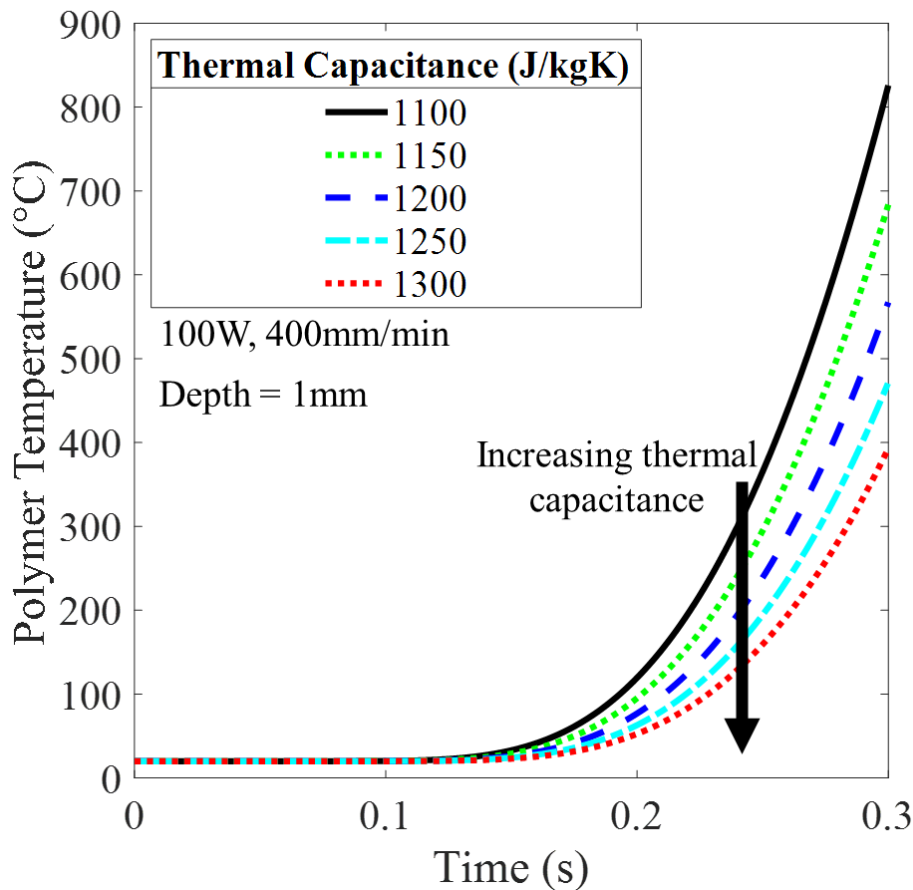


Figure 52: The effect of increasing thermal capacitance on the predicted temperature at a depth of 1mm, a laser power of 100W, and a scan speed of 400mm/min using the semi-infinite model assuming a constant heat flux at the surface.

Figure 53 shows the effect of varying the polymer thermal conductivity on the predicted temperature of a polymer using the same semi-infinite, constant surface heat flux model.

The temperature was calculated at a depth of 1mm, and a laser power of 100W and a scan speed of 400mm/min were used for all calculations. Increasing thermal conductivity resulted in an increase in predicted polymer temperature, indicating that polymer degradation increases in polymers with higher thermal conductivity. As higher thermal conductivity results in faster heat transfer through the polymer, the polymer is more readily able to absorb energy from the laser and will therefore degrade more. This trend suggests that polymers with lower thermal conductivity will be more successful in resisting degradation when exposed to the DED process.

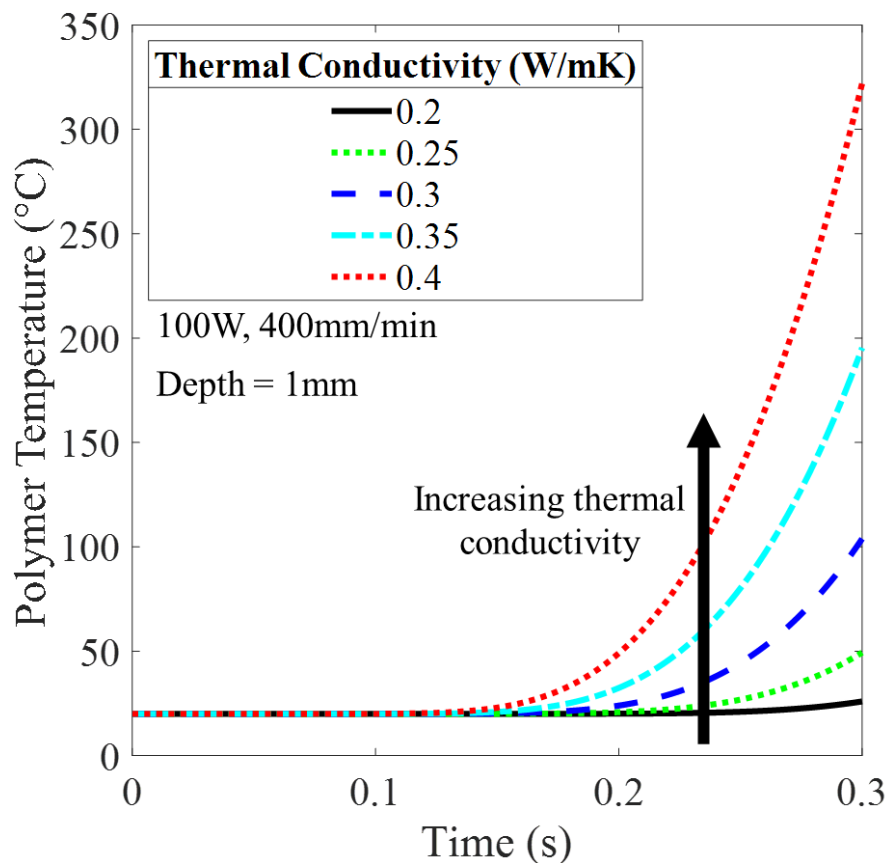


Figure 53: The effect of increasing thermal conductivity on the predicted temperature at a depth of 1mm, a laser power of 100W, and a scan speed of 400mm/min using the semi-infinite model assuming a constant heat flux at the surface.

3.5.2 Rosenthal moving heat source implementation

Rosenthal developed a model to analytically predict the heat distribution resulting from movement of a point energy source across a material [85]. The model has been used extensively in machining and welding applications and was modified for use in this research. Rosenthal considered the scenario shown in Figure 54, where a point source of energy Q moves in the x-direction across a material with velocity v . The temperature at any point of location (x_p, y_p, z_p) at time t can then be determined using the equation

$$T(x_p, y_p, z_p, t) = T_0 + \frac{Q}{2\pi kR} \exp\left(-\frac{v(\xi+R)}{2\alpha}\right) \quad (3.13)$$

where T_0 is the initial temperature of the polymer, k is the thermal conductivity of the material, ξ shifts the coordinate system from the material to the energy source

$$\xi = x_p - vt \quad (3.14)$$

R is the distance from the point of interest to the heat source

$$R = \sqrt{\xi^2 + y_p^2 + z_p^2} \quad (3.15)$$

and α is the thermal diffusivity, given in (3.3).

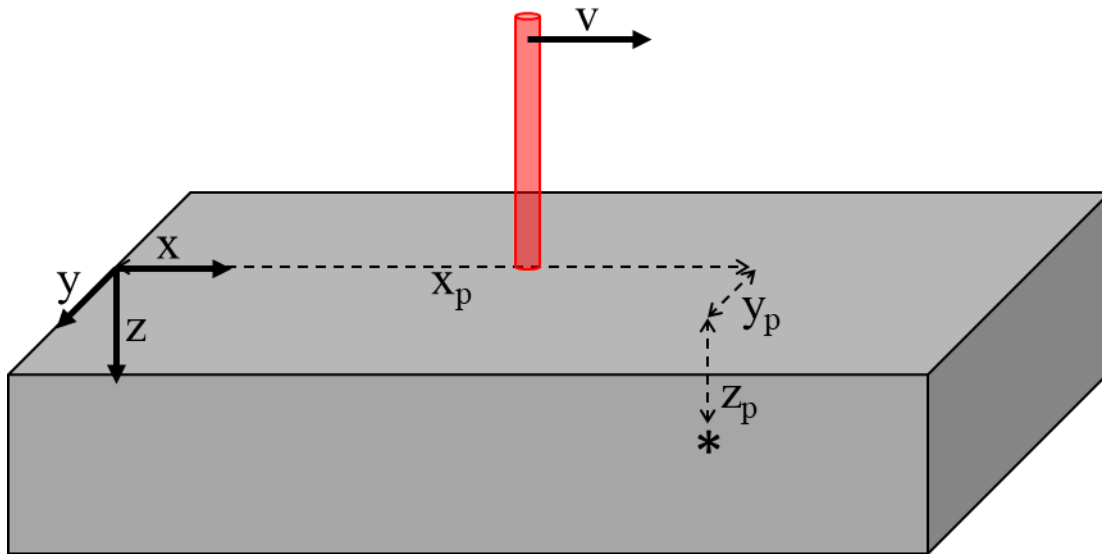


Figure 54: Assumptions used for the Rosenthal model, where a heat source of power Q moves across a material in the x-direction.

The Rosenthal model is traditionally implemented for an arc energy source, with

$$Q = V_{arc} I_{arc} \quad (3.16)$$

where V_{arc} is the voltage of the arc and I_{arc} is the current of the arc. In the case of thermal modeling of the blown-powder-laser DED process on a polymer substrate, the energy source is the laser, and

$$Q = P_{laser} \quad (3.17)$$

The model was implemented in MATLAB using the material properties of CF ABS, a laser power of 100W and a laser velocity of 400mm/min. The models for the other four polymers used in this research are shown in Appendix C. The Rosenthal model predicts temperature over space in three dimensions and over time, so to obtain two dimensional plots, the origin of $x=0$ and $y=0$ was selected for degradation analysis. The laser is at the origin at time $t=0$ and moves at the laser scan speed for the length of the print, set to 12.7mm in this scenario. Figure 55a shows the predicted temperature of the origin at several depths for the entirety of this 12.7mm print. The degradation temperature was reached at a maximum depth of 1.58mm, so it was predicted that the degradation depth of the polymer will be 1.58mm. This prediction was higher than the prediction of the semi-infinite model with the constant heat flux assumption, which predicted a degradation depth of 0.86mm. The increase in degradation depth prediction is due to Rosenthal's consideration of the entirety of the print and the conduction that occurs within the heated polymer during the print.

Like the semi-infinite model, Rosenthal can also be applied to various laser power and laser scan speed scenarios. Figure 55b indicates that an increase in power from 100W to 300W resulted in a degradation depth of 1.89mm, a 20% increase. An increase in power results in more degradation because there is more energy produced by the laser for the same volume of polymer to absorb. Figure 55c indicates that an increase in scan speed from 400mm/min to 800mm/min resulted in a degradation depth of 1.12mm, a 29% decrease. An increase in scan speed results in less degradation because the laser moves across the polymer faster and the polymer therefore has less time to absorb the laser energy. These results support the conclusions drawn with the semi-infinite model that lower power and higher scan speed are ideal for reducing polymer degradation, but the minimization of polymer degradation is bounded by the parameters necessary for successful metal deposition.

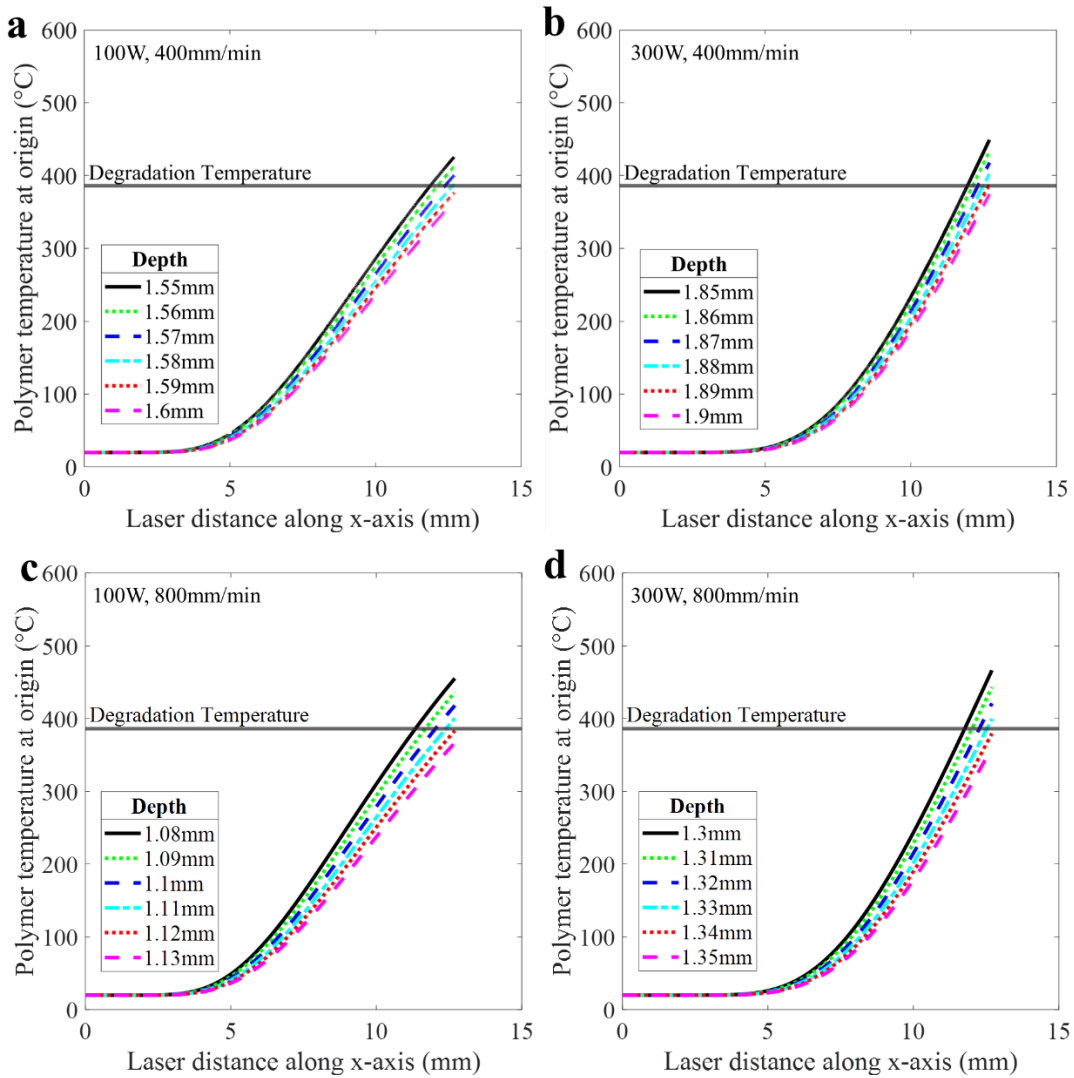


Figure 55: Predicting degradation depth at the origin for a single bead, 12.7mm print using the Rosenthal moving heat source model with print parameters of (a) 100W laser power and 400mm/min scan speed, and (b) 100W laser power and 800mm/min scan speed, (c), 300W laser power and 400mm/min scan speed, and (d) 300W laser power and 800mm/min scan speed.

Similar to the semi-infinite model with a constant heat flux boundary condition, the Rosenthal model can also be used to determine the effect of polymer material properties on the predicted temperature of the polymer and therefore the polymer degradation depth. Figure 56 shows the effect of varying the polymer density on the predicted temperature of a polymer using the same semi-infinite, constant surface heat flux model. The temperature was calculated at a depth of 1mm, and a laser power of 100W and a scan speed of 400mm/min was used for all calculations. Increasing density resulted in a decrease in

predicted polymer temperature, indicating that polymer degradation decreases in polymers with higher densities. Higher density polymers require more energy to degrade because there is more mass per unit volume, which requires more energy from the laser to heat for a given volume of polymer. This trend suggests that higher density polymers will be more successful in resisting degradation when exposed to the DED process.

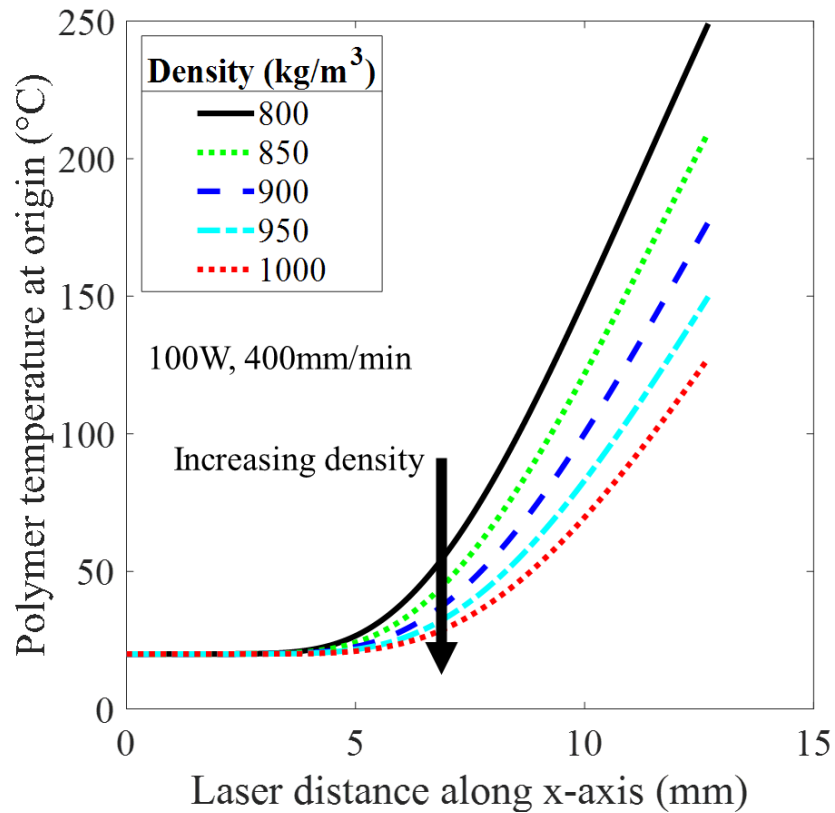


Figure 56: The effect of increasing density on the predicted temperature at a depth of 2mm, a laser power of 100W, and a scan speed of 400mm/min using the Rosenthal model.

Figure 57 shows the effect of varying the polymer thermal capacitance on the predicted temperature of a polymer using the same semi-infinite, constant surface heat flux model. The temperature was calculated at a depth of 1mm, and a laser power of 100W and a scan speed of 400mm/min was used for all calculations. Increasing thermal capacitance resulted in a decrease in predicted polymer temperature, indicating that polymer degradation decreases in polymers with higher thermal capacitance. Thermal capacitance is the amount of heat required to heat a given volume of a material by a unit temperature, so a higher

thermal capacitance means that more energy is required to heat the material. Therefore, polymers with a higher thermal capacitance require more energy to achieve the same change in temperature as polymers with a lower thermal capacitance and will therefore degrade less readily. This trend suggests that polymers with a higher thermal capacitance are more successful in resisting degradation when exposed to the DED process.

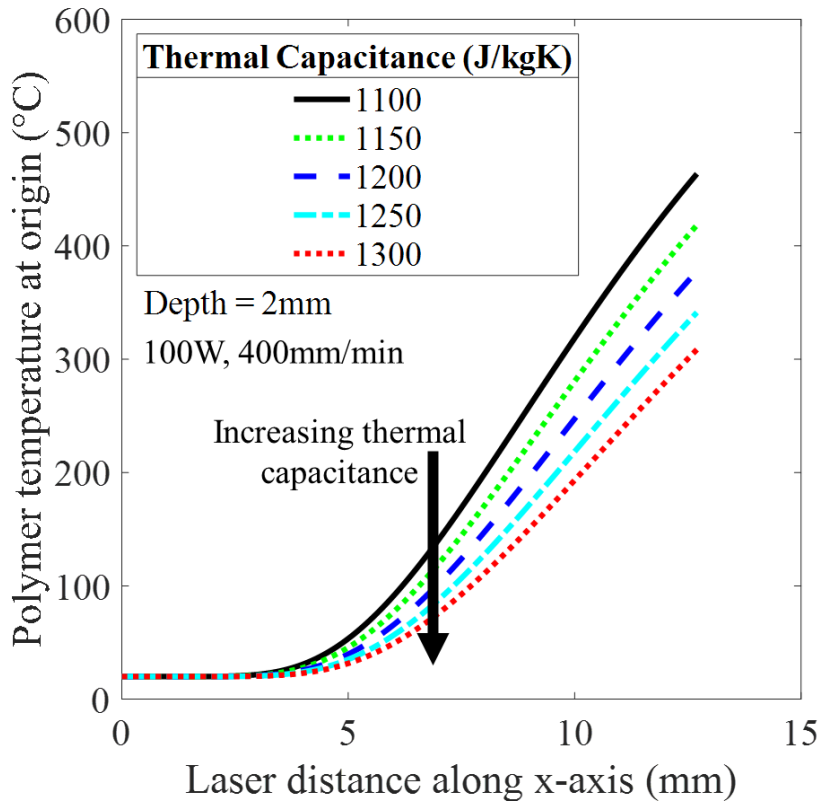


Figure 57: The effect of increasing thermal capacitance on the predicted temperature at a depth of 2mm, a laser power of 100W, and a scan speed of 400mm/min using the Rosenthal model.

Figure 58 shows the effect of varying the polymer thermal conductivity on the predicted temperature of a polymer using the same semi-infinite, constant surface heat flux model. The temperature was calculated at a depth of 1mm, and a laser power of 100W and a scan speed of 400mm/min was used for all calculations. Increasing thermal conductivity resulted in an increase in predicted polymer temperature, indicating that polymer degradation will increase in polymers with higher thermal conductivity. As higher thermal conductivity results in faster heat transfer through the polymer, the polymer is more readily

able to absorb energy from the laser and will therefore degrade more. This trend suggests that polymers with lower thermal conductivity are more successful in resisting degradation when exposed to the DED process.

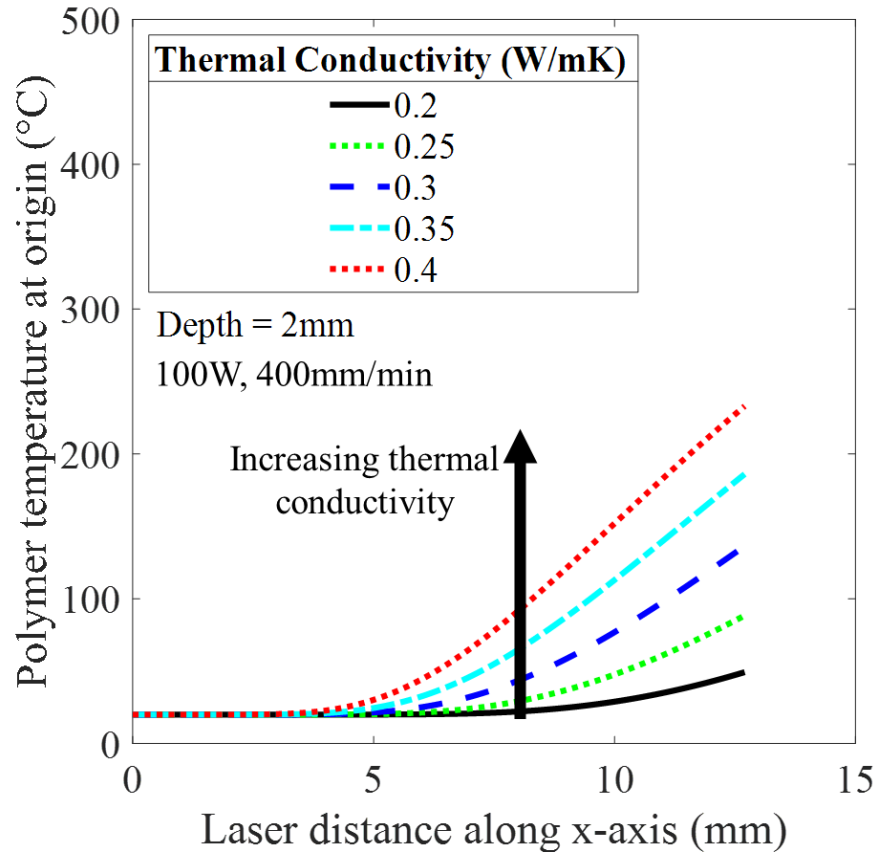


Figure 58: The effect of increasing thermal conductivity on the predicted temperature at a depth of 2mm, a laser power of 100W, and a scan speed of 400mm/min using the Rosenthal model.

3.5.3 Discussion

A comparison of the predicted and measured results for CF ABS is shown in Table 4, and a plot of the results as a function of the heat per unit length is shown in Figure 59. The most accurate predictions were made by the semi-infinite model, although the Rosenthal model had a more accurate series of assumptions. Both the flux-based semi-infinite and Rosenthal models tended to over-predict the degradation, as they did not consider the protective ablative effects provided by the carbon fibers as the polymer degrades. The temperature-based semi-infinite model predicted degradations roughly half as deep as the flux-based semi-infinite model because the temperature-based model did not take laser power into

account. The flux-based semi-infinite model predicted degradations roughly half as deep as the Rosenthal model because the Rosenthal model considered heat transfer via conduction throughout the entirety of the print, while the semi-infinite model only considered degradation that occurs during direct exposure of the polymer to the laser. The Rosenthal predictions were accurate to within a bead width of the DED process, which is accurate enough for this research given that the purpose of the thermal model is to gain an understanding of how much degradation to expect and to explore the effects of polymer properties and print parameters on polymer degradation. The over-prediction of the model also provides a margin of safety, ensuring that the degradation will not be above the prediction.

Table 4. Predicted and measured degradation depths for all CF ABS experiments.

Trial	Predicted degradation (semi-infinite - temperature)	Predicted degradation (semi-infinite - flux)	Predicted degradation (Rosenthal)	Measured degradation
SB01	0.31mm	0.86mm	1.58mm	0.93mm
SB02	0.22mm	0.55mm	1.12mm	0.57mm
SB03	0.31mm	0.91mm	1.89mm	0.97mm
SB04	0.22mm	0.62mm	1.34mm	0.58mm

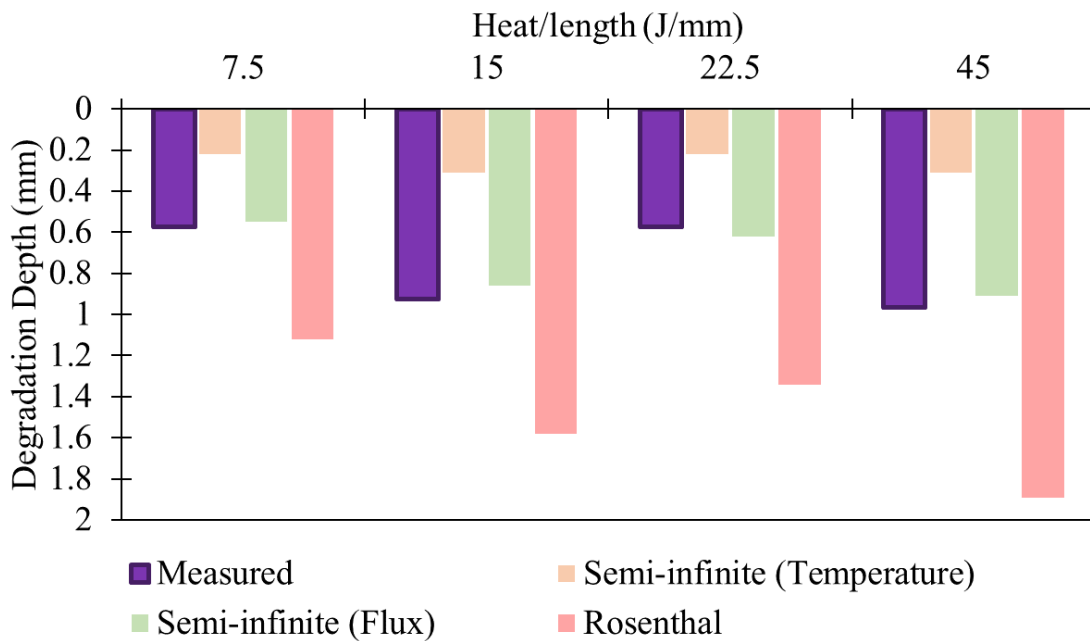


Figure 59: Measured degradation depths of CF ABS compared to the three developed thermal models.

A comparison of the predicted and measured results for GF ABS is shown in Table 5, and a plot of the results as a function of the heat per unit length is shown in Figure 60. As with CF ABS, the most accurate predictions were made by the flux-based semi-infinite model. The flux-based semi-infinite and Rosenthal models tended to over-predict the degradation because neither considered the transmittance of laser energy or the protective ablative effects provided by the glass fibers as the polymer degrades. The temperature-based semi-infinite model predicted degradations roughly one-third as deep as the flux-based semi-infinite model because the temperature-based model did not take laser power into account. The flux-based semi-infinite model predicted degradations roughly half as deep as the Rosenthal model because the Rosenthal model considered the effect of the laser on the temperature of the entire polymer throughout the entirety of the print, while the semi-infinite model only considered degradation that occurs during direct exposure of the polymer to the laser. The Rosenthal predictions were accurate to within a bead width, which is reasonable for this application given that the purpose of the thermal model is to gain an understanding of how much degradation to expect and to explore the effects of polymer

properties and print parameters on polymer degradation. The over-prediction of the model seen in all modeling completed for this research also provides a margin of safety, ensuring that the degradation will not be above the prediction.

Table 5. Predicted and measured degradation depths for all GF ABS experiments.

Trial	Predicted degradation (semi-infinite - temperature)	Predicted degradation (semi-infinite - flux)	Predicted degradation (Rosenthal)	Measured degradation
SB05	0.34mm	0.92mm	1.81mm	0.51mm
SB06	0.24mm	0.62mm	1.28mm	0.29mm
SB07	0.34mm	1.03mm	2.14mm	1.01mm
SB08	0.24mm	0.7mm	1.51mm	0.46mm

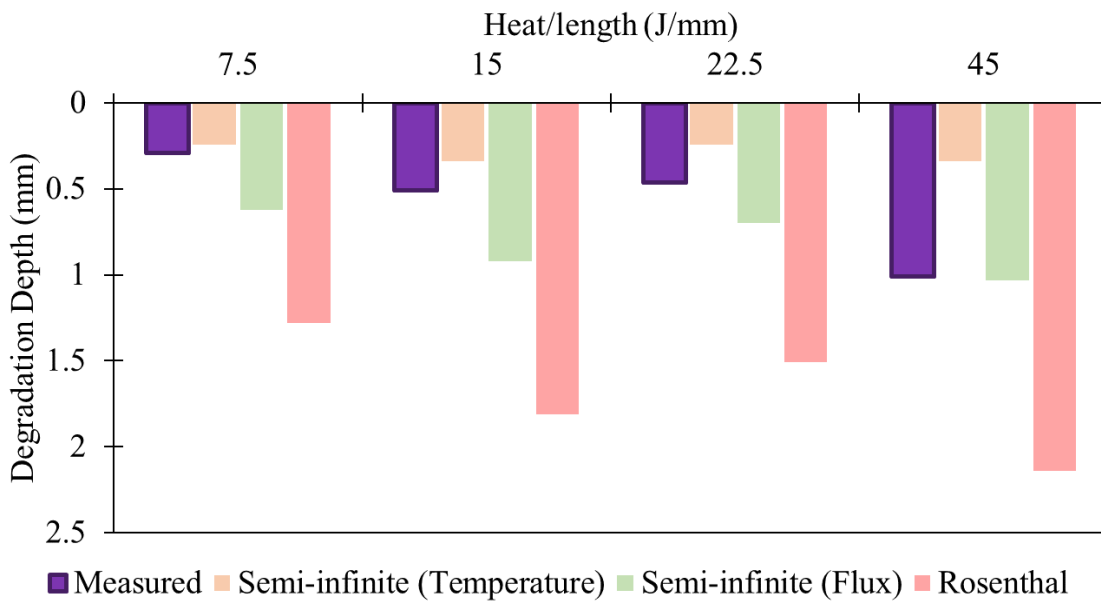


Figure 60: Measured degradation depths of GF ABS compared to the three developed thermal models.

A comparison of the predicted and measured results for GF nylon is shown in Table 6, and a plot of the results as a function of the heat per unit length is shown in Figure 61. As with

CF ABS and GF ABS, the most accurate predictions were made by the semi-infinite model. The semi-infinite and Rosenthal models tended to predict more degradation than was measured, as neither considered the transmittance of laser energy or the ablative effects provided by the glass fibers as the nylon degrades. The temperature-based semi-infinite model predicted degradations roughly one-third as deep as the flux-based semi-infinite model because the temperature-based model did not take laser power into account. The flux-based semi-infinite model predicted degradations roughly half as deep as the Rosenthal model because the Rosenthal model considered the effect of the laser on the temperature of the entire polymer throughout the entirety of the print, while the semi-infinite model only considered degradation that occurs during direct exposure of the polymer to the laser. The Rosenthal predictions had an error less than the bead width of the DED process, which is reasonably accurate given that the purpose of the thermal model is to gain an understanding of how much degradation to expect and to explore the effects of polymer properties and print parameters on polymer degradation. The over-prediction of the model seen in all conditions explored in this research also provides a margin of safety, ensuring that the degradation will not be above the prediction.

Table 6. Predicted and measured degradation depths for all GF nylon experiments.

Trial	Predicted degradation (semi-infinite - temperature)	Predicted degradation (semi-infinite - flux)	Predicted degradation (Rosenthal)	Measured degradation
SB09	0.3mm	0.88mm	1.69mm	0.69mm
SB10	0.21mm	0.59mm	1.19mm	0.25mm
SB11	0.3mm	0.98mm	2.03mm	1.12mm
SB12	0.21mm	0.67mm	1.43mm	0.86mm

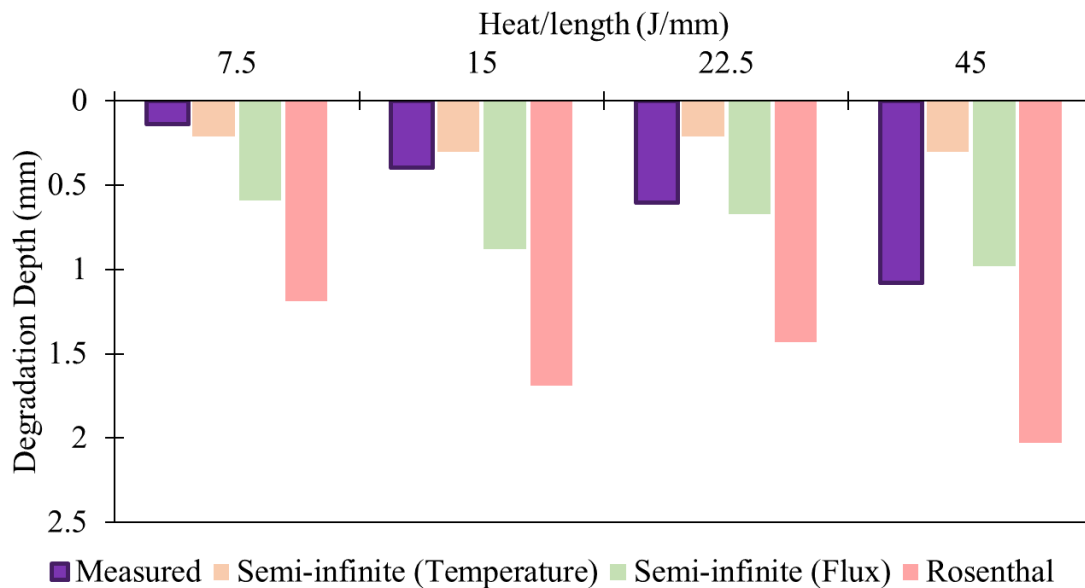


Figure 61: Measured degradation depths of GF nylon compared to the three developed thermal models.

A comparison of the predicted and measured results for PLA is shown in Table 7, and a plot of these results as a function of the heat per unit length is shown in Figure 62. As with the previously discussed polymers, the most accurate predictions were made by the flux-based semi-infinite model. The semi-infinite and Rosenthal models tended to predict more degradation than the experimental results, as neither considered the significant transmissivity of PLA. The temperature-based semi-infinite model predicted degradations roughly one-third as deep as the flux-based semi-infinite model because the temperature-based model did not take laser power into account. The flux-based semi-infinite model predicted degradations roughly half as deep as the Rosenthal model because the Rosenthal model considered the effect of the laser on the temperature of the entire polymer throughout the entirety of the print, while the semi-infinite model only considered degradation that occurs during direct exposure of the polymer to the laser. The Rosenthal overpredictions provide a margin of safety, and the degradation predictions are within a bead width's accuracy, which is acceptable for the purposes of this research.

Table 7. Predicted and measured degradation depths for all PLA experiments.

Trial	Predicted degradation (semi-infinite - temperature)	Predicted degradation (semi-infinite - flux)	Predicted degradation (Rosenthal)	Measured degradation
SB13	0.27mm	0.69mm	1.42mm	0.54mm
SB14	0.19mm	0.47mm	1mm	0.33mm
SB15	0.27mm	0.77mm	1.66mm	0.37mm
SB16	0.19mm	0.53mm	1.17mm	0.22mm

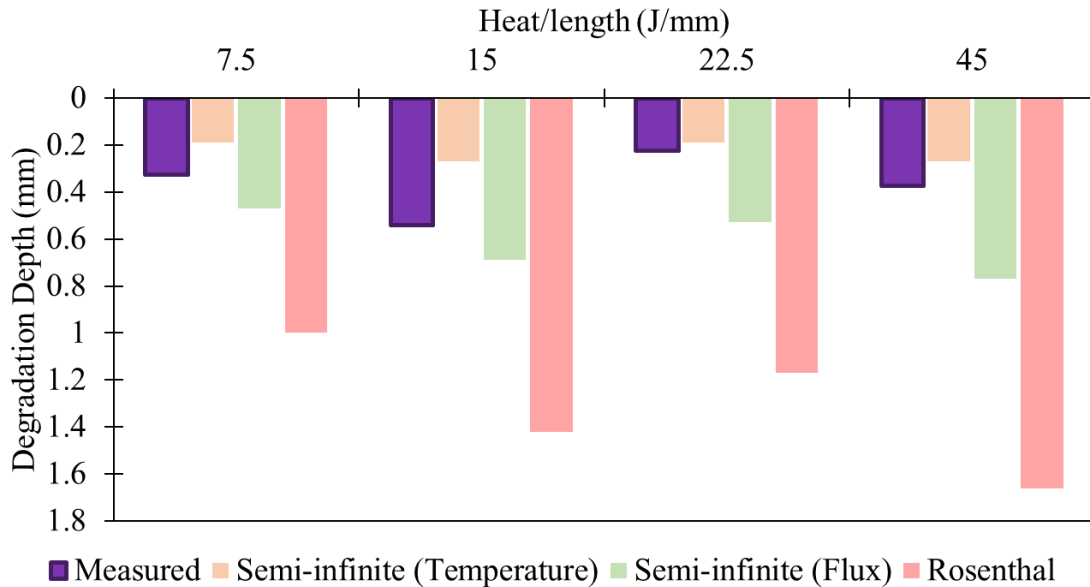


Figure 62: Measured degradation depths of PLA compared to the three developed thermal models.

A comparison of the predicted and measured results for WF PLA is shown in Table 8, and a plot of the results as a function of the heat per unit length is shown in Figure 63. Like the other polymers, the most accurate predictions were made by the semi-infinite model. The semi-infinite and Rosenthal models tended to over-predict degradation depths, as neither considered the transmissivity of WF PLA. The temperature-based semi-infinite model predicted degradations roughly one-third as deep as the flux-based semi-infinite model

because the temperature-based model did not take laser power into account. The flux-based semi-infinite model predicted degradations roughly half as deep as the Rosenthal model because the Rosenthal model considered the effect of the laser on the temperature of the entire polymer throughout the entirety of the print, while the semi-infinite model only considered degradation that occurs during direct exposure of the polymer to the laser.

Table 8. Predicted and measured degradation depths for all WF PLA experiments.

Trial	Predicted degradation (semi-infinite - temperature)	Predicted degradation (semi-infinite - flux)	Predicted degradation (Rosenthal)	Measured degradation
SB17	0.37mm	0.92mm	1.8mm	0.74mm
SB18	0.26mm	0.63mm	1.28mm	0.19mm
SB19	0.37mm	1.03mm	2.14mm	0.83mm
SB20	0.26mm	0.7mm	1.51mm	0.34mm

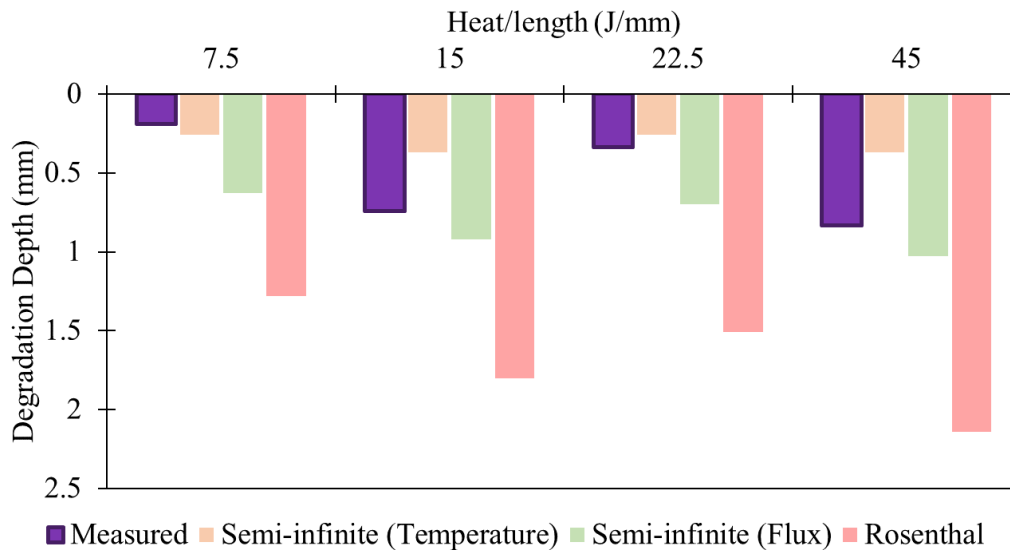


Figure 63: Measured degradation depths of WF PLA compared to the three developed thermal models.

3.6 Conclusions

Successful polymer support structures require that the polymer not be significantly degraded during the deposition process. Degradation on the order of 1mm is acceptable, as the DED process is not precise and the bead width is approximately 2mm, which means that the accuracy of the process is more than 1mm. If more polymer than this is damaged during deposition, the machine will lose accurate knowledge of the location of the polymer surface, and accurate deposition cannot occur. Degradation of five polymers exposed to single-bead DED prints at low and high laser powers and scan speeds were measured. It was found that increasing laser power and decreasing laser scan speed increased degradation, and the relationship between both of these parameters and the degradation depth was found to be nonlinear. To better understand the relationship between polymer material properties, DED print parameters, and polymer degradation, several thermal modeling approaches were used to predict polymer temperature during deposition to gain an approximate understanding of degradation depth. Semi-infinite modeling provided a first approximation of the polymer temperatures when exposed to the laser, and the Rosenthal moving heat source model provided a polymer temperature model with a more accurate set of assumptions. These models determined that degradation depths depend on polymer density, polymer conductivity, polymer thermal capacitance, laser power, and laser scan speed. The general trends between these polymer properties and print parameters and the predicted polymer degradation were explored, and it was found that increasing density, increasing thermal capacitance, decreasing thermal conductivity, decreasing laser power, and increasing laser scan speed all decrease polymer degradation depth. The Rosenthal model generally predicted degradation on the order of 1mm, low enough that deposition is still possible. Compared to the experimental evidence, the Rosenthal model tended to over-predict the degradation depth because the model did not consider polymer transmissivity or the protective ablative effects that occur during degradation, especially in polymers with carbon fiber or glass fiber fillers. This over-prediction serves to provide a margin of safety, as none of the degradation depths will be greater than predicted.

CHAPTER 4. EFFECT OF POLYMER SUBSTRATE ON PRINTED METAL

4.1 Introduction

If the effect of the DED process on the polymer does not inhibit the success of deposition, the second requirement for a successfully polymer support structure is that the composition and properties of the deposited metal must also not be significantly altered by the support structure. In this research, the effect of the polymer substrate on the deposited metal was measured by characterizing the hardness and porosity of 316L stainless steel deposited on carbon-fiber-reinforced ABS (CF ABS) substrates. The structure and composition of 316L stainless steel is discussed, along with its use in DED. As CF ABS is a carbon-based polymer, carbide formation is discussed, along with porosity in DED. The effect of using a polymer substrate on the deposited metal was determined in the case of 316L stainless steel deposited on CF ABS. The methodology and results for these tests are presented, followed by the conclusions of the chapter.

4.2 Background

As 316L stainless steel was used for all experiments in this research, the structure and composition of 316L stainless steel is presented. The specific use case of 316L stainless steel in DED is then discussed. Carbide formation in steels is presented, as the carbon in the CF ABS will affect carbide formation in the deposited metal. Finally, porosity in DED is discussed.

4.2.1 316L stainless steel

The feedstock material used in all experiments in this research is 316L stainless steel powder. Steel is a popular manufacturing material, with almost 2 billion metric tons produced worldwide in 2021 [95]. The material has therefore been the subject of much research, ranging from microstructure analysis to mechanical properties to phase compositions.

4.2.1.1 Structure of stainless steels

In metals, metallic atoms come together via metallic bonding, as illustrated in Figure 64. In metallic bonds, each of the metallic atoms contributes its valence electrons to a cloud of electrons, which surrounds positively charged metal ions [96]. This type of bond results in

highly symmetrical, close-packed crystal structures in solid metals [96]. A crystalline structure is defined as a structure of atoms or molecules in a regular, repeating, three-dimensional pattern with long-range order [96].

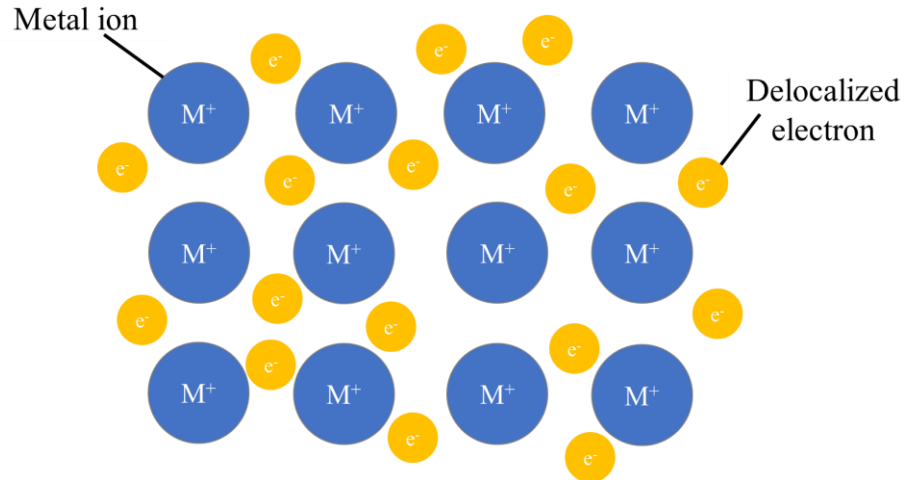


Figure 64: General structure of a metallic bond, in which valence electrons are shared by all the metal atoms.

In a crystal system, a unit cell can be defined which repeats in three-dimensional space. A generic lattice structure and unit cell is shown in Figure 65. The unit cell is characterized by edge lengths and interaxial angles.

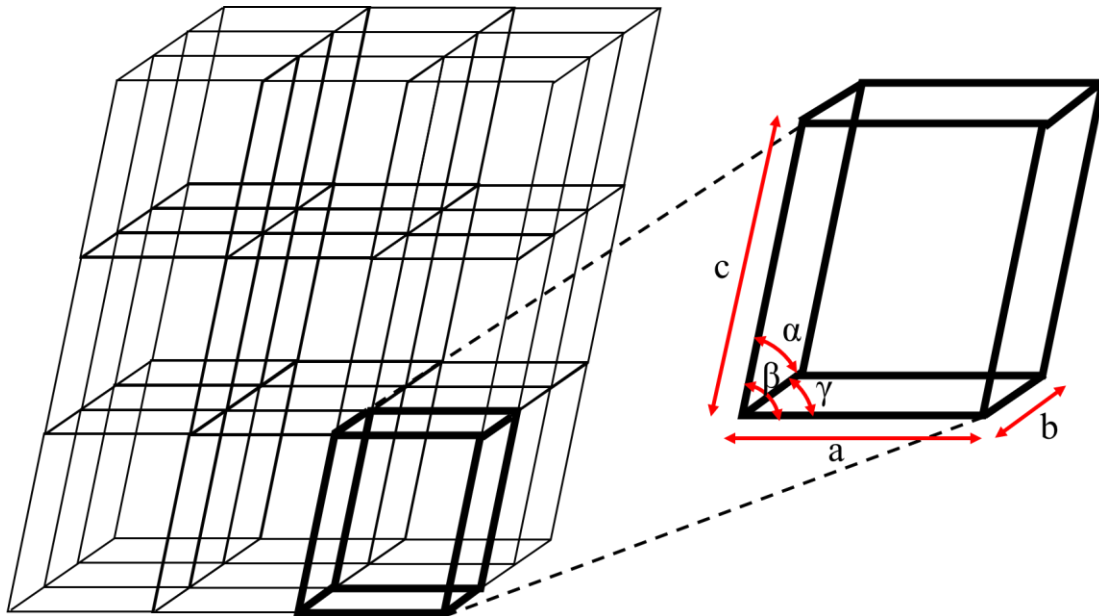


Figure 65: Generic lattice structure and unit cell, with edge lengths and interaxial angles defined.

There are seven basic crystal systems, defined by the edge lengths and interaxial angles listed in Table 9 [96]. These seven systems can be arranged into 14 different Bravais lattices based on atom location, as shown in Figure 66.

Table 9. Crystal system definitions

System	Edge length	Interaxial angle
Triclinic	$a \neq b \neq c$	$\alpha \neq \beta \neq \gamma \neq 90^\circ$
Monoclinic	$a \neq b \neq c$	$\alpha = \gamma = 90^\circ \neq \beta$
Orthorhombic	$a \neq b \neq c$	$\alpha = \beta = \gamma = 90^\circ$
Tetragonal	$a = b \neq c$	$\alpha = \beta = \gamma = 90^\circ$
Hexagonal	$a = b \neq c$	$\alpha = \beta = 90^\circ, \gamma = 120^\circ$
Rhombohedral	$a = b = c$	$\alpha = \beta = \gamma \neq 90^\circ$
Cubic	$a = b = c$	$\alpha = \beta = \gamma = 90^\circ$

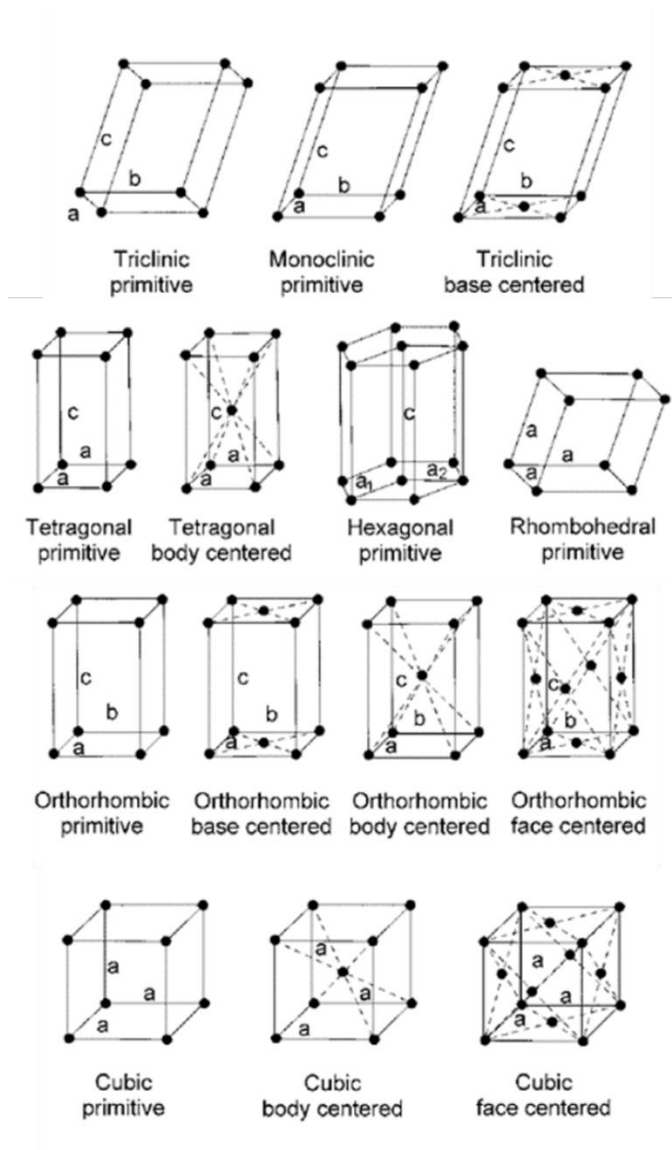


Figure 66: The 14 lattice structures [96].

Stainless steels are categorized based on the predominant metallurgical phase [97]. The three phases that commonly occur in stainless steels are austenite, ferrite, and martensite [97]. Ferrite is the body-centered cubic (BCC) solid solution, as shown in Figure 67a [98]. Austenite is the face-centered cubic (FCC) solid solution, as shown in Figure 67b [98]. Martensite forms during the rapid cooling of austenite, which prevents diffusion of carbon atoms out of the structure, resulting in the body-centered tetragonal (BCT) solid solution, as shown in Figure 67c [98].

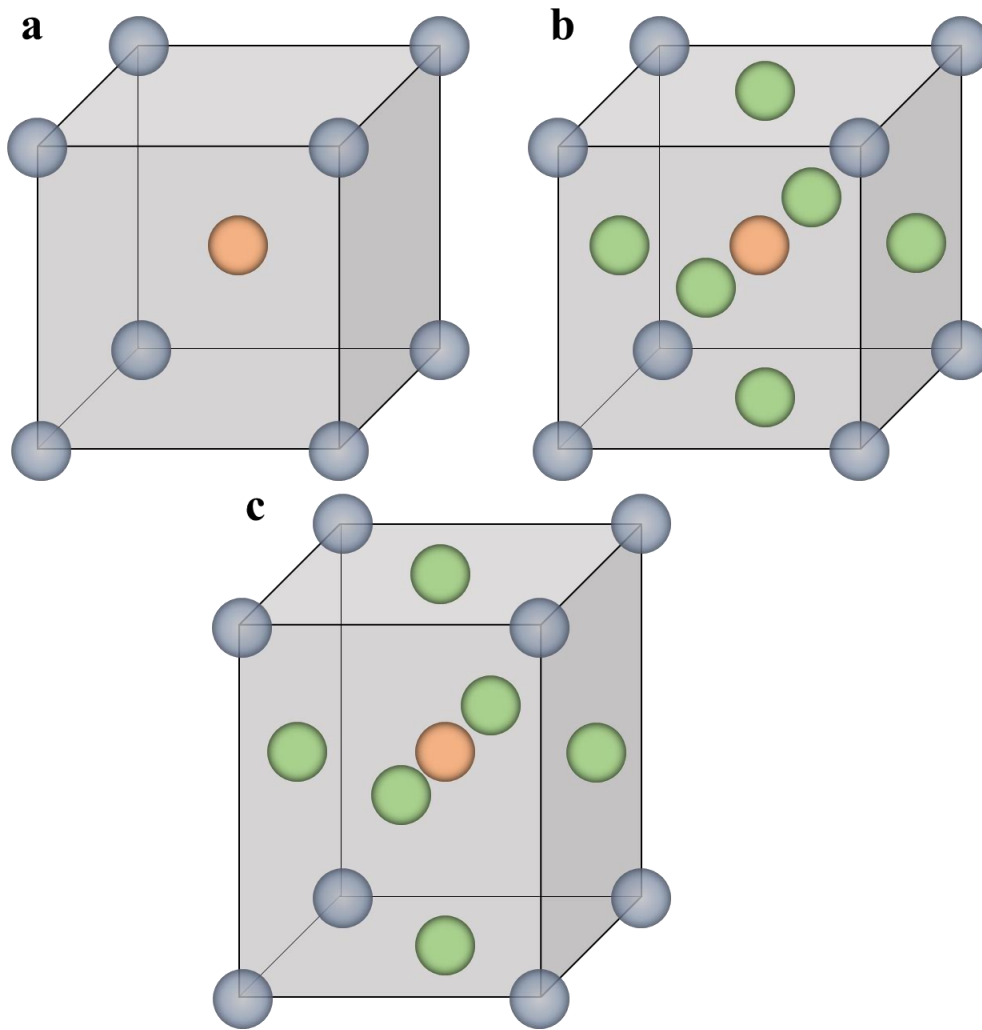


Figure 67: The (a) body-centered cubic (BCC), (b) face-centered cubic (FCC), and (c) body-centered (BCT) tetragonal structures. Corner atoms are shown in blue, face-centered atoms are shown in green, and atoms in the center of the structure are shown in orange.

The material used in this research was 316L stainless steel, an austenitic stainless steel. 316L differs from 316 in carbon content: 316L contains less carbon than 316, which increases its corrosion resistance and improves weldability [99, 100]. Generally, austenitic steels have strengths of around 210 MPa, which can be increased by cold working [100]. Wrought 316L stainless steel has a minimum room-temperature yield strength of 170 MPa and tensile strength of 480MPa [101].

4.2.1.2 Composition of stainless steels

The basis for steels is iron (Fe), which comprises over 95% of steels [102]. Steel is made by dissolving small amounts of carbon (C) into iron. In a carbon-steel solution, the carbon atoms, which have an atomic radius of 70pm, are located in the space between iron atoms, which have an atomic radius of 140pm [102, 103]. As the carbon atoms are significantly smaller than the iron atoms, they form an interstitial alloy with the iron, fitting into the holes in the iron lattice structure. An example of this is shown in the face-centered cubic structure, shown in Figure 68. In austenite, atom diameters of less than approximately 22% the diameter of the iron atom will fit in the voids between the iron atoms in this structure. Because the carbon atom diameter is approximately 50% of the diameter of the iron atom diameter, the carbon atoms push the iron atoms apart slightly, limiting the amount of carbon that can dissolve in iron [104].

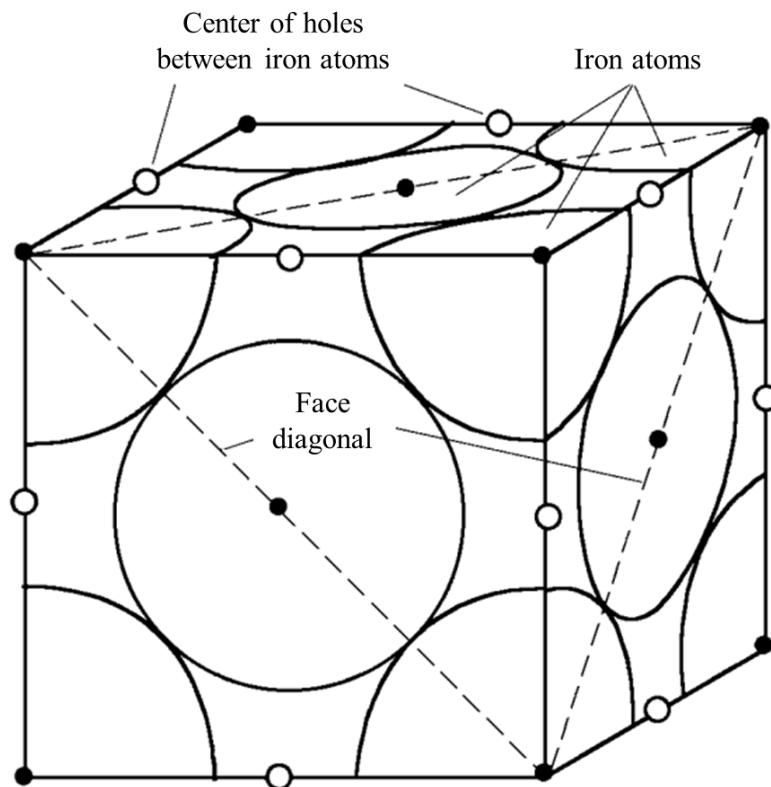


Figure 68: Location of iron atoms in face-centered cubic austenite, with the small circles indicating the centers of holes between iron atoms, where carbon atoms can be located [104].

Modern steels also contain manganese (Mn), sulfur (S), and phosphorus (P) [104]. Stainless steels comprise a group of steels based on the Fe-Cr, Fe-Cr-C, and Fe-Cr-Ni systems [105]. They are a combination of interstitial and substitutional alloys: carbon atoms are small enough to fit in the holes in the iron lattice, while larger atoms like chromium and nickel replace iron atoms in the lattice structure [106]. To be considered stainless, steel must contain at least 10.5% chromium by weight [105]. The presence of chromium at these levels results in the formation of a surface oxide that prevents oxidation and corrosion of the bulk metal underneath [105]. The material used in this research is 316L stainless steel, which in standard wrought form has a carbon content of 0.08%, a manganese content of 2%, a phosphorus content of 0.045%, a sulfur content of 0.03%, a silicon content of 1.0%, a chromium content between 16.0% and 18.0%, a nickel content between 10.0% and 14%, and a molybdenum content between 2.0% and 3.0% [97]. As mentioned previously, the chromium provides corrosion protection and is also a strong carbide former [105, 107]. Nickel primarily serves to promote the austenite phase in austenitic alloys [108]. Manganese also promotes austenite and stabilizes austenite at lower temperatures, as well as preventing hot shortness during casting [109]. Silicon is added as a deoxidizer during melting, and it improves the fluidity of molten steel [109]. Molybdenum improves elevated temperature strength and is sometimes added as a carbide former [109]. Sulfur and phosphorus improve machinability by enabling higher machining speeds and also improve tool life [109].

4.2.1.3 316L stainless steel in DED

316L stainless steel is frequently used in DED, and studies of 316L in DED range from microstructure characterization to fabrication strategies to characterization of mechanical properties [110-113]. This stainless steel can be manufactured as a wire or powder and is therefore suitable for use in both wire-fed and powder-based DED processes. Because 316L stainless steel is widely used in DED, much research has focused on understanding and optimizing laser-powder DED of the material. The characteristics of the feedstock powder, such as chemical composition and grain size, along with recycling of the powder, have been found to affect the final printed components [114, 115]. Print parameters, including laser power and scan speed, also affect the strength, surface quality,

microstructure, internal defects, and mechanical properties of 316L stainless steel components manufactured with DED [116, 117]. Build geometry and orientation, along with post-process heat treatment, were also found to influence the mechanical and microstructural properties of printed 316L stainless steel [118, 119].

4.2.2 Carbide formation

Austenitic steels, such as 316L stainless steel, can only contain up to 0.15% carbon before the solubility limit is reached and carbides begin precipitating, usually in the form of chromium carbide [120]. This is undesirable because chromium in stainless steel enables corrosion resistance, and loss of chromium in solution due to chromium carbide formation decreases the corrosion resistance of the material. The process of chromium depletion is called sensitization.

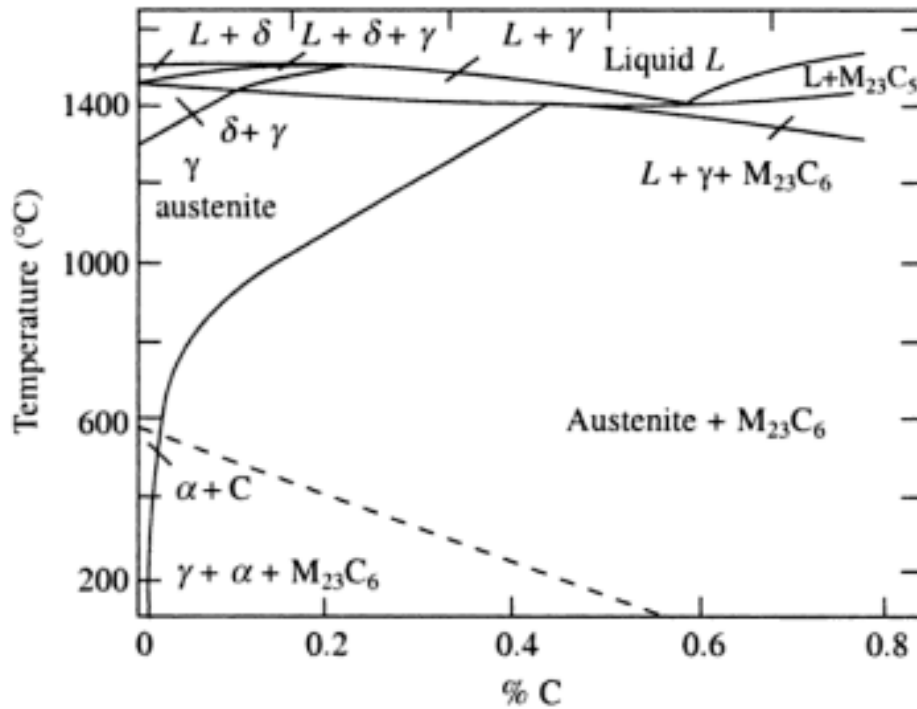


Figure 69: Solubility of carbon with respect to $M_{23}C_6$ carbides in an 18% Cr-8% Ni stainless steel [120].

Along with carbon content, sensitization has been found to depend on both temperature and deformation [121, 122]. As both of these conditions occur in metal AM, some work has been completed on the corrosion resistance of metal AM components, with mixed

results. Laleh *et al.* found that AM 316L stainless steel displays more corrosion resistance than conventional 316L stainless steel and hypothesized that this effect was due to fact that SLM-produced specimens exhibited a high frequency of twin boundaries and low-angle grain boundaries along with fine grains, leading to the avoidance of localized Cr depletion [123]. On the other hand, Macatangay *et al.* found that AM austenitic stainless steel is more susceptible to corrosion and hypothesized that this effect was due to melt pool boundaries being susceptible to accelerated attack and short, elevated temperature exposure inducing sensitization of the grain boundaries [124].

4.2.3 Porosity in DED

The two types of porosity common in laser-powder DED are porosity due to gas entrapment and lack of fusion porosity [125]. Porosity due to gas entrapment usually occurs when gas from the DED system infiltrates the liquid metal and cannot escape prior to solidification. These pores are round and symmetrical in appearance, as shown in Figure 70 [125]. Porosity due to lack of fusion occurs when there is not enough energy to fuse newly deposited material to either the substrate or previously deposited material. As shown in Figure 70, lack of fusion pores are asymmetrical and jagged and tend to occur between beads or at the substrate-component interface [126].

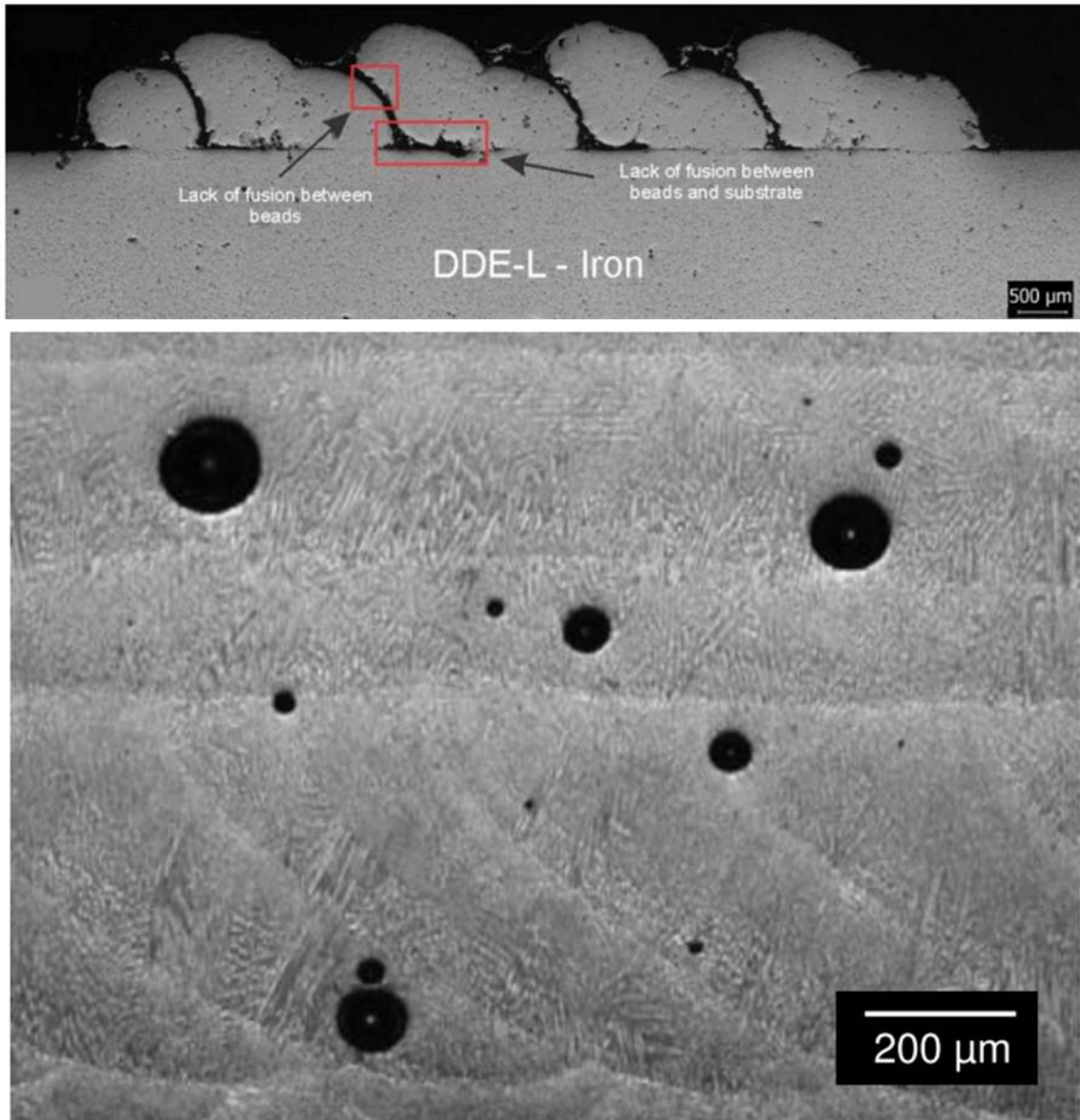


Figure 70: An example of porosity due to lack of fusion (top) and gas entrapment (bottom) [125, 126]

Porosity is generally not desired in these components because mechanical properties tend to decrease as porosity increases, as evidenced in Figure 71 [127, 128].

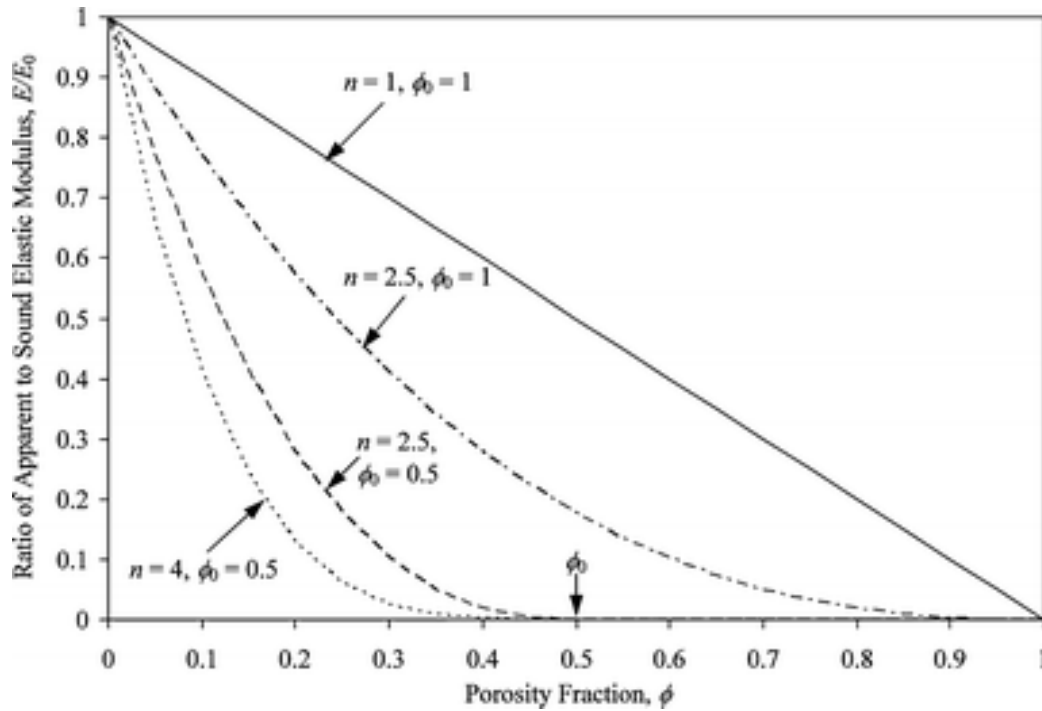


Figure 71: The effect of increasing porosity on the elastic modulus of cast steel [128].

Generally, fully dense parts are desired in all manufacturing processes, and much research has focused on increasing the density of metal AM components. Li *et al.* determined that higher laser power, lower scan speed, narrower hatch spacing and thinner layer thickness result in a much smoother melting surface and consequently a higher densification [129]. Chouhan *et al.* performed a computational study to capture powder particle interaction with the melt pool and resulting porosity formation, molten pool hydrodynamics, and solidification microstructure in the L-DED process [130]. Measurement of porosity can be done via image analysis of cross sections of printed components, and Ziolkowski *et al.* determined x-ray computed tomography (CT) scanning is a good nondestructive way to determine porosity in AM 316L stainless steel parts [131].

4.3 Experiments

To examine the effect of ABS CF polymer support onto the deposited metal, substrates of roughly 50mm in length, 25mm in width, and 12.7mm in height were manufactured and mounted in a Haas VF-5/40XT computer numerical control (CNC) system retrofitted by Hybrid Manufacturing Technologies (HMT) with an AMBIT™ S7-2 High Rate Laser Cladding Head for laser blown-powder DED capabilities. Five layers of five 12.7mm-long

beads with 0.5mm of overlap between beads were deposited to form a box-shaped geometry with MetcoAdd 316L-D (-106/+45um) stainless steel feedstock powder. The AMBIT™ laser had a spot size of 2mm and the layer height was set to 0.7mm, so the final expected dimensions of the geometry were 12.7mm in length, 8mm in width, and 3.5mm in height, as shown in Figure 72. Note that the printing process was continuous, with successive layer deposited immediately upon completion of the prior layer. Deposition settings optimized for 316L stainless steel deposition on stainless steel substrates prior to this work were used, including a laser scan speed of 600mm/min, a shield gas flow of 10 L/min, a carrier gas flow rate of 4 L/min, and a feedstock powder mass flow rate of 8 g/min. Initial testing determined that laser powers above 100W resulted in concerning levels of flaring from the polymer. Because of these safety concerns, laser power, which is usually set between 500W and 750W for stainless steel deposition on stainless steel substrates, was reduced to 100W to address these safety concerns.

After printing, the samples were scanned with a ZEISS METROTOM 800 X-Ray computed tomography (XCT) system operating at a tube voltage of 225 kV, tube power of 500W, and a resolution of 6 μm to obtain 3D images of the components and their interiors. The CT results were then analyzed to quantify the porosity of each component. After printing, the samples were mounted, cross sectioned, and polished for microscopic imaging and electron backscatter diffraction (EBSD). Micro-hardness testing was performed on the mounted cross-section using a LECO AMH55 hardness testing machine with a load of 1 kgf and a dwell time of 15 seconds at 250μm intervals along the build direction, beginning at the bottom of the stainless steel component, which interfaces with the polymer, and ending 1750μm from the bottom of the build.

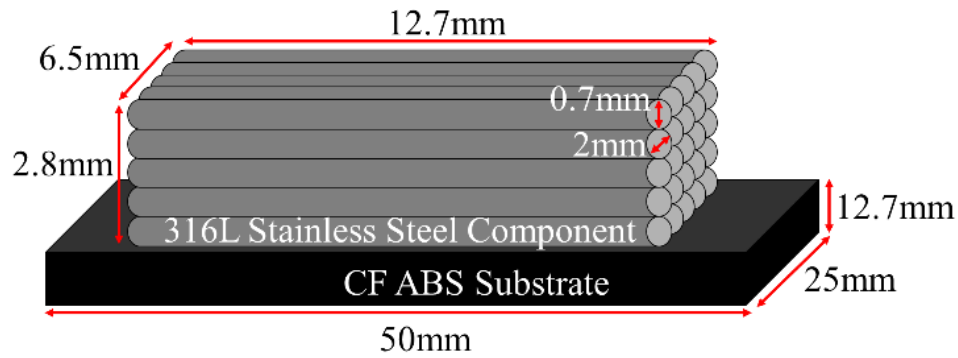


Figure 72: Geometry of 316L stainless steel components printed on CF ABS substrates.

4.4 Results and discussion

4.4.1 Porosity

The solid box-shaped component with continuous printing (no interlayer cooling time) was deposited and is shown with its cross section along the YZ plane in Figure 73. Significant porosity was evident in the cross section, and the rounded appearance of this porosity, marked with arrows, indicates that the porosity is primarily due to gas entrapment. These pores were likely caused by gases from polymer combustion infiltrating the molten metal during deposition.

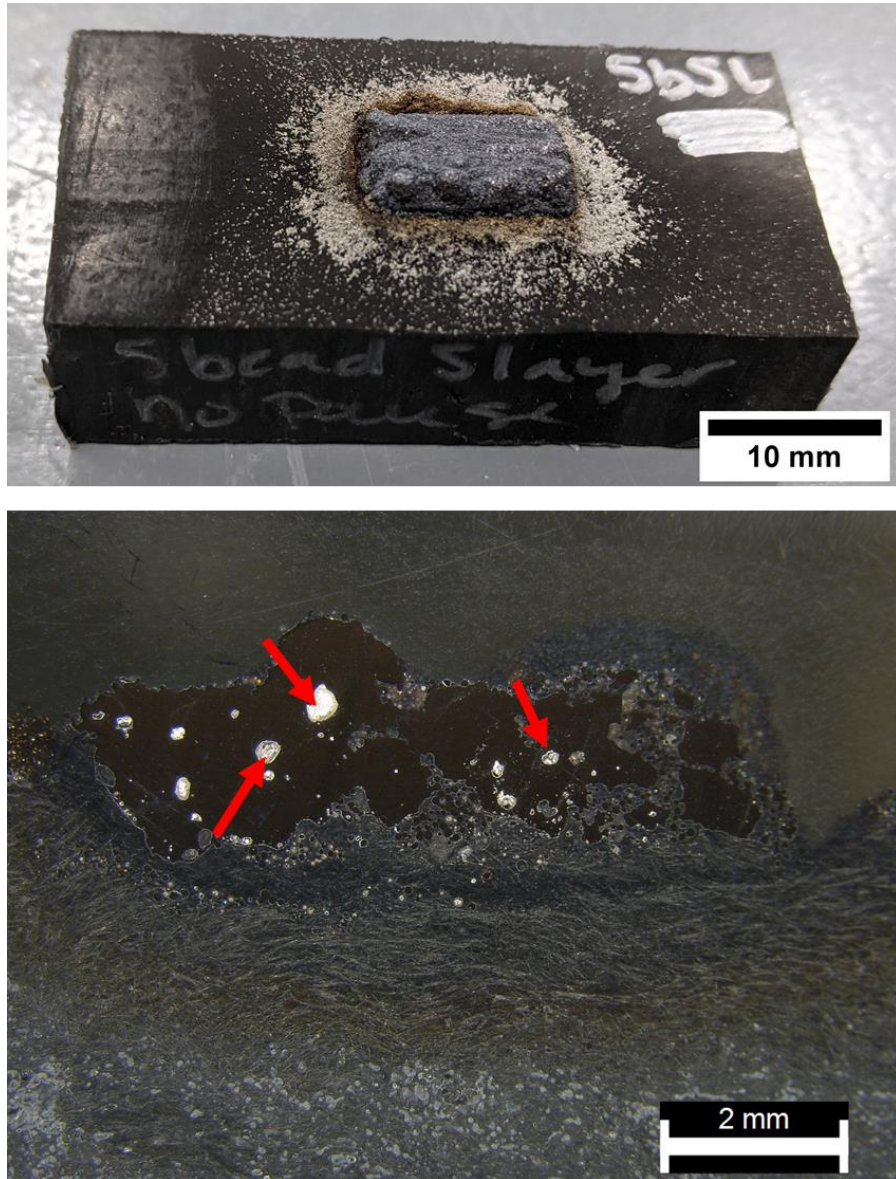


Figure 73: Top-down view (top) and cross-sectioned image (bottom) of a box comprised of five layers of five 12.7mm-long adjacent passes, deposited on CF ABS with no interlayer cooling time, with arrows to indicate porosity due to gas entrapment.

The CT results are shown in Figure 74. The CT scan also indicated that porosity in this component was dominated by gas entrapment porosity, evidenced by the rounded appearance of the pores. Porosity due to lack of fusion defects can also be observed, located at bead interfaces. Lack of fusion porosity was likely due to the low power used to deposit the 316L stainless steel. Because the laser power was lower than generally used in laser powder DED of 316L stainless steel, there was occasionally not enough energy to fuse

adjacent beads to each other. Overall, the component was determined to have a porosity of 8.25%.

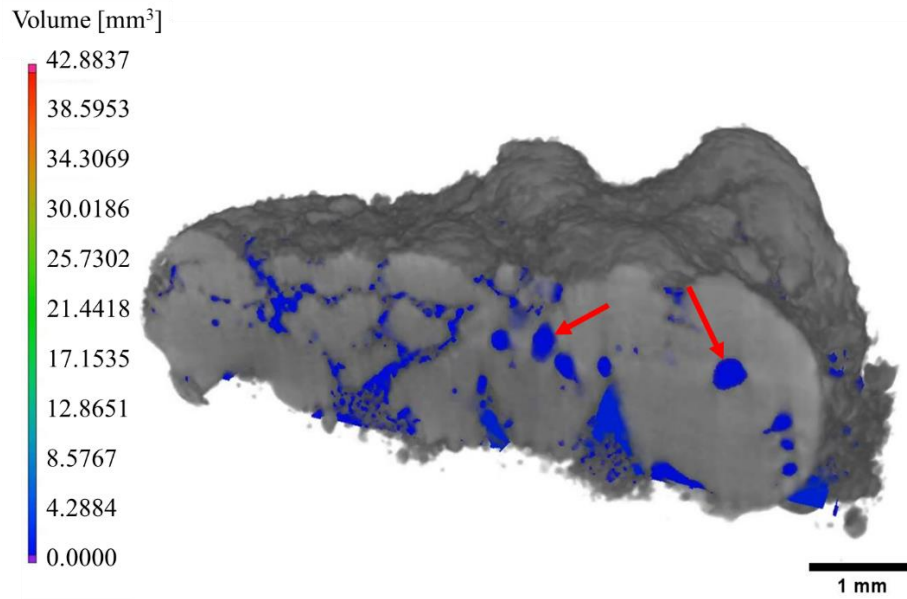


Figure 74: CT scan results showing porosity of 316L stainless steel on CF ABS, with arrows indicating porosity due to gas entrapment.

Figure 75 shows electron backscatter diffraction (EBSD) image indicating the microstructure of 316L stainless steel deposited on a CF ABS substrate. The grains are small and equiaxed for much of the build, although there are some areas in the center of the build that contain larger and more elongated grains. Elongated grains are commonly seen in metal AM components, as the rapid cooling and re-heating of the component as subsequent layers are deposited furthers elongated grain growth between layers [132]. The smaller, equiaxed grains in this build likely occurred because the polymer substrate was at room temperature prior to deposition, rapidly cooling the deposited material.

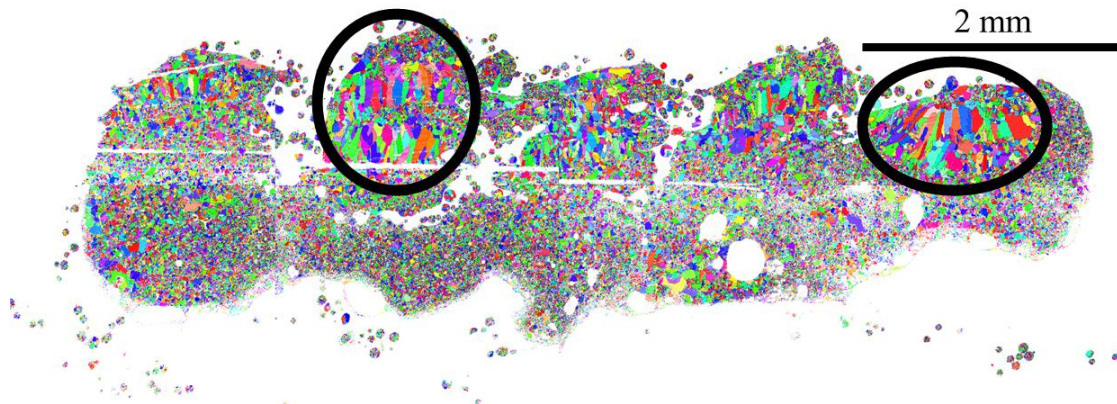


Figure 75: EBSD image showing the microstructure of 316L stainless steel deposited on CF ABS, with larger grains circled.

Figure 76 shows the phase distributions of 316L stainless steel deposited on CF ABS both directly adjacent to the polymer substrate (top) and at the top of the print (bottom). The phase distributions of the metal directly adjacent to the polymer substrate indicate the presence of more chromium carbides and more iron BCC phase compared to the metal at the top of the print. The increase of both chromium carbide and iron BCC phase occurred due to increased carbon content as the result of carbon migration from the polymer into the molten metal. The increased carbon pulled the chromium out of solution, resulting in chromium carbides. The increased BCC content can be attributed to the increased presence of carbon in the interstitials, which increases stress on the FCC phase. The increased carbon in combination with rapid cooling also resulted in more BCC formation. The decrease of chromium carbides and BCC content near the top of the print indicates that the effect of using a polymer substrate on the deposited metal is limited to the first few layers of the print.

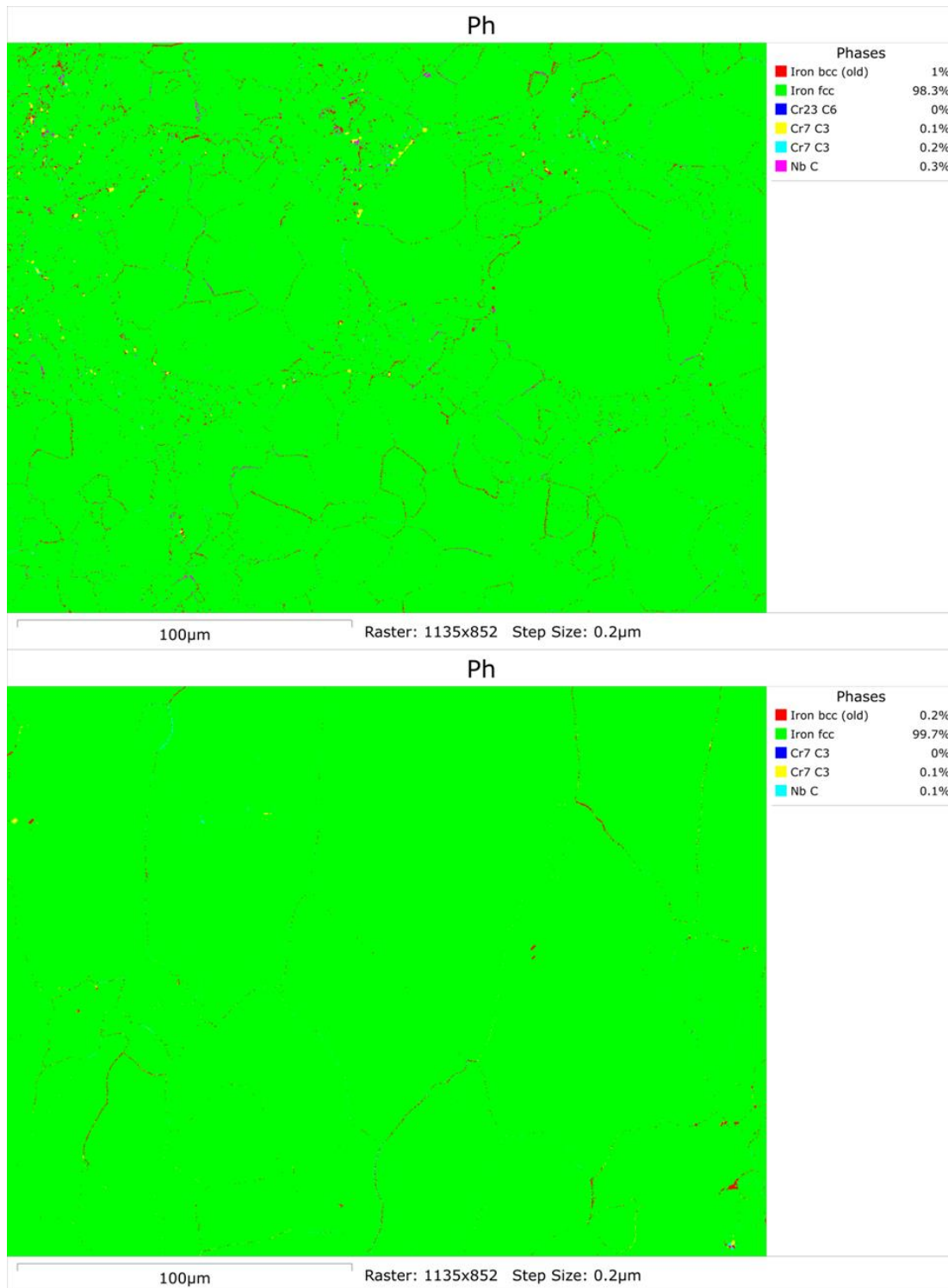


Figure 76: Phase distributions of 316L stainless steel deposited on CF ABS adjacent to the polymer (top) and at the top of the print (bottom). Note that the material adjacent to the polymer has a higher content of chromium carbides and BCC structure.

4.4.2 Hardness effects

Hardness testing was performed on the cross section shown in Figure 73 to quantitatively assess the effects of using a polymer substrate on one mechanical property of the deposited metal. Figure 77 shows the average hardness value at 8 intervals on the cross section of the component with no interlayer cooling time. The error bars indicate the standard deviation of the measurements taken at each distance from the bottom of the build. The hardness of the 316L stainless steel component at the interface, or at 0 μ m from the bottom of the build, was 338 \pm 39. This hardness value is 69% larger than the expected hardness value of 316L stainless steel built by DED, as evaluated by Feldhausen *et al.* [133]. The hypothesis that the hardness of the stainless steel component at the interface is significantly greater than the expected hardness of 200 was validated using a one-sample t-test with a null hypothesis of

$$\mu_{hardness} = 200 \quad (4.1)$$

and an upper one-tailed alternate hypothesis of:

$$\mu_{hardness} > 200 \quad (4.2)$$

To calculate the t-statistic for a one-sample t-test, the following formula was used, where \bar{x} is the sample mean, μ is the hypothesized mean, in this case 200, and $s_{\bar{x}}$ is the standard error of mean.

$$t = \frac{\bar{x} - \mu}{s_{\bar{x}}} \quad (4.3)$$

The t-statistic for the data set of hardness values of the stainless steel at the interface between the metal and the polymer was found to be 6.2, which corresponds to a one-tailed p-value of 0.012 for this data set. Therefore, the null hypothesis was rejected, and the average hardness at the interface was significantly greater than the expected hardness of deposited 316L stainless steel, with 98.8% confidence.

The hardness of the test component trended downwards as the distance from the bottom of the build increased, and the hardness values remained higher than the expected value of 200 until a distance of 1250 μ m from the bottom of the build. The higher-than-expected hardness values were likely due to increased carbon levels in the first several deposited layers of the metal. In 316L stainless steel, an austenitic steel, higher levels of carbon tend to form carbides with chromium, increasing the hardness [109]. The combination of the

laser and deposited molten metal degraded some of the polymer substrate into a carbonaceous char, which then mixed with the molten feedstock prior to solidification. Fluctuations in the hardness values can be observed: for example, the hardness increases between 500 μm and 750 μm instead of continuing the expected downward trajectory. Additionally, the hardness above 1500 μm drops below the expected value of 200. These fluctuations are likely due to other factors that affect the hardness of steel, such as grain size variation. As Hall and Petch discovered in the early 1950s, grain diameter has an inversely proportional relationship with hardness [134, 135]. Decreased grain size diameter at 750 μm and increased grain size diameter at 1500 μm could therefore cause the observed hardness fluctuations.

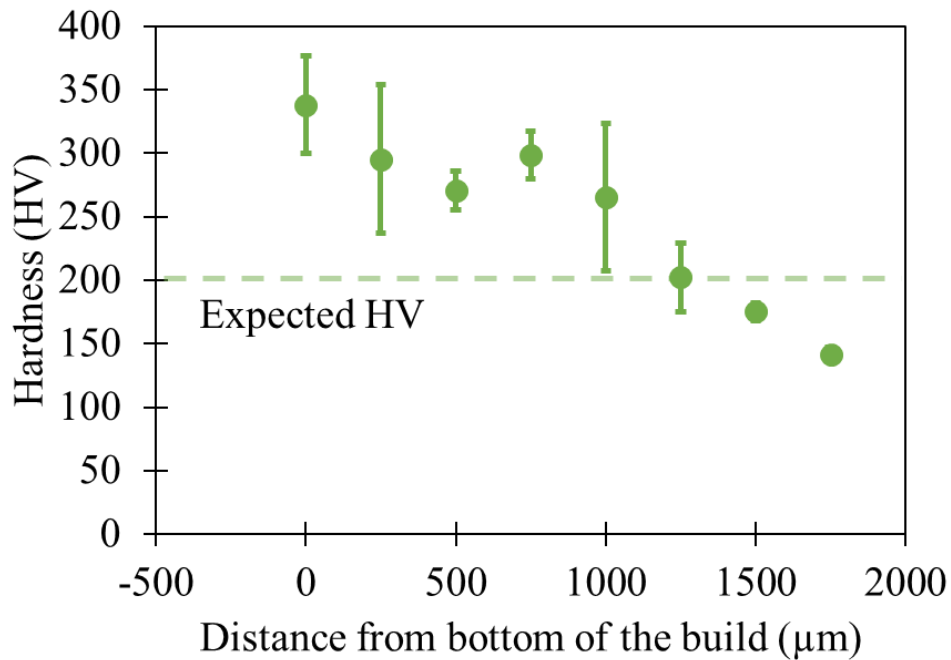


Figure 77: Measured hardness values of 316L stainless steel deposited on CF ABS compared to expected hardness values [133].

4.5 Conclusions

For polymer support structures to be considered successful, the metal deposited on top of the polymer must not be significantly altered due to close contact with the dissimilar

material. Even if metal is deposited on top of the polymer without significant polymer degradation or combustion, polymer supports would not be useful if the final metal component differed significantly in its makeup and properties than the expected metal component. As a case study to determine the effects of polymer support structures on deposited metal, a 316L stainless steel cube was deposited on a CF ABS substrate. The final cube was analyzed to determine the porosity, microstructure, phase distributions, and hardness. The CF ABS substrate was found to increase porosity of 316L stainless steel by entrapment of gas from degradation. Porosity also increased because the power used in deposition was lower than the usual print settings for 316L stainless steel to avoid significant combustion, resulting in lack of fusion defects. Also, carbon migration from the polymer to the deposited metal increased the carbon content of deposited 316L, forming chromium carbides that increased hardness by ~70% and likely reduced corrosion resistance. To prevent the polymer substrate from affecting the deposited metal, a mitigation strategy is required and will be presented in the next chapter.

CHAPTER 5. MITIGATION OF POLYMER EFFECTS ON DEPOSITED METAL BY INTERLAYER COOLING TIME

5.1 Introduction

In Chapter 4, it was determined that the use of a CF ABS substrate in deposition of a 316L stainless steel component affected the porosity, microstructure, and hardness of the metal component. The differences between the expected and actual deposited metal properties were not ideal, and a mitigation strategy to lessen the effects of using a polymer substrate on the deposited metal is desired. The effects of time, temperature, and carbon content on 316L stainless steel are discussed. These effects were used to develop a mitigation strategy: insertion of a cooling period in between each layer of the deposition. Sample components were printed using this strategy, and the porosity, microstructure, and hardness of these mitigated components were compared to the original component tested in Chapter 4. The methodology and results for these tests are presented, followed by the conclusions of the chapter.

5.2 Background

The mechanical properties and microstructure of the deposited 316L stainless steel depend on several factors. The final composition of the steel affects the phases in the steel. As shown in Figure 78, increasing the carbon content increases the presence of gamma phase, sigma phase, carbides, and cementite [136]. 316L stainless steel has a chromium content between 16.5% and 18.5%. At these levels, an increase of carbon content by less than half a percent results in M_{23} carbide formation. To reduce the formation of these carbides, less carbon migration from the polymer to the molten metal is required. This could be achieved by lowering overall temperatures in the polymer and metal, and as diffusion is a temperature-driven process, lower temperatures will result in less migration of carbon into the metal.

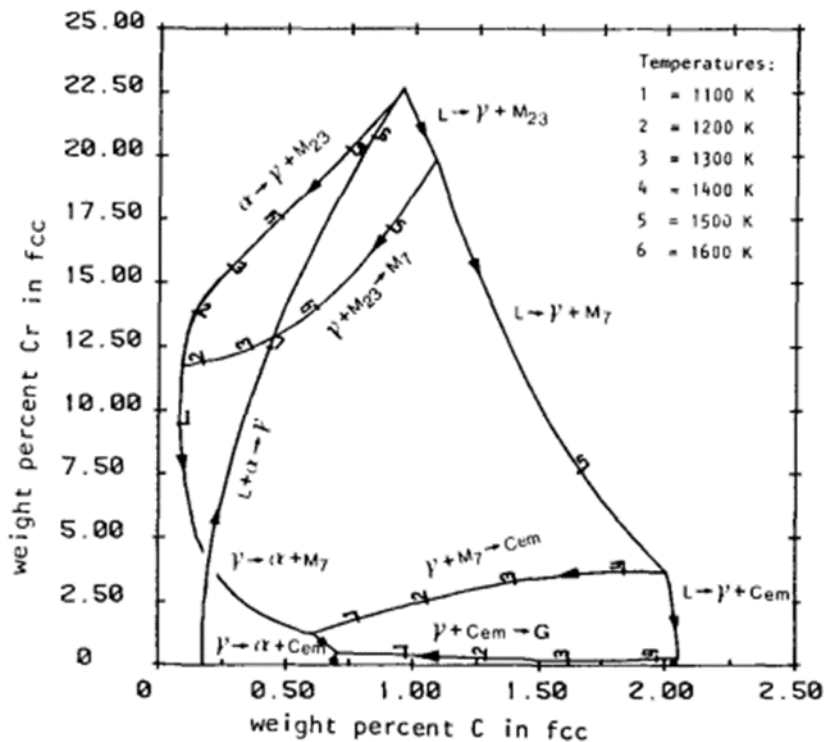


Figure 78: Projection of the calculated FCC surfaces. The lines represent three-phase reactions. The tic marks indicate each hundred degrees starting from 1000 K [136].

Temperature and time also play a significant role in the final microstructure of the deposited material. The time-temperature-precipitate (TTP) diagram shown in Figure 79 indicated that longer time spent at higher temperatures results in carbide and varying phase formations [137]. The DED process does not result in sustained, elevated temperatures, but rather brief periods of elevated temperatures followed by rapid cooling. The curve of most concern is therefore the $M_{23}C_6$ curve, which indicates that increased temperatures increase carbide formation, even if the component does not experience these temperatures for an extended period. To this end, lower overall temperatures and less time at elevated temperatures is required to prevent carbide formation.

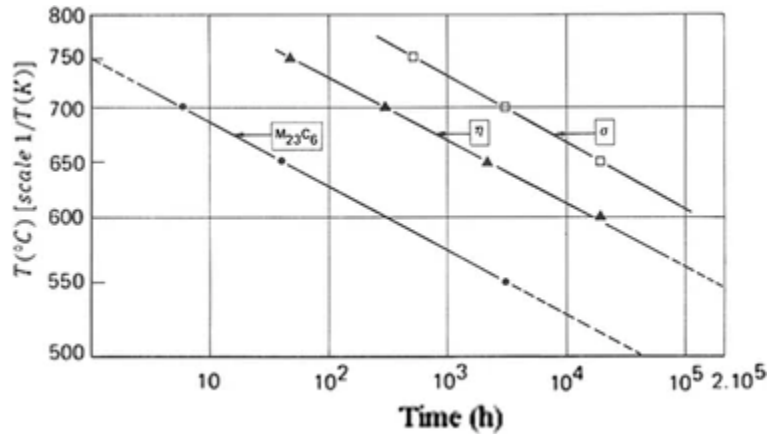


Figure 79: TTP diagram in a temperature range of 823 K to 1023 K (550°C to 750°C) [137].

Because reducing carbide formation requires a reduction in temperature and a reduction of time spent at elevated temperatures, an interlayer cooling time was proposed to mitigate the effects of using a polymer substrate on the deposited metal.

5.3 Methodology

As in Chapter 4, substrates of roughly 50mm in length, 25mm in width, and 12.7mm in height were manufactured and mounted in a Haas VF-5/40XT computer numerical control (CNC) system retrofitted by Hybrid Manufacturing Technologies (HMT) with an AMBIT™ S7-2 High Rate Laser Cladding Head for laser blown-powder DED capabilities. Five layers of five 12.7mm-long beads with 0.5mm of overlap between beads were deposited to form a box-shaped geometry with MetcoAdd 316L-D (-106/+45um) stainless steel feedstock powder. The AMBIT™ laser had a spot size of 2mm and the layer height was set to 0.7mm, so the final expected dimensions of the geometry were 12.7mm in length, 8mm in width, and 3.5mm in height, as shown in Figure 72. Deposition settings optimized for 316L stainless steel deposition on stainless steel substrates prior to this work were used, including a laser scan speed of 600mm/min, a shield gas flow of 10 L/min, a carrier gas flow rate of 4 L/min, and a feedstock powder mass flow rate of 8 g/min. Again, because of safety concerns, laser power was reduced to 100W.

To mitigate the effects of a polymer substrate on the deposited metal, an interlayer cooling time was introduced to reduce the overall temperature of the metal component and the time

spent by the metal at elevated temperatures. After printing, the samples were scanned with a ZEISS METROTOM 800 X-Ray computed tomography (CT) system operating at a tube voltage of 225 kV, tube power of 500W, and a resolution of 6 μm to obtain 3D images of the components and their interiors. The CT results were then analyzed to quantify the porosity of each component. After printing, the samples were mounted, cross sectioned, and polished for microscopic imaging and electron backscatter diffraction (EBSD). Micro-hardness testing was performed on the mounted cross-section using a LECO AMH55 hardness testing machine with a load of 1 kgf and a dwell time of 15 seconds at 250 μm intervals along the build direction, beginning at the bottom of the stainless steel component, which interfaces with the polymer, and ending 1750 μm from the bottom of the build.

5.4 Results and discussion

Figure 80a shows the component printed with no interlayer cooling time, and Figure 80b shows the component printed with 30 seconds of interlayer cooling time. Some oxidation, indicated by dark gray surface of the component, was seen on the component with no cooling time, while the coloration on the component with the interlayer cooling time indicates less oxidation [138]. The component with the interlayer cooling time had less oxidation because the shield gases continue to blow around the component during the cooling time, preventing oxygen from interacting with the component at higher temperatures.



No interlayer cooling time



30s interlayer cooling time

Figure 80: Component printed with no interlayer cooling time (top) and a 30 second interlayer cooling time (bottom). Note the oxidation (dark gray) on the top component compared to the rainbow coloration on the bottom component.

The cross sections of both components shown in Figure 81 indicated that neither component was completely solid, as both showed substantial porosity. The component with no interlayer cooling time, shown in Figure 81 (top), had pores that are round and smooth in appearance which can be attributed to entrapped gas, likely due to gaseous byproducts from polymer degradation infiltrating the molten stainless steel. The component with a 30 second interlayer cooling time, shown in Figure 81 (bottom), had pores that are jagged and located on the boundaries between beads. These pores were lack of fusion defects that can be attributed to the low power used during deposition in combination with the interlayer cooling time, which prevented heat buildup in the component. The porosity was also quantitatively measured in each component, calculating the ratio of pores to total volume. The porosity of the component with no interlayer cooling time was found to be 8.25%, and the porosity of the component with a 30 second interlayer cooling time was found to be

4.49%. The difference in these porosity values indicates that porosity due to gas entrapment is a greater concern during the first several layers of a metal component deposited on a polymer substrate. Therefore, an interlayer cooling time, which prevents heat buildup and reduces polymer degradation, is desirable for these first few layers. However, after enough metal layers are deposited to insulate the component from gas infiltration, the interlayer cooling time should be reduced or eliminated to reduce porosity due to lack of fusion.

Both CF ABS substrates used in these experiments were affected by the DED process. Evidence of polymer degradation can be seen, as well as discoloration to depths of over 2mm, evidence of thermal damage from the DED process on the polymer. However, the effects of the DED process on the polymer did not affect the geometric integrity of the substrate enough to prevent continued deposition of the metal component.

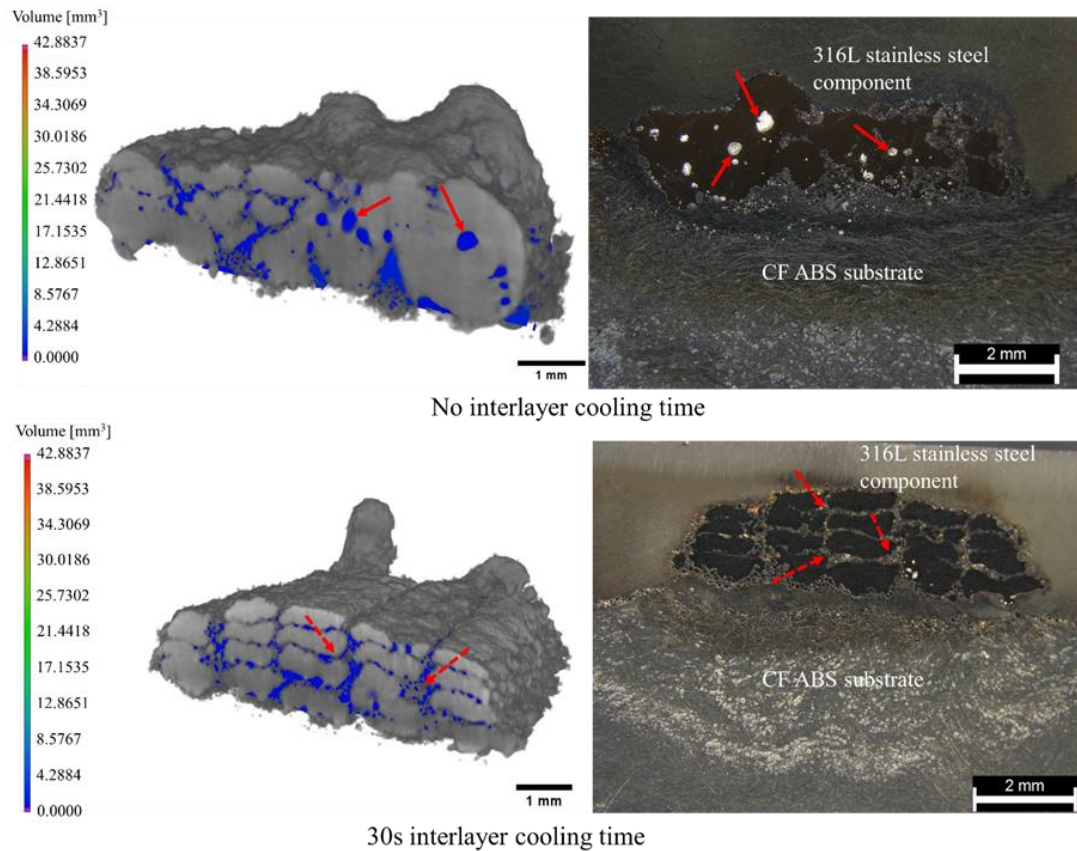


Figure 81: CT scans and microscopic cross-sectional images of 316L stainless steel components printed on CF ABS with no interlayer cooling time (top), with solid arrows indicating porosity due to gas entrapment, and 30 seconds of interlayer cooling time (bottom), with dashed arrows indicating porosity due to lack of fusion.

Figure 82 shows the average hardness value at 8 intervals on the cross section of the component with no interlayer cooling time compared to the component with 30 seconds of interlayer cooling time. The error bars indicate the standard deviation of the measurements taken at each distance from the bottom of the build. No increase in hardness was observed in the component with a 30 second interlayer cooling time, with all hardness values at approximately the expected hardness value for DED 316L stainless steel [133]. The hardness of this component at the interface (0 μ m from the bottom of the build) was 204 ± 38 , a 40% decrease from the hardness value at the interface of the component with no interlayer cooling time.

The data set of hardness values of the metal component with 30 seconds of interlayer cooling time was compared to the expected hardness value of 200 using a one-sample t-test with the null hypothesis in (1) and a two-tailed alternate hypothesis of:

$$\mu_{hardness} \neq 200 \quad (5.1)$$

The t-statistic was calculated using (3) to be 0.32, which corresponds to a two-tailed p-value of 0.76. The null hypothesis was therefore accepted, and the hardness value of the 316L stainless steel component with 30 seconds of interlayer cooling was found to be statistically indistinguishable from the expected hardness value of deposited 316L stainless steel.

The interface hardness value data sets of both components were then compared using a two-sample t-test with null hypothesis

$$\mu_{no\ cooling} = \mu_{30s\ cooling} \quad (5.2)$$

And a two-tailed alternate hypothesis

$$\mu_{no\ cooling} \neq \mu_{30s\ cooling} \quad (5.3)$$

The t-test was performed using the Excel Data Analysis ToolPak with a hypothesized mean difference of 0. The p-value was calculated to be 0.013, so the null hypothesis was rejected, and the average hardness at the metal/polymer interface of the component printed with a 30 second interlayer cooling time was found to be significantly smaller than the average hardness at the same location of the component printed with no interlayer cooling time, with 98.7% confidence.

The difference in hardness between the two cases was likely due to the difference in heat buildup in the components during deposition. Because the component with no interlayer cooling time lost relatively little heat between layers, the heat in the component built up over time, and temperature of the component remained higher throughout the build than the temperature of the component that was cooled for 30 seconds between layers. The component with no interlayer cooling time therefore experienced higher temperatures for longer periods of time, promoting carbon diffusion and the formation of carbides, thereby increasing hardness. The hypothesis that the component without any interlayer cooling melted more readily is also supported by the porosity observed in Figure 81. The porosity

observed in the component with 30 seconds of interlayer cooling time was mostly lack of fusion defects. These defects were the result of insufficient energy input into the system to fully melt the feedstock powder to deposit a new layer on the previous layer with sufficient overlap. On the other hand, the porosity observed in the component with no interlayer cooling time was due to gas entrapment as gaseous byproducts from polymer degradation infiltrated the metal component and were trapped during solidification. Very few lack of fusion pores are visible, indicating that the component retained enough heat that the combination of retained heat and the laser during deposition was enough to fully melt the feedstock and re-melt the previous layer, providing sufficient overlap between layers.

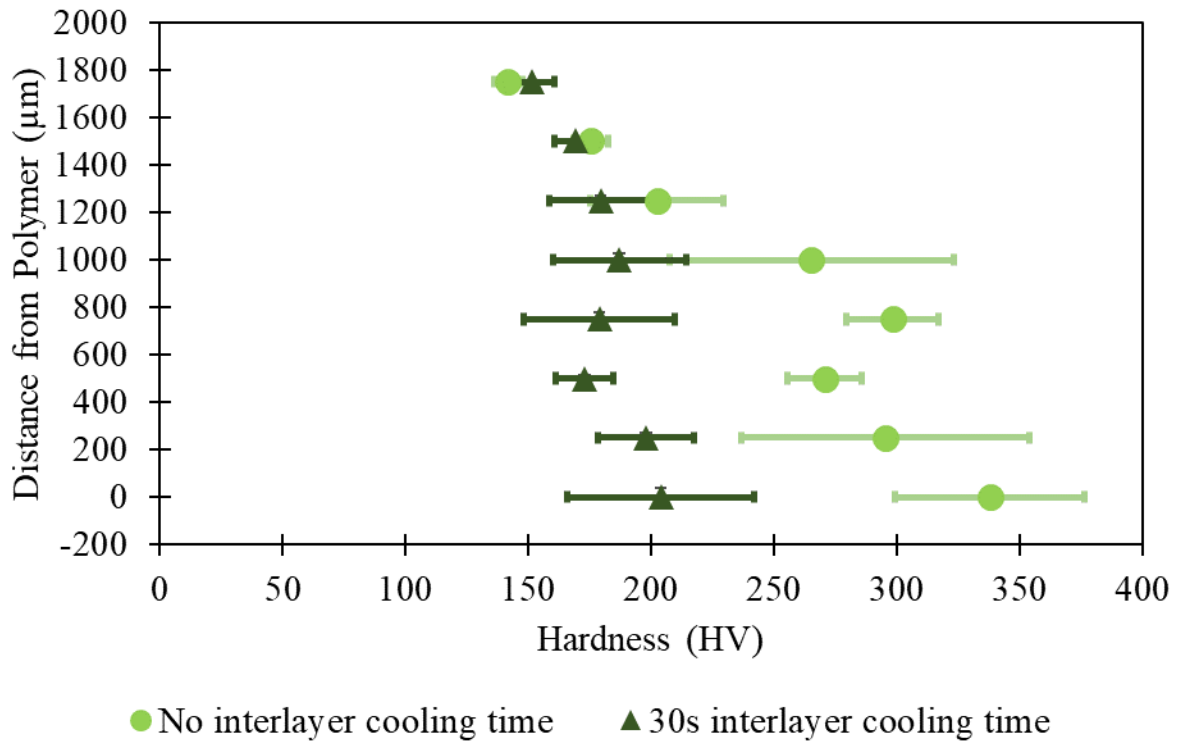


Figure 82: Hardness values for component with no interlayer cooling time (light green circles) and 30 seconds of interlayer cooling time (dark green triangles) compared to the expected hardness value from [133].

Figure 83 shows electron backscatter diffraction (EBSD) image comparing the microstructure of 316L stainless steel deposited on a CF ABS substrate with no interlayer cooling time (top) and a 30 second interlayer cooling time (bottom). The grains were smaller and more equiaxed in the component with the interlayer cooling time. The smaller grain size occurred because this component did not experience sustained, elevated

temperatures like the component with no interlayer cooling time. Therefore, conditions for grain growth were not met.

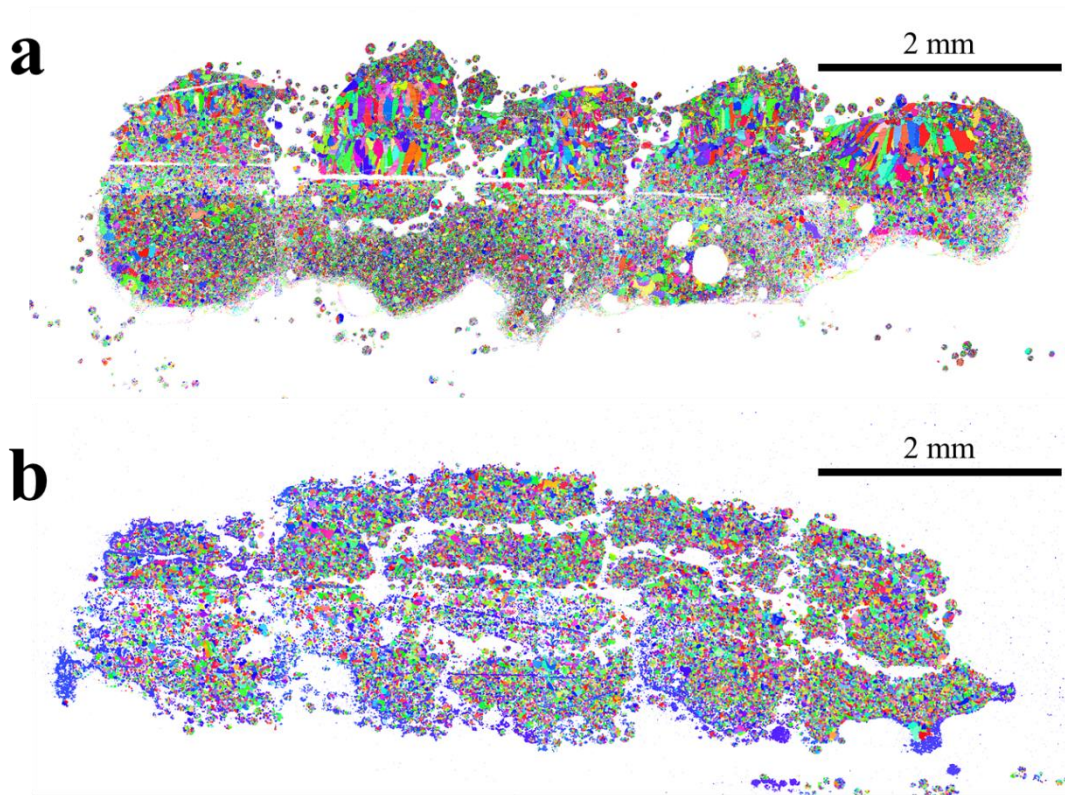


Figure 83: EBSD image showing grain sized for a component printed with (a) no interlayer cooling time and (b) 30 seconds of interlayer cooling time. Note that the grain sizes in the component with an interlayer cooling time are smaller.

Figure 84 shows the phase distributions of 316L stainless steel deposited on CF ABS directly adjacent to the polymer substrate of the component with no interlayer cooling time (top) compared to the component with a 30 second interlayer cooling time (bottom). The phase distribution of the component with no interlayer cooling time indicates the presence of more chromium carbides compared to the component with a 30 second interlayer cooling time. The decrease of chromium carbide with an introduction of an interlayer cooling time was due to decreased carbon content because of slower carbon migration from the polymer to the metal. Additionally, the interlayer cooling time kept the overall component temperature lower and decreased the amount of time spent by the metal at higher temperatures. This adjustment to the time-temperature scenario experienced by the metal decreased formation of chromium carbides.

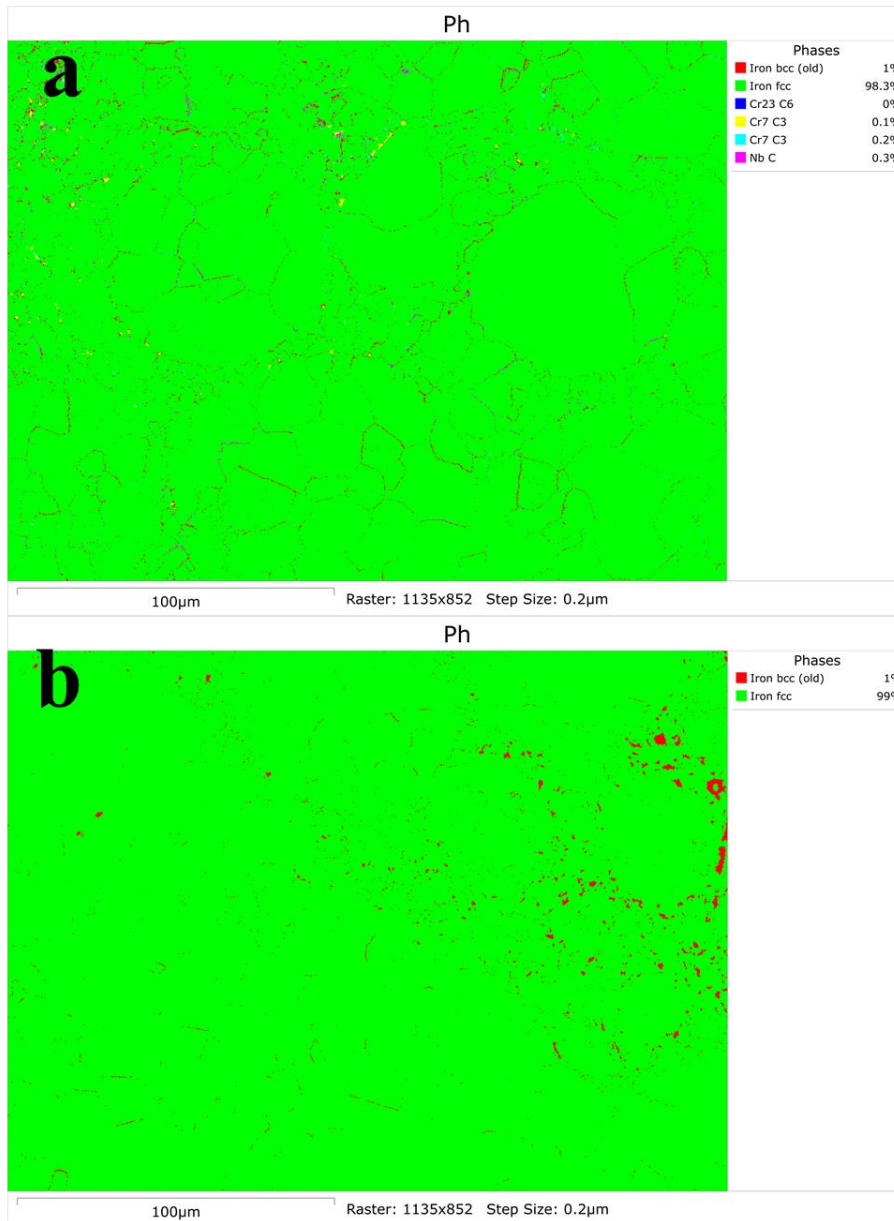


Figure 84: Carbides are present near the substrate in (a) the component with no interlayer cooling time, but not in (b) the component with 30 seconds of interlayer cooling time. Note the reduction of chromium carbides in the component with an interlayer cooling time.

5.5 Conclusions

In Chapter 4, the effects of using a CF ABS substrate on the porosity, microstructure, and hardness of a deposited 316L stainless steel component were determined. To mitigate these effects, an interlayer cooling time was introduced to the printing process. The interlayer cooling time served to lower the overall temperature of the metal component and reduce the time spent by the component at elevated temperatures. This effect resulted in less carbon diffusion from the polymer to the molten metal and moved the deposited 316L stainless steel outside of the time-temperature regime required for carbide formation. The interlayer cooling time resulted in smaller grains and a decrease in carbide concentration. The cooling time also prevents porosity due to gas entrapment, lowering porosity from approximately 8% to approximately 4%. The dominant porosity type changed from gas entrapment to lack of fusion, as the component with an interlayer cooling time retained less heat, decreasing the energy available to fuse beads together. Overall, the interlayer cooling time successfully mitigated the effects of using a polymer substrate on a deposited metal component, although the low power required to print on a polymer still resulted in some porosity.

CHAPTER 6. POLYMER SUPPORT DEMONSTRATION

6.1 Introduction

Successful polymer support structures in metal DED would expand the design space of DED, enabling more complex geometries to be built without significantly adding to the cost of the process. Two examples of geometries that are impossible to build using 3-axis DED systems are steep overhangs and bridges. To demonstrate the application of polymer supports, both an overhang, in the form of a cantilever beam, and a bridge were manufactured using polymer supports. The procedure for printing these components, made with 316L stainless steel and supported by CF ABS, is presented. The results of these demonstrations are presented, followed by the conclusions of the chapter.

6.2 Methodology

To demonstrate a successful polymer support structure, a bridge and a cantilever geometry were deposited with 316L stainless steel using CF ABS support structures. All geometries were manufactured using with MetcoAdd 316L-D (-106/+45 um) stainless steel feedstock powder in a Haas VF-5/40XT computer numerical control (CNC) system retrofitted by Hybrid Manufacturing Technologies (HMT) with an AMBIT™ S7-2 High Rate Laser Cladding Head for laser blown-powder DED capabilities. Deposition settings optimized for 316L stainless steel deposition on stainless steel substrates prior to this work were used, including a laser scan speed of 600mm/min, a shield gas flow of 10L/min, a carrier gas flow rate of 4L/min, and a feedstock powder mass flow rate of 8g/min. Based on previous work in this research, power was set to 100W. An interlayer cooling time was introduced to reduce the overall temperature of the metal component and the time spent by the metal at elevated temperatures.

The procedure for printing the supported geometries is shown in Figure 85. A slot was machined out of a 316L stainless steel substrate. A piece of CF ABS was then used to fill the slot. The CF ABS acted as a support during the cantilever and bridge depositions. Finally, the polymer was manually removed to reveal the metal geometry.

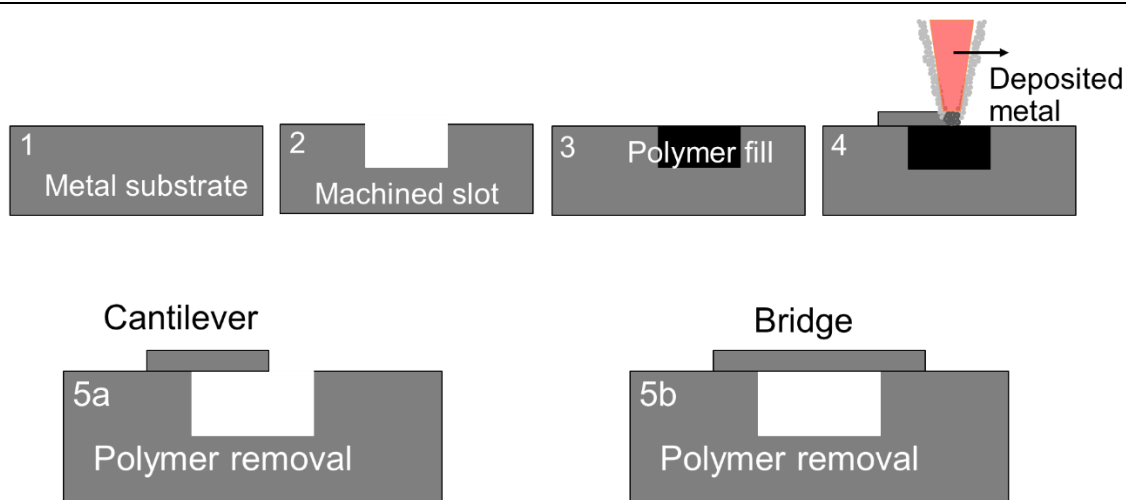


Figure 85: Process for the polymer support structure demonstration.

6.3 Results and discussion

Figure 86 shows the cantilever structure with its CF ABS support (top) and after the CF ABS support was removed (bottom). The CF ABS provided support to the metal print without degrading to the point of hindering print accuracy. The polymer support was also easy to remove after deposition: no adhesion occurred between the metal and the polymer. However, accuracy of the final geometry was affected by warping, as shown in Figure 86 (bottom). The large thermal gradients inherent in the metal DED process resulted in residual stresses in the component. Because the cantilever geometry has one free end, the component was not constrained and therefore warped under the effect of these residual stresses. The effect of residual stresses on deposited geometries has been studied previously. Plati *et al.* developed a 3D finite element model to predict distortions in laser cladding on a cantilever substrate, and Saleeby and Feldhausen experimentally determined the effect of severe thermal cycling due to laser-powder DED on a cantilever substrate [139, 140].

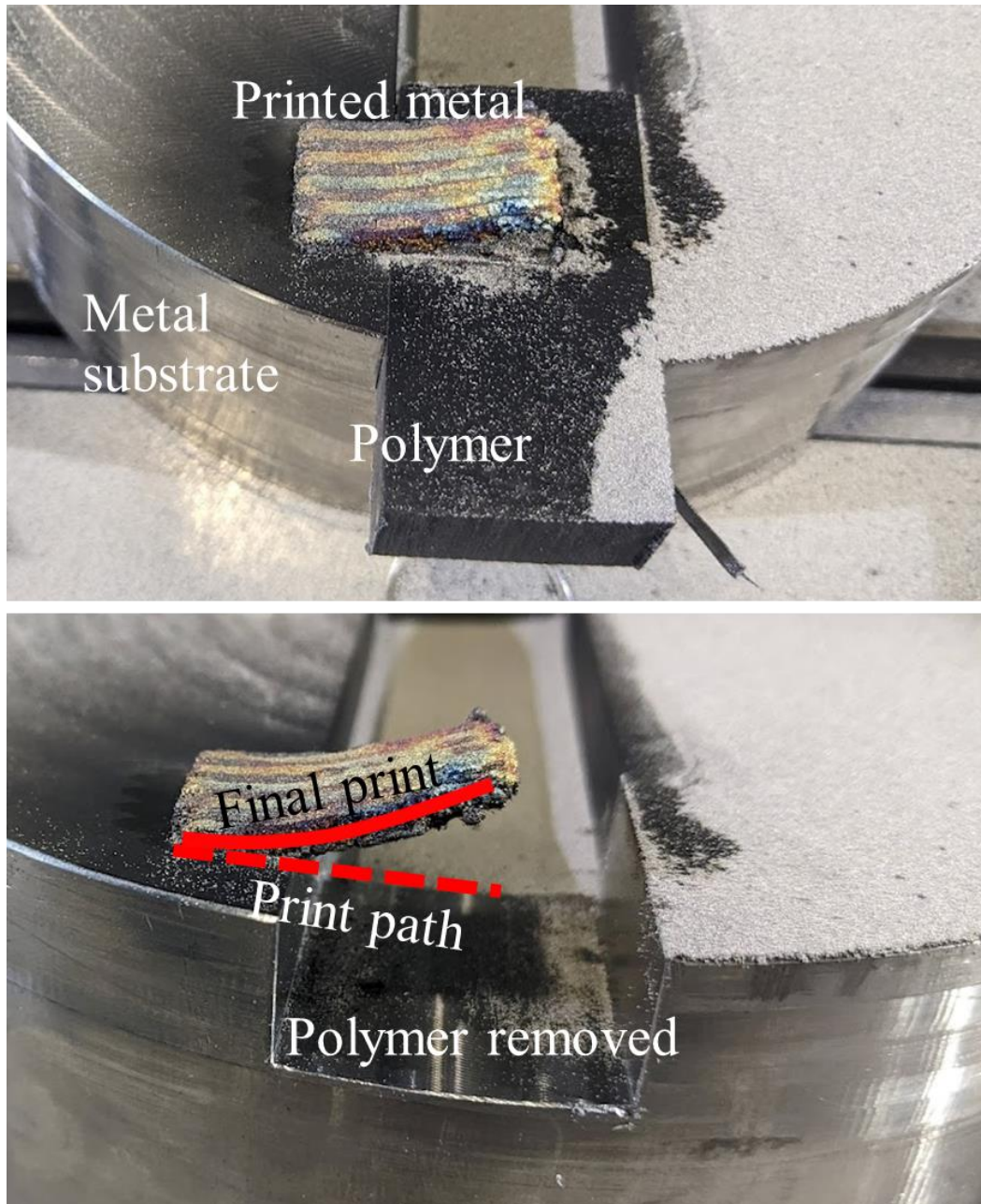


Figure 86: A 316L stainless steel cantilever structure printed on top of a CF ABS support. The cantilever is shown with the support (top) and with the support removed (bottom).

Figure 87 shows a full bridge attempt under an insufficient polymer press-fit condition. In this experiment, a small gap was present between the polymer support and the metal substrate during deposition. This gap resulted in a break in the metal deposition, which caused an incomplete bridge and warping to occur at this break point.

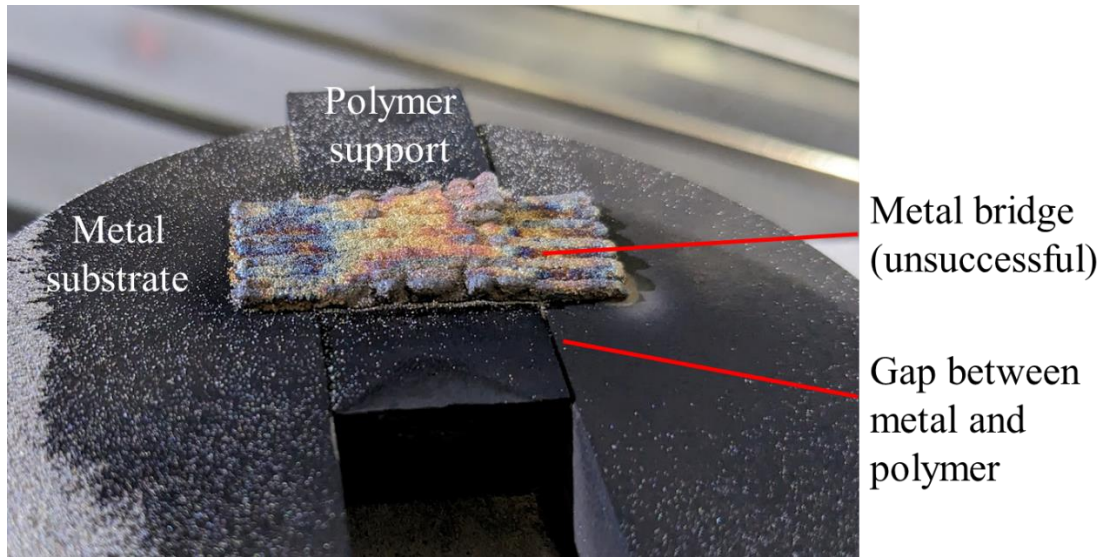


Figure 87: A failed 316L stainless steel bridge structure printed on top of a CF ABS support that was incorrectly press fit into the metal.

Figure 88 shows a bridge print using a fully press-fit polymer support structure. 316L stainless steel was successfully deposited over both a metal substrate and a polymer support to create a bridge. The bridge's rainbow appearance is due to oxidation levels. The surface finish of the bridge component is rough, as is expected with DED components. The individual beads can be observed, indicating that lack of fusion defects are likely. These defects are expected based on the analysis provided in Chapter 5. The bridge component was deposited with an interlayer cooling time of 30 seconds, lowering the overall temperature of the component and decreasing the energy available to fuse beads to each other during the build.

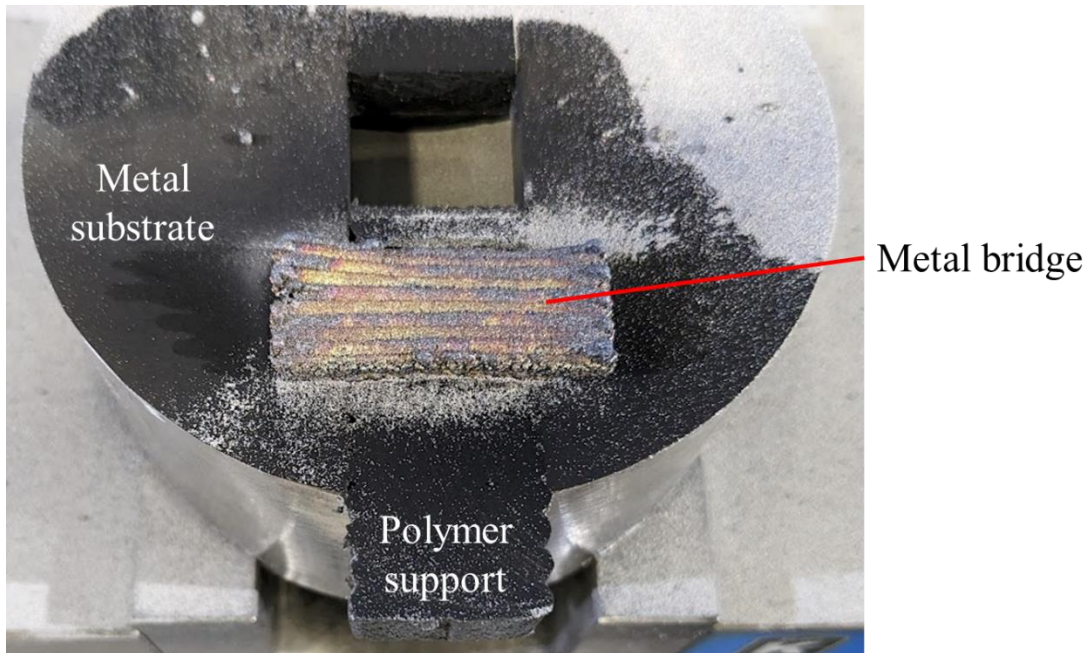


Figure 88: A 316L stainless steel bridge structure printed on top of a CF ABS support.

6.4 Conclusions

Support structures in additive manufacturing are used to hold up elements of the printed component that would otherwise fall during printing due to the design of the component. Support structures in metal AM serve two other critical functions: providing anchoring points and transferring heat away from the component during printing. This research has shown that certain polymers can survive the DED process and hold up a printed component. However, these polymer supports are less capable of heat transfer and cannot provide anchor points for the print. Because of this, polymer support structures are limited in the geometries they can enable: unconstrained geometries like the cantilever cannot be printed accurately, while constrained geometries like the bridge can be successfully printed.

CHAPTER 7. CONCLUSIONS

The objective of this research was to investigate polymers as support structures in the metal DED process by exploring two key research areas: (1) the effect of the metal DED process on a polymer substrate, and (2) the effect of a polymer substrate on the deposited metal DED component.

In the first research area, it was determined that for a polymer to succeed as a support structure, the geometric integrity of the polymer must not be significantly affected during the metal DED process. Additionally, combustion of the polymer should remain under control during deposition to avoid safety concerns. An understanding of polymer combustion, spanning CF ABS, GF ABS, GF nylon, WF PLA, and PLA, due to DED exposure was developed, and a tradeoff between polymer degradation and metal deposition quality was discovered. A low laser power of 100W is required for at least the first few layers to prevent sustained combustion of the polymer substrate. For successful melting and resolidification of metal feedstock powder in DED to occur, the polymer must have a high absorptivity: the polymers that enabled deposition of 316L stainless steel in this research had absorbances greater than 2 absorbance units. Polymers with high temperature fillers, such as glass fibers or carbon fibers, were shown to be effective in mitigating the extreme thermal conditions experienced by the polymer during deposition. Proof of non-detrimental polymer degradation due to DED exposure was established via both experiments and modeling. Single-bead experiments were used to measure polymer degradation, and a series of thermal models was developed to show the influence of DED parameters and polymer material properties on the penetration of heat into the polymer substrate. Higher polymer density, higher polymer thermal capacitance, lower polymer thermal conductivity, lower laser power, and higher laser scan speed were determined to decrease degradation and combustion. Both the experimental measurements and thermal model predictions indicated degradation on the order of 1mm, an acceptable level of degradation based on the precision of the DED system.

In the second research area, it was determined that the composition and properties of the deposited metal must not be significantly altered by the support structure. An

understanding of the effect of a polymer substrate (CF ABS) on the hardness, microstructure, and porosity of a deposited metal (316L stainless steel) was established. Polymer substrates affected the deposited metal via both the migration of carbon from the polymer to the metal and the infiltration of offgassing into the molten metal. It was concluded that gas from polymer degradation was trapped in the molten deposited metal, increasing the porosity due to gas entrapment. Carbon from the polymer migrated into the molten metal, causing carbide formation and increasing the hardness of the deposited metal by approximately 70%. To prevent these effects, a mitigation strategy was developed to prevent these effects by implementing an interlayer cooling time. The interlayer cooling time lowered the overall temperature of the deposited component and decreased the time spent by the component at higher temperatures. The change to the thermal history of the component resulted in less carbon migration from the polymer and moved the component out of the time-temperature regime required for carbide formation. The mitigation strategy was proven to reduce hardness to the expected level for DED 316L stainless steel. Additionally, the introduction of an interlayer cooling time prevented much of the gas due to polymer degradation from infiltrating the metal component, thereby reducing porosity due to gas entrapment from 8% to 4%.

By addressing the challenges of polymer degradation due to DED exposure and metal composition alterations due to polymer exposure, the polymer support structure approach for DED components was validated. The methodology developed allowed for the demonstration of several polymer-supported DED components. A cantilever print indicated the necessity of anchor points of the DED component on the metal substrate to prevent warping, and a failed bridge print indicated that a press-fit polymer support is required to prevent breaks in the metal deposition. These guidelines, along with the appropriate polymer selection, print parameters, and print strategy from the rest of this research, enabled the build of a polymer-supported bridge geometry manufactured with DED.

CHAPTER 8. FUTURE WORK

As polymer support structures in DED had not been explored prior to this work, there are a multitude of opportunities for research expansion. From a materials perspective, investigating other polymers and testing other support materials, such as ceramics, thermosets, or coated polymers would provide insight into the effectiveness of a variety of non-metals as support structures in the DED process. Print planning and toolpath design should also be considered, as the components printed in this research all followed the same toolpath, and printing toolpath is known to affect the thermal history of printed components. Post-processing steps such as machining should also be considered, both with respect to toolpath planning in hybrid manufacturing system and to ensure deposited components can withstand the forces experienced during machining. The effect of deposited metal component size and complexity on the polymer degradation and support effectiveness should also be investigated. The thermal circuit model developed in this research would be useful for closed-loop feedback control of polymer-supported components during deposition. The components printed in this research could also be manufactured in an inert environment to determine the effect of using a shield gas versus a fully inert environment. From a metallurgy perspective, the effect of a wider number of variables, including laser power, laser scan speed, print path, component geometry, metal feedstock material, and substrate material on the microstructure, composition, and mechanical properties of deposited DED component should be investigated. The potential for hydrogen cracking in deposited components due to infiltration of hydrogen gas from polymer degradation into the deposited metal component will also be critical in the long-term success of polymer support structures.

Overall, this research provided insight into the polymer properties and characteristics required for a successful support structure and proved that mitigation of the effects of a polymer substrate on the deposited DED component is possible. The technological readiness of polymer support structures in the metal DED process was moved from an idea to a lab-validated process.

APPENDIX A. FAILED PEEK SUBSTRATE

PEEK was also tested initially as a potential polymer substrate material due to its relatively high degradation temperature. However, the interaction of PEEK with the DED process resulted in expansion of the PEEK directly exposed to the laser, which catastrophically warped the deposited 316L stainless steel, as shown in Figure 89. This failure was deemed to be a risk to the DED print head, and PEEK was not evaluated in subsequent trials.

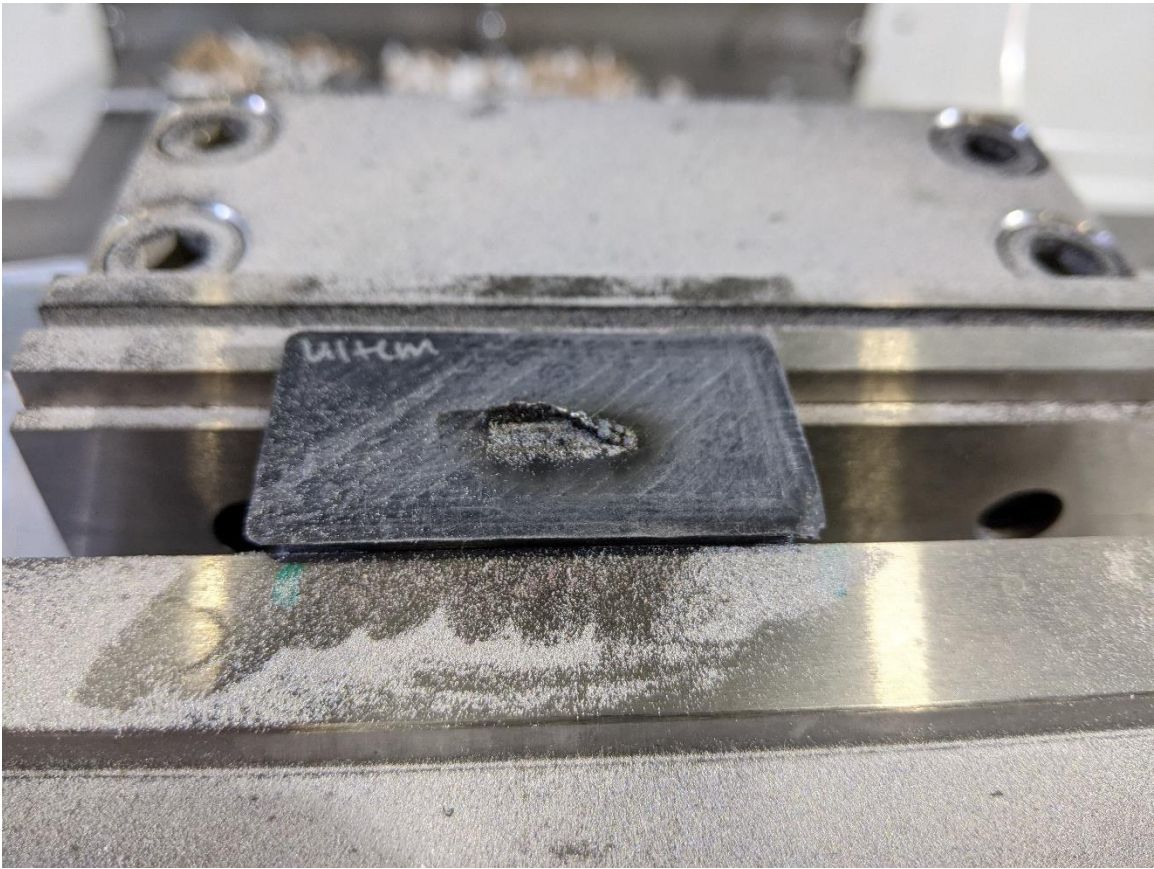


Figure 89: 316L stainless steel deposition attempt on PEEK, which resulted in expansion of the polymer and an unsuccessful build.

APPENDIX B. G-CODE

B.1 Single-layer experiments

B.1.1 400mm/min trials

%

O03048

(For high speed camera setup - will not move in Y after print)

(1/2in bead, single layer)

(scan speed = 400mm/min)

(2021_09_14)

(Using high feed G1 F5000. instead of G0.)

(T0 D=0. CR=0. - ZMIN=0. - water jet)

N10 G90 G94 G17

N15 G21

N20 G53 G0 Z0.

(Feature Construction2)

N25 T22 M6

N30 G54

N35 M11

(N40 G0 A0.)

N45 M10

N50 G0 X0. Y0.

N55 G43 Z11.151 H22

N60 M98 P9102 (UPDATE TO MATCH CURRENT RECIPE)

N65 M110 (MEDIA ON)

N70 G4 P20000 (DWELL TO STABILIZE POWDER FLOW)

N75 G0 Z0.5

N80 G1 Z0. F400.

N85 M120 (START DEPOSITION)

G1 X12.7

N7495 M121 (STOP DEPOSITION)

N7500 G0 Z11.151

N7505 M111 (MEDIA OFF)

N7510 G4 P5000 (DWELL TO PROTECT OPTICS)

N7515 M5

N7520 G53 G0 Z0.

(N7525 X0.)

(N7530 G53 G0 Y0.)

(N7535 G0 A0.)

N7540 M30

%

B.1.2 800mm/min trials

%

O03049

(For high speed camera setup - will not move in Y after print)

(1/2in bead, single layer)

(scan speed = 800mm/min)

(2021_09_14)

(Using high feed G1 F5000. instead of G0.)

(T0 D=0. CR=0. - ZMIN=0. - water jet)

N10 G90 G94 G17

N15 G21

N20 G53 G0 Z0.

(Feature Construction2)

N25 T22 M6

N30 G54

N35 M11

(N40 G0 A0.)
N45 M10
N50 G0 X0. Y0.
N55 G43 Z11.151 H22
N60 M98 P9102 (UPDATE TO MATCH CURRENT RECIPE)
N65 M110 (MEDIA ON)
N70 G4 P20000 (DWELL TO STABILIZE POWDER FLOW)
N75 G0 Z0.5
N80 G1 Z0. F800.
N85 M120 (START DEPOSITION)
G1 X12.7

N7495 M121 (STOP DEPOSITION)

N7500 G0 Z11.151
N7505 M111 (MEDIA OFF)
N7510 G4 P5000 (DWELL TO PROTECT OPTICS)

N7515 M5
N7520 G53 G0 Z0.
(N7525 X0.)
(N7530 G53 G0 Y0.)
(N7535 G0 A0.)
N7540 M30

%

B.2 Metal characterization experiments

B.2.1 No interlayer cooling time

%

O03047

(For high speed camera setup - will not move in Y after print)

(1/2in 5 beads, 5 layers - 0.7mm increments)

(2021_09_14)

(Using high feed G1 F5000. instead of G0.)

(T0 D=0. CR=0. - ZMIN=0. - water jet)

N10 G90 G94 G17

N15 G21

N20 G53 G0 Z0.

(Feature Construction2)

N25 T22 M6

N30 G54

N35 M11

(N40 G0 A0.)

N45 M10

N50 G0 X0. Y0.

N55 G43 Z11.151 H22

N60 M98 P9102 (UPDATE TO MATCH CURRENT RECIPE)

N65 M110 (MEDIA ON)

N70 G4 P20000 (DWELL TO STABILIZE POWDER FLOW)

N75 G0 Z0.5

N80 G1 Z0. F600.

N85 M120 (START DEPOSITION)

G1 X12.7 Y0.

X12.7 Y1.5

X0. Y1.5

X0. Y3.

X12.7 Y3.

X12.7 Y4.5

X0. Y4.5

X0. Y6.

X12.7 Y6.

N7495 M121 (STOP DEPOSITION)

N75 G0 Z1.4

N80 G1 Z0.7 F600.

G1 X0 Y0

N85 M120 (START DEPOSITION)

G1 X12.7 Y0.

X12.7 Y1.5

X0. Y1.5

X0. Y3.

X12.7 Y3.

X12.7 Y4.5

X0. Y4.5

X0. Y6.

X12.7 Y6.

N7495 M121 (STOP DEPOSITION)

N75 G0 Z2.1

N80 G1 Z1.4 F600.

G1 X0 Y0

N85 M120 (START DEPOSITION)

G1 X12.7 Y0.

X12.7 Y1.5

X0. Y1.5

X0. Y3.

X12.7 Y3.

X12.7 Y4.5

X0. Y4.5

X0. Y6.

X12.7 Y6.
N7495 M121 (STOP DEPOSITION)

N75 G0 Z2.8
N80 G1 Z2.1 F600.
G1 X0 Y0
N85 M120 (START DEPOSITION)
G1 X12.7 Y0.
X12.7 Y1.5
X0. Y1.5
X0. Y3.
X12.7 Y3.
X12.7 Y4.5
X0. Y4.5
X0. Y6.
X12.7 Y6.
N7495 M121 (STOP DEPOSITION)

N75 G0 Z3.5
N80 G1 Z2.8 F600.
G1 X0 Y0
N85 M120 (START DEPOSITION)
G1 X12.7 Y0.
X12.7 Y1.5
X0. Y1.5
X0. Y3.
X12.7 Y3.
X12.7 Y4.5
X0. Y4.5
X0. Y6.
X12.7 Y6.

N7495 M121 (STOP DEPOSITION)

N7500 G0 Z11.151

N7505 M111 (MEDIA OFF)

N7510 G4 P5000 (DWELL TO PROTECT OPTICS)

N7515 M5

N7520 G53 G0 Z0.

(N7525 X0.)

(N7530 G53 G0 Y0.)

(N7535 G0 A0.)

N7540 M30

%

B.2.2 10 second interlayer cooling time

%

O03051

(1/2in 5 beads, 5 layers - 0.7mm increments, 1s between layers)

(will not move in Y after print)

(2021_09_28)

(Using high feed G1 F5000. instead of G0.)

(T0 D=0. CR=0. - ZMIN=0. - water jet)

N10 G90 G94 G17

N15 G21

N20 G53 G0 Z0.

(Feature Construction2)

N25 T22 M6

N30 G54

N35 M11

(N40 G0 A0.)
N45 M10
N50 G0 X0. Y0.
N55 G43 Z11.151 H22
N60 M98 P9102 (UPDATE TO MATCH CURRENT RECIPE)
N65 M110 (MEDIA ON)
N70 G4 P20000 (DWELL TO STABILIZE POWDER FLOW)
N75 G0 Z0.5
N80 G1 Z0. F600.
N85 M120 (START DEPOSITION)
G1 X12.7 Y0.
X12.7 Y1.5
X0. Y1.5
X0. Y3.
X12.7 Y3.
X12.7 Y4.5
X0. Y4.5
X0. Y6.
X12.7 Y6.

N7495 M121 (STOP DEPOSITION)

G4 P10000

N75 G0 Z1.4
N80 G1 Z0.7 F600.
G1 X0 Y0
N85 M120 (START DEPOSITION)
G1 X12.7 Y0.
X12.7 Y1.5
X0. Y1.5

X0. Y3.
X12.7 Y3.
X12.7 Y4.5
X0. Y4.5
X0. Y6.
X12.7 Y6.
N7495 M121 (STOP DEPOSITION)

G4 P10000

N75 G0 Z2.1
N80 G1 Z1.4 F600.
G1 X0 Y0
N85 M120 (START DEPOSITION)
G1 X12.7 Y0.
X12.7 Y1.5
X0. Y1.5
X0. Y3.
X12.7 Y3.
X12.7 Y4.5
X0. Y4.5
X0. Y6.
X12.7 Y6.
N7495 M121 (STOP DEPOSITION)

G4 P10000

N75 G0 Z2.8
N80 G1 Z2.1 F600.
G1 X0 Y0
N85 M120 (START DEPOSITION)

G1 X12.7 Y0.
X12.7 Y1.5
X0. Y1.5
X0. Y3.
X12.7 Y3.
X12.7 Y4.5
X0. Y4.5
X0. Y6.
X12.7 Y6.
N7495 M121 (STOP DEPOSITION)

G4 P10000

N75 G0 Z3.5
N80 G1 Z2.8 F600.
G1 X0 Y0
N85 M120 (START DEPOSITION)
G1 X12.7 Y0.
X12.7 Y1.5
X0. Y1.5
X0. Y3.
X12.7 Y3.
X12.7 Y4.5
X0. Y4.5
X0. Y6.
X12.7 Y6.
N7495 M121 (STOP DEPOSITION)

N7500 G0 Z11.151
N7505 M111 (MEDIA OFF)
N7510 G4 P5000 (DWELL TO PROTECT OPTICS)

N7515 M5

N7520 G53 G0 Z0.

(N7525 X0.)

(N7530 G53 G0 Y0.)

(N7535 G0 A0.)

N7540 M30

%

B.2.3 30 second interlayer cooling time

%

O03050

(1/2in 5 beads, 5 layers - 0.7mm increments, 30s between layers)

(will not move in Y after print)

(2021_09_28)

(Using high feed G1 F5000. instead of G0.)

(T0 D=0. CR=0. - ZMIN=0. - water jet)

N10 G90 G94 G17

N15 G21

N20 G53 G0 Z0.

(Feature Construction2)

N25 T22 M6

N30 G54

N35 M11

(N40 G0 A0.)

N45 M10

N50 G0 X0. Y0.

N55 G43 Z11.151 H22

N60 M98 P9102 (UPDATE TO MATCH CURRENT RECIPE)

N65 M110 (MEDIA ON)

N70 G4 P20000 (DWELL TO STABILIZE POWDER FLOW)

N75 G0 Z0.5

N80 G1 Z0. F600.

N85 M120 (START DEPOSITION)

G1 X12.7 Y0.

X12.7 Y1.5

X0. Y1.5

X0. Y3.

X12.7 Y3.

X12.7 Y4.5

X0. Y4.5

X0. Y6.

X12.7 Y6.

N7495 M121 (STOP DEPOSITION)

G4 P30000

N75 G0 Z1.4

N80 G1 Z0.7 F600.

G1 X0 Y0

N85 M120 (START DEPOSITION)

G1 X12.7 Y0.

X12.7 Y1.5

X0. Y1.5

X0. Y3.

X12.7 Y3.

X12.7 Y4.5

X0. Y4.5

X0. Y6.

X12.7 Y6.

N7495 M121 (STOP DEPOSITION)

G4 P30000

N75 G0 Z2.1

N80 G1 Z1.4 F600.

G1 X0 Y0

N85 M120 (START DEPOSITION)

G1 X12.7 Y0.

X12.7 Y1.5

X0. Y1.5

X0. Y3.

X12.7 Y3.

X12.7 Y4.5

X0. Y4.5

X0. Y6.

X12.7 Y6.

N7495 M121 (STOP DEPOSITION)

G4 P30000

N75 G0 Z2.8

N80 G1 Z2.1 F600.

G1 X0 Y0

N85 M120 (START DEPOSITION)

G1 X12.7 Y0.

X12.7 Y1.5

X0. Y1.5

X0. Y3.

X12.7 Y3.

X12.7 Y4.5
X0. Y4.5
X0. Y6.
X12.7 Y6.
N7495 M121 (STOP DEPOSITION)

G4 P30000

N75 G0 Z3.5
N80 G1 Z2.8 F600.
G1 X0 Y0
N85 M120 (START DEPOSITION)
G1 X12.7 Y0.
X12.7 Y1.5
X0. Y1.5
X0. Y3.
X12.7 Y3.
X12.7 Y4.5
X0. Y4.5
X0. Y6.
X12.7 Y6.
N7495 M121 (STOP DEPOSITION)

N7500 G0 Z11.151
N7505 M111 (MEDIA OFF)
N7510 G4 P5000 (DWELL TO PROTECT OPTICS)

N7515 M5
N7520 G53 G0 Z0.
(N7525 X0.)
(N7530 G53 G0 Y0.)

(N7535 G0 A0.)

N7540 M30

%

APPENDIX C. SINGLE BEAD TEST IMAGES

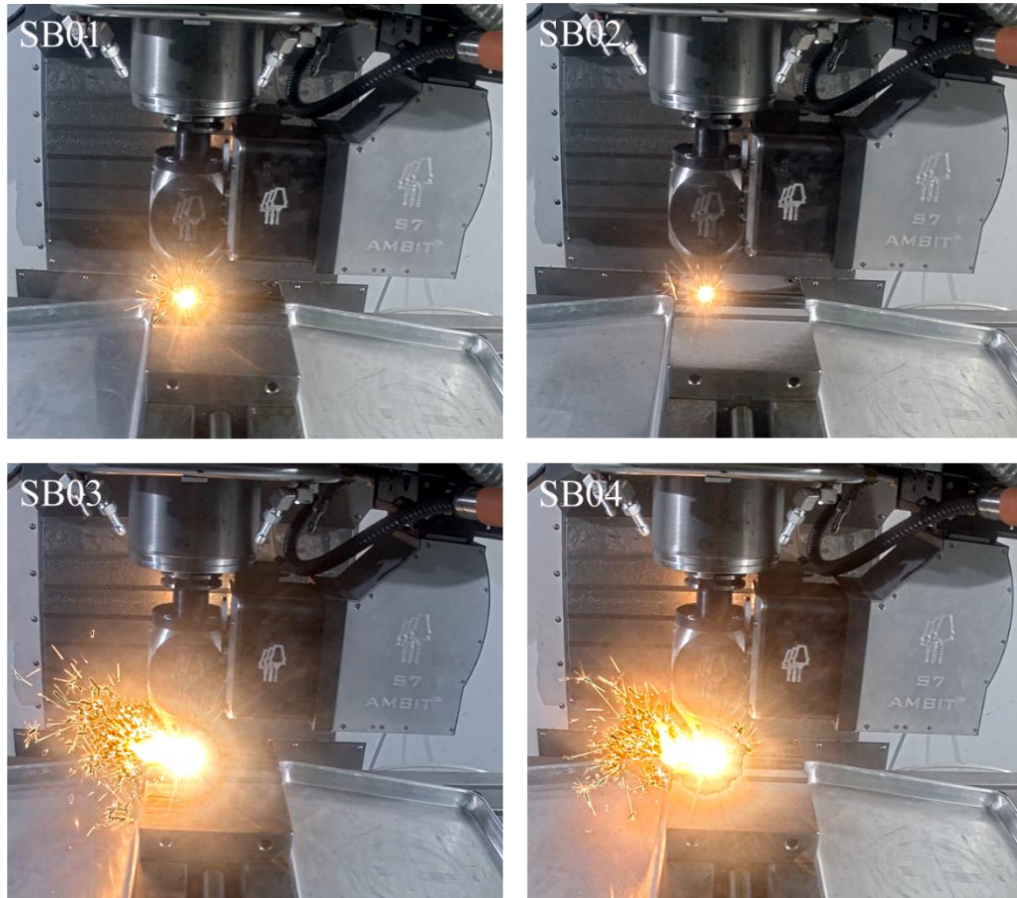


Figure 90: In-process stills for CF ABS single-bead experiments.

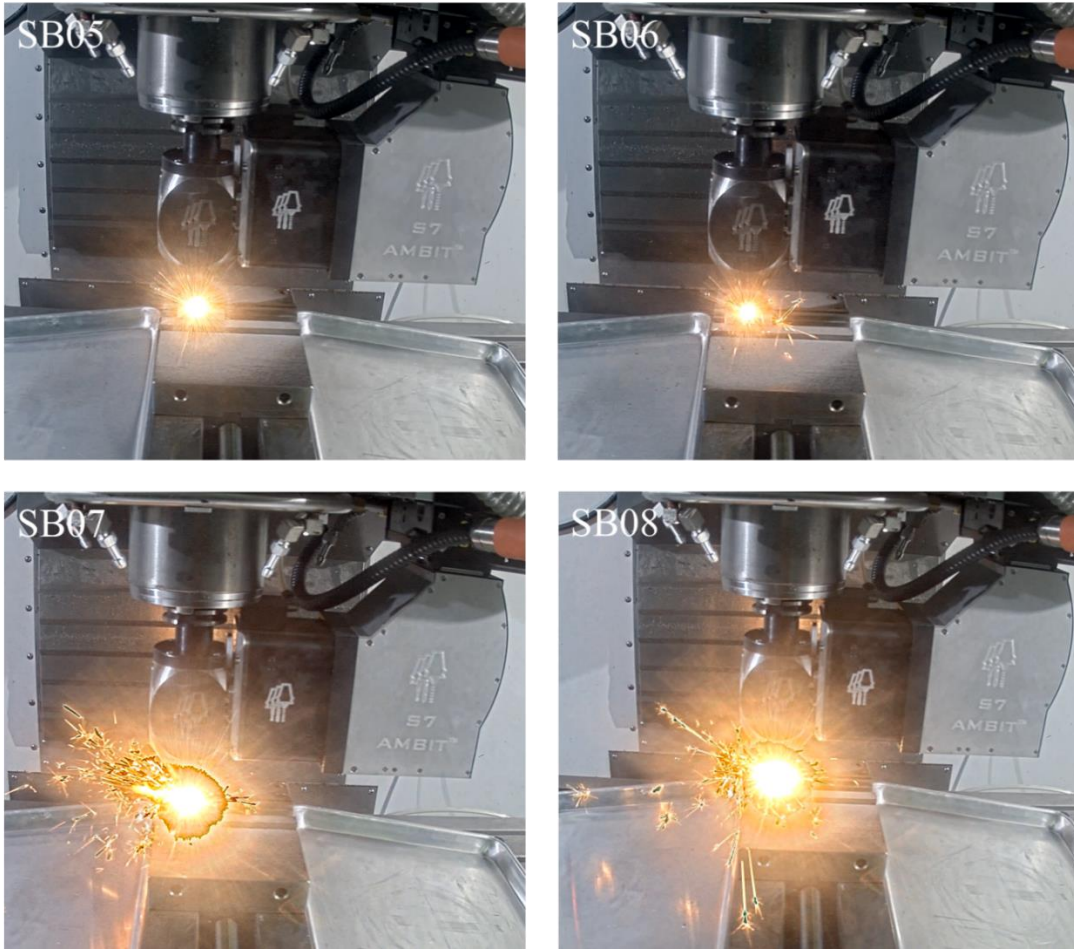


Figure 91: In-process stills for GF ABS single-bead experiments.

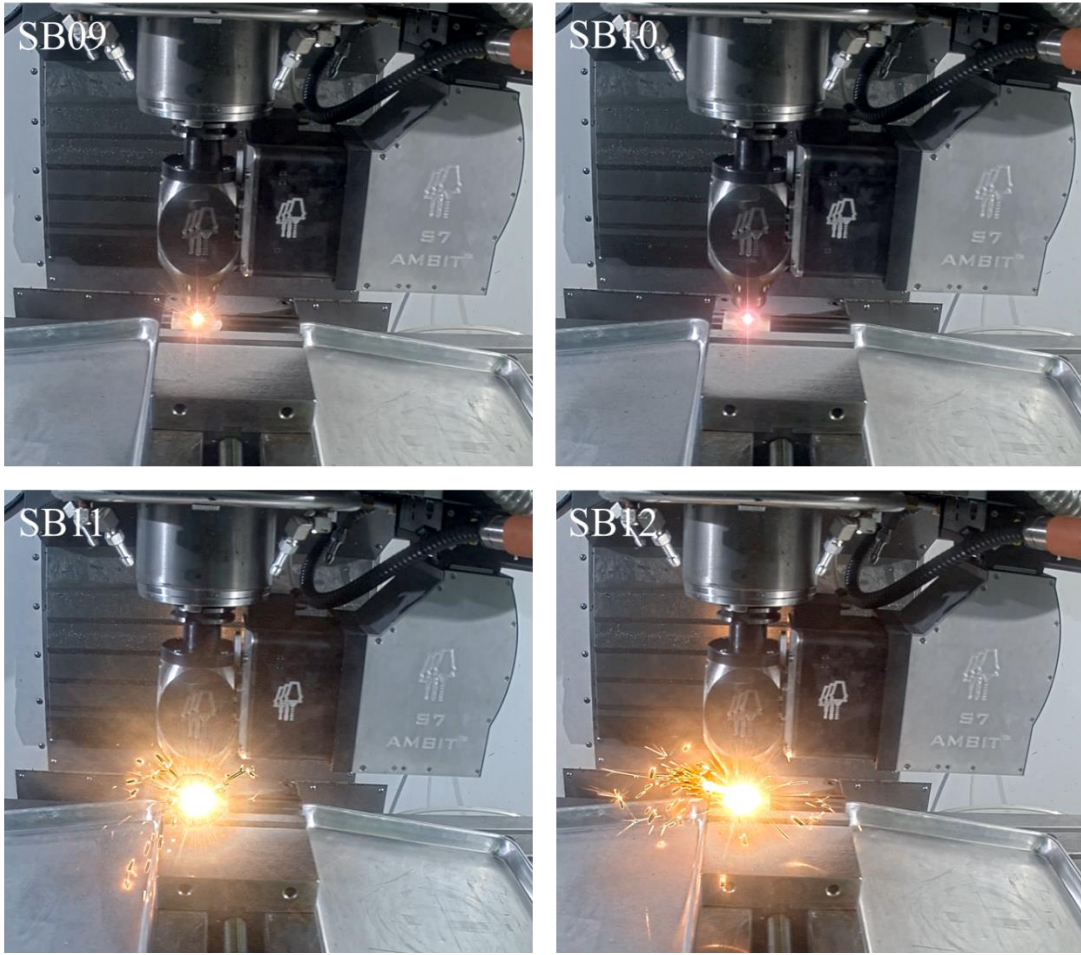


Figure 92: In-process stills for GF nylon single-bead experiments.

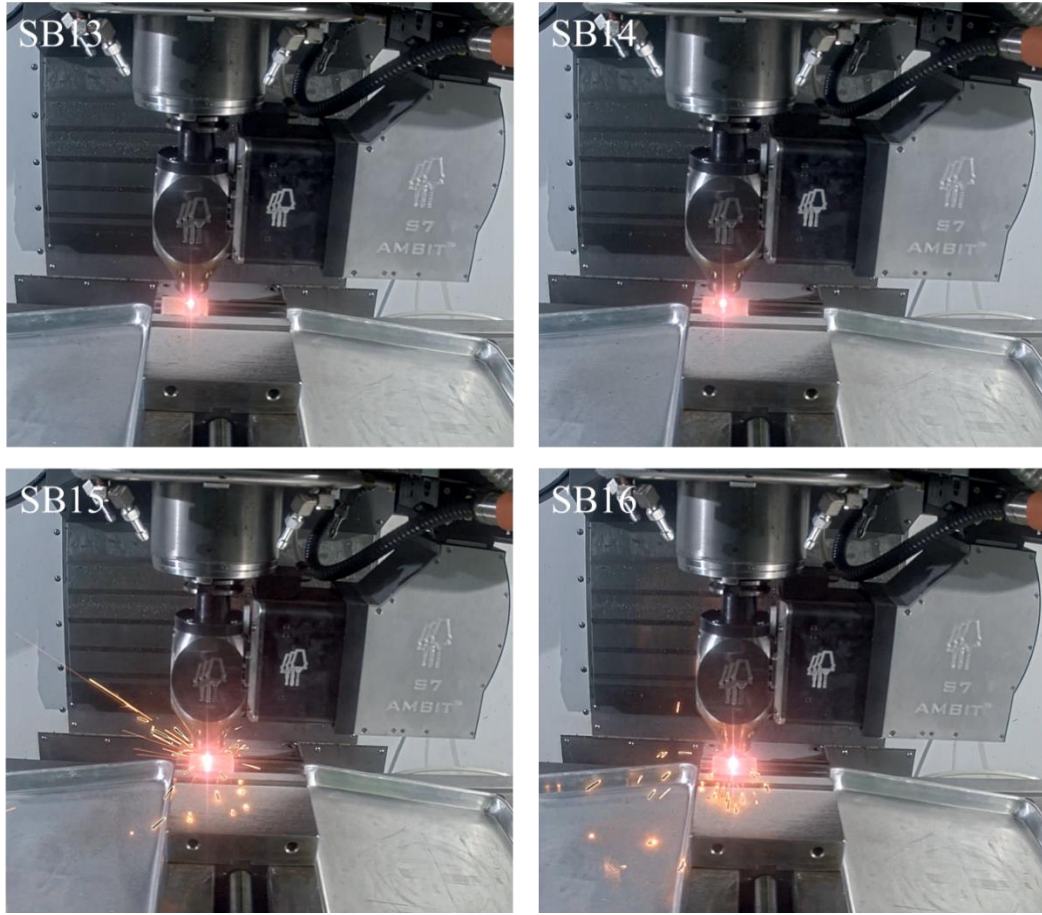


Figure 93: In-process stills for PLA single-bead experiments.

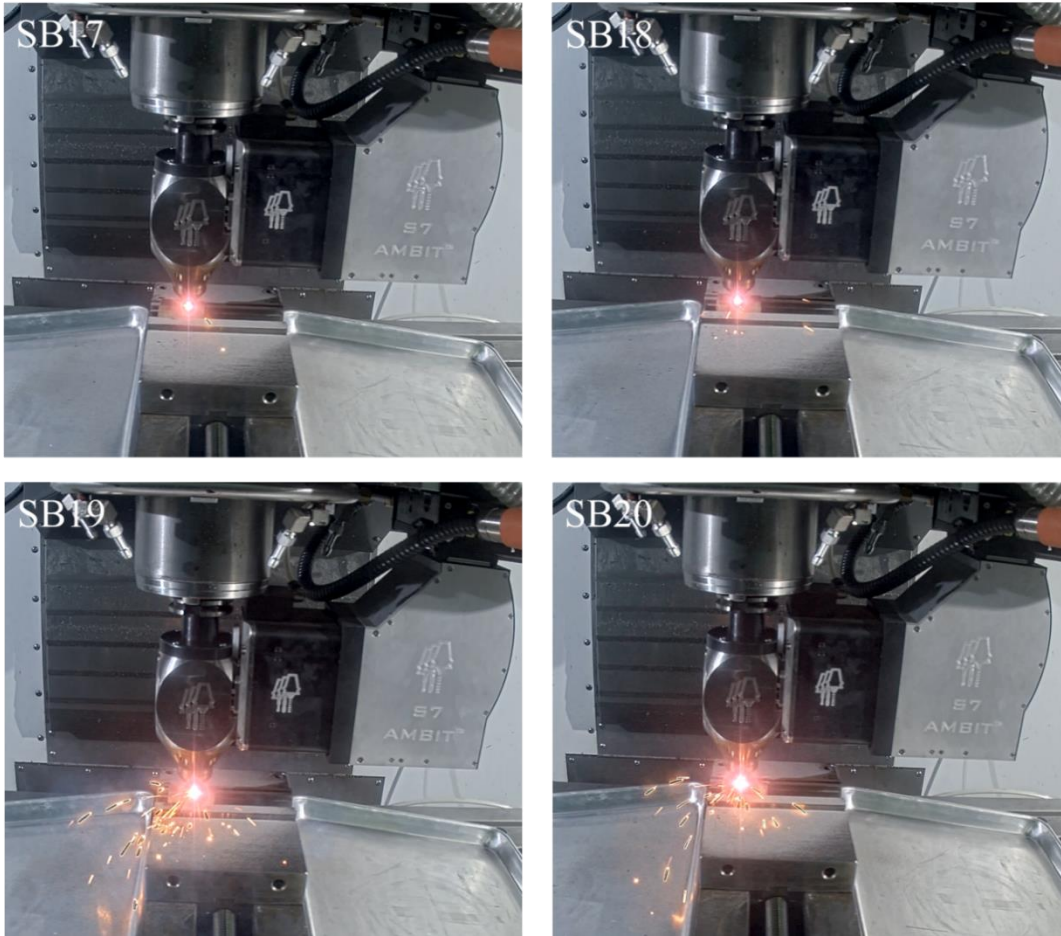


Figure 94: In-process stills for WF PLA single-bead experiments.

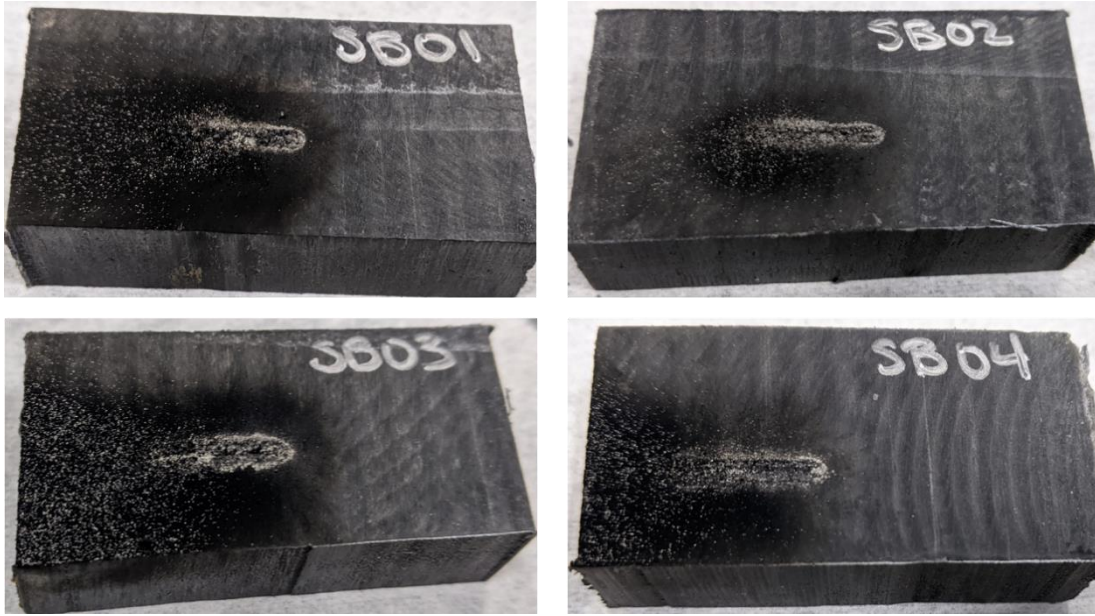


Figure 95: Post-print substrates for CF ABS single-bead experiments.

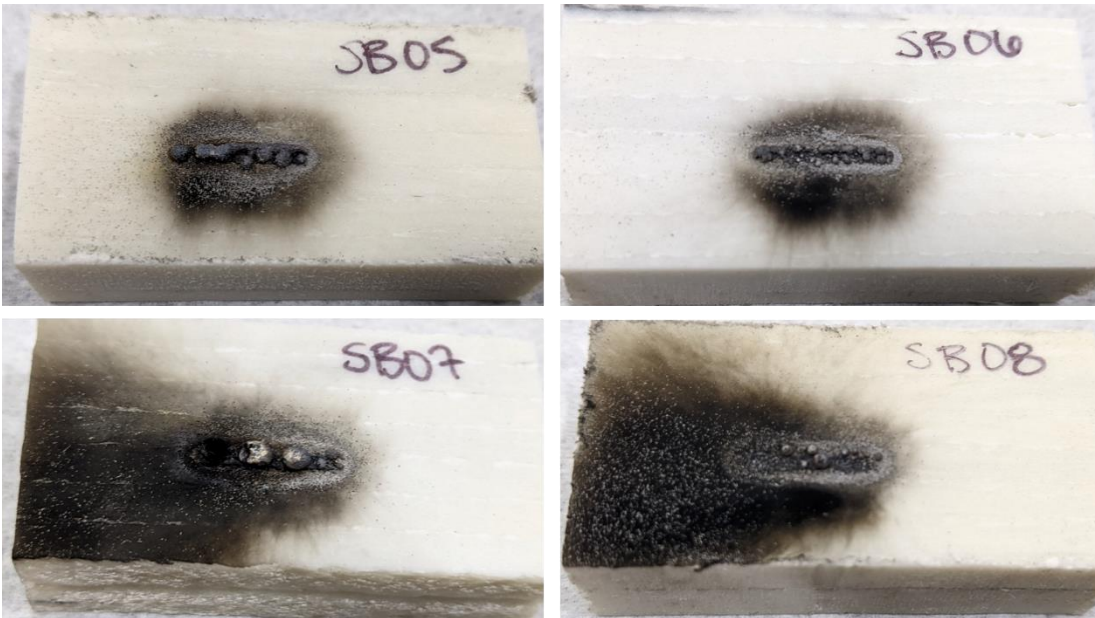


Figure 96: Post-print substrates for GF ABS single-bead experiments.

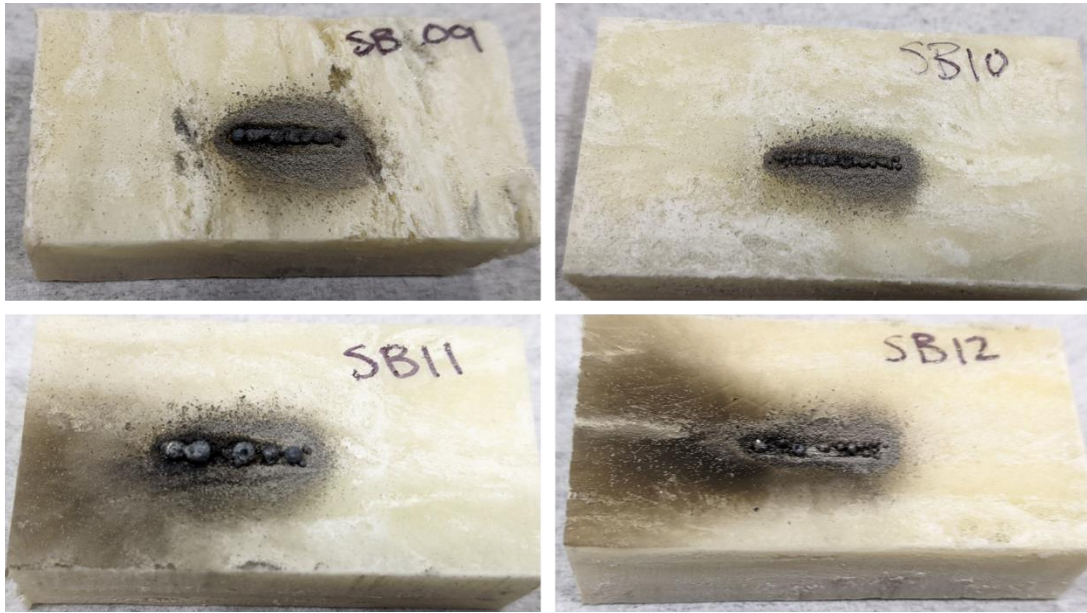


Figure 97: Post-print substrates for GF nylon single-bead experiments.

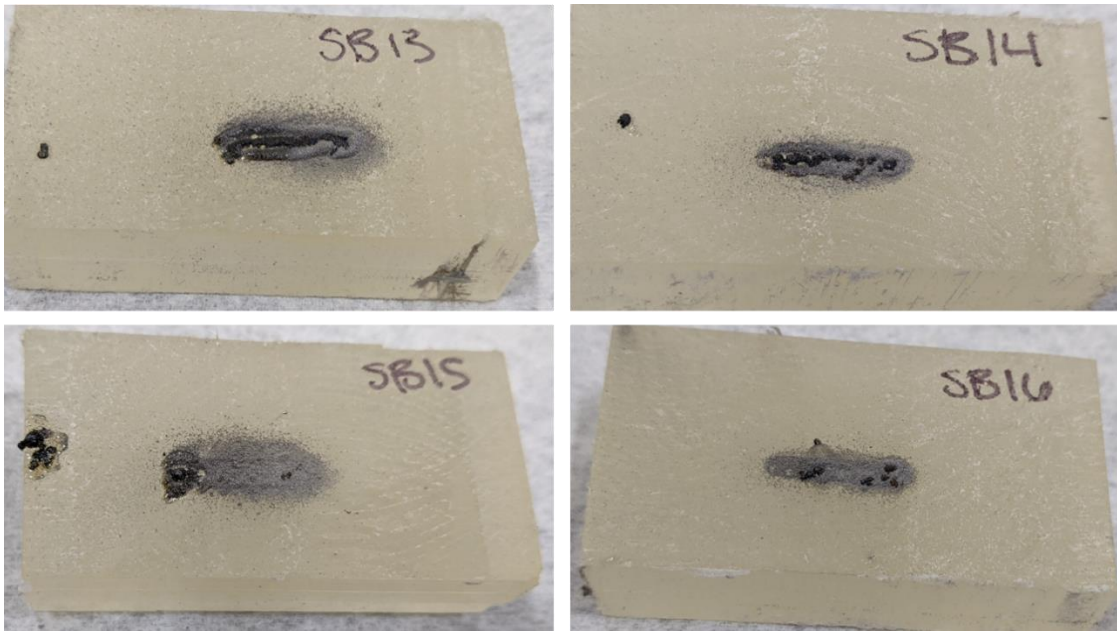


Figure 98: Post-print substrates for PLA single-bead experiments.



Figure 99: Post-print substrates for WF PLA single-bead experiments.

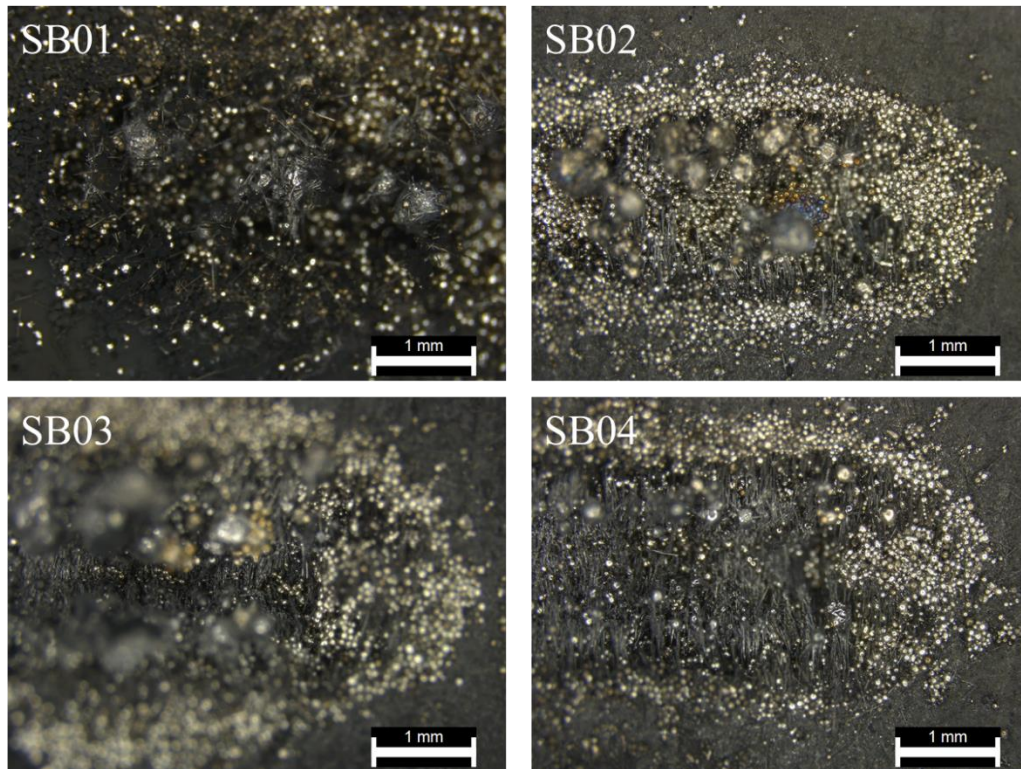


Figure 100: Top-down microscopic images for CF ABS single-bead experiments.

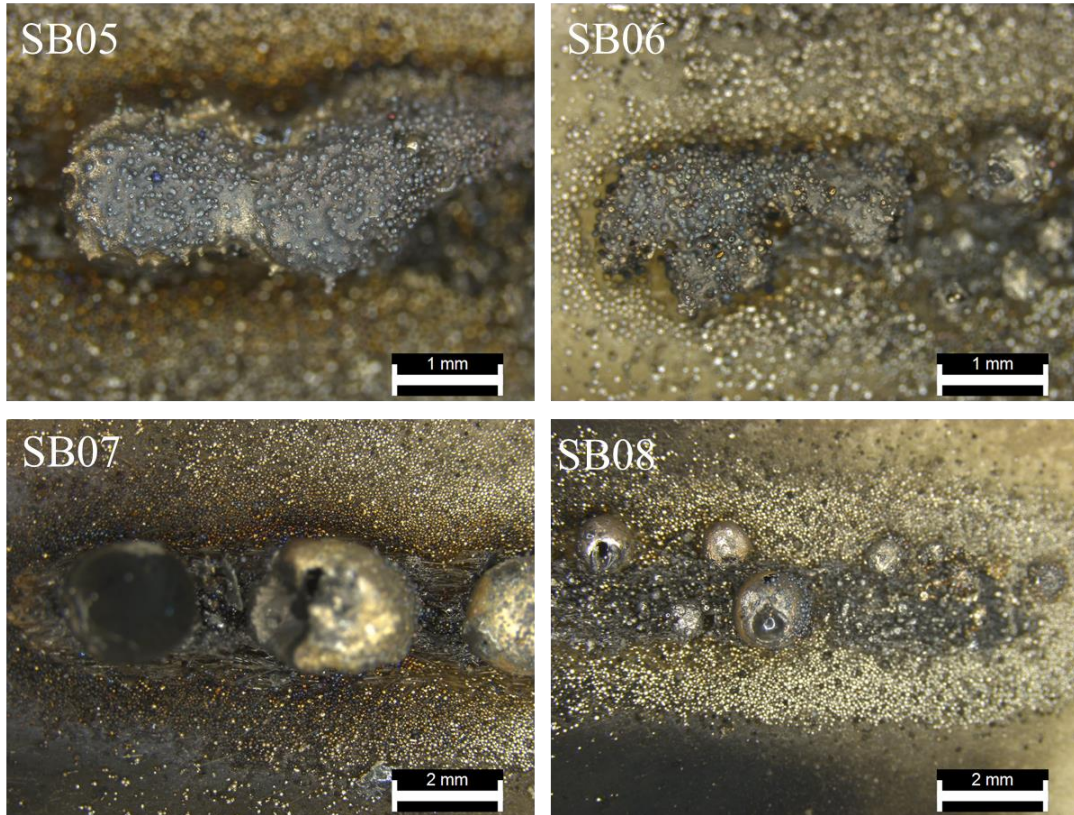


Figure 101: Top-down microscopic images for GF ABS single-bead experiments.

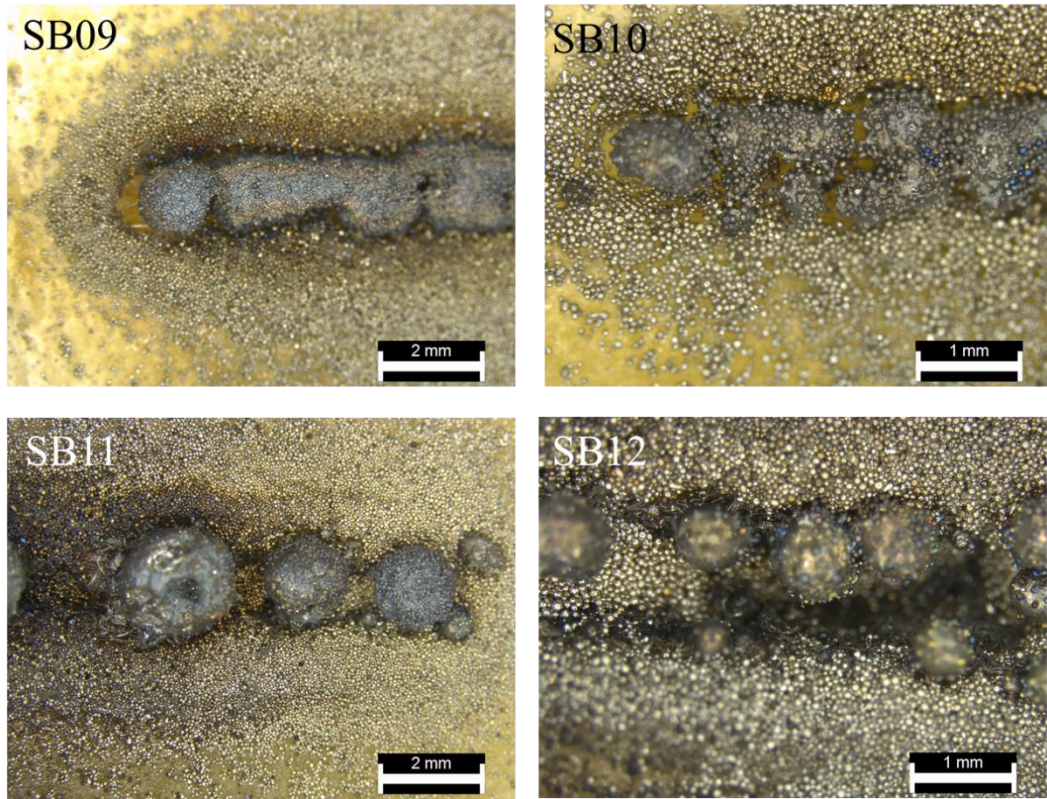


Figure 102: Top-down microscopic images for GF nylon single-bead experiments.

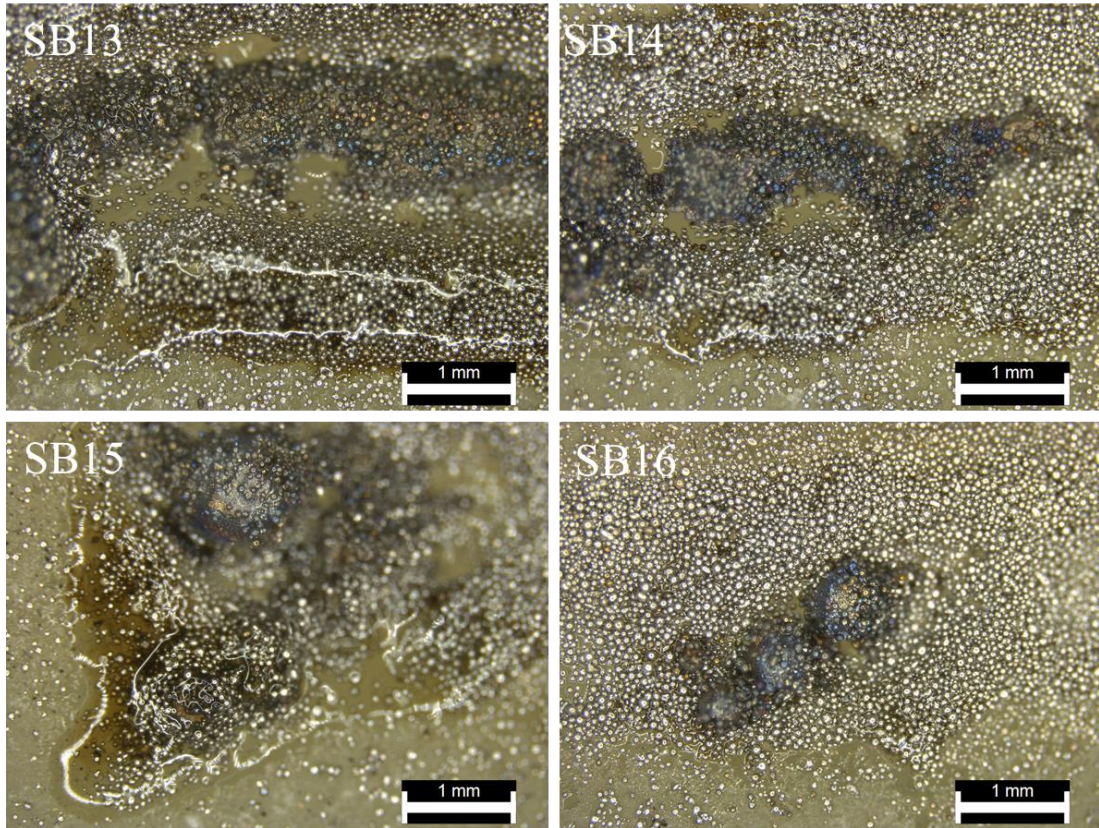


Figure 103: Top-down microscopic images for PLA single-bead experiments.

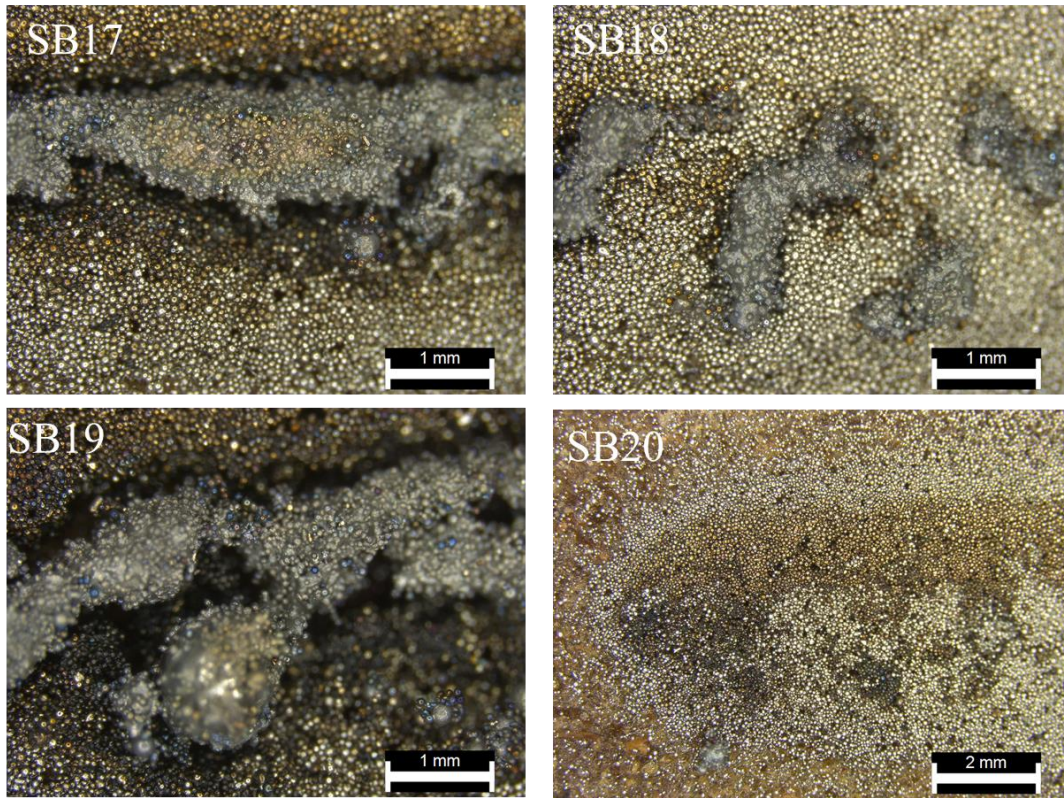


Figure 104: Top-down microscopic images for PLA single-bead experiments.

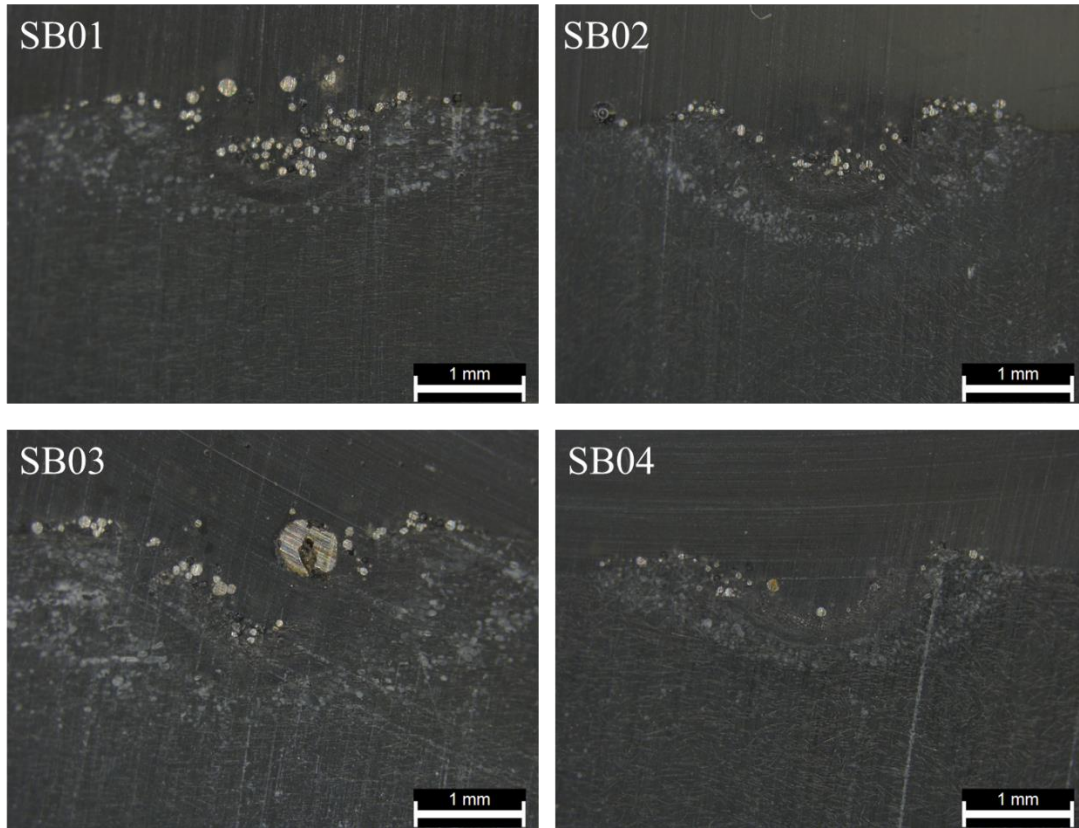


Figure 105: Cross-sectional microscopic images for CF ABS single-bead experiments.

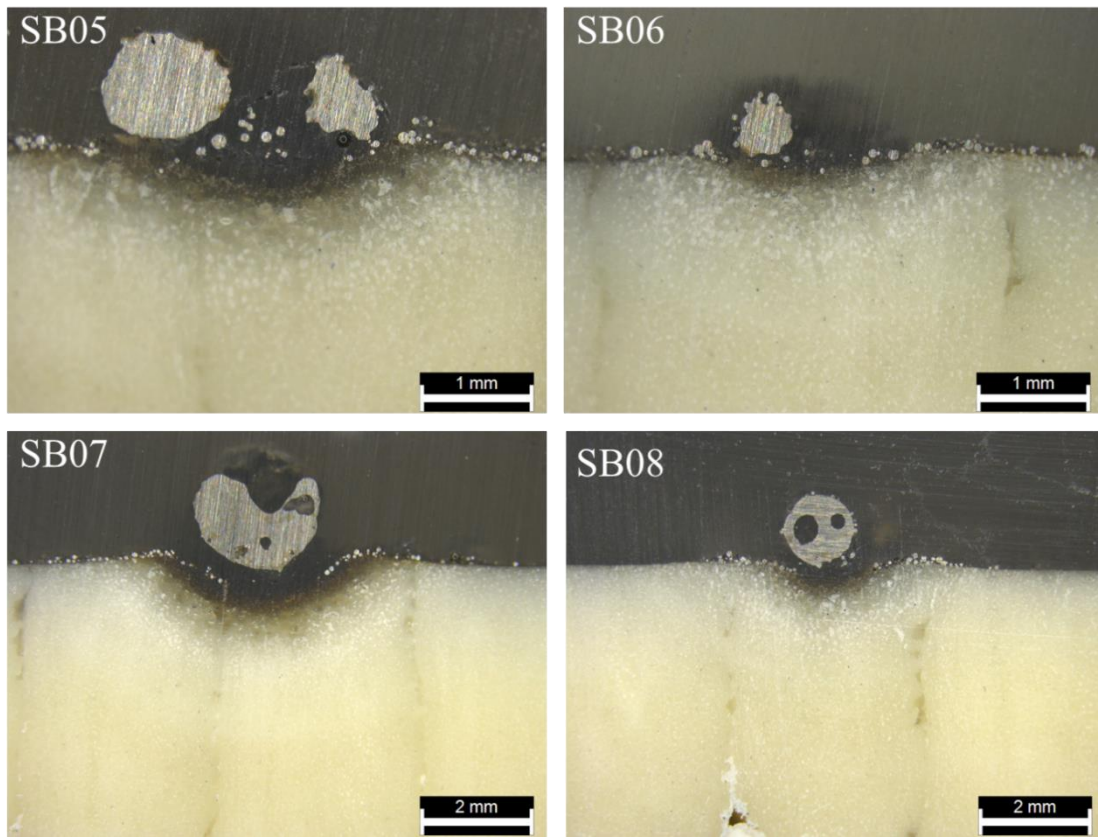


Figure 106: Cross-sectional microscopic images for GF ABS single-bead experiments.

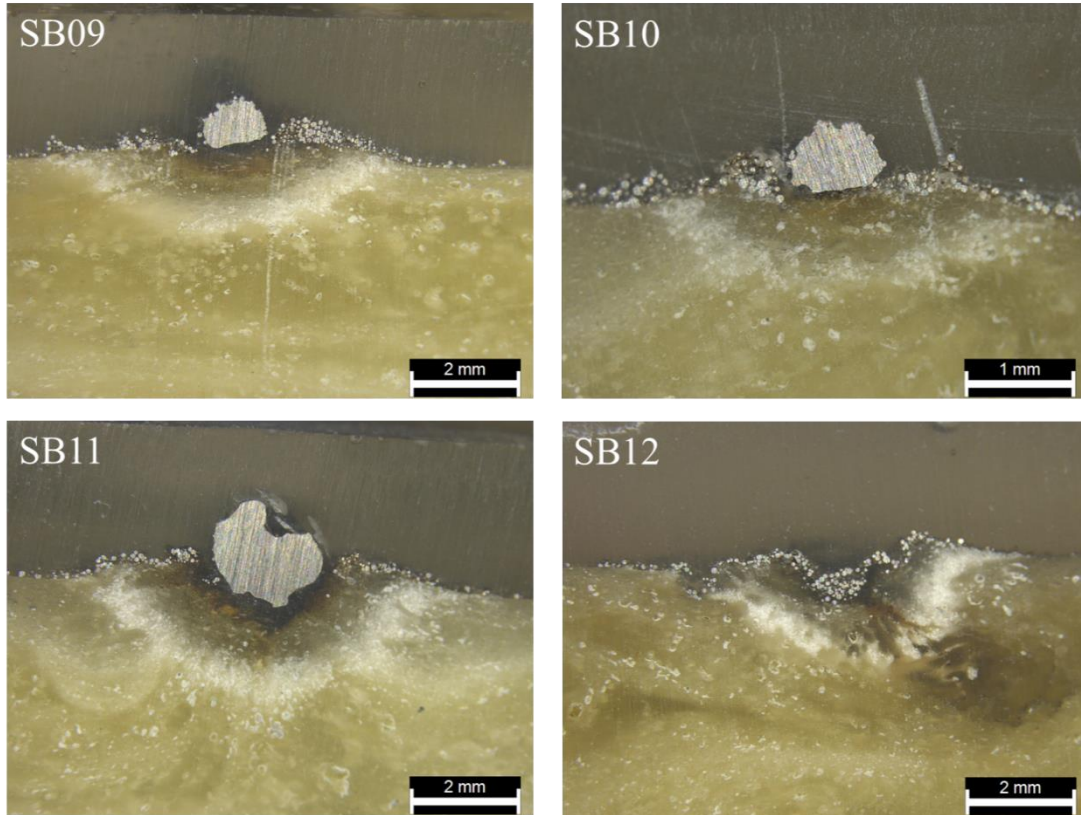


Figure 107: Cross-sectional microscopic images for GF nylon single-bead experiments.

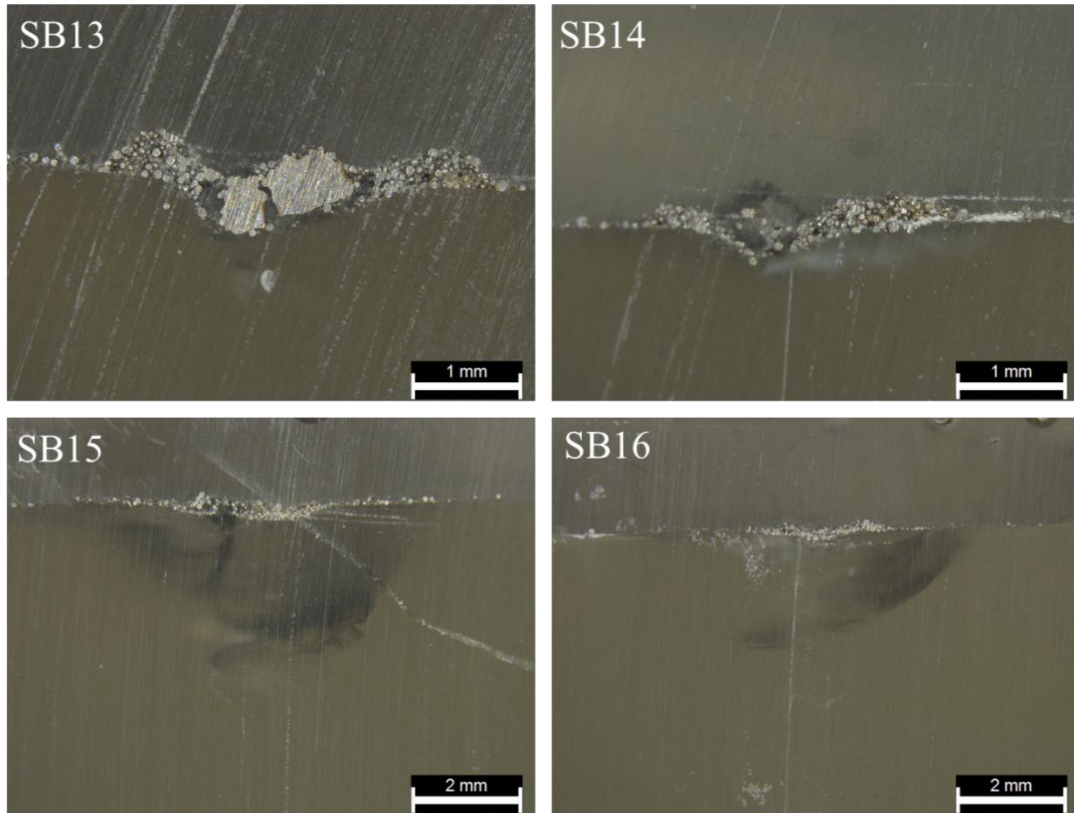


Figure 108: Cross-sectional microscopic images for PLA single-bead experiments.

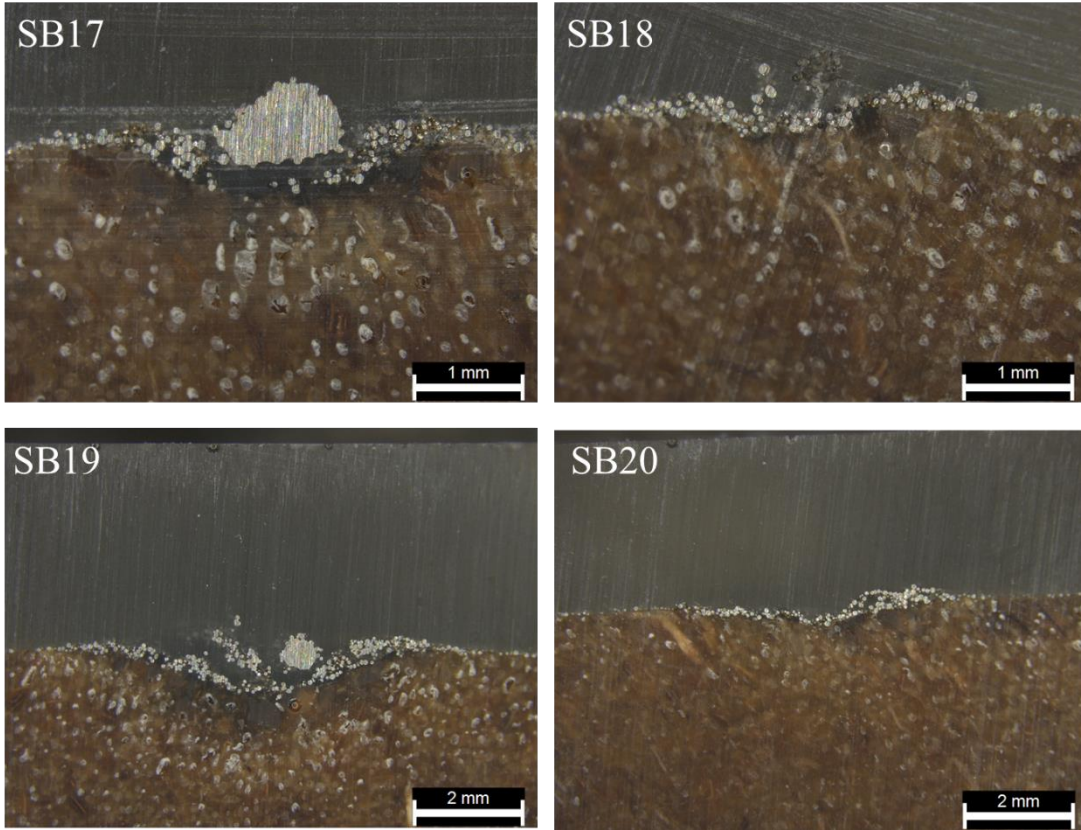


Figure 109: Cross-sectional microscopic images for WF PLA single-bead experiments.




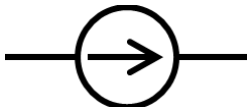
APPENDIX D. THERMAL CIRCUIT MODELING

Thermal circuit modeling provides a basic model enabling multi-layer recursion and providing a state space representation of the system.

D.1 Background

Thermal circuit models, in which electrical circuits equivalents are used as an analogy for heat transfer, are employed in steady-state, one-dimensional conduction scenarios. Conduction heat transfer has an electrical analogy, where electric current is analogous to heat flow, electric voltage is analogous to temperature, and electric resistance is analogous to thermal resistance. The circuit components used in thermal circuit modeling, along with their symbols, the values they represent, and the units of those values, are shown in Table 10 [141, 142]. A resistor indicates thermal resistance, representing the heat flow impedance of the material. A capacitor indicates thermal capacitance, which indicates the internal energy storage of the material. A voltage source indicates a source of fixed temperature, and a current source indicates a heat source.

Table 10. Thermal circuit components [141, 142].

Component	Symbol	Representative value	Units
Resistor		Thermal resistance	°C/W
Capacitor		Thermal capacitance	J/°C
Voltage source		Temperature source	°C
Current source		Heat source	W

Using these elements, thermal circuits representing conduction heat transfer scenarios, such as the one shown in Figure 126, can be drawn. The temperature at various points in the scenario can then be solved using standard equations that describe relationships in circuits, such as Kirchoff's current law, Kirchoff's voltage law, and Ohm's law [142].

D.2 Thermal circuit implementation

D.2.1 Single layer metal deposition model

To predict the temperatures of both the metal and polymer in response to deposition of metal on a polymer substrate, a metal bead is assumed to be instantaneously deposited on a polymer substrate as shown in Figure 110.

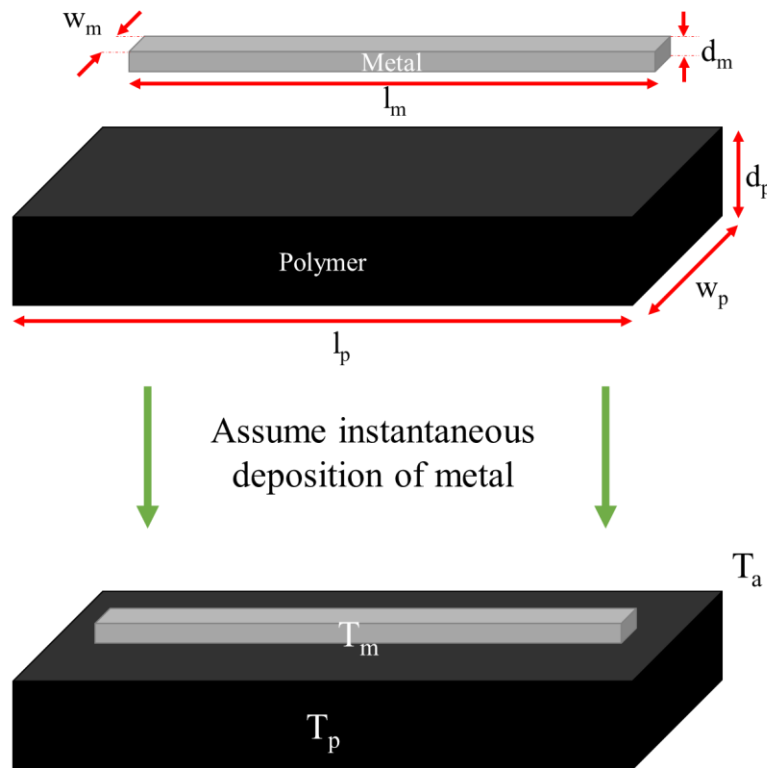


Figure 110: Geometry assumptions used to predict metal temperature T_m and polymer temperature T_p in response to deposition of metal on a polymer substrate.

This scenario can be modeled with a thermal circuit, where the heat flow is analogous to the flow of current and voltages are analogous to temperatures. Thermal capacitances of the polymer and the metal are represented by capacitors and the conduction within materials and convection at the surfaces of materials are represented by resistors. As shown in Figure 111, the thermal capacitances of the polymer and metal are represented by C_p and C_m , respectively. Conduction within the polymer and within the metal is represented by $R_{p,cond}$ and $R_{m,cond}$, respectively. Convection at the surface of the polymer and at the surface of the metal is represented by $R_{p,conv}$ and $R_{m,conv}$, respectively. Conduction through the metal to the interface between the polymer and the metal is given by $R_{cond,mp}$, and

conduction through the polymer to the interface between the polymer and the metal is given by $R_{\text{cond,pm}}$. The ambient temperature, temperature of the metal, and temperature of the polymer were represented by T_a , T_m , and T_p , respectively. The values of the thermal resistivities and capacitances are dependent on the material properties and geometric parameters listed in Table 11.

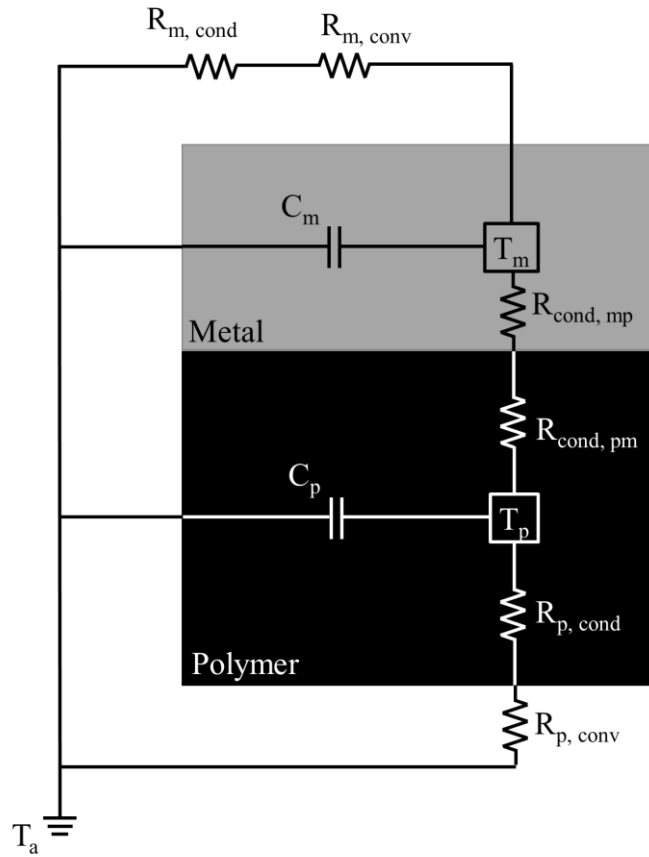


Figure 111: Thermal circuit diagram for a single bead of metal deposited on a polymer substrate.

Table 11. Properties and parameters used to define thermal resistivity and capacitance.

Variable	Polymer Type
h_{air}	Thermal coefficient of air [$\text{W}/\text{m}^2\text{K}$]
l_m	Length of metal bead [m]
w_m	Width of metal bead [m]
d_m	Height of metal bead [m]

l_p	Length of polymer substrate [m]
w_p	Width of polymer substrate [m]
d_p	Height of polymer substrate [m]
ρ_m	Density of metal [kg/m ³]
ρ_p	Density of polymer [kg/m ³]
$c_{p,m}$	Specific heat capacity of metal [J/kgK]
$c_{p,p}$	Specific heat capacity of polymer [J/kgK]
k_m	Thermal conductivity of metal [W/mK]
k_p	Thermal conductivity of polymer [W/mK]

The thermal capacitances of the metal and polymer are defined as

$$C_m = l_m w_m d_m \rho_m c_{p,m} \quad (D.1)$$

$$C_p = l_p w_p d_p \rho_p c_{p,p} \quad (D.2)$$

The thermal resistivities due to convection of the metal and the polymer in ambient temperature are given by

$$R_{m,conv} = \frac{1}{h_{air} l_m w_m} \quad (D.3)$$

$$R_{p,conv} = \frac{1}{h_{air} l_p w_p} \quad (D.4)$$

The thermal resistivities due to conduction of heat through the metal to the surface of the metal and through the polymer to the surface of the polymer are defined as

$$R_{m,cond} = \frac{d_m}{2k_m l_m w_m} \quad (D.5)$$

$$R_{p,cond} = \frac{d_p}{2k_p l_p w_p} \quad (D.6)$$

The thermal resistivities due to conduction of heat through the metal to the surface of the polymer and through the polymer to the surface of the metal are given by

$$R_{cond,mp} = \frac{d_m}{2k_m l_m w_m} \quad (D.7)$$

$$R_{cond,pm} = \frac{d_p}{2k_p l_p w_p} \quad (D.8)$$

Each set of thermal resistances in series is combined by adding the resistances to obtain the simplified circuit diagram in Figure 112.

$$R_{m,amb} = R_{m,cond} + R_{m,conv} \quad (D.9)$$

$$R_{p,amb} = R_{p,cond} + R_{p,conv} \quad (D.10)$$

$$R_{cond,eff} = R_{cond,mp} + R_{cond,pm} \quad (D.11)$$

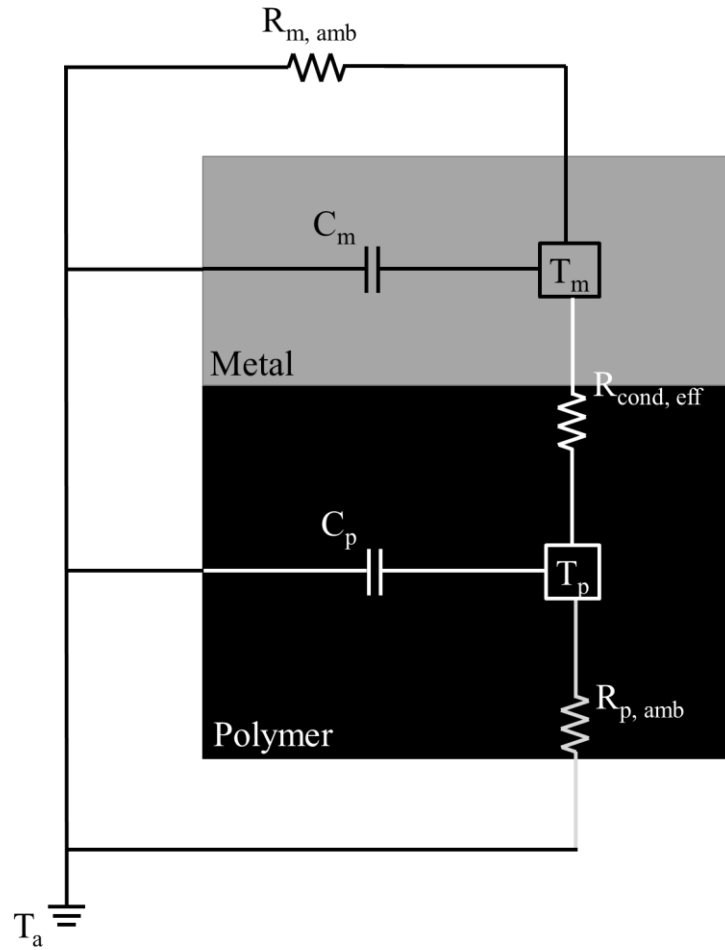


Figure 112: Simplified thermal circuit diagram for a single bead of metal deposited on a polymer substrate.

Kirchhoff's current law, which states that the currents entering a node must equal the currents leaving a node, is applied to the T_m and T_p nodes, with heat flow Q being analogous to current flow.

$$0 = Q_{C_m} + Q_{R_{m,amb}} + Q_{R_{cond,eff}} \quad (D.12)$$

$$Q_{R_{cond,eff}} = Q_{C_p} + Q_{R_{p,amb}} \quad (D.13)$$

Heat flow through a thermal capacitor is equivalent to the thermal capacitance multiplied by the derivative of the temperature at that node, and heat flow through a thermal resistor is equivalent to the difference in temperatures across the resistor divided by the thermal resistance.

$$0 = C_m \frac{dT_m(t)}{dt} + \frac{T_m(t) - T_a}{R_{m,amb}} + \frac{T_m(t) - T_p(t)}{R_{cond,eff}} \quad (D.14)$$

$$\frac{T_m(t) - T_p(t)}{R_{cond,eff}} = C_p \frac{dT_p(t)}{dt} + \frac{T_p(t) - T_a}{R_{p,amb}} \quad (D.15)$$

This set of first-order differential equations can be re-arranged in state space format, where \mathbf{x} is the state vector, \mathbf{u} is the input vector, and \mathbf{y} is the output vector. A is the state matrix, B is the input matrix, C is the output matrix, and D is the feedforward matrix.

$$\dot{\mathbf{x}} = A\mathbf{x} + B\mathbf{u} \quad \mathbf{y} = C\mathbf{x} + D\mathbf{u} \quad (D.16)$$

$T_{m,a}$ and $T_{p,a}$ are defined as shown in Equations 3.17 and 3.18. The final temperatures of the metal and polymer are determined by adding the ambient temperature to the substituted variables after the solution is derived.

$$T_{m,a}(t) = T_m(t) - T_{amb} \quad (D.17)$$

$$T_{p,a}(t) = T_p(t) - T_{amb} \quad (D.18)$$

These equations are substituted into Equations 3.13 and 3.14 to yield Equations 3.19 and 3.20. These substitutions enabled the following coupled first-order differential equations, describing the temperatures of the metal and the polymer after the deposition of the metal on the polymer.

$$\frac{dT_{m,a}(t)}{dt} = -\left(\frac{1}{C_m R_{m,a}} + \frac{1}{C_m R_{cond,eff}}\right) T_{m,a}(t) + \left(\frac{1}{C_m R_{cond,eff}}\right) T_{p,a}(t) \quad (D.19)$$

$$\frac{dT_{p,a}(t)}{dt} = \left(\frac{1}{C_p R_{cond,eff}}\right) T_{m,a}(t) - \left(\frac{1}{C_p R_{p,a}} + \frac{1}{C_p R_{cond,eff}}\right) T_{p,a}(t) \quad (D.20)$$

These equations can be written in state space format, with the following state vector.

$$\mathbf{x} = \begin{bmatrix} T_{m,a}(t) \\ T_{p,a}(t) \end{bmatrix} \quad (\text{D.21})$$

As the system reacts to initial conditions rather than a temperature or heat flow input, there is no input matrix or input vector.

$$\begin{bmatrix} \dot{T}_{m,a}(t) \\ \dot{T}_{p,a}(t) \end{bmatrix} = \begin{bmatrix} -\left(\frac{1}{C_m R_{m,a}} + \frac{1}{C_m R_{cond,eff}}\right) & \frac{1}{C_m R_{cond,eff}} \\ \frac{1}{C_p R_{cond,eff}} & -\left(\frac{1}{C_p R_{p,a}} + \frac{1}{C_p R_{cond,eff}}\right) \end{bmatrix} \begin{bmatrix} T_{m,a}(t) \\ T_{p,a}(t) \end{bmatrix} \quad (\text{D.22})$$

The output vector is defined as the following to predict the temperature of the metal and polymer.

$$\mathbf{y} = \begin{bmatrix} T_{m,a} \\ T_{p,a} \end{bmatrix} = \begin{bmatrix} 1 & 0 \\ 0 & 1 \end{bmatrix} \begin{bmatrix} T_{m,a}(t) \\ T_{p,a}(t) \end{bmatrix} \quad (\text{D.23})$$

The system in state space format was entered into MATLAB for analysis, using the variable values listed in Table 12.

Table 12. Variable values used for temperature prediction.

Variable	Value
h_{air}	10 W/m ² K
l_m	0.0127 m
w_m	0.002 m
d_m	0.001 m
l_p	0.05 m
w_p	0.025 m
d_p	0.015 m
ρ_m	7500 kg/m ³
ρ_p	1080 kg/m ³
$c_{p,m}$	500 J/kgK
$c_{p,p}$	1584 J/kgK
k_m	13 W/mK
k_p	0.262 W/mK

The eigenvalues of the A matrix with these variable values, which are equivalent to the poles of the system, are -0.012 and -0.0003. Two negative poles indicate that the system is stable and temperatures of both the metal and the polymer will approach room temperature over time in response to initial temperature conditions. The poles are also real, indicating that the system is overdamped and that the temperatures will not oscillate while settling, as expected of a hot component cooling to ambient temperature. Each of these two poles corresponds to one of the materials. The time constant is equivalent to the negative reciprocal of the pole.

$$\tau = \frac{-1}{p} \quad (\text{D.24})$$

And the temperature response of the system is proportional to the exponential function of time multiplied by the negative inverse of the time constant.

$$T = Ae^{-t/\tau} + C \quad (\text{D.25})$$

The metal, which cools at a faster rate than the polymer due to its higher thermal conductivity and lower thermal capacitance, corresponds to the larger pole, and the polymer corresponds to the smaller pole. This conclusion can be confirmed by plotting the response of both the polymer and the metal and calculating the time constant from these plots.

The initial temperature of the metal is assumed to be the melting temperature of the metal, which is 1380°C for 316L stainless steel, and the initial temperature of the polymer is assumed to be ambient temperature. These initial conditions are implemented into the system model in MATLAB to predict the temperature responses of the polymer and metal, shown in Figure 113. The initial temperature of the metal does raise the bulk temperature of the polymer but only by 4°C. As the metal pole is three orders of magnitude larger than the polymer pole, dominant pole theory explains the limited temperature rise of the polymer. Therefore, even though a thin layer of polymer might degrade upon direct contact with molten metal, the bulk of the polymer is not heated enough to reach the melting point of the polymer and significantly damage the geometric integrity of the component.

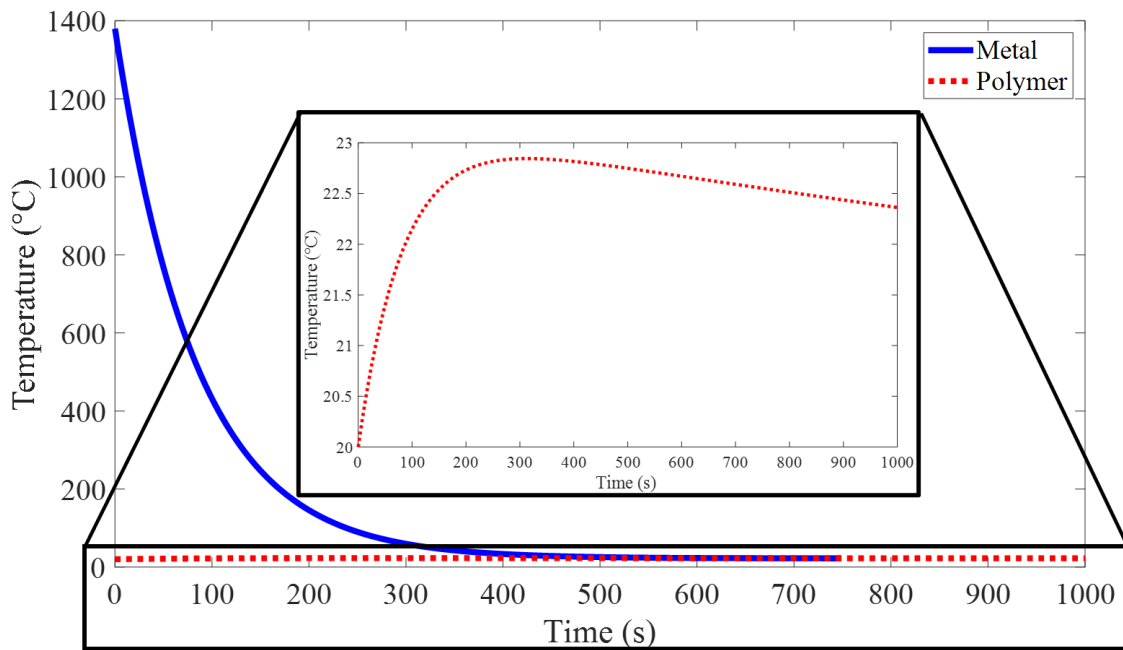


Figure 113: The predicted temperatures of a single metal deposition (top) and the polymer substrate (bottom) over time in response to initial temperature conditions.

Alternatively, the system can be modeled as a metal bead resting on top of a polymer substrate that is exposed to energy from the laser, as shown in Figure 114.

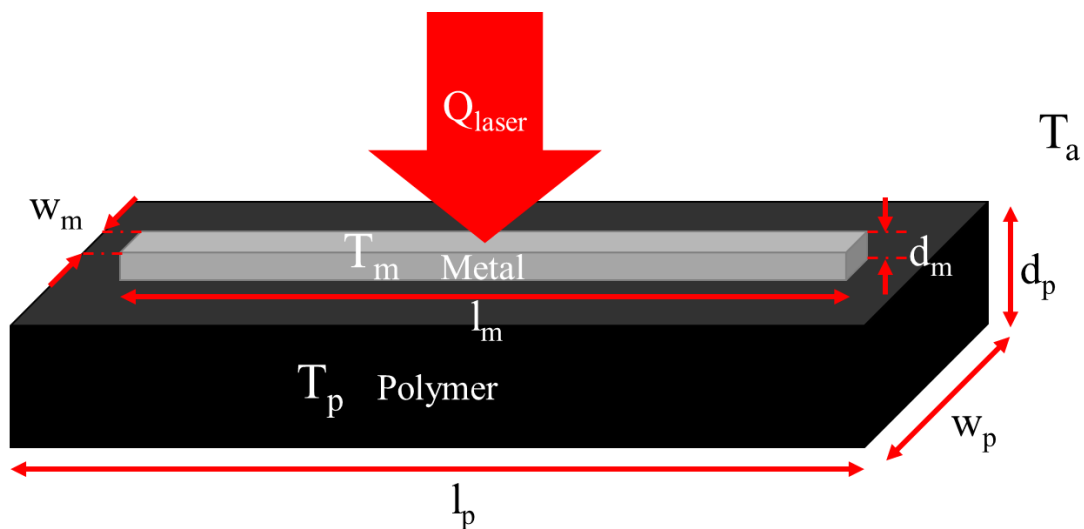


Figure 114: A metal bead on a polymer substrate exposed to energy from the laser.

This scenario is modeled as the thermal circuit shown in Figure 115, where all thermal resistivity and thermal capacitance values are defined in equations 3.1 – 3.8 and where the heat flow from the laser is defined as follows, where P_{laser} is the laser power.

$$Q_{laser} = P_{laser}t_{exposure} \quad (D.26)$$

The exposure time $t_{exposure}$ is the time the laser is active during the deposition and is defined as the scan speed multiplied by the length of the metal bead.

$$t_{exposure} = s_{scan}l_m \quad (D.27)$$

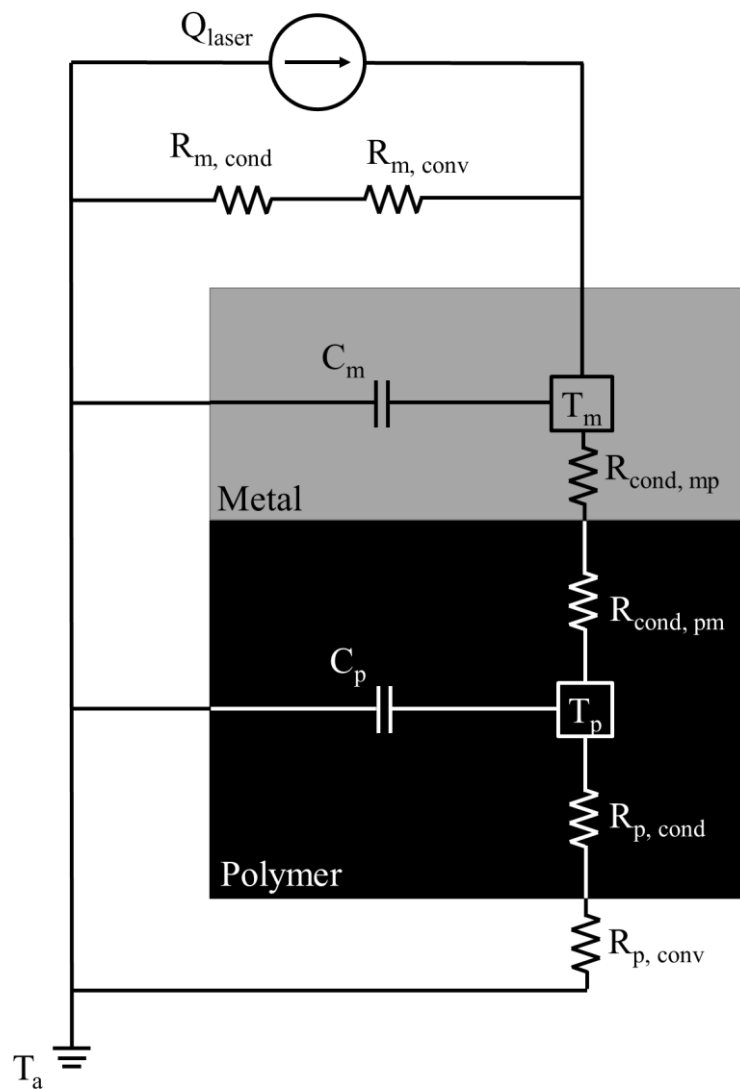


Figure 115: Thermal circuit of a metal bead on a polymer substrate exposed to energy from a laser.

The thermal circuit in Figure 115 is simplified by combining pairs of resistances in series, as done in equations 3.9-3.11 to obtain the simplified thermal circuit shown in Figure 116.

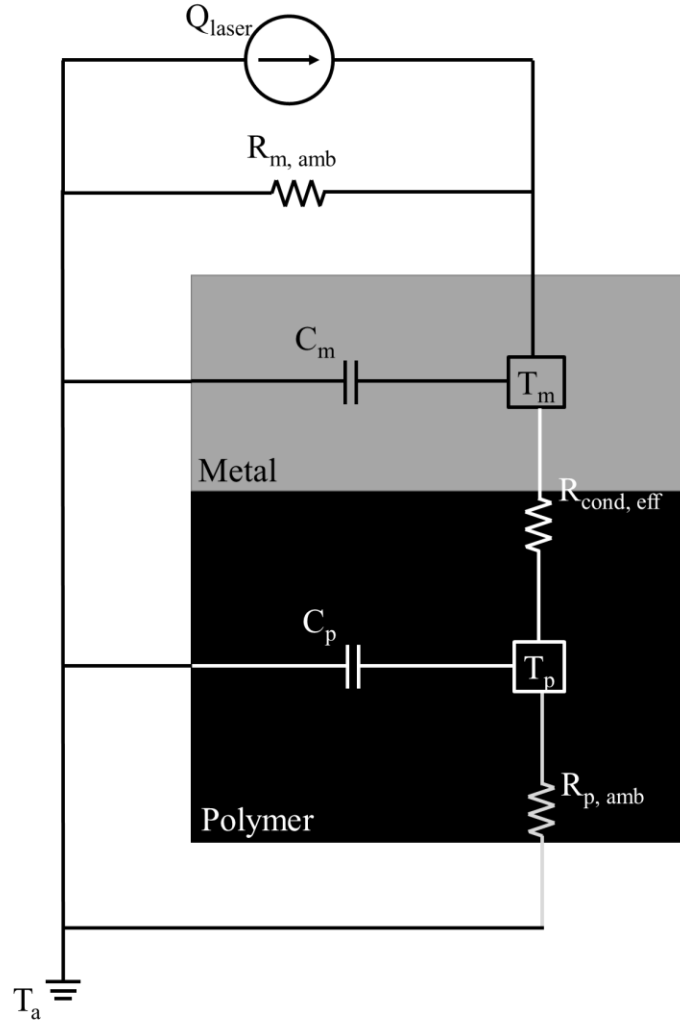


Figure 116: Simplified thermal circuit of a metal bead on a polymer substrate exposed to energy from a laser.

Like the analysis in equations 3.12 and 3.13, Kirchhoff's current law, which states that the currents (heat flow) entering a node must equal the currents (heat flow) leaving a node, was applied to the T_m and T_p nodes, with heat flow Q being analogous to current flow.

$$Q_{laser} = Q_{C_m} + Q_{R_{m,amb}} + Q_{R_{cond,eff}} \quad (D.28)$$

$$Q_{R_{cond,eff}} = Q_{C_p} + Q_{R_{p,amb}} \quad (D.29)$$

Heat flow through a thermal capacitor is equivalent to the product of the thermal capacitance and the derivative, with respect to time, of the temperature at that node. Heat flow through a thermal resistor is the quotient of the difference in temperatures across the resistor and the thermal resistance.

$$Q_{laser} = C_m \frac{dT_m(t)}{dt} + \frac{T_m(t)-T_a}{R_{m,amb}} + \frac{T_m(t)-T_p}{R_{cond,eff}} \quad (D.30)$$

$$\frac{T_m(t)-T_p}{R_{cond,eff}} = C_p \frac{dT_p(t)}{dt} + \frac{T_p(t)-T_a}{R_{p,amb}} \quad (D.31)$$

This set of first-order differential equations can be re-arranged in state space format, where \mathbf{x} is the state vector, u is the input, \mathbf{y} is the output vector, A is the state matrix, B is the input matrix, C is the output matrix, and D is the feedforward matrix, as shown in equation 3.16. Again, the variable substitutions in equations 3.17 and 3.18 are made prior to defining the system to enable state format. The final temperatures of the metal and polymer are then determined by summing the ambient temperature to the substituted variables after the solution is derived. These substitutions enabled the following coupled first-order differential equations, describing the temperatures of the metal and the polymer after the deposition of the metal on the polymer.

$$\frac{dT_{m,a}(t)}{dt} = -\left(\frac{1}{C_m R_{m,a}} + \frac{1}{C_m R_{cond,eff}}\right) T_{m,a}(t) + \left(\frac{1}{C_m R_{cond,eff}}\right) T_{p,a}(t) + \frac{Q_{laser}}{C_m} \quad (D.32)$$

$$\frac{dT_{p,a}(t)}{dt} = \left(\frac{1}{C_p R_{cond,eff}}\right) T_{m,a}(t) - \left(\frac{1}{C_p R_{p,a}} + \frac{1}{C_p R_{cond,eff}}\right) T_{p,a}(t) \quad (D.33)$$

These equations are then organized in state space format, with the following state vector.

$$\mathbf{x} = \begin{bmatrix} T_{m,a}(t) \\ T_{p,a}(t) \end{bmatrix} \quad (D.34)$$

The input is the energy from the laser, so the input is as follows

$$u = Q_{laser} \quad (D.35)$$

The state space format is then defined with the following state and input matrices

$$A = \begin{bmatrix} -\left(\frac{1}{C_m R_{m,a}} + \frac{1}{C_m R_{cond,eff}}\right) & \frac{1}{C_m R_{cond,eff}} \\ \frac{1}{C_p R_{cond,eff}} & -\left(\frac{1}{C_p R_{p,a}} + \frac{1}{C_p R_{cond,eff}}\right) \end{bmatrix} \quad (D.36)$$

$$B = \begin{bmatrix} \frac{1}{C_m} \\ 0 \end{bmatrix} \quad (D.37)$$

The output vector is defined as the following to predict the temperature of the metal and polymer.

$$\mathbf{y} = [1 \quad 1] \begin{bmatrix} T_{m,a}(t) \\ T_{p,a}(t) \end{bmatrix} \quad (\text{D.38})$$

The system in state space format was entered into MATLAB for analysis, using the variable values listed in Table 12.

The eigenvalues of the A matrix with these variable values, which are equivalent to the poles of the system, are -0.012 and -0.003. Two negative poles indicate that the system is stable and temperatures of both the metal and the polymer approach room temperature over time in response to initial temperature conditions. The poles are also real, indicating that the system is overdamped and that the temperatures do not oscillate while settling, as expected of a hot component cooling to ambient temperature. Each of these two poles corresponds to a specific material. The time constant is equivalent to the negative reciprocal of the pole.

$$\tau = \frac{-1}{p} \quad (\text{D.39})$$

And the temperature response of the system is proportional to the exponential function of time multiplied by the negative inverse of the time constant.

$$T = Ae^{-t/\tau} + C \quad (\text{D.40})$$

The metal, which cools at a faster rate than the polymer due to its higher thermal conductivity and lower thermal capacitance, corresponds to the larger pole, and the polymer corresponds to the smaller pole. This conclusion can be confirmed by plotting the response of both the polymer and the metal and calculating the time constant from these plots.

The laser power was set to be 100W and the scan speed of the laser was set to be 600mm/min. These conditions were used to calculate a power impulse of 127W, which was implemented into the system model in MATLAB to predict the temperature responses of the polymer and metal, shown in Figure 117. The temperatures of both the metal and the polymer over time in response to power input from the laser are within 5% of the

temperatures in response to initial temperature conditions, plotted in Figure 117, supporting both analyses.

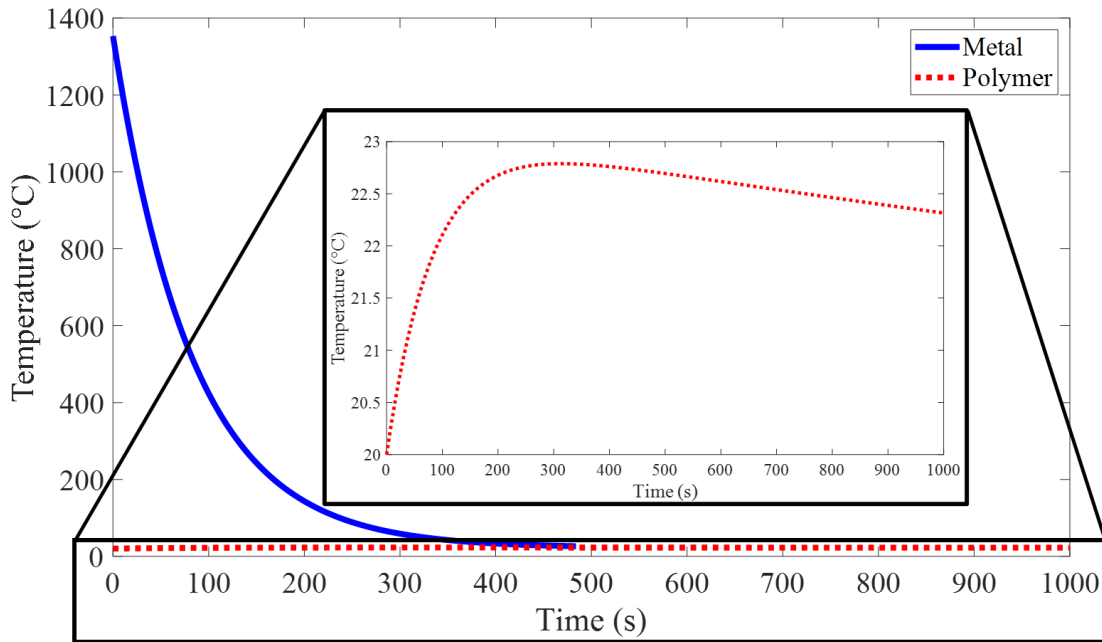


Figure 117: The predicted temperatures of a single metal deposition (top) and the polymer substrate (bottom) over time in response to a power impulse input.

D.2.2 Multi-layer metal deposition model

A multi-layer model for a second deposited bead, assumed to be instantaneously deposited at the melting temperature of the metal as shown in Figure 118, was then developed following the thermal circuit methodology introduced in 3.1, where the heat flow is analogous to the flow of current and voltages are analogous to temperatures. Again, thermal capacitances of the polymer and the metal are represented by capacitors and the conduction within materials and convection at the surfaces of materials are represented by resistors. As shown in Figure 119, the thermal capacitances of the polymer and metal are represented by C_p and C_m , respectively. Conduction within the polymer and within the metal is represented by $R_{p,cond}$ and $R_{m,cond}$, respectively. Convection at the surface of the polymer

and at the surface of the metal is represented by $R_{p,conv}$ and $R_{m,conv}$, respectively. Conduction through each metal bead to the other metal bead is also represented by $R_{m,cond}$. Conduction through the metal to the interface between the polymer and the metal is represented by $R_{cond,mp}$, and conduction through the polymer to the interface between the polymer and the metal is represented by $R_{cond,pm}$. The ambient temperature, temperature of the second metal bead, temperature of the first metal bead, and temperature of the polymer are represented by T_a , $T_{m,2}$, $T_{m,1}$, and T_p , respectively. The values of the thermal resistivities and capacitances are dependent on the material properties and geometric parameters listed in Table 11.

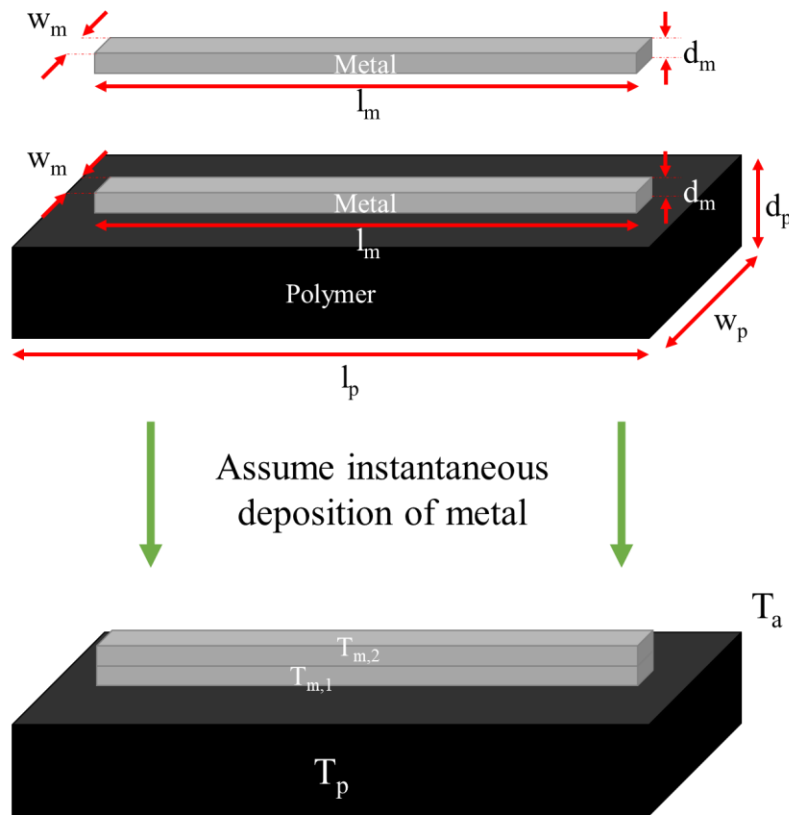


Figure 118: Geometry assumptions used to predict metal temperature T_m and polymer temperature T_p in response to deposition of a second metal bead on a polymer substrate.

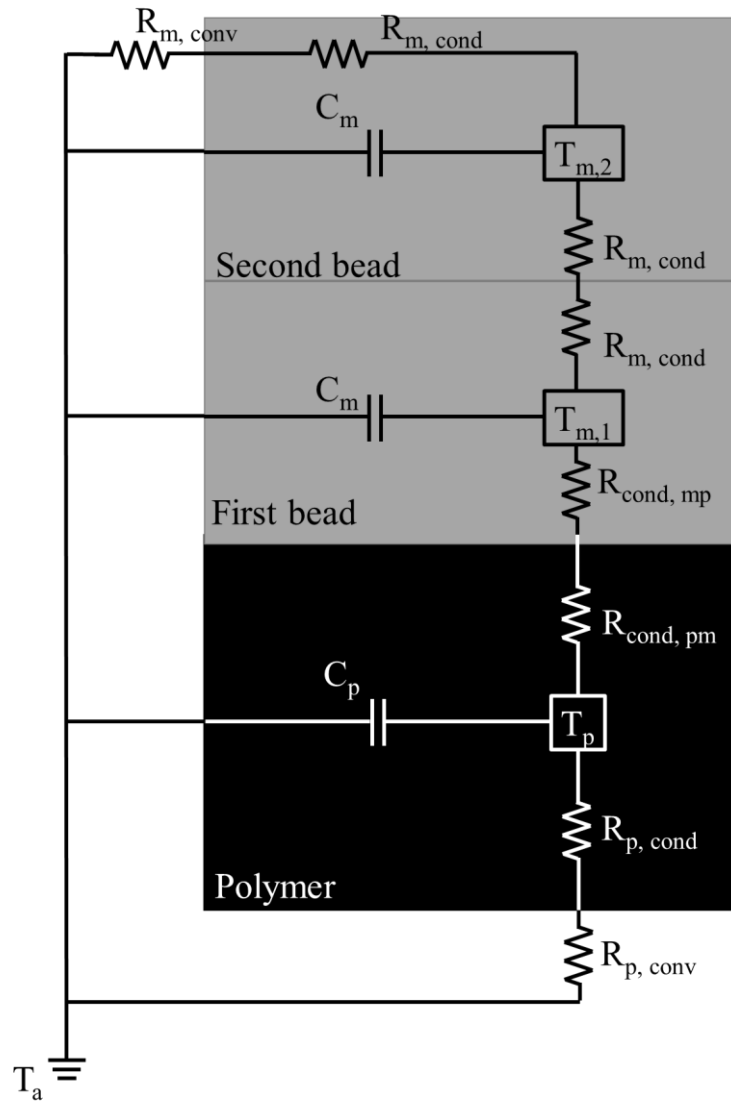


Figure 119: Thermal circuit diagram for two beads of metal deposited on a polymer substrate.

The thermal capacitances of the metal and polymer are defined in 3.1 and 3.2, and the thermal resistivities due to convection of the metal and the polymer in ambient temperatures are defined in 3.3 and 3.4. The thermal resistivities due to conduction of heat through the metal to the surface of the metal and through the polymer to the surface of the polymer are defined in 3.5 and 3.6, and the thermal resistivities due to conduction of heat through the metal to the surface of the polymer and through the polymer to the surface of the metal are defined in 3.7 and 3.8. Each set of thermal resistances in series is combined

by adding the resistances as shown in 3.9, 3.10, and 3.11 to obtain the simplified circuit diagram in Figure 120.

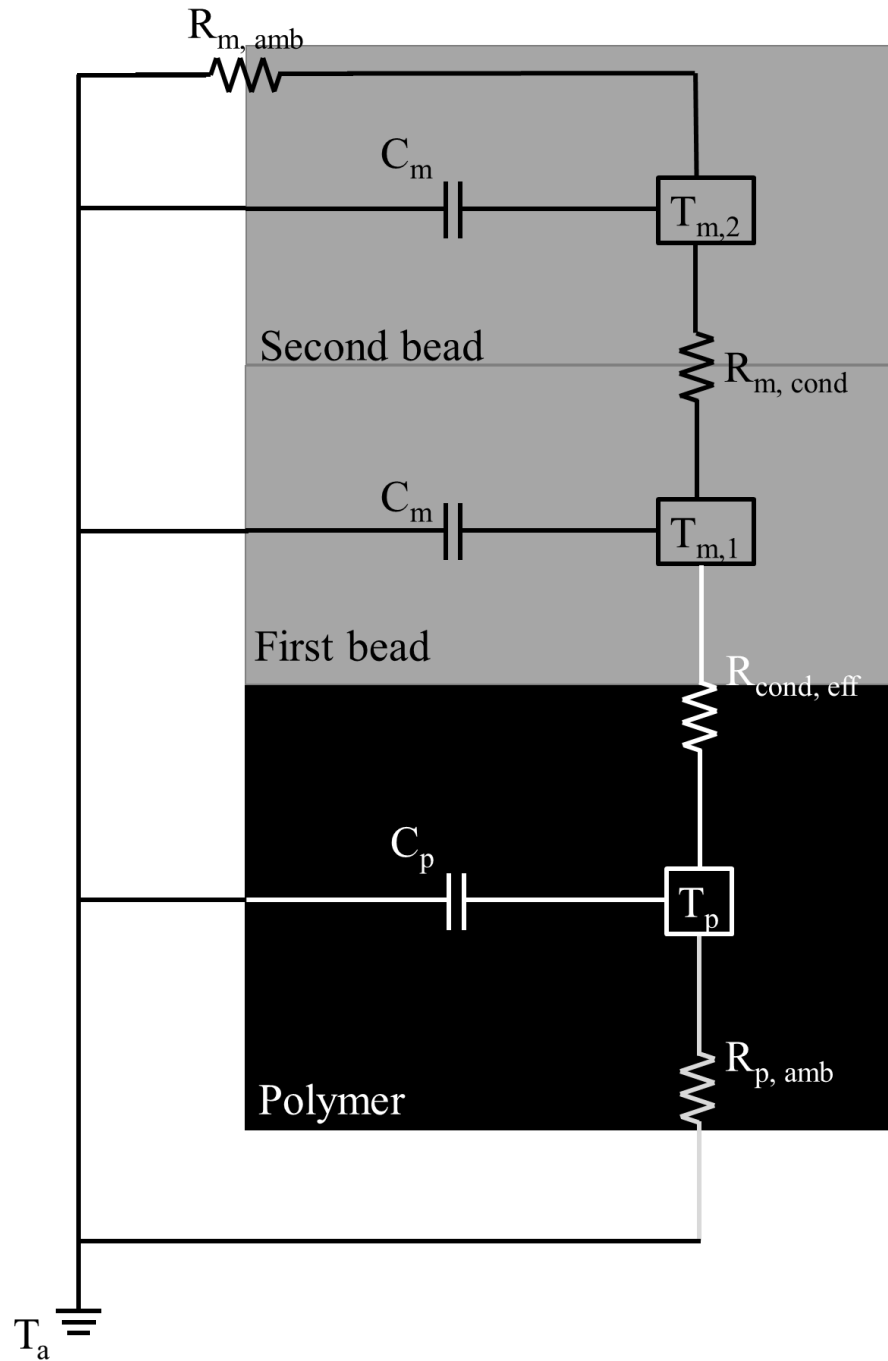


Figure 120: Simplified thermal circuit diagram for two beads of metal deposited on a polymer substrate.

Kirchhoff's current law, which states that the currents (heat flow) entering a node must equal the currents (heat flow) leaving a node, is applied to the $T_{m,2}$, $T_{m,1}$, and T_p nodes, with heat flow Q being analogous to current flow.

$$0 = Q_{C_m} + Q_{R_{m,amb}} + Q_{R_{m,cond}} \quad (D.41)$$

$$Q_{R_{m,cond}} = Q_{C_m} + Q_{R_{cond,eff}} \quad (D.42)$$

$$Q_{R_{cond,eff}} = Q_{C_p} + Q_{R_{p,amb}} \quad (D.43)$$

Heat flow through a thermal capacitor is equivalent to the product of the thermal capacitance and the derivative, with respect to time, of the temperature at that node, and heat flow through a thermal resistor is equivalent to the quotient of the difference in temperatures across the resistor and the thermal resistance.

$$0 = C_m \frac{dT_{m,2}(t)}{dt} + \frac{T_{m,2}(t) - T_a}{R_{m,amb}} + \frac{T_{m,2}(t) - T_{m,1}(t)}{R_{m,cond}} \quad (D.44)$$

$$\frac{T_{m,2}(t) - T_{m,1}(t)}{R_{m,cond}} = C_m \frac{dT_{m,1}(t)}{dt} + \frac{T_{m,1}(t) - T_p(t)}{R_{cond,eff}} \quad (D.45)$$

$$\frac{T_{m,1}(t) - T_p(t)}{R_{cond,eff}} = C_p \frac{dT_p(t)}{dt} + \frac{T_p(t) - T_a}{R_{p,amb}} \quad (D.46)$$

This set of first-order differential equations can be re-arranged in state space format, where \mathbf{x} is the state vector, \mathbf{u} is the input, and \mathbf{y} is the output, as shown in 3.16. The following three variable substitutions are made prior to defining the system to enable state format. The final temperatures of the metal and polymer are then determined by summing the ambient temperature and the substituted variables after the solution is derived.

$$T_{m,2,a}(t) = T_{m,2}(t) - T_{amb} \quad (D.47)$$

$$T_{m,1,a}(t) = T_{m,1}(t) - T_{amb} \quad (D.48)$$

$$T_{p,a}(t) = T_p(t) - T_{amb} \quad (D.49)$$

These substitutions enable the following coupled first-order differential equations, describing the temperatures of the metal and the polymer after the deposition of the metal on the polymer.

$$\frac{dT_{m,2,a}(t)}{dt} = - \left(\frac{1}{C_m R_{m,amb}} + \frac{1}{C_m R_{m,cond}} \right) T_{m,2}(t) + \left(\frac{1}{C_m R_{m,cond}} \right) T_{m,1}(t) \quad (D.50)$$

$$\frac{dT_{m,1,a}(t)}{dt} = \left(\frac{1}{C_m R_{m,cond}} \right) T_{m,2}(t) - \left(\frac{1}{C_m R_{m,cond}} + \frac{1}{C_m R_{cond,eff}} \right) T_{m,1}(t) + \left(\frac{1}{C_m R_{cond,eff}} \right) T_{p,a}(t) \quad (D.51)$$

$$\frac{dT_{p,a}(t)}{dt} = \left(\frac{1}{C_p R_{cond,eff}} \right) T_{m,1,a}(t) - \left(\frac{1}{C_p R_{p,a}} + \frac{1}{C_p R_{cond,eff}} \right) T_{p,a}(t) \quad (D.52)$$

These equations are then organized in state space format, with the following state vector.

$$\mathbf{x} = \begin{bmatrix} T_{m,2,a}(t) \\ T_{m,1,a}(t) \\ T_{p,a}(t) \end{bmatrix} \quad (D.53)$$

As the system reacts to initial conditions rather than a temperature or heat flow input, there is no input matrix or input vector, and the state matrix is defined as follows.

$$A = \begin{bmatrix} -\left(\frac{1}{C_m R_{m,amb}} + \frac{1}{C_m R_{m,cond}} \right) & \frac{1}{C_m R_{m,cond}} & 0 \\ \frac{1}{C_m R_{m,cond}} & -\left(\frac{1}{C_m R_{m,cond}} + \frac{1}{C_m R_{cond,eff}} \right) & \frac{1}{C_m R_{cond,eff}} \\ 0 & \frac{1}{C_p R_{cond,eff}} & -\left(\frac{1}{C_p R_{p,a}} + \frac{1}{C_p R_{cond,eff}} \right) \end{bmatrix} \quad (D.54)$$

The output vector is defined as the following to predict the temperature of the upper metal bead, lower metal bead, and polymer.

$$\mathbf{y} = [1 \quad 1 \quad 1] \begin{bmatrix} T_{m,2,a}(t) \\ T_{m,1,a}(t) \\ T_{p,a}(t) \end{bmatrix} \quad (D.55)$$

The system in state space format is entered into MATLAB for analysis, using the variable values listed in Table 12.

The eigenvalues of the state matrix with these variable values, which are equivalent to the poles of the system, are -6.9, -0.006, and -0.0003. Three negative poles indicate that the system is stable and that temperatures of both metal layers and the polymer approach room temperature over time in response to initial temperature conditions. The poles are also real, indicating that the system is overdamped and that the temperatures do not oscillate while settling, as expected of a heated component cooling to ambient temperature. Each of these three poles corresponds one section of material. The top metal layer, which cools at the fastest rate due to a higher thermal conductivity than the polymer and more exposure to ambient temperature than the bottom metal layer, corresponds to the larger pole, the bottom metal layer corresponds to the second largest pole, and the polymer corresponds to the

smaller pole. This conclusion can be confirmed by plotting the response of both the polymer and the metal and calculating the time constant from these plots.

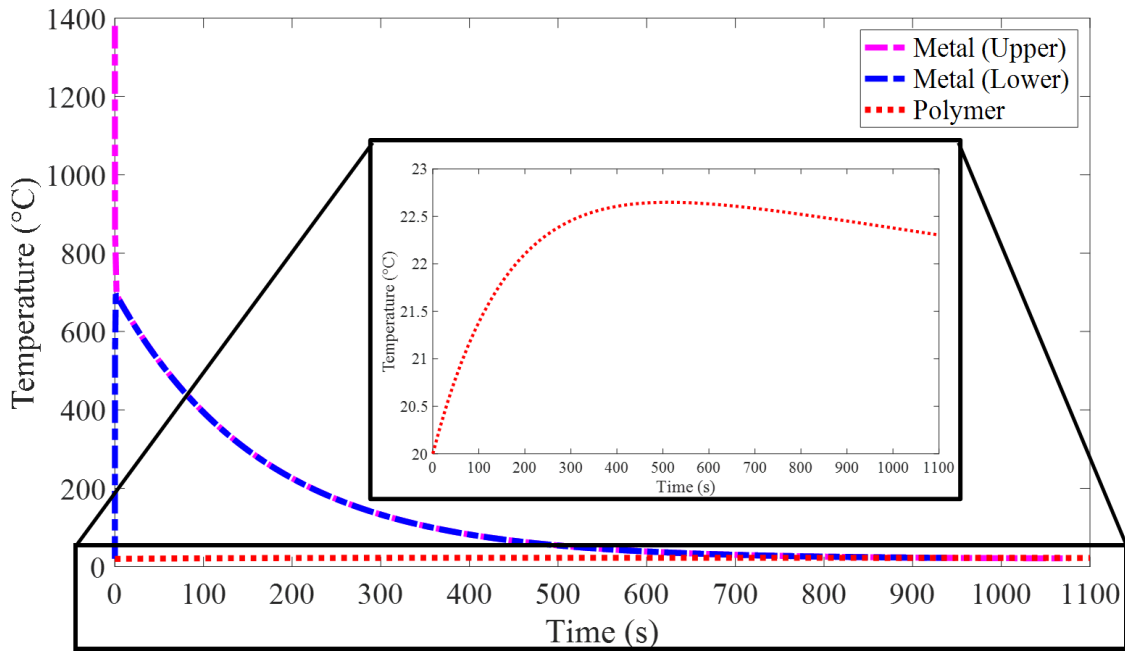


Figure 121: The predicted temperatures of a second deposited metal bead (top), the first deposited bead (middle), and the polymer substrate (bottom) over time in response to initial temperature conditions.

Alternatively, the system can be modeled as a metal bead resting on top of a polymer substrate that is exposed to energy from the laser, as shown in Figure 122.

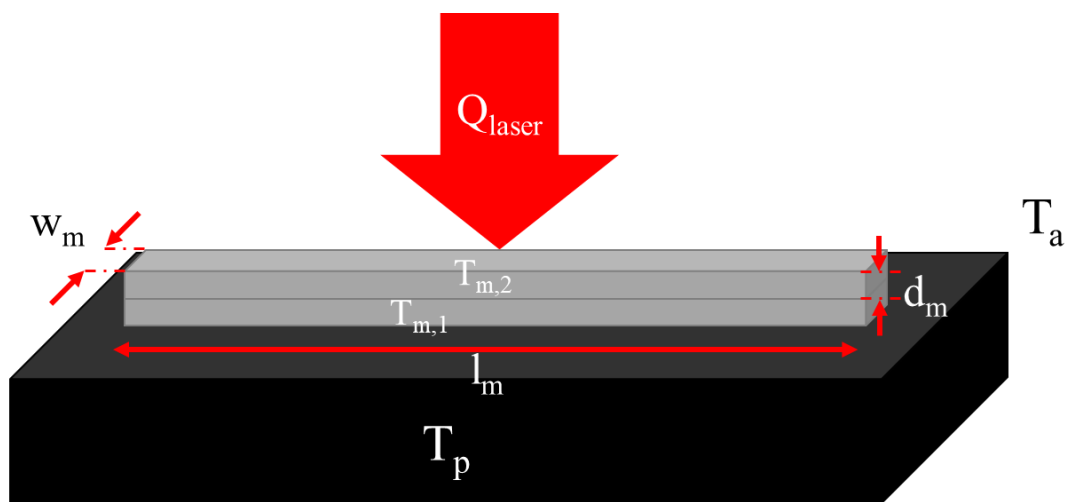


Figure 122: A second metal bead on a polymer substrate exposed to energy from the laser.

This scenario is modeled as the thermal circuit shown in Figure 123, where all thermal resistivity and thermal capacitance values are defined in equations 3.1 – 3.8 and where the energy from the laser is defined in 3.27 and 3.28.

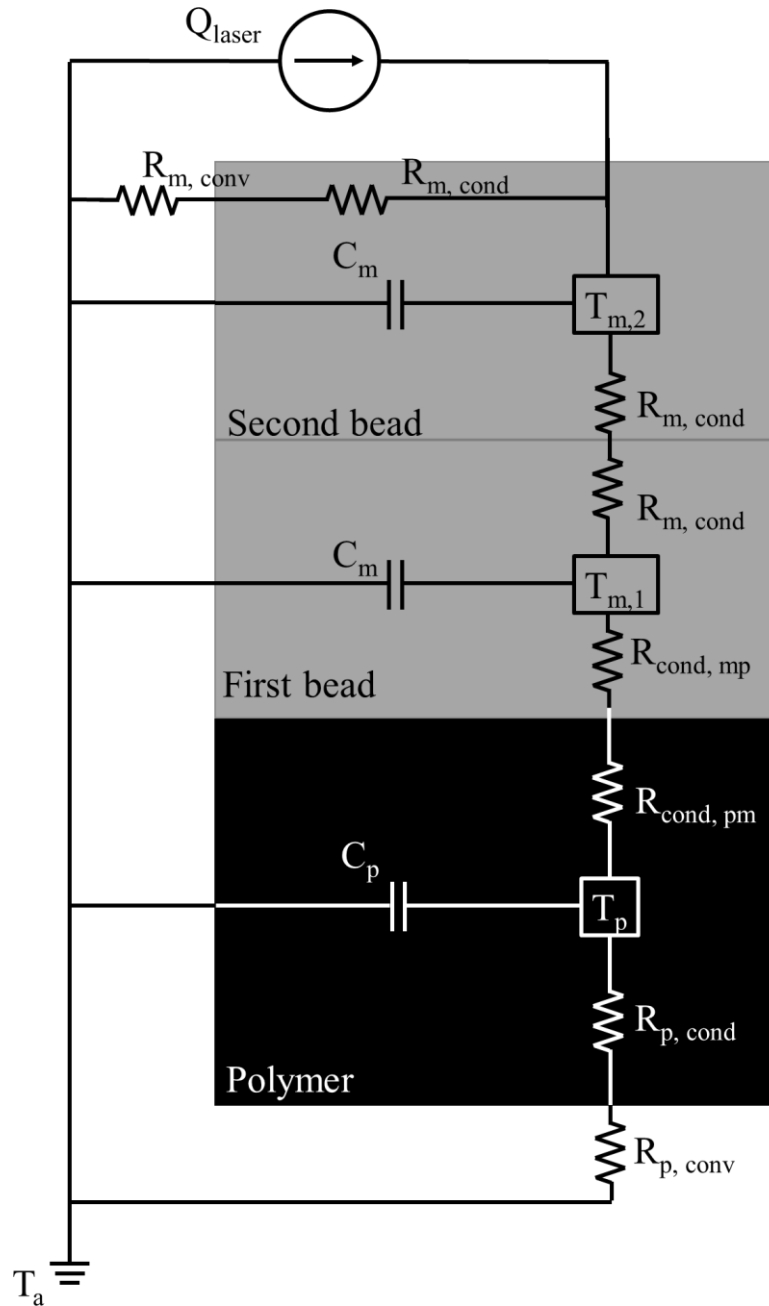


Figure 123: Thermal circuit of a second metal bead on a polymer substrate exposed to energy from a laser.

The thermal circuit in Figure 123 is simplified by combining pairs of resistances in series, as done in equations 3.9-3.11 to obtain the simplified thermal circuit shown in Figure 124.

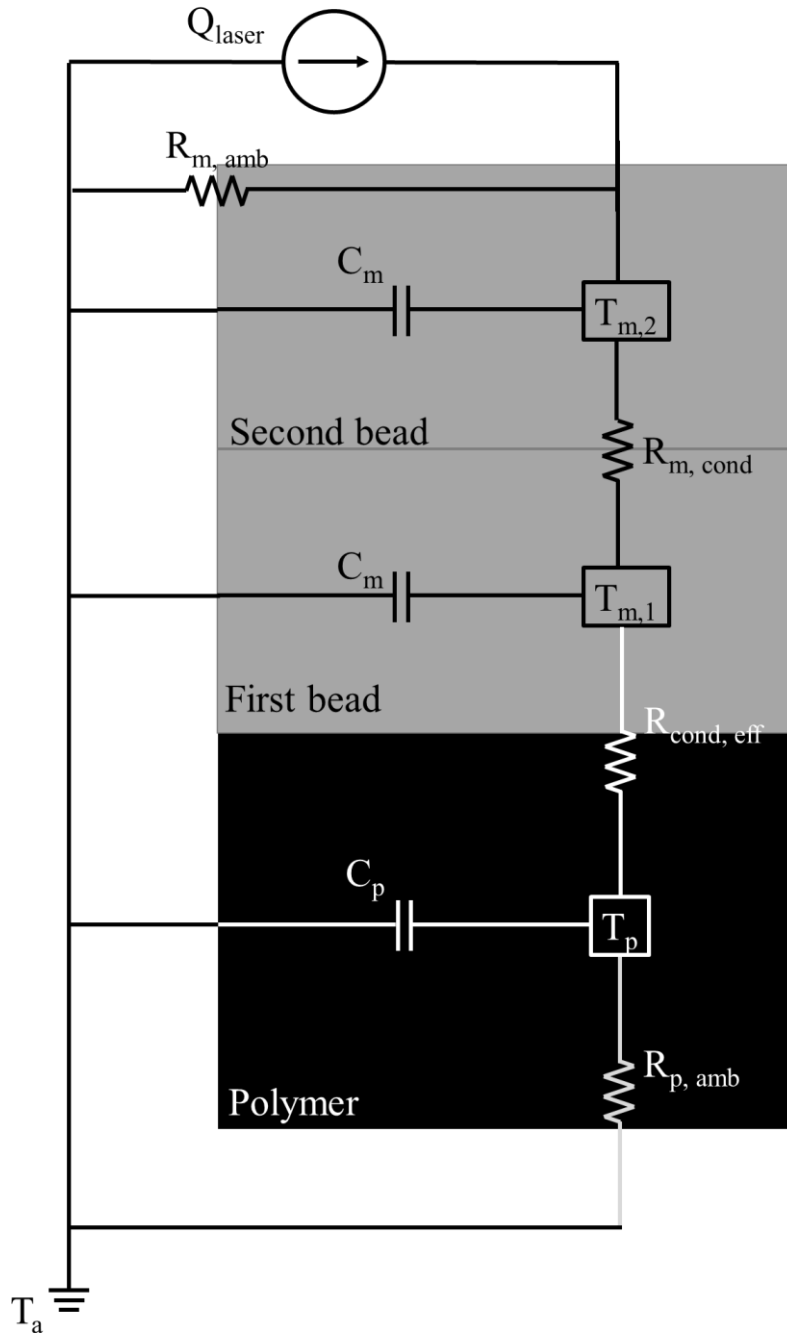


Figure 124: Simplified thermal circuit of a second metal bead on a polymer substrate exposed to energy from a laser.

Like the analysis in equations 3.43-3.45, Kirchoff's current law, which states that the currents (heat flow) entering a node must equal the currents (heat flow) leaving a node, is applied to the $T_{m,2}$, $T_{m,1}$, and T_p nodes, with heat flow Q being analogous to current flow.

$$Q_{laser} = Q_{C_m} + Q_{R_{m,amb}} + Q_{R_{m,cond}} \quad (D.56)$$

$$Q_{R_{m,cond}} = Q_{C_m} + Q_{R_{cond,eff}} \quad (D.57)$$

$$Q_{R_{cond,eff}} = Q_{C_p} + Q_{R_{p,amb}} \quad (D.58)$$

Heat flow through a thermal capacitor is equivalent to the product of the thermal capacitance and the derivative, with respect to time, of the temperature at that node, and heat flow through a thermal resistor is equivalent to the quotient of the difference in temperatures across the resistor the thermal resistance.

$$Q_{laser} = C_m \frac{dT_{m,2}(t)}{dt} + \frac{T_{m,2}(t) - T_a}{R_{m,amb}} + \frac{T_{m,2}(t) - T_{m,1}(t)}{R_{m,cond}} \quad (D.59)$$

$$\frac{T_{m,2}(t) - T_{m,1}(t)}{R_{m,cond}} = C_m \frac{dT_{m,1}(t)}{dt} + \frac{T_{m,1}(t) - T_p(t)}{R_{cond,eff}} \quad (D.60)$$

$$\frac{T_{m,1}(t) - T_p(t)}{R_{cond,eff}} = C_p \frac{dT_p(t)}{dt} + \frac{T_p(t) - T_a}{R_{p,amb}} \quad (D.61)$$

This set of first-order differential equations can be re-arranged in state space format, where \mathbf{x} is the state vector, u is the input, and \mathbf{y} is the output, as shown in equation 3.16. Again, the variable substitutions in equations 3.17 and 3.18 are made prior to defining the system to enable state format. The final temperatures of the metal and polymer are then determined by summing the ambient temperature and the substituted variables after the solution is derived. These substitutions enable the following coupled first-order differential equations, describing the temperatures of the metal and the polymer after the deposition of the metal on the polymer.

$$\frac{dT_{m,2,a}(t)}{dt} = - \left(\frac{1}{C_m R_{m,amb}} + \frac{1}{C_m R_{m,cond}} \right) T_{m,2}(t) + \left(\frac{1}{C_m R_{m,cond}} \right) T_{m,1}(t) \quad (D.62)$$

$$\frac{dT_{m,1,a}(t)}{dt} = \left(\frac{1}{C_m R_{m,cond}} \right) T_{m,2}(t) - \left(\frac{1}{C_m R_{m,cond}} + \frac{1}{C_m R_{cond,eff}} \right) T_{m,1}(t) + \left(\frac{1}{C_m R_{cond,eff}} \right) T_{p,a}(t) \quad (D.63)$$

$$\frac{dT_{p,a}(t)}{dt} = \left(\frac{1}{C_p R_{cond,eff}} \right) T_{m,1,a}(t) - \left(\frac{1}{C_p R_{p,a}} + \frac{1}{C_p R_{cond,eff}} \right) T_{p,a}(t) \quad (D.64)$$

These equations are then organized in state space format, with the following state vector.

$$\mathbf{x} = \begin{bmatrix} T_{m,2,a}(t) \\ T_{m,1,a}(t) \\ T_{p,a}(t) \end{bmatrix} \quad (D.65)$$

The input is the energy from the laser, so the input is as follows

$$u = Q_{laser} \quad (D.66)$$

The state space format is then defined with the following state and input matrices

$$A = \begin{bmatrix} -\left(\frac{1}{c_m^{Rm,amb}} + \frac{1}{c_m^{Rm,cond}}\right) & \frac{1}{c_m^{Rm,cond}} & 0 \\ \frac{1}{c_m^{Rm,cond}} & -\left(\frac{1}{c_m^{Rm,cond}} + \frac{1}{c_m^{Rcond,eff}}\right) & \frac{1}{c_m^{Rcond,eff}} \\ 0 & \frac{1}{c_p^{Rcond,eff}} & -\left(\frac{1}{c_p^{Rp,a}} + \frac{1}{c_p^{Rcond,eff}}\right) \end{bmatrix} \quad (D.67)$$

$$B = \begin{bmatrix} \frac{1}{c_m} \\ 0 \\ 0 \end{bmatrix} \quad (D.68)$$

The output vector is defined as the following to predict the temperature of the upper metal bead, lower metal bead, and polymer.

$$\mathbf{y} = [1 \quad 1 \quad 1] \begin{bmatrix} T_{m,2,a}(t) \\ T_{m,1,a}(t) \\ T_{p,a}(t) \end{bmatrix} \quad (D.69)$$

The system in state space format was entered into MATLAB for analysis, using the variable values listed in Table 12. The laser power is set to be 100W and the scan speed of the laser is set to be 600mm/min. These conditions are used to calculate a power impulse of 127W, which is implemented into the system model in MATLAB to predict the temperature responses of the polymer and metal, shown in Figure 117.

The eigenvalues of the state matrix with these variable values, which are equivalent to the poles of the system, are -6.93, -0.006, and -0.0003. Two negative poles indicate that the system is stable and temperatures of both metal layers and the polymer approach room temperature over time in response to laser heat flow input. The poles are also real, indicating that the system is overdamped and that the temperatures do not oscillate while settling, as expected of a hot component cooling to ambient temperature. Each of these three poles corresponds one section of material. The top metal layer, which cools at the fastest rate due to a higher thermal conductivity than the polymer and more exposure to

ambient temperature than the bottom metal layer, corresponds to the larger pole, the bottom metal layer corresponds to the second largest pole, and the polymer corresponds to the smaller pole. This conclusion can be confirmed by plotting the response of both the polymer and the metal and calculating the time constant from these plots.

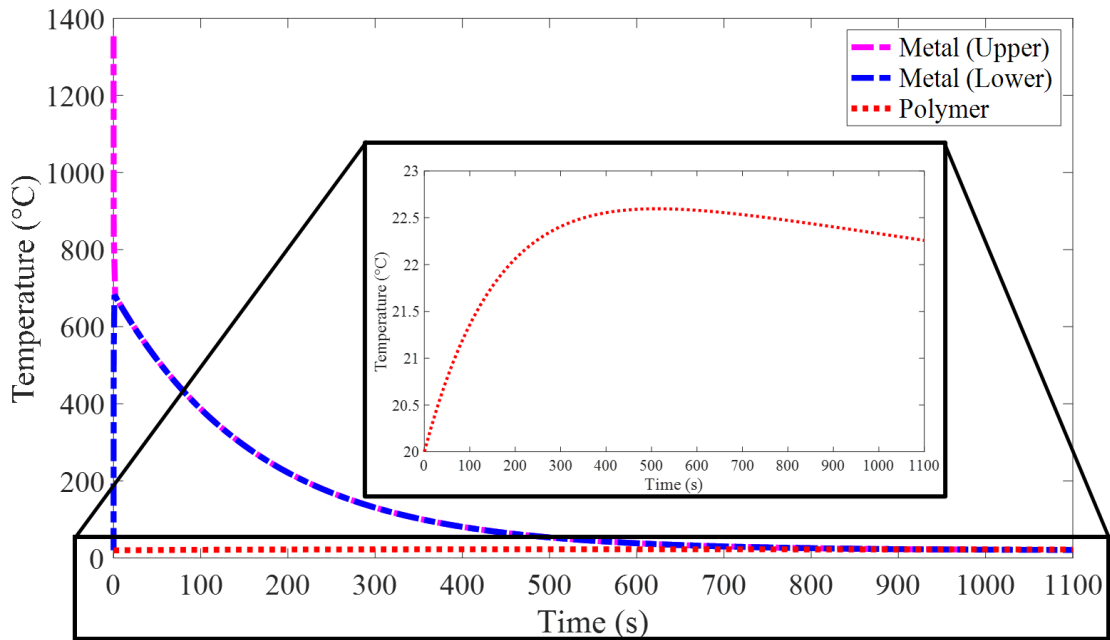


Figure 125: The predicted temperatures of a second deposited metal bead (top), the first deposited bead (middle), and the polymer substrate (bottom) over time in response to an impulse.

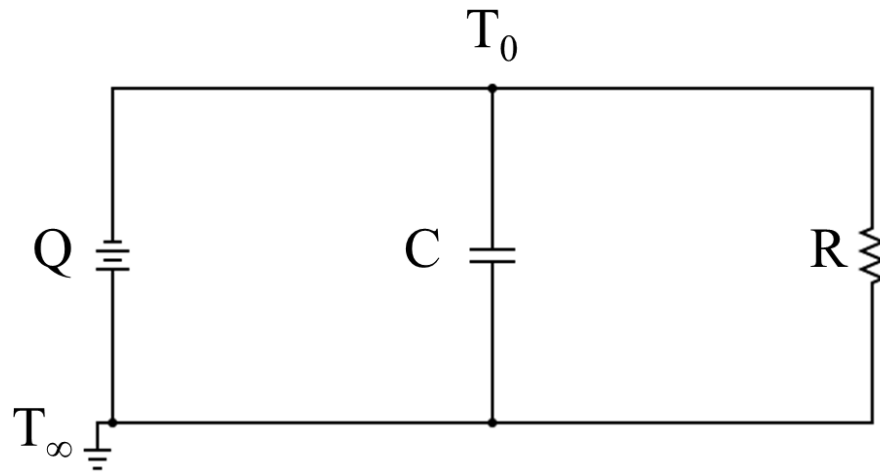


Figure 126: An example of a thermal circuit in which a heat source Q is applied to a material with thermal capacitance C and thermal resistance R .

Thermal circuits are useful in representing 1-dimensional heat transfer scenarios. For example, Swift *et al.* used thermal circuit modeling to derive the thermal heat flow in power transformers, and Peng *et al.* used thermal circuits to estimate part temperature history during powder bed fusion [143, 144]. These circuit models are particularly useful in situations that might require state-space representation of the heat transfer scenario, such as in controls and optimization applications. For example, Ghiaus and Hazyuk used thermal circuit modeling to calculate the optimal thermal load of intermittently heated buildings via an unconstrained optimal control algorithm [145]. Although thermal circuit models are useful in these applications, their applicability is constrained by the 1-dimensional lumped parameter assumptions required to complete the model.

APPENDIX E. THERMAL MODEL RESULTS

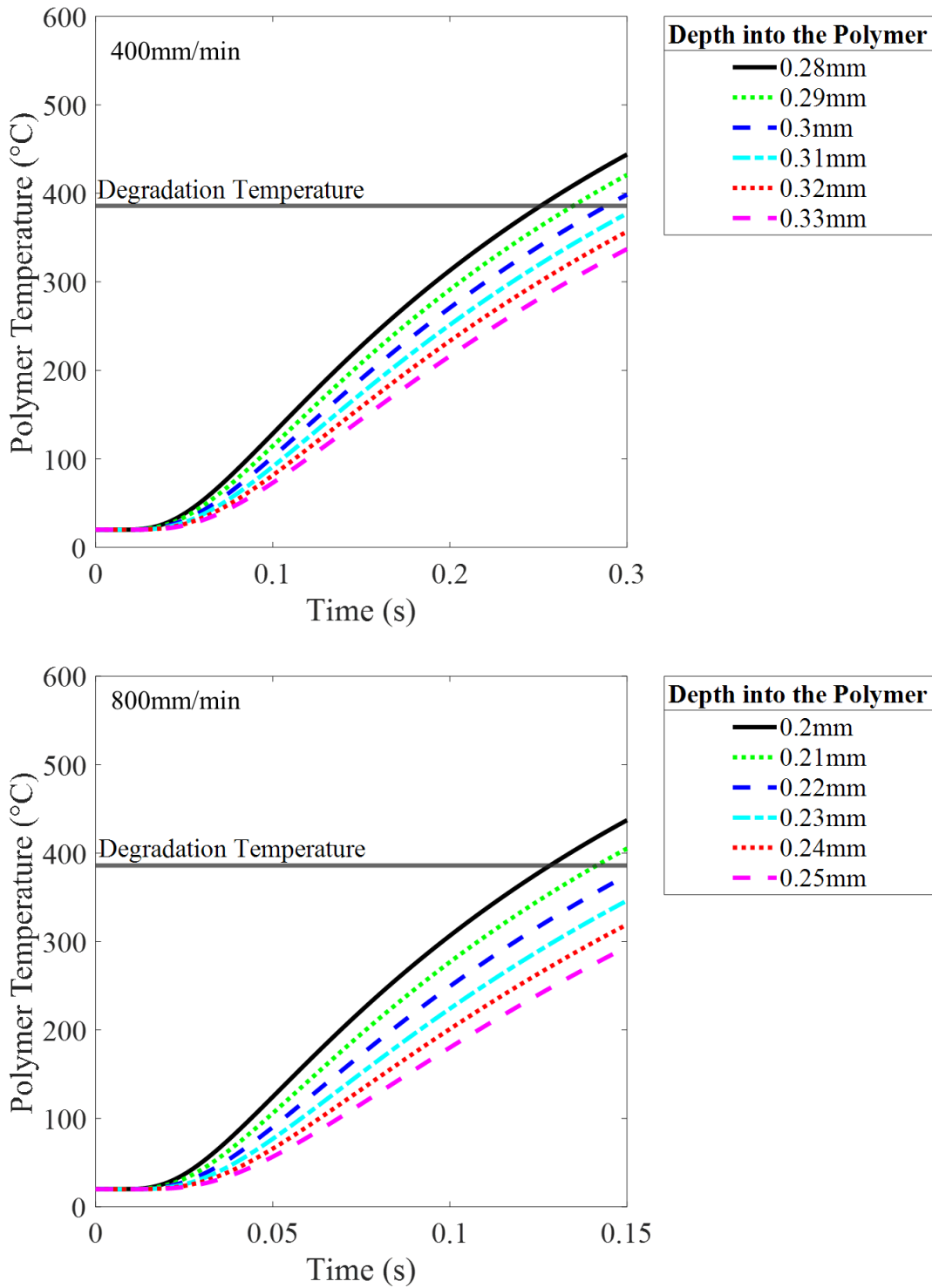


Figure 127: Semi-infinite temperature model results for varying laser speed on CF ABS.

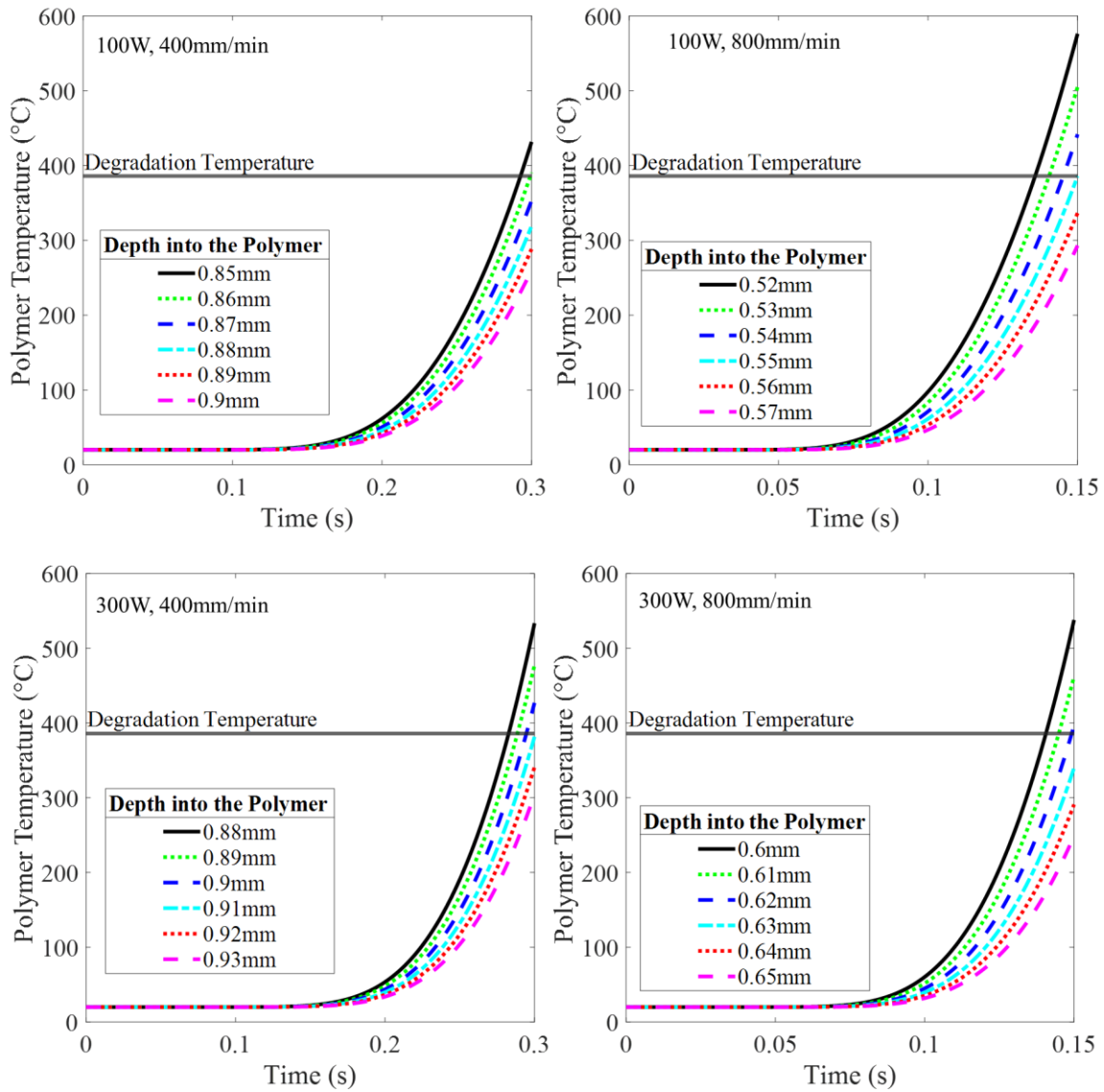


Figure 128: Semi-infinite flux model results for varying laser speed and power on CF ABS.

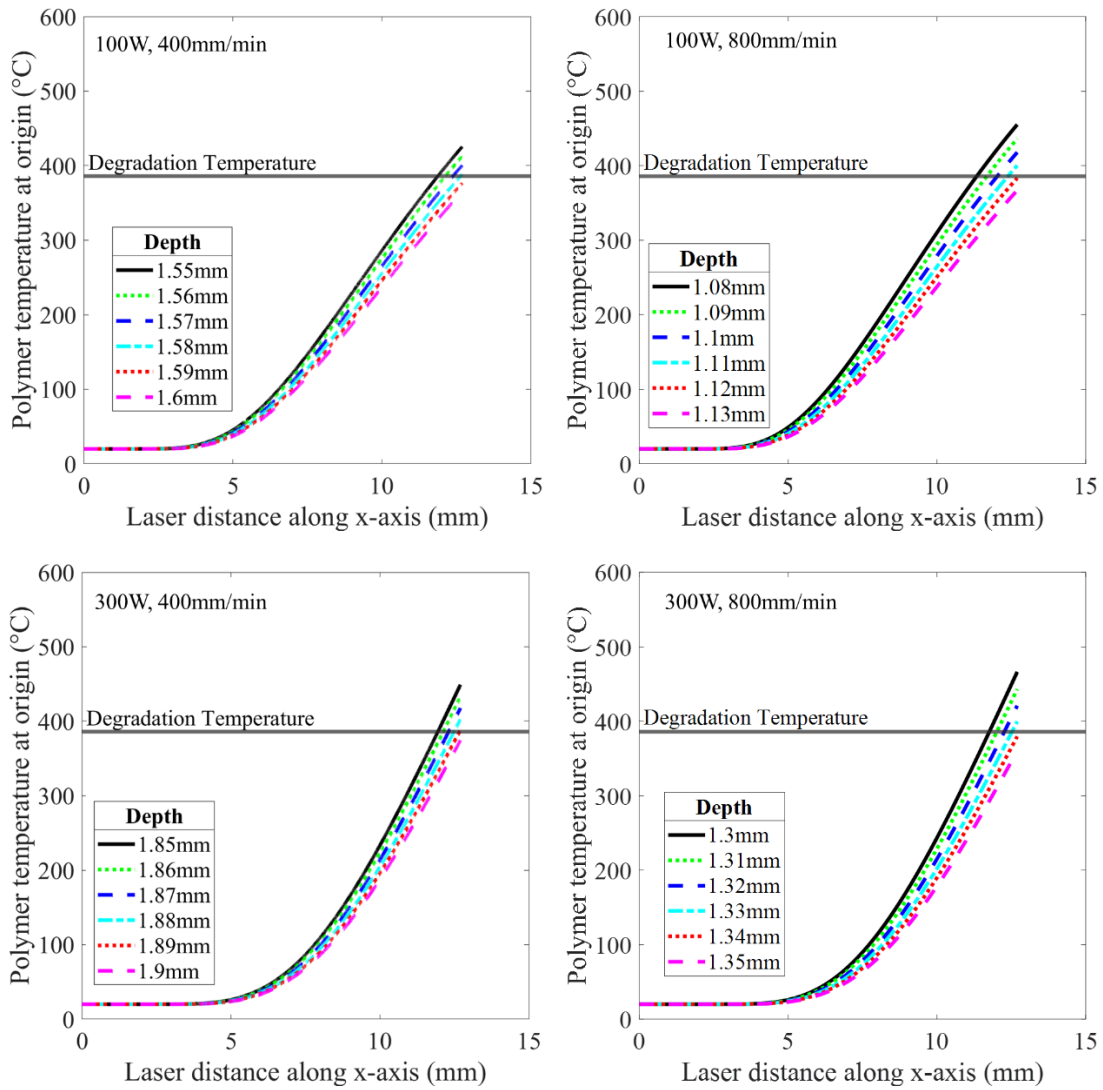


Figure 129: Rosenthal model results for varying laser speed and power on CF ABS.

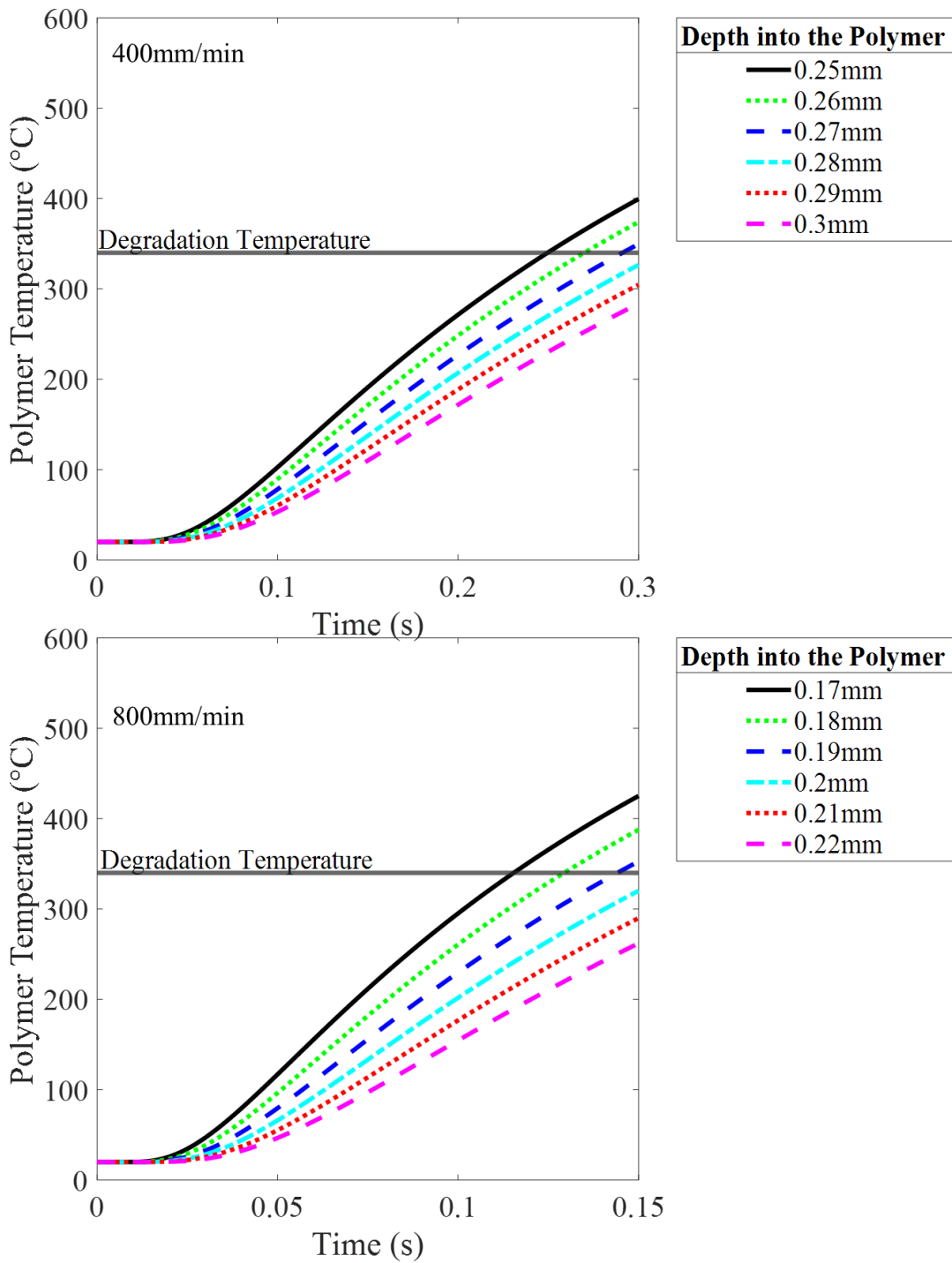


Figure 130: Semi-infinite temperature model results for varying laser speed on PLA.

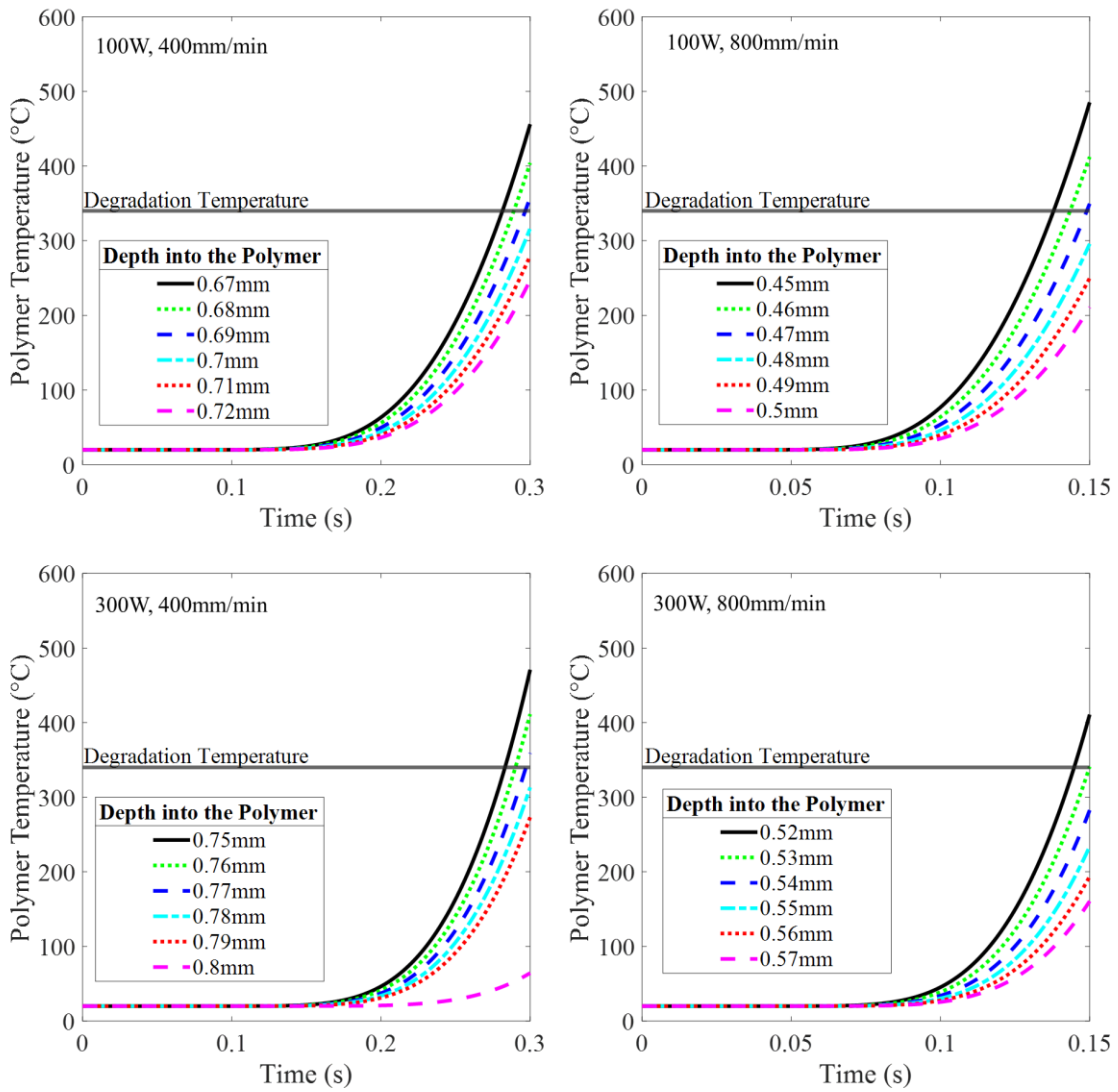


Figure 131: Semi-infinite flux model results for varying laser speed and power on PLA.

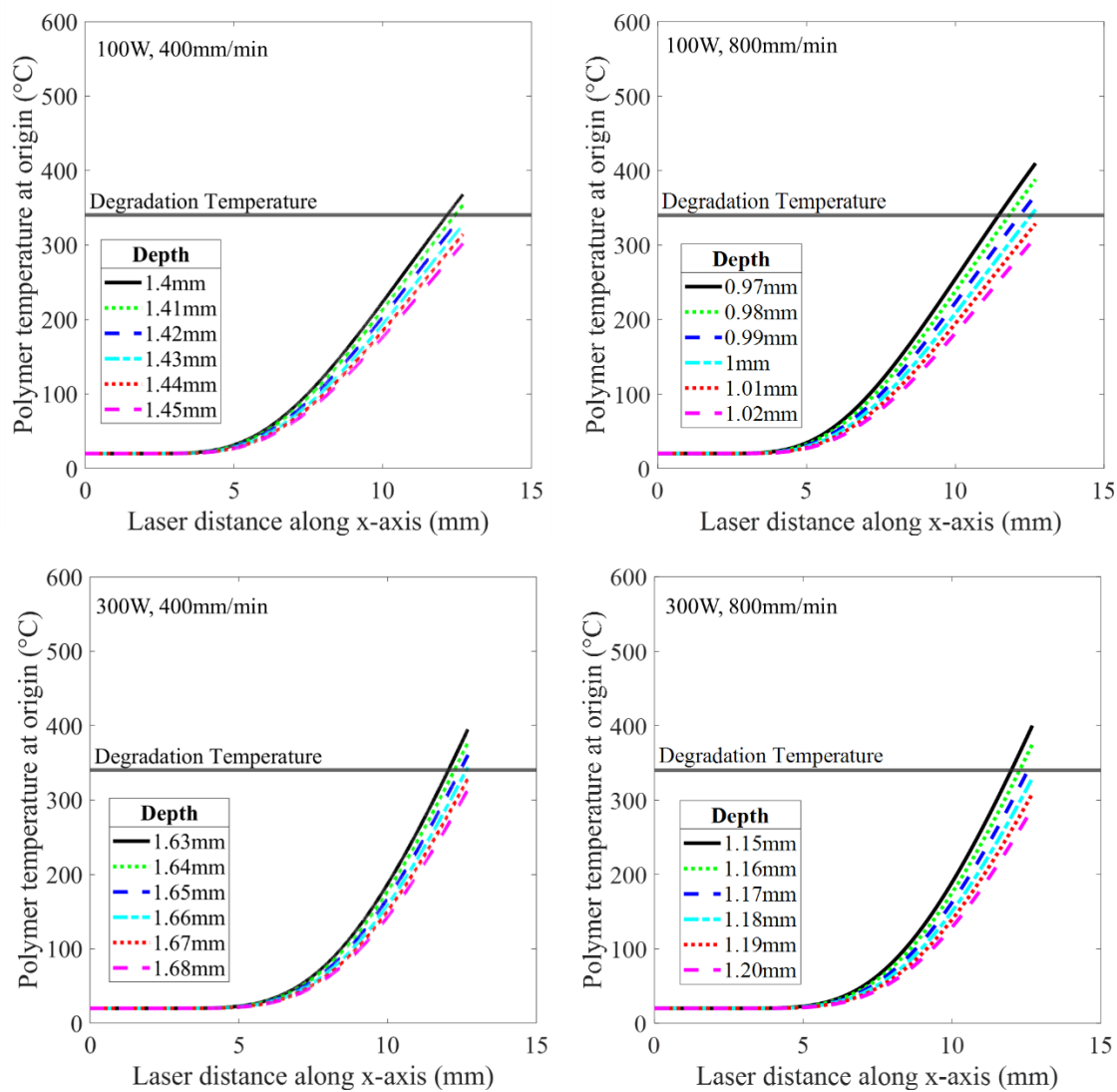


Figure 132: Rosenthal model results for varying laser speed and power on PLA.

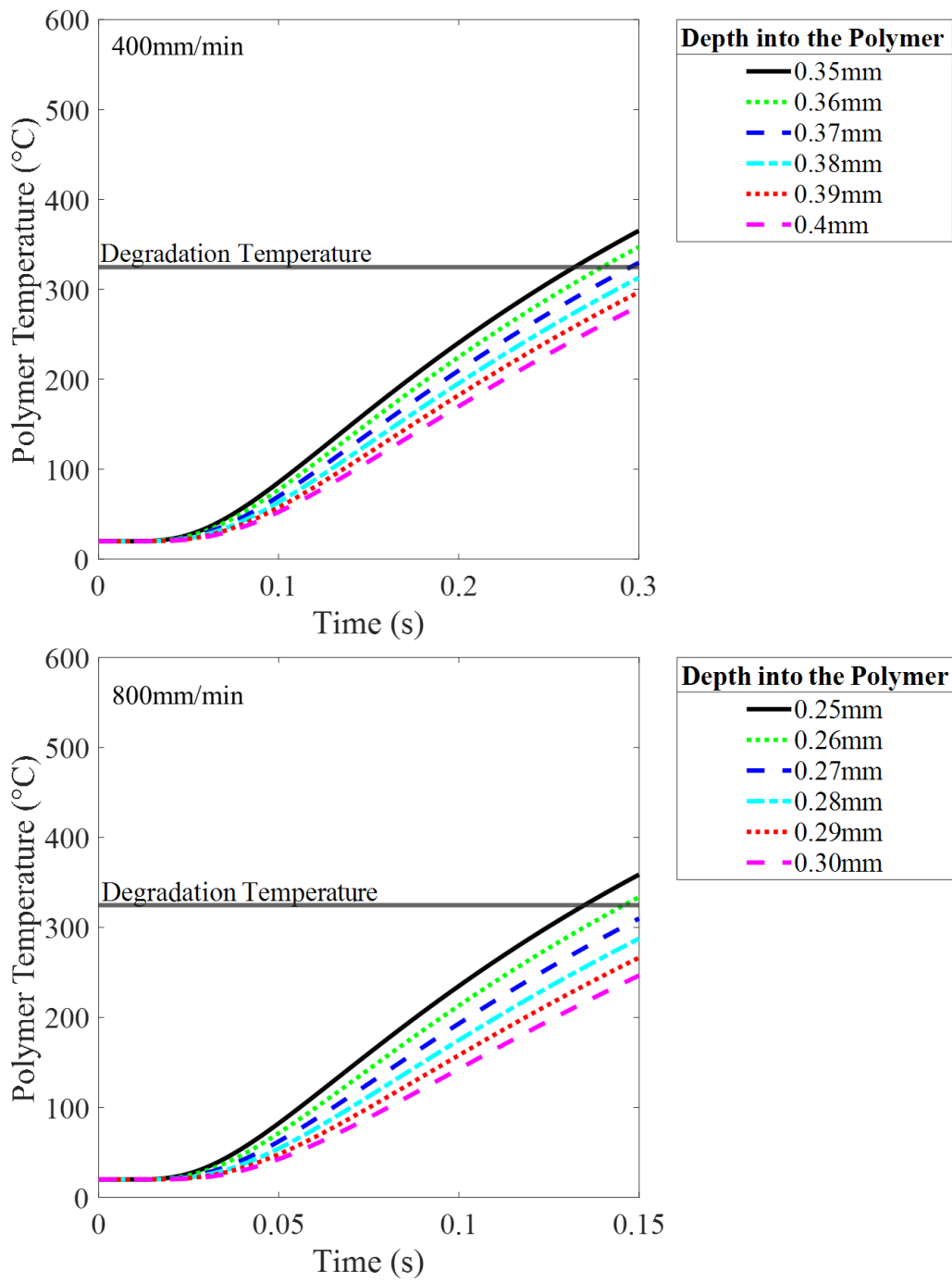


Figure 133: Semi-infinite temperature model results for varying laser speed on WF PLA.

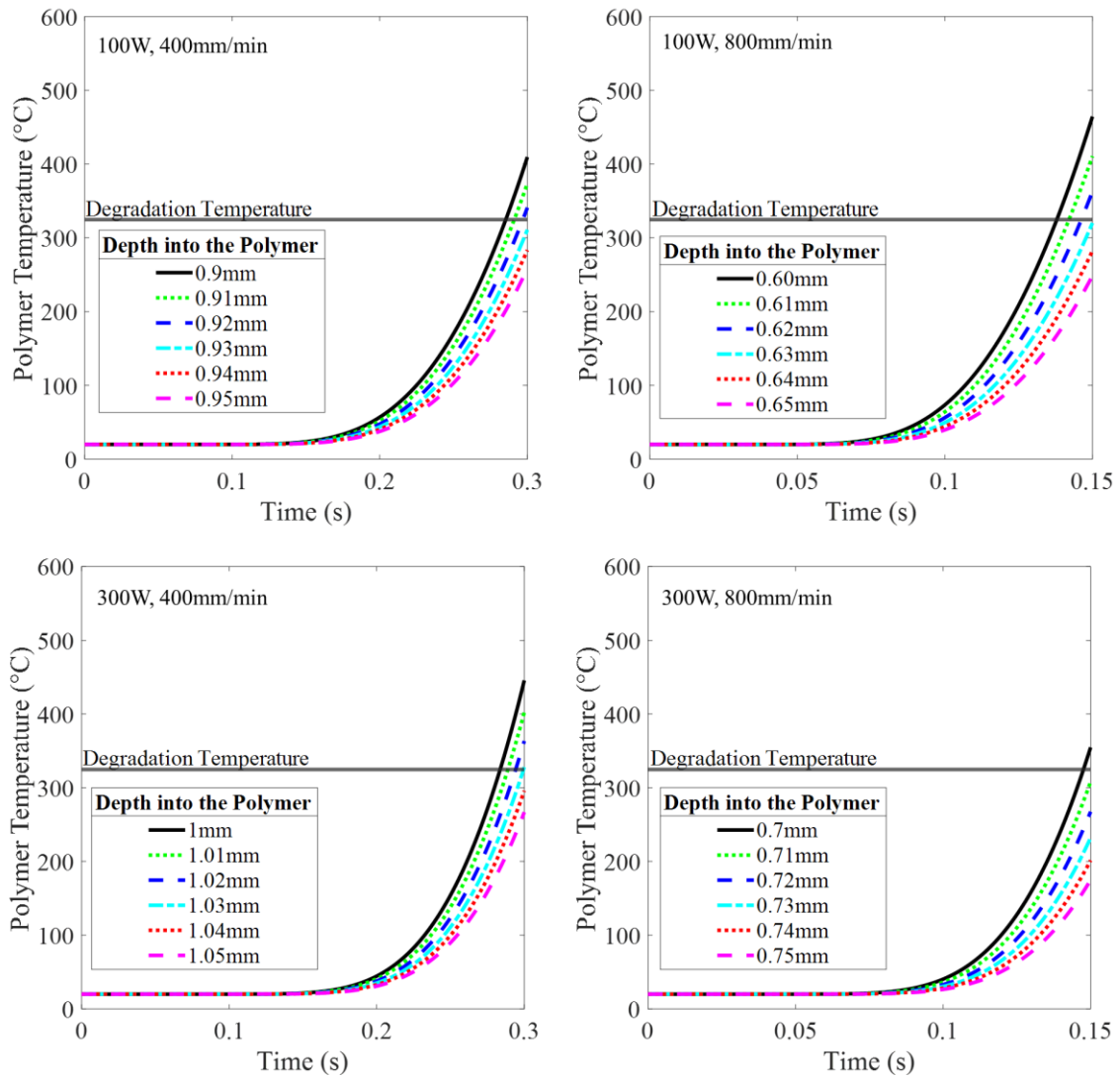


Figure 134: Semi-infinite flux model results for varying laser speed and power on WF PLA.

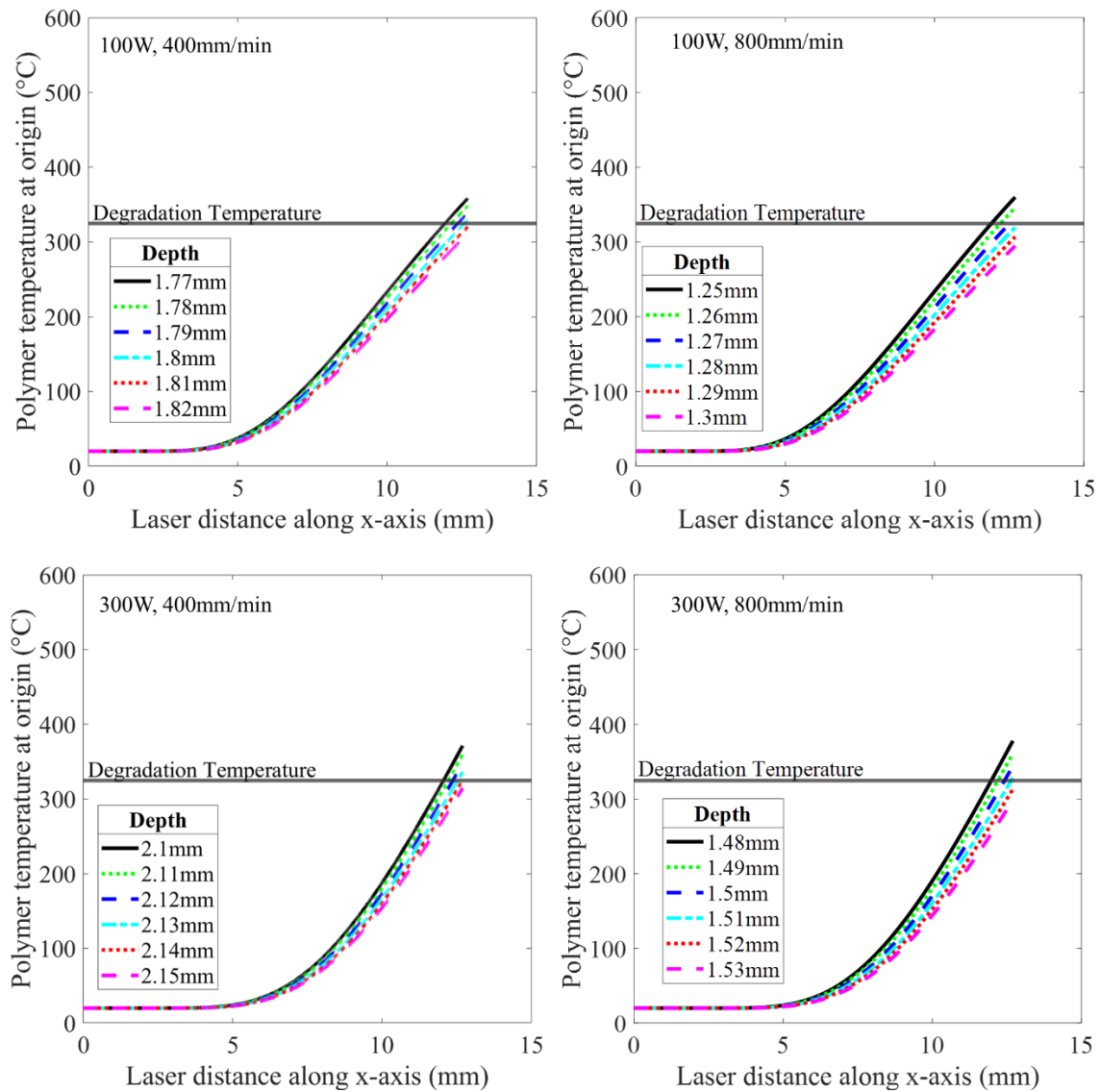


Figure 135: Rosenthal model results for varying laser speed and power on WF PLA.

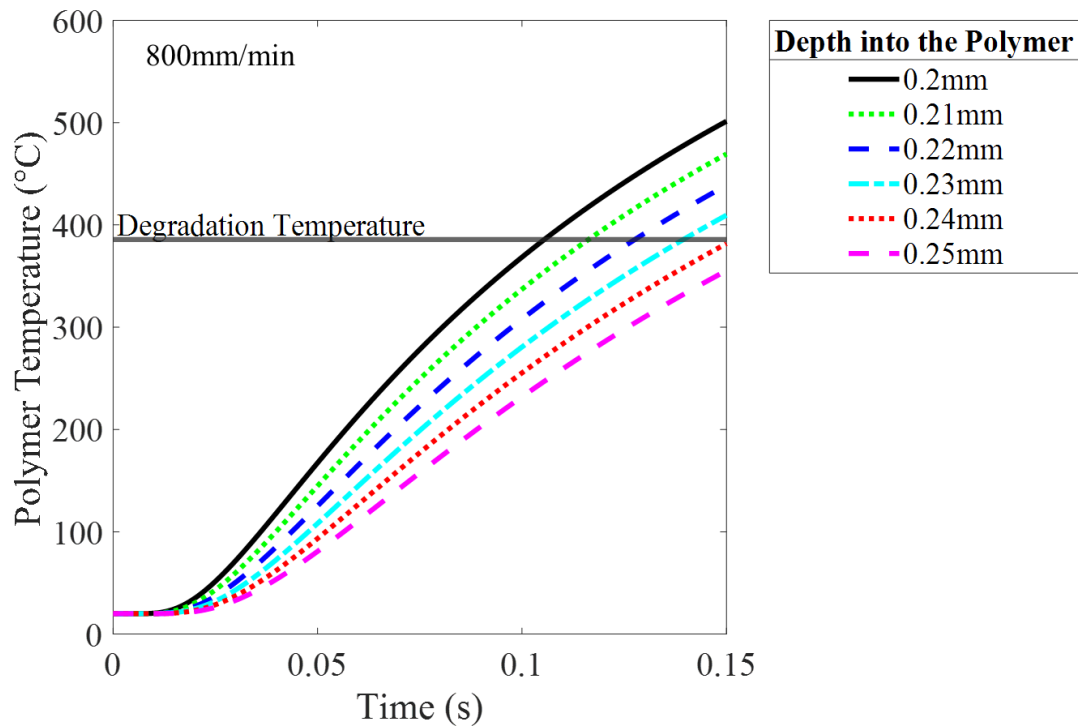
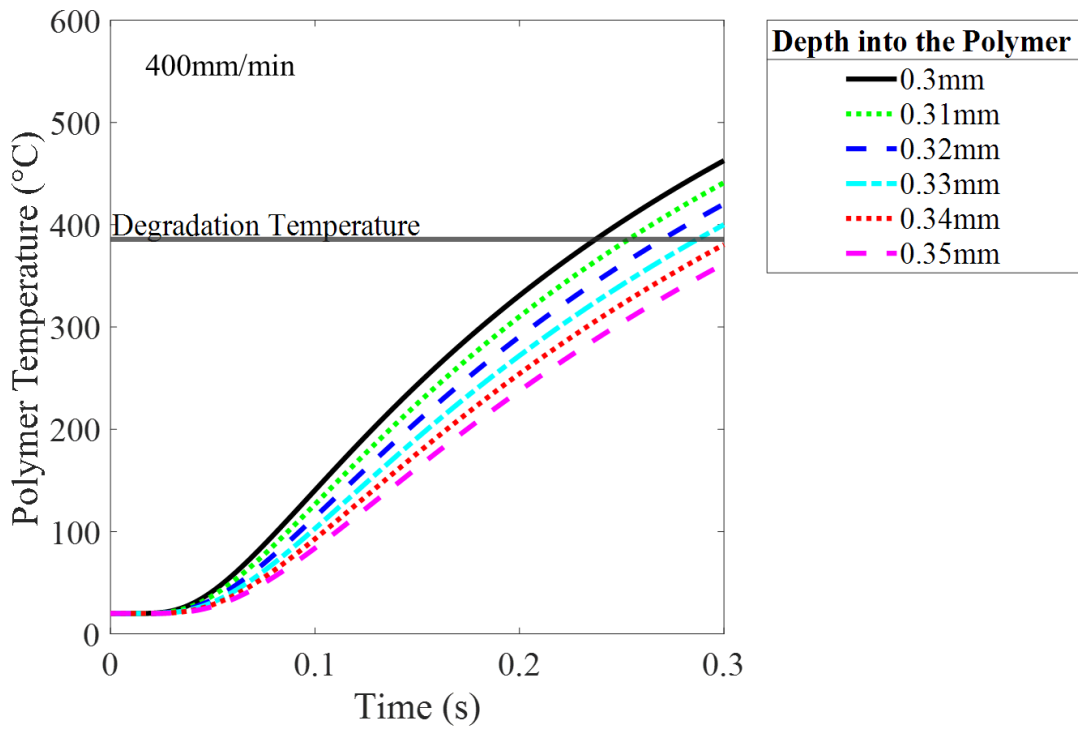


Figure 136: Semi-infinite temperature model results for varying laser speed on GF ABS.

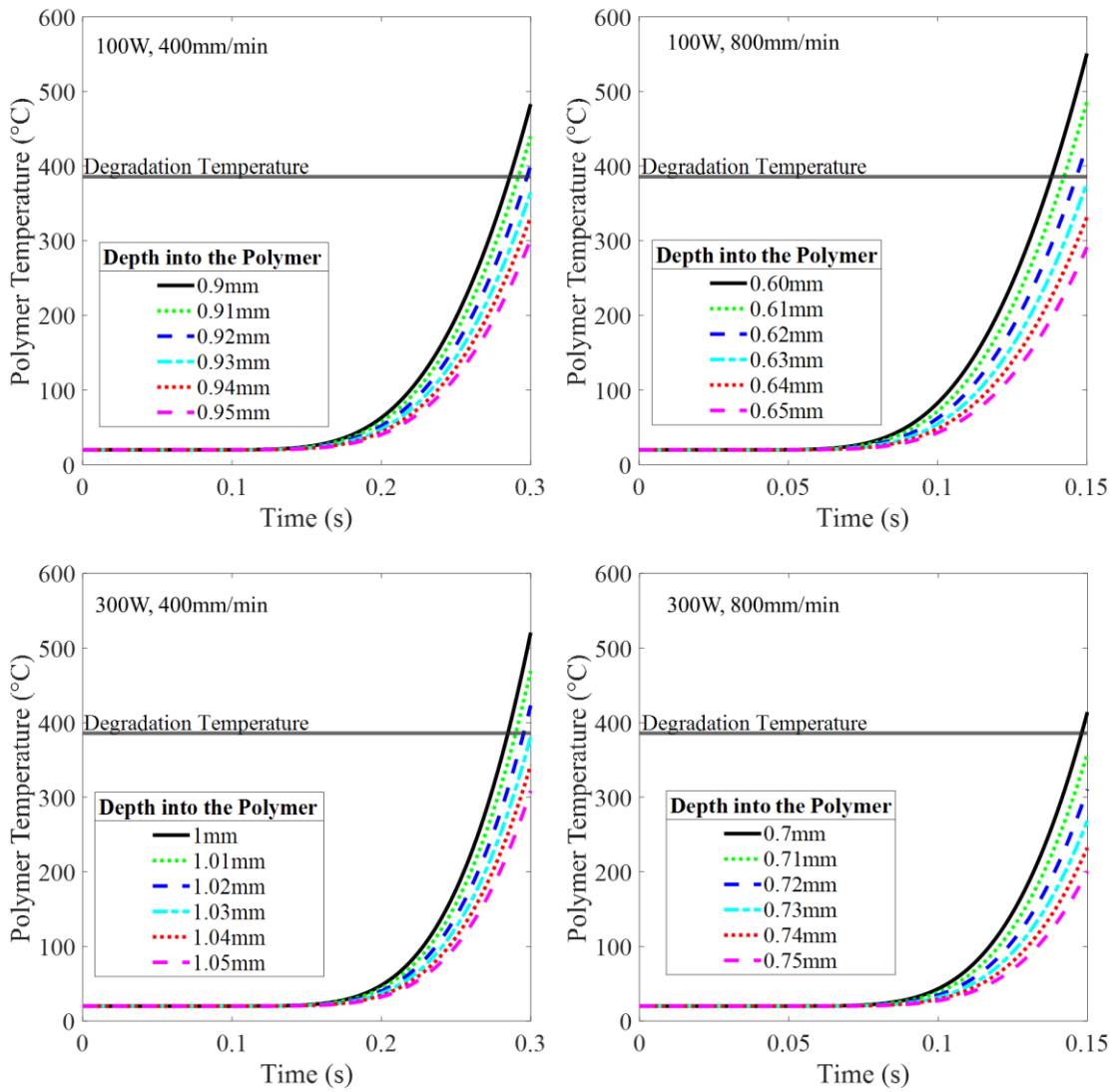


Figure 137: Semi-infinite flux model results for varying laser speed and power on GF ABS.

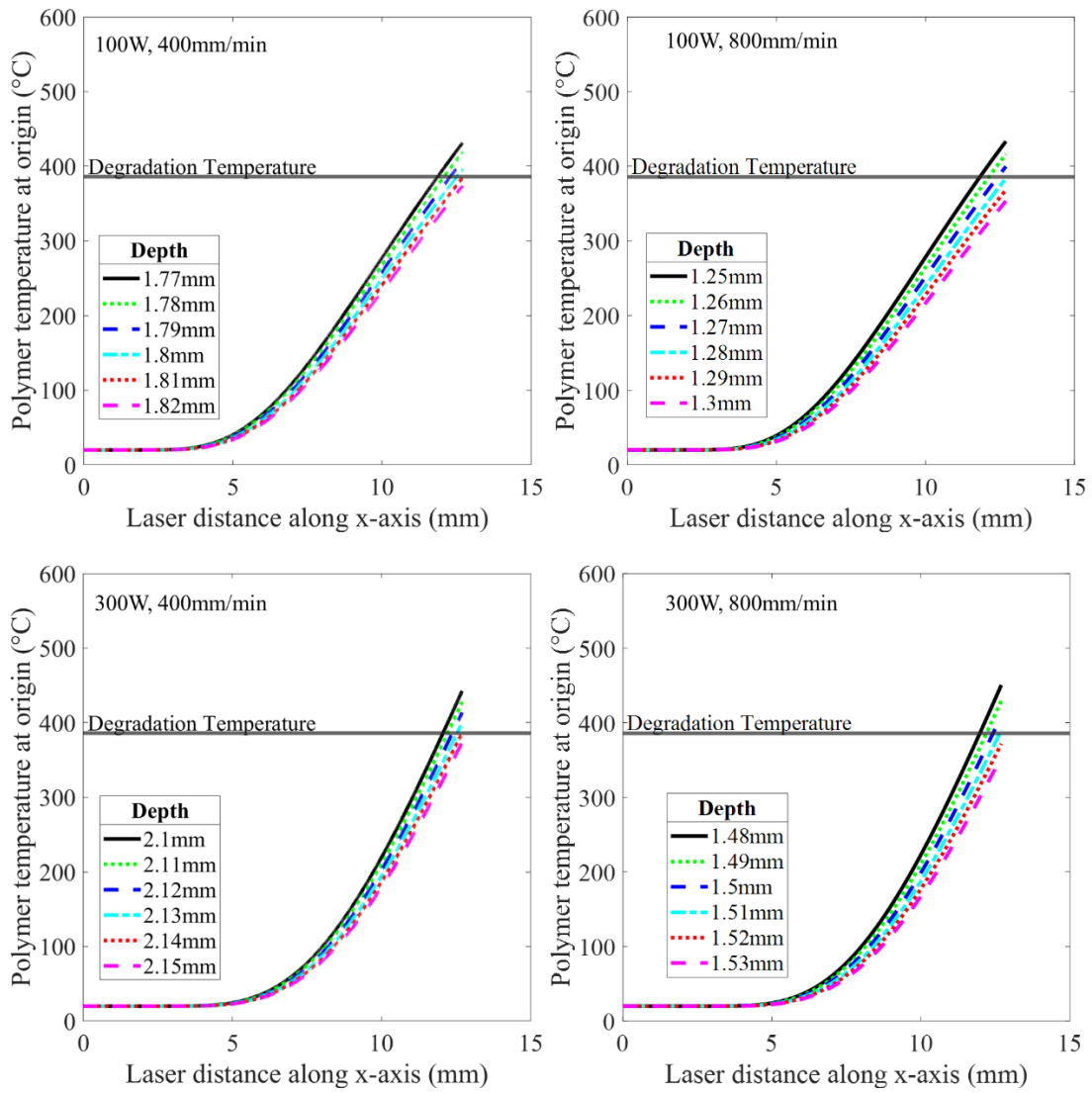


Figure 138: Rosenthal model results for varying laser speed and power on GF ABS.

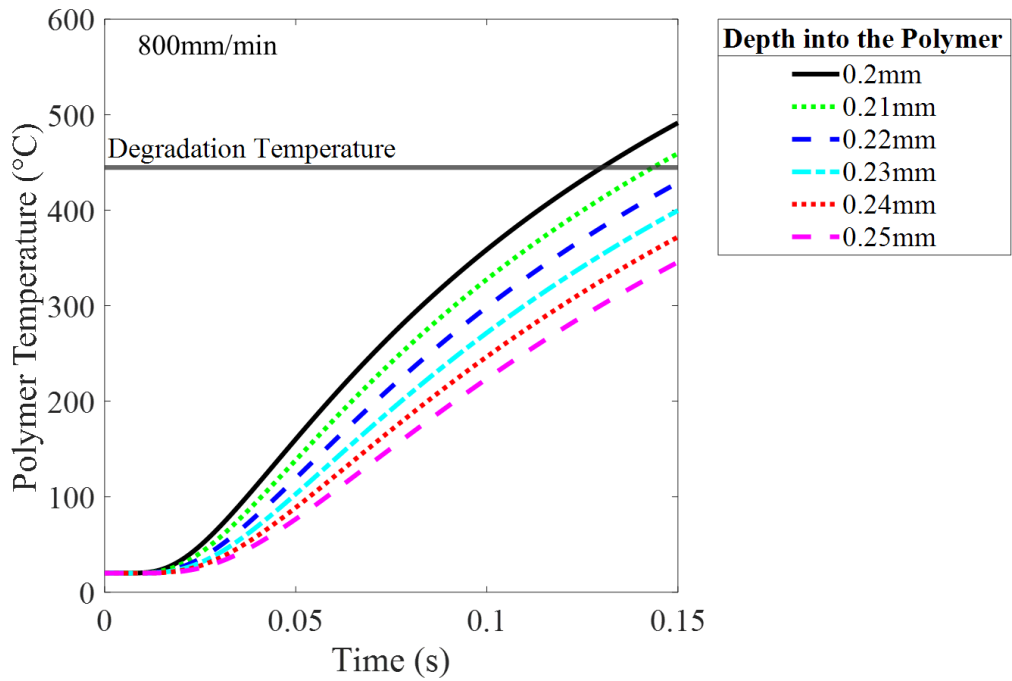
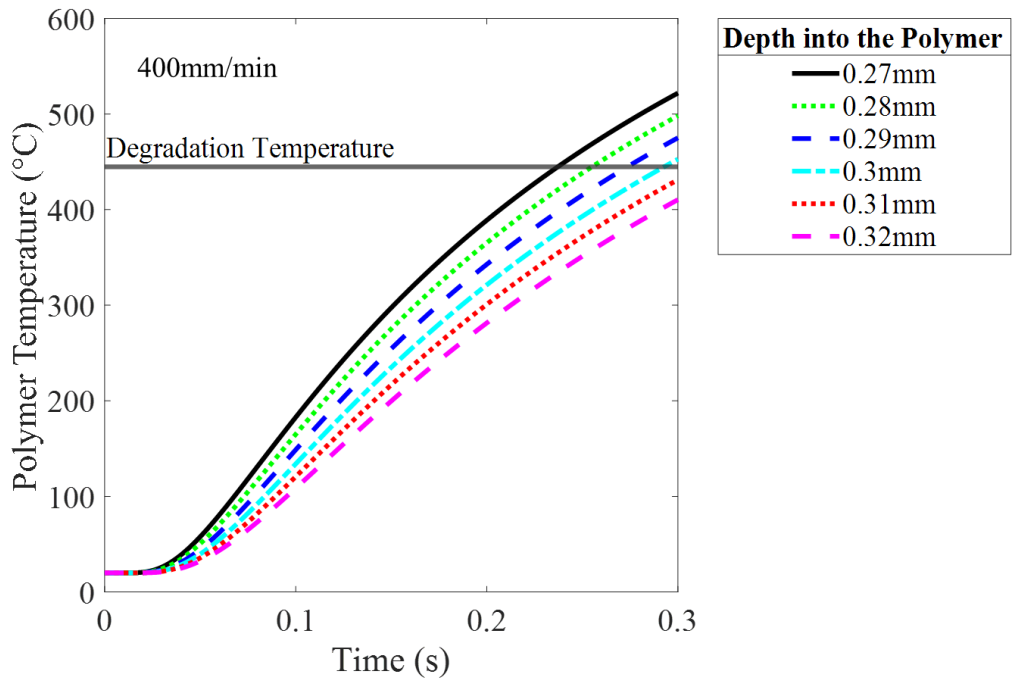


Figure 139: Semi-infinite temperature model results for varying laser speed on GF nylon.

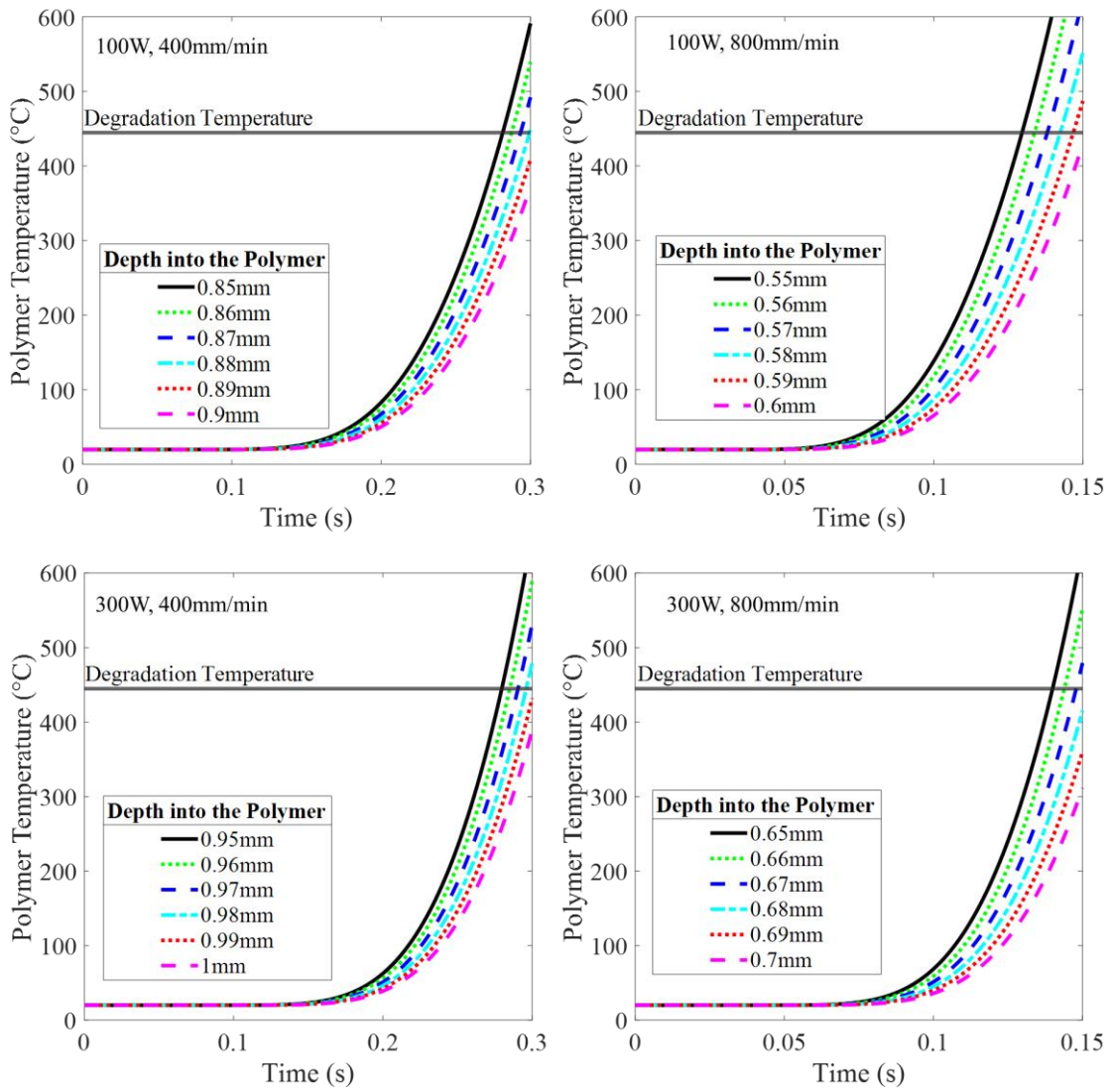


Figure 140: Semi-infinite flux model results for varying laser speed and power on GF nylon.

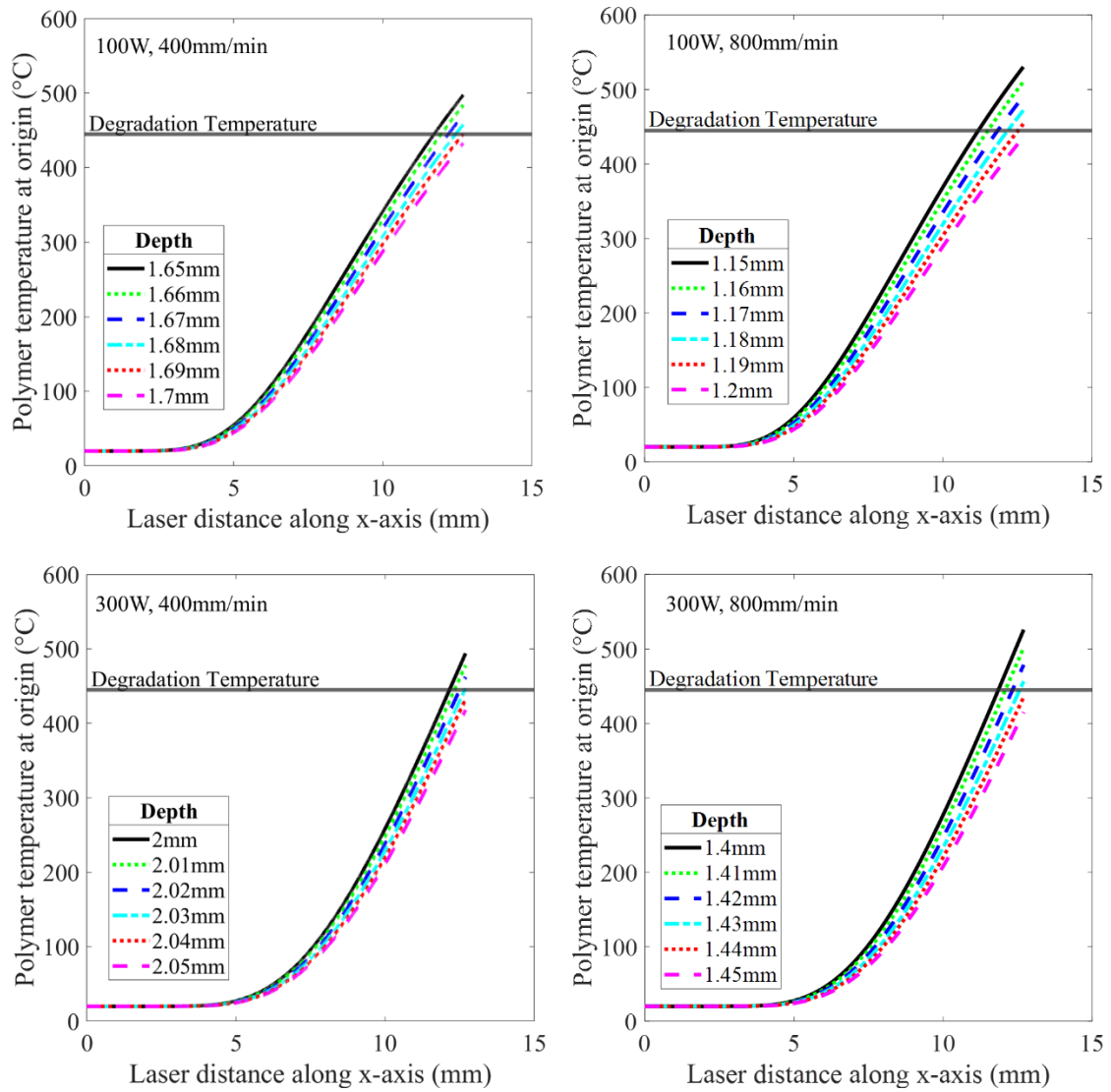


Figure 141: Rosenthal model results for varying laser speed and power on GF nylon.

BIBLIOGRAPHY

- [1] *Standard Terminology for Additive Manufacturing Technologies*, A. International, West Conshohocken, PA, 2012. [Online]. Available: www.astm.org
- [2] "Metal Binder Jetting," (in en-US), *Digital Alloys*, 2019/07/11/T14:11:23-04:00 2019. [Online]. Available: <https://www.digitalalloys.com/blog/binder-jetting/files/427/binder-jetting.html>.
- [3] "VC-500A/5x AM HWD." [Online]. Available: <https://www.mazakusa.com/machines/vc-500a-5x-am-hwdfiles/375/vc-500a-5x-am-hwd.html>.
- [4] K. Saleeby, T. Feldhausen, L. Love, and T. Kurfess, "Rapid retooling for emergency response with hybrid manufacturing," *Smart and Sustainable Manufacturing Systems*, vol. 4, no. 3, 2020.
- [5] H. Bikas, A. Lianos, and P. Stavropoulos, "A design framework for additive manufacturing," *The International Journal of Advanced Manufacturing Technology*, vol. 103, no. 9, pp. 3769-3783, 2019.
- [6] D. Thomas, "The development of design rules for selective laser melting," University of Wales, 2009.
- [7] M. Brezocnik, Z. Lestan, S. Stepisnik, and M. Milfelner, "The use of LENS technology for producing implants," *Trends Dev Mach Assoc Technol*, vol. 14, pp. 625-628, 2010.
- [8] D. M. A. Keicher, NM), Love, James W. (Los Lunas, NM), Dullea, Kevin J. (Albuquerque, NM), Bullen, James L. (Edgewood, NM), Gorman, Pierrette H. (Placitas, NM), Smith, Mark E. (Tijeras, NM), "Forming structures from CAD solid models," United States Patent Appl. 6811744, 2004. [Online]. Available: <https://www.freepatentsonline.com/6811744.html>
- [9] M. Ziaee and N. B. Crane, "Binder jetting: A review of process, materials, and methods," *Additive Manufacturing*, vol. 28, pp. 781-801, 2019/08/01/ 2019, doi: <https://doi.org/10.1016/j.addma.2019.05.031>.
- [10] I. Gibson, D. Rosen, and B. Stucker, "Powder Bed Fusion Processes," in *Additive Manufacturing Technologies: 3D Printing, Rapid Prototyping, and Direct Digital Manufacturing*. New York, NY: Springer New York, 2015, pp. 107-145.
- [11] S. Sun, M. Brandt, and M. Easton, "Powder bed fusion processes: An overview," *Laser Additive Manufacturing*, pp. 55-77, 2017.
- [12] I. Gibson, D. Rosen, and B. Stucker, "Directed Energy Deposition Processes," in *Additive Manufacturing Technologies: 3D Printing, Rapid Prototyping, and Direct Digital Manufacturing*. New York, NY: Springer New York, 2015, pp. 245-268.
- [13] W. E. Frazier, "Metal Additive Manufacturing: A Review," *Journal of Materials Engineering and Performance*, vol. 23, no. 6, pp. 1917-1928, 2014/06/01 2014, doi: 10.1007/s11665-014-0958-z.
- [14] A. Dass and A. Moridi, "State of the art in directed energy deposition: From additive manufacturing to materials design," *Coatings*, vol. 9, no. 7, p. 418, 2019.
- [15] <https://hybridmanutech.com/> (accessed).
- [16] *How 3D Metal Printing Saves Time and Lowers Costs: DED for Repair of Industrial Components*. Optomec. [Online]. Available: http://www.optomec.com/wp-content/uploads/2019/04/DED-Webinar-QA_FINAL_04.4.19.pdf

- [17] A. Paskual, P. Álvarez, and A. Suárez, "Study on arc welding processes for high deposition rate additive manufacturing," *Procedia Cirp*, vol. 68, pp. 358-362, 2018.
- [18] M. Ostolaza, J. I. Arrizubieta, A. Lamikiz, and M. Cortina, "Functionally Graded AISI 316L and AISI H13 Manufactured by L-DED for Die and Mould Applications," (in English), *Appl Sci-Basel*, vol. 11, no. 2, p. 771, Jan 2021, doi: ARTN 771
10.3390/app11020771.
- [19] T. Feldhausen, "Development and evaluation of interfacial structures for hybrid manufacturing," Doctor of Philosophy, Mechanical Engineering, Georgia Institute of Technology, 2020.
- [20] S. Bontha, N. W. Klingbeil, P. A. Kobryn, and H. L. Fraser, "Effects of process variables and size-scale on solidification microstructure in beam-based fabrication of bulky 3D structures," *Materials Science and Engineering: A*, vol. 513-514, pp. 311-318, 2009/07/15/ 2009, doi: <https://doi.org/10.1016/j.msea.2009.02.019>.
- [21] J. Beuth and N. Klingbeil, "The role of process variables in laser-based direct metal solid freeform fabrication," *JOM*, vol. 53, no. 9, pp. 36-39, 2001/09/01 2001, doi: 10.1007/s11837-001-0067-y.
- [22] "Design Guidelines: Direct Metal Laser Sintering (DMLS)." [Online]. Available: <https://www.stratasysdirect.com/resources/design-guidelines/direct-metal-laser-sintering-old>
- [23] D. M. Keicher, J. L. Bullen, P. H. Gorman, J. W. Love, K. J. Dullea, and M. E. Smith, "Forming structures from CAD solid models," ed: Google Patents, 2002.
- [24] G. Zhao, G. Ma, J. Feng, and W. Xiao, "Nonplanar slicing and path generation methods for robotic additive manufacturing," *The International Journal of Advanced Manufacturing Technology*, vol. 96, no. 9, pp. 3149-3159, 2018/06/01 2018, doi: 10.1007/s00170-018-1772-9.
- [25] L. Yuan *et al.*, "Application of multidirectional robotic wire arc additive manufacturing process for the fabrication of complex metallic parts," *IEEE Transactions on Industrial Informatics*, vol. 16, no. 1, pp. 454-464, 2019.
- [26] T. F. Lam, Y. Xiong, A. G. Dharmawan, S. Foong, and G. S. Soh, "Adaptive process control implementation of wire arc additive manufacturing for thin-walled components with overhang features," *The International Journal of Advanced Manufacturing Technology*, pp. 1-11, 2019.
- [27] "Dissolvable Supports in Powder Bed Fusion-Printed Stainless Steel," *3D Printing and Additive Manufacturing*, vol. 4, no. 1, pp. 3-11, 2017, doi: 10.1089/3dp.2016.0043.
- [28] C. Lefky, B. Zucker, D. Wright, A. Nassar, T. Simpson, and O. Hildreth, "Dissolvable Supports in Powder Bed Fusion-Printed Stainless Steel. 3D Printing and Additive Manufacturing 4 (1): 3–11," ed, 2016.
- [29] C. S. Lefky, A. R. Nassar, T. Simpson, and O. J. Hildreth, "Dissolvable metal supports for printed metal parts," in *2016 International Solid Freeform Fabrication Symposium*, 2016: University of Texas at Austin.
- [30] B. N. Zucker, C. Lefky, and O. Hildreth, "Dissolvable Metal Supports-Simplifying Metals Printing," 2016.

- [31] O. J. Hildreth, A. R. Nassar, K. R. Chasse, and T. W. Simpson, "Dissolvable metal supports for 3D direct metal printing," *3D Printing and Additive Manufacturing*, vol. 3, no. 2, pp. 90-97, 2016.
- [32] D. Aspinwall, R. Dewes, J. Burrows, M. Paul, and B. Davies, "Hybrid high speed machining (HSM): System design and experimental results for grinding/HSM and EDM/HSM," *Cirp Annals-manufacturing Technology - CIRP ANN-MANUF TECHNOLOG*, vol. 50, pp. 145-148, 12/31 2001, doi: 10.1016/S0007-8506(07)62091-5.
- [33] Z. Zhu, V. G. Dhokia, A. Nassehi, and S. T. Newman, "A review of hybrid manufacturing processes—state of the art and future perspectives," *International Journal of Computer Integrated Manufacturing*, vol. 26, no. 7, pp. 596-615, 2013.
- [34] J. R. Dufloy, B. Callebaut, J. Verbert, and H. De Baerdemaeker, "Laser Assisted Incremental Forming: Formability and Accuracy Improvement," *CIRP Annals*, vol. 56, no. 1, pp. 273-276, 2007/01/01/ 2007, doi: <https://doi.org/10.1016/j.cirp.2007.05.063>.
- [35] R. Molian, C. Neumann, P. Shrotriya, and P. Molian, "Novel Laser/Water-Jet Hybrid Manufacturing Process for Cutting Ceramics," *Journal of Manufacturing Science and Engineering*, vol. 130, no. 3, 2008, doi: 10.1115/1.2844592.
- [36] K. Lorenz, J. Jones, D. Wimpenny, and M. Jackson, "A review of hybrid manufacturing," in *2014 International Solid Freeform Fabrication Symposium*, 2015: University of Texas at Austin.
- [37] Okuma. <https://www.okuma.com/laser> (accessed 2022).
- [38] O. Kerbrat, P. Mognol, and J. Y. Hascoet, "Manufacturing complexity evaluation at the design stage for both machining and layered manufacturing," *CIRP Journal of Manufacturing Science and Technology*, vol. 2, no. 3, pp. 208-215, 2010/01/01/ 2010, doi: <https://doi.org/10.1016/j.cirpj.2010.03.007>.
- [39] Y. Yang, Y. Gong, S. Qu, Y. Rong, Y. Sun, and M. Cai, "Densification, surface morphology, microstructure and mechanical properties of 316L fabricated by hybrid manufacturing," *The International Journal of Advanced Manufacturing Technology*, vol. 97, no. 5, pp. 2687-2696, 2018.
- [40] A. A. Krimpenis, V. Papapaschos, and E. Bontarenko, "HydraX, a 3D printed robotic arm for hybrid manufacturing. Part I: Custom design, manufacturing and assembly," *Procedia Manufacturing*, vol. 51, pp. 103-108, 2020.
- [41] M. Pranieicz, T. Kurfess, and C. Saldana, "Adaptive geometry transformation and repair for hybrid manufacturing," *Procedia Manufacturing*, vol. 26, pp. 228-236, 2018.
- [42] L. Ren, K. Eiamsa-ard, J. Ruan, and F. Liou, "Part repairing using a hybrid manufacturing system," in *International Manufacturing Science and Engineering Conference*, 2007, vol. 42908, pp. 1-8.
- [43] K. N. Reddy and A. Kumar, "Capacity investment and inventory planning for a hybrid manufacturing–remanufacturing system in the circular economy," *International Journal of Production Research*, vol. 59, no. 8, pp. 2450-2478, 2021.
- [44] A. Smith, L. Wrobel, B. McCalla, P. Allan, and P. Hornsby, "A computational model for the cooling phase of injection moulding," *Journal of materials processing technology*, vol. 195, no. 1-3, pp. 305-313, 2008.

- [45] D. Tomasoni, S. Colosio, L. Giorleo, and E. Ceretti, "Design for additive manufacturing: thermoforming mold optimization via conformal cooling channel technology," *Procedia Manufacturing*, vol. 47, pp. 1117-1122, 2020.
- [46] M. Soshi, J. Ring, C. Young, Y. Oda, and M. Mori, "Innovative grid molding and cooling using an additive and subtractive hybrid CNC machine tool," *CIRP Annals*, vol. 66, no. 1, pp. 401-404, 2017/01/01/ 2017, doi: <https://doi.org/10.1016/j.cirp.2017.04.093>.
- [47] R. G. Gould, "The LASER, light amplification by stimulated emission of radiation," in *The Ann Arbor conference on optical pumping, the University of Michigan*, 1959, vol. 15, no. 128, p. 92.
- [48] T. H. Maiman, "Stimulated optical radiation in ruby," 1960.
- [49] C. H. T. Arthur L Schawlow, "Masers and maser communications system," United States Patent US2929922, 1960.
- [50] W. M. Steen, *Laser material processing*, 2nd ed. ed. London ;: Springer, 1998.
- [51] A. Einstein, "Zur quantentheorie der strahlung," *Phys. Z.*, vol. 18, p. 124, 1917.
- [52] R. Ladenburg, "Untersuchungen über die anomale Dispersion angeregter Gase," *Zeitschrift für Physik*, vol. 48, no. 1, pp. 15-25, 1928/01/01 1928, doi: 10.1007/BF01351571.
- [53] A. E. Siegman, *Lasers*. University science books, 1986.
- [54] H. Kogelnik and T. Li, "Laser Beams and Resonators," *Appl. Opt.*, vol. 5, no. 10, pp. 1550-1567, 1966/10/01 1966, doi: 10.1364/AO.5.001550.
- [55] M. J. Weber, *Handbook of laser wavelengths*. CRC press, 2018.
- [56] C. Ageorges and L. Ye, *Fusion bonding of polymer composites*. Springer Science & Business Media, 2002.
- [57] C. S. Davis, K. E. Hillgartner, S. H. Han, and J. E. Seppala, "Mechanical strength of welding zones produced by polymer extrusion additive manufacturing," *Additive manufacturing*, vol. 16, pp. 162-166, 2017.
- [58] V. Schöppner and K. P. KTP, "Mechanical properties of fused deposition modeling parts manufactured with Ultem* 9085," in *Proceedings of the 69th Annual Technical Conference of the Society of Plastics Engineers (ANTEC'11), Boston, MA, USA*, 2011, pp. 1-5.
- [59] J. E. Seppala, S. H. Han, K. E. Hillgartner, C. S. Davis, and K. B. Migler, "Weld formation during material extrusion additive manufacturing," *Soft matter*, vol. 13, no. 38, pp. 6761-6769, 2017.
- [60] Q. Sun, G. Rizvi, C. Bellehumeur, and P. Gu, "Effect of processing conditions on the bonding quality of FDM polymer filaments," *Rapid prototyping journal*, 2008.
- [61] F. Bachmann and U. Russek, *Laser welding of polymers using high-power diode lasers* (Laser Processing of Advanced Materials and Laser Microtechnologies). SPIE, 2003.
- [62] E. De La Perrelle, T. Moss, and H. Herbert, "The measurements of absorptivity and reflectivity," *Infrared Physics*, vol. 3, no. 1, pp. 35-43, 1963.
- [63] M. J. Troughton, "8.1 Process Description," in *Handbook of Plastics Joining - A Practical Guide (2nd Edition)*: William Andrew Publishing.
- [64] D. Grewell, P. Rooney, and V. A. Kagan, "Relationship between Optical Properties and Optimized Processing Parameters for through-Transmission Laser Welding of

- Thermoplastics," *Journal of Reinforced Plastics and Composites*, vol. 23, no. 3, pp. 239-247, 2004, doi: 10.1177/0731684404030732.
- [65] M. Chen, G. Zak, and P. J. Bates, "Effect of carbon black on light transmission in laser welding of thermoplastics," *Journal of Materials Processing Technology*, vol. 211, no. 1, pp. 43-47, 2011/01/01/ 2011, doi: <https://doi.org/10.1016/j.jmatprotec.2010.08.017>.
- [66] M. Ilie, J.-C. Kneip, S. Mattei, A. Nichici, C. Roze, and T. Girasole, "Through-transmission laser welding of polymers – temperature field modeling and infrared investigation," *Infrared Physics & Technology*, vol. 51, no. 1, pp. 73-79, 2007/07/01/ 2007, doi: <https://doi.org/10.1016/j.infrared.2007.02.003>.
- [67] N. Kumar and A. Bandyopadhyay, "A State-of-the-Art Review of Laser Welding of Polymers — Part I: Welding Parameters," *Welding Journal*, Article vol. 100, no. 7, pp. 221-s-228-s, 07// 2021, doi: 10.29391/2021.100.019.
- [68] W. Horn, "Strategies for Polymer Welding with High-Power Diode Lasers," *Key engineering materials*, vol. 447-448, pp. 277-281, 2010, doi: 10.4028/www.scientific.net/KEM.447-448.277.
- [69] T. Ussing, L. V. Petersen, C. B. Nielsen, B. Helbo, and L. Højslet, "Micro laser welding of polymer microstructures using low power laser diodes," *International journal of advanced manufacturing technology*, vol. 33, no. 1, pp. 198-205, 2007, doi: 10.1007/s00170-007-0969-0.
- [70] N. Masmiaati and P. K. Philip, "Investigations on laser percussion drilling of some thermoplastic polymers," *Journal of Materials Processing Technology*, vol. 185, no. 1, pp. 198-203, 2007/04/30/ 2007, doi: <https://doi.org/10.1016/j.jmatprotec.2006.03.151>.
- [71] S. Fatimah, M. Ishak, and S. N. Aqida, "CO₂ Laser Cutting of Glass Fiber Reinforce Polymer Composite," (in English), *IOP Conference Series. Materials Science and Engineering*, vol. 36, no. 1, Sep 2012 2021-08-25 2012, doi: <http://dx.doi.org/10.1088/1757-899X/36/1/012033>.
- [72] N. K. Tolochko, Y. V. Khlopkov, S. E. Mozzharov, M. B. Ignatiev, T. Laoui, and V. I. Titov, "Absorptance of powder materials suitable for laser sintering," (in English), *Rapid Prototyping Journal*, vol. 6, no. 3, pp. 155-160, 2000 2021-09-10 2000, doi: <http://dx.doi.org/10.1108/13552540010337029>.
- [73] J. H. Brannon and J. R. Lankard, "Pulsed CO₂ laser etching of polyimide," *Applied Physics Letters*, vol. 48, no. 18, pp. 1226-1228, 1986, doi: 10.1063/1.96989.
- [74] H. Hügel and F. Dausinger, "1.1 Fundamentals of laser-induced processes," *Laser applications*, pp. 3-25, 2004.
- [75] S. Engler, R. Ramsayer, and R. Poprawe, "Process studies on laser welding of copper with brilliant green and infrared lasers," *Physics Procedia*, vol. 12, pp. 339-346, 2011.
- [76] H.-C. Tran, Y.-L. Lo, and M.-H. Huang, "Analysis of scattering and absorption characteristics of metal powder layer for selective laser sintering," *IEEE/ASME Transactions On Mechatronics*, vol. 22, no. 4, pp. 1807-1817, 2017.
- [77] J. Trapp, A. M. Rubenchik, G. Guss, and M. J. Matthews, "In situ absorptivity measurements of metallic powders during laser powder-bed fusion additive manufacturing," *Applied Materials Today*, vol. 9, pp. 341-349, 2017/12/01/ 2017, doi: <https://doi.org/10.1016/j.apmt.2017.08.006>.

- [78] L. J. Love and C. Duty, "Cincinnati big area additive manufacturing (BAAM)," *Oak Ridge, TN*, 2015.
- [79] W. L. Hawkins, "Polymer Degradation," in *Polymer Degradation and Stabilization*, W. L. Hawkins Ed. Berlin, Heidelberg: Springer Berlin Heidelberg, 1984, pp. 3-34.
- [80] M. Platz, R. A. Moss, and M. Jones, *Reviews of reactive intermediate chemistry*. Hoboken, N.J: Wiley-Interscience, 2007.
- [81] M. Favaloro, "Ablative Materials," in *Kirk-Othmer Encyclopedia of Chemical Technology*.
- [82] A. Balakrishnan, W. Nicolet, S. Sandhu, and J. Dodson, "Galileo probe thermal protection: Entry heating environments and spallation experiments design," 1979.
- [83] R. Farmer, "Extended heating ablation of carbon phenolic and silica phenolic," AIR FORCE MATERIALS LAB WRIGHT-PATTERSON AFB OH, 1974.
- [84] M. Trojan, "Transient Heat Conduction in Semi-infinite Solid with Surface Convection," in *Encyclopedia of Thermal Stresses*, R. B. Hetnarski Ed. Dordrecht: Springer Netherlands, 2014, pp. 6181-6186.
- [85] D. Rosenthal, "Mathematical Theory of Heat Distribution during Welding and Cutting," *Welding Journal*, vol. 20, pp. 220-234, 1941.
- [86] A. Plotkowski, M. M. Kirka, and S. S. Babu, "Verification and validation of a rapid heat transfer calculation methodology for transient melt pool solidification conditions in powder bed metal additive manufacturing," *Additive Manufacturing*, vol. 18, pp. 256-268, 2017/12/01/ 2017, doi: <https://doi.org/10.1016/j.addma.2017.10.017>.
- [87] P. Promopattum, S.-C. Yao, P. C. Pistorius, and A. D. Rollett, "A Comprehensive Comparison of the Analytical and Numerical Prediction of the Thermal History and Solidification Microstructure of Inconel 718 Products Made by Laser Powder-Bed Fusion," *Engineering*, vol. 3, no. 5, pp. 685-694, 2017/10/01/ 2017, doi: <https://doi.org/10.1016/J.ENG.2017.05.023>.
- [88] J. C. Jaeger, "Moving Sources of Heat and the Temperature of Sliding Contacts," 1942.
- [89] R. Komanduri and Z. B. Hou, "Thermal analysis of the laser surface transformation hardening process," *International Journal of Heat and Mass Transfer*, vol. 44, no. 15, pp. 2845-2862, 2001/08/01/ 2001, doi: [https://doi.org/10.1016/S0017-9310\(00\)00316-1](https://doi.org/10.1016/S0017-9310(00)00316-1).
- [90] R. Komanduri and Z. B. Hou, "Thermal analysis of the arc welding process: Part I. General solutions," *Metallurgical and Materials Transactions B*, vol. 31, no. 6, pp. 1353-1370, 2000/12/01 2000, doi: 10.1007/s11663-000-0022-2.
- [91] B. Ribic, T. Palmer, and T. DeRoy, "Problems and issues in laser-arc hybrid welding," *International materials reviews*, vol. 54, no. 4, pp. 223-244, 2009.
- [92] M. Ericsson and R. Sandström, "Influence of welding speed on the fatigue of friction stir welds, and comparison with MIG and TIG," *International journal of fatigue*, vol. 25, no. 12, pp. 1379-1387, 2003.
- [93] N. N. Rykalin, "Calculation of heat processes in welding," 1960.
- [94] C. Hamilton, S. Dymek, and A. Sommers, "A thermal model of friction stir welding in aluminum alloys," *International Journal of Machine Tools and Manufacture*,

- vol. 48, no. 10, pp. 1120-1130, 2008/08/01/ 2008, doi: <https://doi.org/10.1016/j.ijmachtools.2008.02.001>.
- [95] "Total production of crude steel." World Steel Association. https://worldsteel.org/steel-by-topic/statistics/annual-production-steel-data/P1_crude_steel_total_pub/CHN/IND/WORLD_ALL (accessed February 24, 2022).
- [96] A. C. Reardon, "2.4 Crystal Structure of Metals," in *Metallurgy for the Non-Metallurgist (2nd Edition)*: ASM International.
- [97] J. C. Lippold and D. J. Kotecki, "1.3 Types of Stainless Steel and Their Application," in *Welding Metallurgy and Weldability of Stainless Steels*: John Wiley & Sons.
- [98] R. Abbaschian, L. Abbaschian, and R. E. Reed-Hill, *Physical metallurgy principles*, 4th ed. ed. Stamford, CT: Cengage Learning, 2009.
- [99] P. Korinko and S. Malene, "Considerations for the weldability of types 304L and 316L stainless steel," *practical failure analysis*, vol. 1, pp. 61-68, 2001.
- [100] J. C. Lippold and D. J. Kotecki, "6.1 Standard Alloys and Consumables," in *Welding Metallurgy and Weldability of Stainless Steels*: John Wiley & Sons.
- [101] J. C. Lippold and D. J. Kotecki, "6.3 Welding Metallurgy," in *Welding Metallurgy and Weldability of Stainless Steels*: John Wiley & Sons.
- [102] J. D. Verhoeven, "1. Pure Iron," in *Steel Metallurgy for the Non-Metallurgist*: ASM International.
- [103] B. Weiss and R. Stickler, "Phase instabilities during high temperature exposure of 316 austenitic stainless steel," *Metallurgical and Materials Transactions B*, vol. 3, no. 4, pp. 851-866, 1972.
- [104] J. D. Verhoeven, "3. Steel and the Iron-Carbon Phase Diagram," in *Steel Metallurgy for the Non-Metallurgist*: ASM International.
- [105] J. C. Lippold and D. J. Kotecki, "1.1 Definition of a Stainless Steel," in *Welding Metallurgy and Weldability of Stainless Steels*: John Wiley & Sons.
- [106] "Substitutional Alloys," 2021/2/3/. [Online]. Available: <https://chem.libretexts.org/@go/page/2594>.
- [107] J. C. Lippold and D. J. Kotecki, "3.1.8 Interstitial Elements: Carbon and Nitrogen," in *Welding Metallurgy and Weldability of Stainless Steels*: John Wiley & Sons.
- [108] J. C. Lippold and D. J. Kotecki, "3.1.2 Nickel," in *Welding Metallurgy and Weldability of Stainless Steels*: John Wiley & Sons.
- [109] J. C. Lippold and D. J. Kotecki, "3.1 Alloying Elements in Stainless Steels," in *Welding Metallurgy and Weldability of Stainless Steels*: John Wiley & Sons.
- [110] Z. E. E. Tan, J. H. L. Pang, J. Kaminski, and H. Pepin, "Characterisation of porosity, density, and microstructure of directed energy deposited stainless steel AISI 316L," *Additive Manufacturing*, vol. 25, pp. 286-296, 2019/01/01/ 2019, doi: <https://doi.org/10.1016/j.addma.2018.11.014>.
- [111] F. Weng, S. Gao, J. Jiang, J. Wang, and P. Guo, "A novel strategy to fabricate thin 316L stainless steel rods by continuous directed energy deposition in Z direction," *Additive Manufacturing*, vol. 27, pp. 474-481, 2019/05/01/ 2019, doi: <https://doi.org/10.1016/j.addma.2019.03.024>.
- [112] J. S. Kim, B. J. Kang, and S. W. Lee, "An experimental study on microstructural characteristics and mechanical properties of stainless-steel 316L parts using

- directed energy deposition (DED) process," *Journal of Mechanical Science and Technology*, vol. 33, no. 12, pp. 5731-5737, 2019.
- [113] A. Saboori, A. Aversa, G. Marchese, S. Biamino, M. Lombardi, and P. Fino, "Microstructure and mechanical properties of AISI 316L produced by directed energy deposition-based additive manufacturing: A review," *Applied Sciences*, vol. 10, no. 9, p. 3310, 2020.
- [114] A. Saboori *et al.*, "An investigation on the effect of powder recycling on the microstructure and mechanical properties of AISI 316L produced by Directed Energy Deposition," *Materials Science and Engineering: A*, vol. 766, p. 138360, 2019/10/24/ 2019, doi: <https://doi.org/10.1016/j.msea.2019.138360>.
- [115] D. Boisselier and S. Sankaré, "Influence of powder characteristics in laser direct metal deposition of SS316L for metallic parts manufacturing," *Physics Procedia*, vol. 39, pp. 455-463, 2012.
- [116] B. Zheng *et al.*, "On the evolution of microstructure and defect control in 316L SS components fabricated via directed energy deposition," *Materials Science and Engineering: A*, vol. 764, p. 138243, 2019.
- [117] D.-R. Eo, S.-H. Park, and J.-W. Cho, "Inclusion evolution in additive manufactured 316L stainless steel by laser metal deposition process," *Materials & Design*, vol. 155, pp. 212-219, 2018/10/05/ 2018, doi: <https://doi.org/10.1016/j.matdes.2018.06.001>.
- [118] M. Mukherjee, "Effect of build geometry and orientation on microstructure and properties of additively manufactured 316L stainless steel by laser metal deposition," *Materialia*, vol. 7, p. 100359, 2019/09/01/ 2019, doi: <https://doi.org/10.1016/j.mtla.2019.100359>.
- [119] A. Yadollahi, N. Shamsaei, S. M. Thompson, and D. W. Seely, "Effects of process time interval and heat treatment on the mechanical and microstructural properties of direct laser deposited 316L stainless steel," *Materials Science and Engineering: A*, vol. 644, pp. 171-183, 2015/09/17/ 2015, doi: <https://doi.org/10.1016/j.msea.2015.07.056>.
- [120] H. S. Khatak and B. Raj, *Corrosion of austenitic stainless steels: mechanism, mitigation and monitoring*. Woodhead publishing, 2002.
- [121] A. Advani, L. Murr, D. Atteridge, and R. Chelakara, "Mechanisms of deformation-induced grain boundary chromium depletion (sensitization) development in type 316 stainless steels," *Metallurgical Transactions A*, vol. 22, no. 12, pp. 2917-2934, 1991.
- [122] A. Advani, L. Murr, D. Atteridge, R. Chelakara, and S. Bruemmer, "Deformation effects on intragranular carbide precipitation and transgranular chromium depletion in type 316 stainless steels," *Corrosion*, vol. 47, no. 12, pp. 939-947, 1991.
- [123] M. Laleh *et al.*, "On the unusual intergranular corrosion resistance of 316L stainless steel additively manufactured by selective laser melting," *Corrosion science*, vol. 161, p. 108189, 2019.
- [124] D. A. Macatangay, S. Thomas, N. Birbilis, and R. G. Kelly, "Unexpected Interface Corrosion and Sensitization Susceptibility in Additively Manufactured Austenitic Stainless Steel," *Corrosion*, vol. 74, no. 2, pp. 153-157, 2017, doi: 10.5006/2723.

- [125] G. Ng, A. Jarfors, G. Bi, and H. Zheng, "Porosity formation and gas bubble retention in laser metal deposition," *Applied Physics A*, vol. 97, no. 3, pp. 641-649, 2009.
- [126] L. E. dos Santos Paes, M. Pereira, F. A. Xavier, W. L. Weingaertner, and L. O. Vilarinho, "Lack of fusion mitigation in directed energy deposition with laser (DED-L) additive manufacturing through laser remelting," *Journal of Manufacturing Processes*, vol. 73, pp. 67-77, 2022.
- [127] N. Kurgan, "Effect of porosity and density on the mechanical and microstructural properties of sintered 316L stainless steel implant materials," *Materials & Design*, vol. 55, pp. 235-241, 2014/03/01/ 2014, doi: <https://doi.org/10.1016/j.matdes.2013.09.058>.
- [128] R. A. Hardin and C. Beckermann, "Effect of porosity on the stiffness of cast steel," *Metallurgical and Materials Transactions A*, vol. 38, no. 12, pp. 2992-3006, 2007.
- [129] R. Li, Y. Shi, Z. Wang, L. Wang, J. Liu, and W. Jiang, "Densification behavior of gas and water atomized 316L stainless steel powder during selective laser melting," *Applied Surface Science*, vol. 256, no. 13, pp. 4350-4356, 2010/04/15/ 2010, doi: <https://doi.org/10.1016/j.apsusc.2010.02.030>.
- [130] A. Chouhan, A. Aggarwal, and A. Kumar, "A computational study of porosity formation mechanism, flow characteristics and solidification microstructure in the L-DED process," *Applied Physics A*, vol. 126, no. 11, p. 833, 2020/10/07 2020, doi: 10.1007/s00339-020-04013-3.
- [131] G. Ziółkowski, E. Chlebus, P. Szymczyk, and J. Kurzac, "Application of X-ray CT method for discontinuity and porosity detection in 316L stainless steel parts produced with SLM technology," *Archives of civil and mechanical engineering*, vol. 14, no. 4, pp. 608-614, 2014.
- [132] T. Feldhausen, N. Raghavan, K. Saleeby, L. Love, and T. Kurfess, "Mechanical Properties and Microstructure of 316L Stainless Steel Produced by Hybrid Manufacturing," *Journal of Materials Processing Technology*, p. 116970, 2020/11/22/ 2020, doi: <https://doi.org/10.1016/j.jmatprotec.2020.116970>.
- [133] T. Feldhausen, N. Raghavan, K. Saleeby, L. Love, and T. Kurfess, "Mechanical properties and microstructure of 316L stainless steel produced by hybrid manufacturing," *Journal of Materials Processing Technology*, vol. 290, p. 116970, 2021/04/01/ 2021, doi: <https://doi.org/10.1016/j.jmatprotec.2020.116970>.
- [134] E. O. Hall, "The Deformation and Ageing of Mild Steel: III Discussion of Results," *Proceedings of the Physical Society. Section B*, vol. 64, no. 9, pp. 747-753, 1951/09/01 1951, doi: 10.1088/0370-1301/64/9/303.
- [135] N. J. Petch, "The Cleavage Strength of Polycrystals," 1953.
- [136] J.-O. Andersson, "A thermodynamic evaluation of the Fe-Cr-C system," *Metallurgical Transactions A*, vol. 19, pp. 627-636, 1988.
- [137] H. Sahlaoui and H. Sidhom, "Experimental Investigation and Analytical Prediction of σ -Phase Precipitation in AISI 316L Austenitic Stainless Steel," *Metallurgical and Materials Transactions A*, vol. 44, no. 7, pp. 3077-3083, 2013/07/01 2013, doi: 10.1007/s11661-013-1647-5.
- [138] "D18.2:2009 Guide to Weld Discoloration Levels on Inside of Austenitic Stainless Steel Tube (Large) Historical," ed: American Welding Society, 2009.

- [139] A. Plati, J. Tan, I. Golosnoy, R. Persoons, K. Van Acker, and T. Clyne, "Residual stress generation during laser cladding of steel with a particulate metal matrix composite," *Advanced engineering materials*, vol. 8, no. 7, pp. 619-624, 2006.
- [140] K. S. Saleeby and T. Feldhausen, "Effect of Dynamic Laser Processing with In-Situ Thermal Monitoring on Thin Wall Distortion," presented at the Additive Manufacturing with Powder Metallurgy Conference, Portland, Oregon, 2022.
- [141] "Thermal Circuit Theory," in *Building Heat Transfer*, 2004, pp. 57-73.
- [142] G. Sidebotham, *Heat Transfer Modeling An Inductive Approach*, 1st ed. 2015. ed. Cham: Springer International Publishing, 2015.
- [143] H. Peng *et al.*, "Fast prediction of thermal distortion in metal powder bed fusion additive manufacturing: Part 1, a thermal circuit network model," *Additive Manufacturing*, vol. 22, pp. 852-868, 2018.
- [144] G. Swift, T. S. Molinski, and W. Lehn, "A fundamental approach to transformer thermal modeling. I. Theory and equivalent circuit," *IEEE transactions on Power Delivery*, vol. 16, no. 2, pp. 171-175, 2001.
- [145] C. Ghiaus and I. Hazyuk, "Calculation of optimal thermal load of intermittently heated buildings," *Energy and Buildings*, vol. 42, no. 8, pp. 1248-1258, 2010.